공학박사학위논문

직접분사식 가솔린 엔진의 연소 및 입자상물질 배출 모델 개발

Development of Combustion and Soot Emission Models for Direct-Injection Spark-Ignition Engines

2017 년 8 월

서울대학교 대학원

기계항공공학부

김 주 한

직접분사식 가솔린 엔진의 연소 및 입자상물질 배출 모델 개발

Development of Combustion and Soot Emission Models for Direct-Injection Spark-Ignition Engines

지도교수 민 경 덕

이 논문을 공학박사 학위논문으로 제출함

2017 년 5 월

서울대학교 대학원

기계항공공학부

김 주 한

김주한의 공학박사 학위논문을 인준함

2017 년 6 월

위 원 장 고 상 근 (인)

부위원장 민 경 덕 (인)

위 원 송 한 호 (인)

위 원 도 형 록 (인)

위 원 최 회 명 (인)

Abstract

Development of Combustion and Soot Emission Models for Direct-Injection Spark-Ignition Engines

Joohan Kim
Department of Mechanical and Aerospace Engineering
The Graduate School
Seoul National University

Energy issue of fossil fuel depletion and environmental issue of global warming have been the powerful spur to develop a more efficient engine. Direct-injection spark-ignition (DISI) engine combined with turbocharging technology, renowned as one of the most pursued solutions for next-generation powertrain, is capable of increasing thermal efficiency by their abilities to mitigate knock and to reduce pumping loss. Despite these merits, the direct injection deteriorates the homogeneity degree of the air-fuel mixture and induces the fuel film deposition on the wall. Consequently, the unfavorable particulate matter emission increases in significant level compared to the conventional port fuel injection engine. In the light of environmental and public health concerns, the EU imposed a regulatory limit on the particulate number (PN) of $6x10^{12}$/km as of September of 2014, and the target will be tightened to $6x10^{11}$/km in 2017. This goal is challenging to meet without an after-treatment system. Thus, a substantial optimization of the combustion chamber and operating strategies should be conducted systematically.

Though the fundamentals of soot formation are same for both Diesel and DISI engines, the air-fuel mixture preparation and the combustion processes are different. In Diesel engine, the turbulent diffusion combustion after the fuel injection is

proceeded, and the soot is mainly formed in the core of spray plume. By contrast, in DISI engines, the locally fuel-rich mixture is formed due to the fuel film deposition and the short mixing time, and the soot is produced in the behind of the turbulent propagating flame near wall region. Therefore, it is required to develop the numerical models relevant to DISI engine application.

The aim of this study is to develop combustion and soot emission models for DISI engines, and it comprises three major modeling concerns. Firstly, to improve the prediction accuracy of air-fuel mixture field inside the cylinder, a six-component surrogate fuel that covers the wide range of boiling point, as well as the same aromatic content of real gasoline, was developed and validated with the gasoline analysis data. In addition, the Kelvin-Helmholtz Rayleigh-Taylor (KH-RT) model for spray break-up was calibrated against the droplet size distribution and penetration length data obtained from a set of rig-experiments.

Secondly, the partially-premixed turbulent combustion in DISI engines was modeled by the G-equation. A new correlation for the laminar burning velocity of gasoline fuel was developed with an emphasis on the prediction improvement of burning velocity in the fuel-rich mixture. In regard to the effect of aromatic hydrocarbons on burning velocity for fuel-rich branch, the laminar burning velocities of three hydrocarbons, iso-octane, n-heptane, and toluene, were calculated by PREMIX code in conjunction with detailed mechanism developed in LLNL, and were blended by the energy fraction based mixing rule to derive the laminar burning velocity of gasoline.

Thirdly, a detailed soot modeling framework including the gas-phase polycyclic aromatic hydrocarbons (PAHs) formation as well as the solid-phase soot aerosol dynamics were proposed with the level-set flamelet library approach and two soot models. To determine the chemical composition behind of flame front including the PAHs' concentrations, a detailed chemical mechanism which contains the reaction pathway of PAHs up to coronene ($C_{24}H_{12}$) was employed to calculate the laminar

premixed flamelet equation under wide thermos-chemical conditions. From the full solution of flamelet equation, five representative PAHs were adopted for the soot precursors. For the soot evolution, a semi-empirical soot model was developed, in which the soot nucleation was described as PAHs dimerization. Furthermore, the method of moment interpolative closure (MOMIC) was also coupled to the flamelet library to explore the state-of-the-art predictability.

The developed models were validated under three sets of engine experiments with various operating conditions. Firstly, the soot emission similarity between the surrogate fuel and real gasoline was verified by conducting the PFI engine experiment with the variation of equivalence ratio at hot operating condition. Secondly, the preliminary evaluation for the sub-models was carried out by comparing the combustion and soot emission results with that measured from the DISI engine experiment under a catalyst heating condition. Finally, the developed models were validated against the DISI engine experiment by varying the injection strategies under cold steady-state operating condition. Based on the modeling and validation work, the combustion and soot emission models developed in this study can be actively used for the engine development and optimization process in the future.

Keywords: DISI Engine, Combustion, Soot Emission, Gasoline Surrogate Fuel, Flamelet Library Approach, Detailed Soot Model Framework

Student Number: 2010-20663

Table of Contents

List of Figures

List of Tables

Nomenclature

A/F	Air/Fuel Ratio
aBDC	After Bottom Dead Center
aIGN	After Ignition
aTDC	After Top Dead Center
bBDC	Before Bottom Dead Center
BC	Black Carbon
BDC	Bottom Dead Center
BEV	Battery Electric Vehicle
bTDC	Before Top Dead Center
CDA	Cylinder De-Activation
CFD	Computational Fluid Dynamics
CFR	Cooperative Fuel Research
cHRR	Cumulative Heat Release Rate
COV	Cycle of Variation
CVVL	Continuous Variable Valve Lift
CVVT	Continuous Variable Valve Timing
DBE	Double Bond Equivalent
DC	Distillation Curve
DI	Direct Injection
DISI	Direct Injection Spark Ignition
DNS	Direct Numerical Simulation
DPF	Diesel Particulate Filter
EGR	Exhaust Gas Recirculation
EPA	Environmental Protect Agency
EU	European Union
EVC	Exhaust Valve Closing
FBP	Final Boiling Point

FCEV	Fuel Cell Electric Vehicle
FCHEV	Fuel Cell Hybrid Electric Vehicle
FESEM	Field Emission Scanning Electron Microscopy
FTP	Federal Test Procedure
GCR	Group Chemistry Representation
GPF	Gasoline Particulate Filter
GTDI	Gasoline Turbocharged Direct Injection
gIMEP	Gross Indicated Mean Effective Pressure
HACA	H-Abstraction-C_2H_2-Addition
HCCI	Homogeneous Charge Compression Ignition
HEV	Hybrid Electric Vehicle
HRR	Heat Release Rate
IBP	Initial Boiling Point
ICCD	Intensified Charge-Coupled Device
IVC	Intake Valve Closing
KH	Kelvin-Helmholtz
LBV	Laminar Burning Velocity
LIF	Laser Induced Fluorescence
LTC	Low Temperature Combustion
MFB	Mass Fraction Burned
MOMIC	Method of Moments Interpolative Closure
MON	Motored Octane Number
NA	Naturally Aspirated
NEDC	New European Driving Cycle
nIMEP	Net Indicated Mean Effective Pressure
NTC	Negative Temperature Coefficient
PAH	Polycyclic Aromatic Hydrocarbon
PHEV	Plug-in Hybrid Electric Vehicle
PM	Particulate Matter
PN	Particulate Number

PRF	Primary Reference Fuel
PSDF	Particle Size Distribution Function
RANS	Reynolds-Averaged Navier-Stokes
RAYLIX	Rayleigh-Scattering Laser-Induced Incandescence and Extinction
RNG	Renormalized Group theory
RON	Research Octane Number
RT	Rayleigh-Taylor
RVP	Reid Vapor Pressure
SI	Spark Ignition
TDC	Top Dead Center
TRF	Toluene Reference Fuel
WLTC	World-harmonized Light-duty Test Cycle
WSR	Well-stirred Reactor

Chapter 1. Introduction

1.1 Background and Motivation

Worldwide concerns about global warming and fossil fuel depletion have led to a substantial cut in CO_2 emissions from passenger cars, enforced by regulatory boards. The European Union (EU) has approved the reduction of the amount of CO_2 to a target of 95 g/km until 2020, while the United States and Canada have specified a target of 89 g/km by 2025 [1]. South Korea has also imposed a target of 97 g/km similar to EU. However, the regulation takes effect on 2020 which is five years earlier. The regulation level of EU represents an approximately 30% reduction compared to the current limit of 130 g/km, while the that of U.S. and Canada indicates 44% reduction against the level now imposed of 158 g/km. Furthermore, the amount of CO_2 should be suppressed by 7.1% per year to achieve the limit for South Korea, which is the most stringent regulation among the world.

There has been continuous research and considerable efforts to develop an alternative powertrain for a vehicle that runs either with hydrogen or by electricity. It was usually claimed that the sales of internal combustion engine would be diminished, while the market share of hybrid electric vehicle (HEV), fuel cell electric vehicle (FCEV) and battery electric vehicle (BEV) would be increased. However, the market outlook from the authoritative source [2] indicated that it is too early to predict the bright prospects for those alternative vehicles, and it still forecasted that the mainstream of vehicle powertrain will be the internal combustion engine.

The vehicle equipped with an internal combustion engine converts the chemical energy of hydrocarbon fuel into the heat energy by combustion, and thereby into the

mechanical energy by the reciprocating piston movement [3]. The former is characterized as combustion efficiency, η_c, whereas the latter is quantified as thermal efficiency, η_t, and the product of these two factors is known as the fuel conversion efficiency (η_f) that indicates the efficient degree of the engine. From this overall perspective, the improvement of thermal efficiency plays the key role for meeting the upcoming stringent CO_2 emission regulation as well as the fuel economy regulation.

Advanced fuel economy technologies have been introduced to the spark-ignition (SI) engine application for increasing the thermal efficiency and reducing the pumping losses. For instance, the direct injection (DI), turbocharger system, continuous variable valve timing (CVVT) and lift (CVVL), cylinder deactivation (CDA), and so forth. Among them, the direct-injection technology with a turbocharging system in spark-ignition engines, known as downsized direct-injection spark-ignition (DISI), has received significant attention because of its improved fuel economy and increased power output. The fuel economy is improved by its higher compression ratio and larger sweet-spot area of the BSFC map in contrast with the conventional natural-aspirated port fuel injection (PFI) engine [4].

Despite these advantages, DISI engines suffer from undesirable soot emissions. The direct injection induces the partially-premixed mixture and liquid film deposition during the mixing process, and the local rich combustion and pool fire leads to a significant production of soot particles [5]. It has been demonstrated that the soot emission depends on the engine operating conditions and parameters, among which the cold driving condition and injection strategies tend to predominate [6-10]. Several experimental studies found that the injection timing, fuel rail pressure, and coolant temperature substantially affect the emissions level [7, 11, 12]. Also, an optically accessible engine with a high-speed camera, endoscope, and laser diagnostic revealed

that inhomogeneity, wall wetting, spray-valve interaction, and injector coking would attribute to the soot emissions [13-15].

The particulate size and number are much smaller and greater than those of Diesel engines with DPF, so the soot emission from DISI engines has emerged as a significant issue in the automotive industry. Considering environmental and public health concerns, the EU imposed a regulatory limit on the particulate number (PN) of $6x10^{12}$/km as of September of 2014, and the target will be tightened to $6x10^{11}$/km in 2017 [16]. This goal is challenging to meet without an after-treatment system. Thus, a substantial optimization of the combustion chamber and operating strategies should be conducted systematically.

Particulate formation and oxidation are the local phenomena and are affected by the thermodynamic and chemical state of the mixture distribution, so that a mean cylinder quantity is unable to explain the emission level fully. Furthermore, the particle size distribution ranges from nucleation mode to accumulation mode, and the favored conditions for their formation mechanisms are different. Therefore, a comprehensive understanding is required for the optimization task. Recently, computational fluid dynamics (CFD) has become an essential step in the engine development process because it can offer a quantitative analysis and minimize prototype development cost.

To reap the advantages of simulation, the distinct features of in-cylinder physics in DISI engines should be figured out, and a set of models that relevant to those physics has to be formulated. With a focus on soot emission, the accuracy of simulation result relies on the precise description of the air-fuel mixture field before the spark onset, and the combustion as well as the post-flame reaction process. Furthermore, it is worth to mention that the modeling should obtain the consistency

in the level of detail between each physics, the efficiency in the computational time, and the sensitivity to engine parameter variation. In the following, an extensive literature review will be drawn. By posing the definition of terminology for soot emission, the fundamentals of soot formation mechanism is discussed. Then, the soot emission characteristics in DISI engines found from the experiments are summarized. Finally, the progress on the soot modeling for DISI engines are reviewed and their limitations are addressed.

1.2 Literature Review

1.2.1 Definition of Terminology for Soot Emission

The terminologies for soot and particulate matter (PM) are defined before starting the main discussion. PM emitted from the vehilces equipped with an internal combustion engine is a complex compound that consists of volatile (i.e. soluble) and nonvolatile component (i.e. insoluble) because not only non-hydrocarbon constituent in the additives in the transportation fuel but also the lubricant oil stripped from the cylinder wall can participate in the combustion process. Three major classes exist in the volatile compound. One is the organic fraction, either soluble or volatile, which is a chemical compound of hydrocarbon added with nitrogen, oxygen, and sulfur elements. Other two are the water-soluble sulfate fraction (SO_4^{2-}) and the nitrate fraction (NO_3^-). For a nonvolatile fraction, it is made up by the carbonaceous fraction and ash fraction. The former is usually known as soot and black carbon (BC), and it arises from the carbon atom in fuel. The ash fraction is a sundry inorganic compound in which the metal predominates the total fraction, and it originates from the inorganic component in fuel.

From X-ray diffraction investigation [17] (see Fig. 1.6), it is shown that the carbon atoms of a primary soot particle are packed into hexagonal face-centered arrays, commonly referred to as platelets. Platelets are arranged in layers to form crystallites, and there are typically two to five platelets per crystallite. Figure 1.7 shows a typical PM structure from a DISI engine powered vehicle without equipping the gasoline particulate filter (GPF) [10]. An overall shape is a chain-like form where the primary particles take place at the core and the volatile organic fraction wrap around the soot. It is demonstrated that the individual solid spherules ranged in size from 20 to 100 nm.

Furthermore, the size of engine aerosol varies in the sub-micron range due to the coagulation as well as aggregation of soot aerosol dynamics. It has been identified that three different modes exist in engine aerosol [18]. One is the nucleation mode has diameter ranges of 3 to 30 nm and consists of volatile organic and sulfate fraction. Though its mass does not exceed 10% of total mass, it contributes most particle numbers up to 90%. Following the nucleation mode is the accumulation mode that has diameter ranges of 20-500 nm and consists of the carbonaceous aggregates and absorbed material. The last one is the coarse mode which usually comprises the re-entrained accumulation mode particles and the crankcase oil.

Based on the above discussion, in this study, "soot" rather than "particulate" is used for the engine-out emission with the meaning of carbonaceous fraction. For the tailpipe emission from vehicles, it is relevant to use "particulate" because of additional reaction can be introduced into the exhaust system. Accordingly, the number density and mass density predicted from the soot model accounts for the carbon addition rather than that of volatile organic compound and ash compound. The "soot nuclei" describes the nascent soot, while the "primary particle" indicates the diameter size of 20-30 nm.

1.2.2 Fundamentals of Soot Formation Process

Though the soot emission characteristics can be varied along the application, but the fundamentals of soot formation are the same regardless of the types of fuel and flame. During the combustion, the chemical reaction under high temperature breaks the parent hydrocarbon fuels into smaller one and converts to the final combustion product across the flame [19]. In the fuel-rich condition, the recombination of propargyl radicals (C_3H_3) or the addition of acetylene (C_2H_2) to C_4 species, the so-

called odd carbon atom and even carbon atom pathway, respectively, initiate the formation of the first aromatic rings such as benzene (C_6H_6) or phenyl radical (C_6H_5). Then, the first ring hydrocarbon undergoes the "H-Abstraction-C_2H_2-Addition (HACA)" process to be grown up for condensed multi-ring soot precursor as known as polycyclic aromatic hydrocarbon (PAH) [20]. Until now, the reaction is in gas-phase and the order of molecule size.

It has been documented that the transition of gas-phase species to solid particles is probably the least understood part of the soot formation process [19]. After much argument, it turns out that the soot inception is mainly governed by the physical process of PAH dimerization [20] rather than the ionic reaction [21] or purely chemical growth [22]. The soot nuclei as the smallest solid particles have diameters in the range of 1.5-2 nm, which correspond to the 100-400 carbon atoms [23]. Then the soot particles start to grow either by the chemical reaction of HACA growth or by the physical process of PAH condensation on their surface. Simultaneously, the soot particles collide each other to form bigger one; the coagulation indicates the complete coalescence to form a spherical particle, while the aggregation depicts the fractal structure by the chains of particles. The oxidation via oxygen molecule and OH radicals is effective for the whole process.

In summary, the PAH formation is governed by the rate-controlling reaction between the small aliphatic and by the HACA growth. The soot nucleation is correlated with the dimerization of PAHs, and the soot particle evolution is governed by the aerosol dynamics. Hence, these gas-phase as well as solid-phase processes are closely linked together, so that both of them should be considered in soot emission modeling.

1.2.3 Soot Emission Characteristics in DISI engines

Though it's not for DISI engine, as a pioneering research, [24-26] conducted a combined experimental and modeling investigation to examine the soot formation in SI engine. In their studies, at first, the effect of engine operating conditions, such as the global and local air/fuel (A/F) ratios, coolant and lubricant oil temperature, spark timing, and exhaust gas recirculation (EGR) on PM formation were investigated experimentally [24]. They demonstrated that the A/F ratio has most significant impact on PM; the emission level can be increased by as many as three orders of magnitude when the A/F ratio is either increased or decreased 30% from stoichiometric. Liquid fuel that participates the combustion is also an influential factor for PM emission, and it is affected by the fuel injection timing such as close valve injection or open valve injection, the coolant and intake charge temperature.

Then, the effect of fuel type, lubricant oil and catalytic converter on PM formation were explored with a set of engine experiments [25]. It has been documented that the PM emission varies by up to 6 order of magnitude between different fuels investigated at the same A/F ratio. Lubricant oil might contribute a certain portion to PM emission within 0 to 40% under their examined condition. Finally, they [26] derived an empirical correlation of PM mass considering the nucleation, oxidation, and growth physics of PM, and the model was verified under the vast amount of engine parameter such as equivalence ratio, fuel injection timing, coolant and lubricant oil temperature, spark timing, EGR, engine speed and load. Although their studies are based on the SI engine rather than incorporating direct-injection, the fundamentals of underlying physics of PM formation in the combustion type of SI engine were intensively analyzed.

Numerous experimental research have been conducted to characterize the soot emission from DISI engines by varying the operating conditions and strategies. Choi et al. [10] studied the effect of engine operating conditions on the PM emissions from a DISI engine powered vehicle. In their research, the vehicle equipped with a 2.4 L naturally-aspirated DISI engine was incorporated to run the New European Driving Cycle (NEDC) mode test. It has been reported that the most of the soot particles were emitted during the cold driving condition, such as cold idling, cold acceleration, and cold steady run. Among them the cold acceleration recorded the highest amount of soot emission during the cycle, and the total sum of the soot emission from cold condition was up to 70%. Indeed, the mitigated fuel vaporization and less homogeneous mixture inside the cylinder deteriorated the soot emission level.

Velji et al. [27] conducted an optical engine experiment with RAYLIX technique, which is a combination of Rayleigh-scattering, laser-induced incandescence and extinction to measure the temporally and spatially resolved soot concentration, mean soot diameter, and number density. It has been observed that the main sources of soot emission in homogeneous DISI engines were the pool fire on the piston surface. By contrast, the stratified DISI engines showed the soot formation occurred in the free combustion chamber volume due to the locally fuel-rich mixture region and it was followed by the pool fire on the piston.

Whitaker et al. [9] investigated the soot emission from a gasoline turbocharged direct injection (GTDI) engine with optical measurement. It has been demonstrated that the spray impingement on the piston and liner led a significant localized luminous diffusive flame during the combustion process. They discussed that the key parameter to reduce the soot emission would be the abatement of fuel impingement on the piston surface. To optimize the operating strategy, the multiple injections, spray patterns, and fuel injection pressure were further studied. It was shown that the multiple injection

as well as the high injection pressure had potential to improve the soot emission level in GTDI engines.

Farron et al. [7] performed a detailed investigation of particulate sizing and number count from a DISI engine with the variation of engine load, air-fuel ratio, spark timing, injection timing, fuel rail pressure, and oil and coolant temperatures. It was found that the soot emission increased with following parameters: retarded injection timing due to wall wetting and spray impingement, increased engine load for higher injection mass, rich air-fuel ratio because of less oxidizer, decreased injection rail pressure owing to increased fuel droplet size, and low coolant temperature by inhomogeneity of mixture preparation. Among them, the fuel rail pressure, injection timing, and the cold start showed the great impact on the soot emission level compared to the baseline measurement data.

In addition, the injector coking and spray-valve interaction were also to be known as the minor sources for the soot emission. Berndorfer et al. [14] attempted to establish a correlation between soot emission and luminous diffusive flame during the combustion process with an emphasis on the coked injectors. It has been measured that the strong visible signal by a bright diffusive flame event was radiated from the region close to the injector tip after the main combustion. They found that the higher soot emissions were recorded along the higher index of injector diffusion flame. It was asserted that the part of fuel was stored in the coked injector tip area and was released later in the combustion cycle that caused a locally bright diffusive combustion event.

Steimle et al. [5] carried out the optically accessible engine experiment *via* an endoscope to examine the soot emission sources in the cylinder. In their work, a spray-guided DISI engine was used where the central injection of fuel took place. It was

documented that a noticeable component wetting during the injection phase occurred, where the intake valves interact with the fuel spray during the valve opening duration. Consequently, the luminous diffusion flame was developed on the periphery of the intake valve seat area.

In summary, the soot emission from DISI engines can be classified into two major categories: one is the inhomogeneity and the other one is wall wetting. These primary sources become severe when the coolant temperature is low, such as cold-start driving condition. Thus, it can be concluded that the soot emission characteristics in DISI engines are totally different from that in Diesel engines due to the fuel delivery method and types of combustion.

1.2.4 Key Features of Soot Emission Modeling for DISI Engines

Based upon review on the theoretical description of soot processes and the experimental findings for soot emission in DISI engines, it can be concluded that there are three major key features should be resolved in soot modeling for DISI engines. Firstly, as the fuel is delivered by direct injection, the spray quality in terms of the droplet size distribution as well as the penetration length should be well-described. Furthermore, as only the finite time is allowed for fuel vaporization and air-fuel mixing, a surrogate fuel which can describe the full boiling range of real gasoline should be formulated. Secondly, as the flame propagation governs the combustion process and the soot formation arises from the local-fuel rich mixture, the model should captures the mass burning rate in that mixture. Thirdly, the model framework has to cover the PAH formation and the soot aerosol dynamics processes. The chemical mechanism for prediction of PAH concentration is preferred rather than the

assumption with the simple algebraic equation, because the PAHs play the key role and bridges the gap between combustion chemistry and soot particle evolution.

Before to be focused on the soot modeling progress for DISI engine, the overall modeling approach proposed for internal combustion engines are briefly presented as follow. For the prediction of PAH concentration, in the engine research field, the acenaphthylene ($C_{12}H_8$) [28] or pyrene ($C_{16}H_{10}$) [29] were used for the soot precursor, and some of the works were incorporated non-PAH as for the precursor, such as parent fuel [30], acetylene [31], ethane [32]. By contrast, in the flame research field, the chemical mechanisms for larger PAH formation have been developed in that the larger PAH, such as cyclopenta[cd]pyrene ($C_{18}H_{10}$) [33] or coronene ($C_{24}H_{12}$) [34], were predicted as the final outcome. For the soot evolution modeling, there are two categories in the modeling approach: one is the semi-empirical approach that can calculate the averaged quantities of soot number density and volume fraction, and the other one is the detailed approach that provides further information on the size distribution even in the chemical structure of soot, and these will be reviewed in Chapter 5. Both modeling approaches have already been applied for the Diesel engine application [35-41], however, only the semi-empirical one was adopted for the DISI engine so far [30, 32, 42, 43].

1.2.5 Progress on Soot Modeling of DISI Engines

Unlike the long history of soot emission modeling in Diesel engine due to their NOx/PM trade-off issue, relatively a few studies were carried out to analyze and examine the PM formation in an SI engine. Recently, several CFD modeling studies have been proposed as the regulatory board begin to reinforce the regulations on PM and PN emission from DISI vehicles. Kwon et al. [30] simulated the pollutant of

gaseous as well as soot in a DISI engine under hot operating condition. Toluene reference fuel was used for surrogate fuel, and the generic soot model by Fusco et al. [36] was adopted to simulate the soot emission in DISI engines. The soot model started with fuel pyrolysis described in Arrhenius equation, and the acetylene was provided by the flamelet library. Though it was shown that the emission level were well coincidence to the experimental values, the soot model was too simple to describe the complex physics of the soot processes, and it required to calibrate for matching the emission level by adjusting model constant.

Jiao and Reitz [44] performed CFD simulations to study the particulate formation in SI engine by varying the mixture equivalence ratio from 0.98 to 1.5 under the premixed condition. The reason for using premixed condition is to focus on gas-phase chemical reaction and to exclude inhomogeneity and wall film effect during simulation. In their study, a semi-detailed soot model for Diesel and low-temperature combustion (LTC) application [29] and chemical kinetics of n-heptane/toluene oxidation [45] were adopted. Based on the well-matched combustion phasing, it is reported that the model qualitatively captures the size distribution behavior but no direct comparison results. Also, only the simulation results of soot concentration were shown without any comment on measured value.

Sukegawa and Oryoji [46] investigated two numerical approaches for estimating the nucleation rate in SI engines. Similar to the work [44], they also used premixed condition with the same purpose. They proposed two approaches that one assumes the chemical reaction in a computational cell as that occurred in the zero-dimensional homogeneous reactor and the other one presume one-dimensional flame propagation. For the pre-tabulation of the database, the 0-D approach uses a chemical mechanism [47] which describes the laminar flame of C_1-C_2 hydrocarbon with PAH growth up to five aromatic rings, and 1-D approach adopts a chemical mechanism [48] which

simulates the laminar flame of n-butane with PAH reaction, respectively. It was shown that the 1-D flame approach for database establishment was more suitable to predict the soot emission level measured from engine experiments, where the particulate number was drastically increased with respect to the equivalence ratio around 1.45. However, no other simulation results regarding the soot concentration and size distribution were presented.

Reaction Design group [42] conducted a CFD simulation of soot formation in a DISI engine. A detailed chemical kinetics was developed by using Model Fuel Library and Surrogate Blend Optimizer which is their commercial products, and it was used to provide the flame speed, burned composition, and pyrene concentration as the soot precursor. A pseudo-gas soot model, which was originally developed for LTC Diesel application, was adopted. For the model validation, IFPEN engine data including the soot measurement using planar laser-induced incandescence and laser extinction method were used, and the simulation results were compared to the 2-D averaged soot volume fraction in the laser-passed plane. Though it highlights the comparison between optical measurement and CFD simulation, neither the soot number density nor the soot concentration from the exhaust was compared in the study.

Jiao and Reitz [49] investigated the effect of operating parameters on soot emission in DISI engines. The same soot model proposed in previous research [44] was adopted, and the engine parameters that fuel composition, spray cone angle, start of injection timing, and wall temperature were varied. The changes in the soot emission level was indicated, however, no experimental data were compared to verify the model prediction.

Dong et al. [32] proposed an improved Hiroyasu two-step model to simulate the soot formation in a downsized DISI engine. The injection timing from 330° CA bTDC

to 180° CA bTDC by 30° CA step were swept, and a chemical mechanism consisting 22-species was incorporated to provide the precursor, ethylene (C_2H_4). It was reported that the two-equation model relatively well captured the emission level from engine experiments. However, only the soot mass was compared against the measured value so that the number density prediction was neglected in the study.

As the spray-wall interaction and hence the fuel film are known as a major contributor to soot emission in DISI engines, the modeling study focused on these physics also can be found in the literature. Köpple et al. [50] investigated the spray-wall interaction via a rig-experiment using infrared-thermography and fluorescence technique to observe the wall temperature drop due to the fuel film wetting. A surrogate fuel was formulated as a ternary mixture of n-hexane, iso-octane, and n-decane, and it was compared against the single component of n-heptane regarding deposited fuel film mass. The investigation was extended to engine simulation in their follow-up study [51], where the soot emission results were shown but with the soot volume fraction only.

Recent the state-of-the-art modeling research that covers the soot emission from wall films in a DISI engine was conducted by Jiao and Reitz [43]. The simulation model contains several Engine Research Center sub-models including fuel break-up, gas-jet theory, droplet collision and vaporization, spray-wall interaction, and the semi-detailed soot model as shown previously [29]. In addition to these model chain, the wall film model was revised to account for the grid independence, and the toluene pyrolysis mechanism was introduced to consider the reaction pathway in fuel-rich condition effectively. Based on a series validation of sub-models, finally, the model was simulated in GTDI engine against a simpler model set. Though the model was comprehensively verified in rig-experiment level, the validation by the measured engine-out soot emission in number and concentration was not shown in the study.

Figure 1.8 illustrates the summary of the previous research as stated above. The parameters shown in the table are the important factors should be considered in the soot emission modeling for DISI engines. There are several things commonly found in the literature. First, the surrogate fuel for real gasoline used in some studies cannot fully resolve the wide volatility characteristics. Secondly, either overly simplified soot model such as two-equation or generic soot model, or the model used in the Diesel engine application were adopted. Thirdly, most studies use the well-stirred reactor approach to calculate the reaction behind of flame front and to provide burned chemical compositions. Indeed it is the popular approach, but it requires a reduced chemical mechanism for CFD simulation to mitigate computational overload. Finally, no previous work was validated the simulation results of not only soot concentration but also soot number density against measurement value.

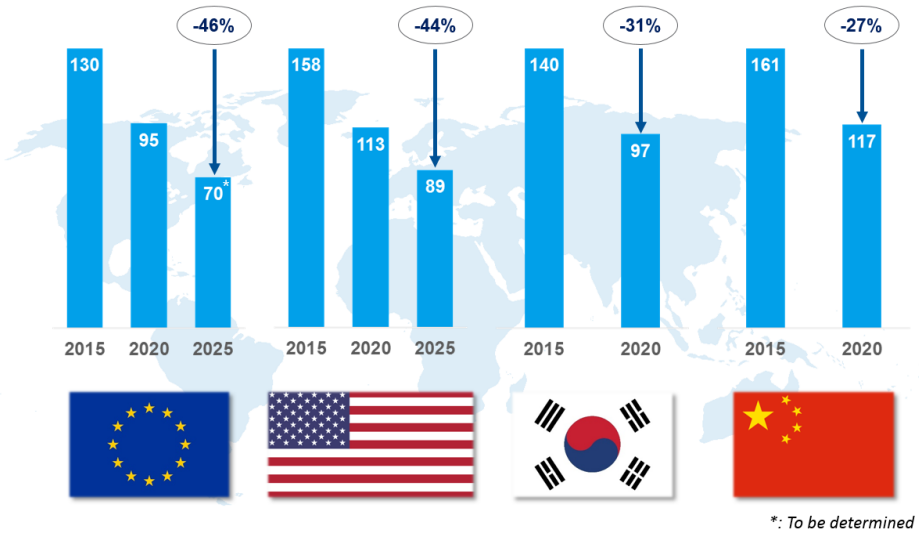

Figure 1.1 Comparison of worldwide CO_2 regulations for new passenger cars [1].

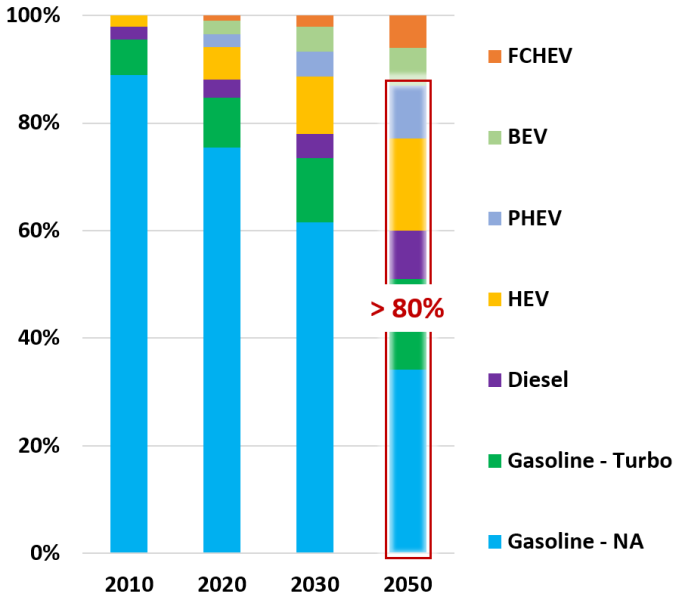

Figure 1.2 New vehicle market share for 2010-2050 predicted by MIT [2].

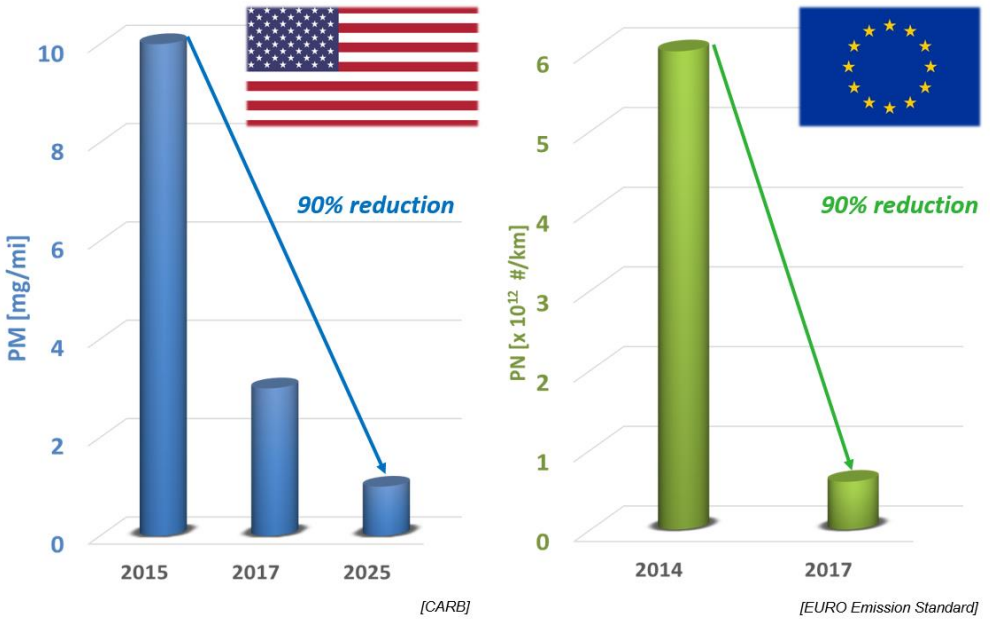

Figure 1.3 Regulations on Particulate matter from DISI engine powered vehicles [16].

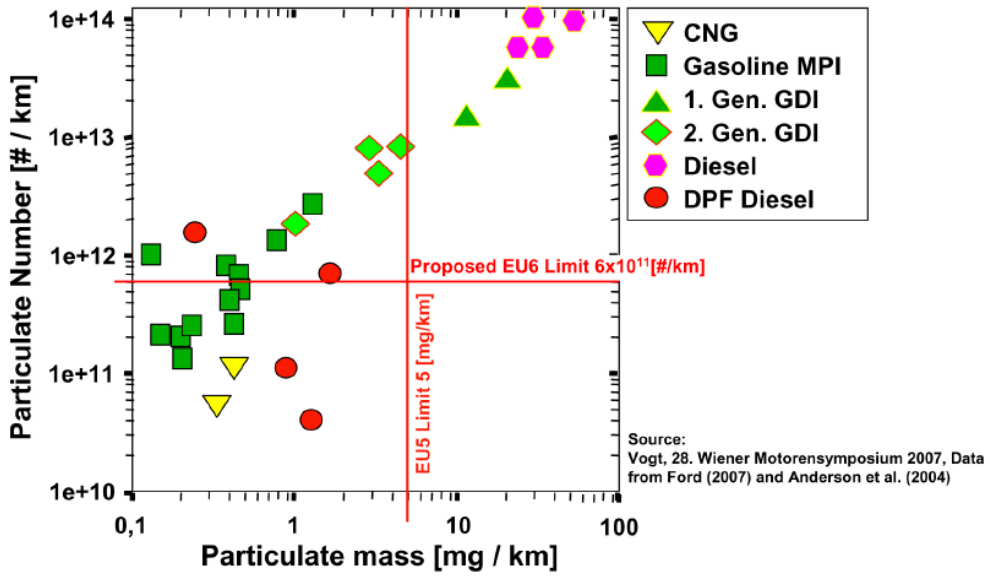

Figure 1.4 Particulate matter emissions from gasoline and Diesel engines [52].

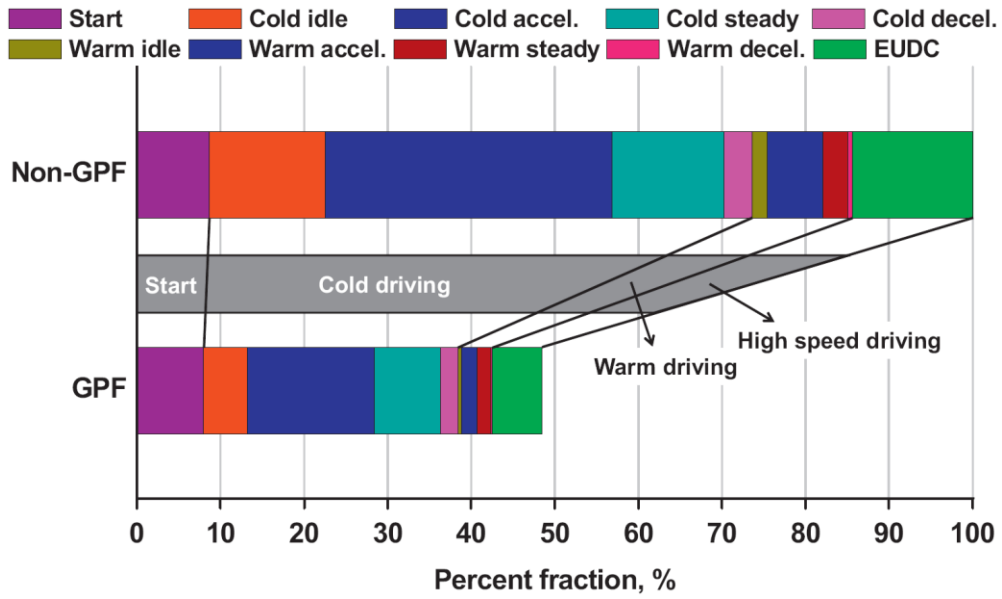

Figure 1.5 Particulate matter emission from a 2.4L DISI engine powered vehicle according to various driving conditions [10].

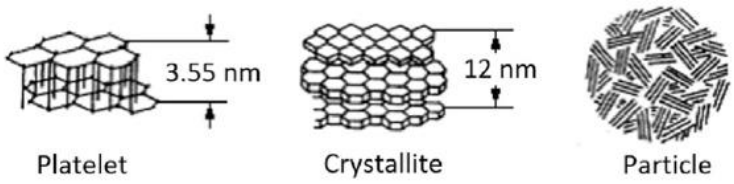

Figure 1.6 Structure of primary particle analyzed by the X-ray diffraction [53].

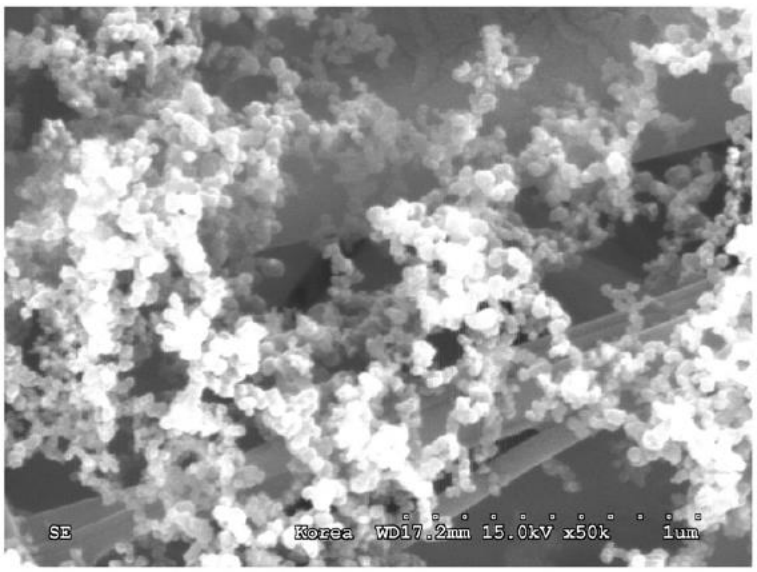

Figure 1.7 FESEM image of particulate matter from a non-GPF DISI vehicle that filtrated on fluorocarbon-coated glass filter [10].

	Kwon et al., (2012)	Dong et al., (2016)	Naik et al., (2014)	Jiao and Reitz (2015)
Surrogate fuel	TRF	(Not mentioned)	7-component	10-component
Soot precursor	Fuel	C_2H_4	Pyrene ($C_{16}H_{10}$)	
Soot processes	Empirical *(Fusco's 8-step)*	Empirical *(Hiroyasu's 2-eqn.)*	Semi-empirical *(PAH reaction + phenomenon model)*	
Validation Target	#, V	V	No exp. data comparison	

#: soot number density [#/cc]
V: soot volume fraction [cc/cc]

Figure 1.8 Progress and limitation of preceding work on soot emission modeling for DISI engines.

1.3 Research Objectives

It is evident that the inhomogeneous air-fuel mixture and the fuel film wetting are the primary sources of the soot emission in DISI engines, and the injection parameters and wall temperature contribute to those physics significantly. In contrast to the Diesel engine where turbulent diffusion flame governs the entire combustion process, in DISI engines, the turbulent flame propagation under partially-premixed condition dominates, and the combustion of fuel-rich mixture leads the PAH formation as well as soot emission. The detailed description of the soot formation in DISI engines has not yet been conducted, so it is worth to explore the state-of-the-art model of soot aerosol dynamics for DISI engine application.

Therefore, the aim of this work is to develop the combustion and soot emission models for DISI engines based on the level-set flamelet library approach and two different soot models. The modeling comprises three major sub-models as follow:

1. Modeling for air-fuel mixture field
- *Six-component gasoline surrogate fuel*
- *Spray break-up model calibration*

2. Modeling for fuel-rich combustion
- *Laminar burning velocity of gasoline fuel*

3. Modeling of soot formation
- *Flamelet library including PAH concentrations*
- *Soot aerosol dynamics by a semi-empirical model and the method of moments interpolative closure (MOMIC) [54]*

In the engine development point of view, the model should able to predict the soot emission level for both number density and soot concentration according to the variation of engine operating parameters. Therefore, the developed models were validated under three sets of engine experiments with various operating conditions. Firstly, the soot emission similarity between the surrogate fuel and real gasoline was verified by conducting the PFI engine experiments with the variation of equivalence ratio at a hot operating condition. Secondly, a preliminary evaluation for the developed sub-models was carried out by comparing with the combustion and soot emission data measured from the DISI engine experiment under the catalyst heating condition. Finally, the developed models were validated against the DISI engine experiment by varying the injection strategies under cold steady-state operating condition.

1.4 Structure of Thesis

This work is divided into eight main chapter. In chapter 2, the basic principle of flow, and modeling methodology of spray and liquid film are reviewed. In chapter 3, the surrogate fuel development of six-component spray surrogate coupled with combustion surrogate is described. In chapter 4, the partially premixed combustion process is modeled by G-equation level set approach. With a focus on burning rate in the fuel-rich mixture, a new correlation for the laminar burning velocity of gasoline fuel is derived. In chapter 5, the flamelet library approach is presented, and the formulation of two soot models are discussed. Based on the model development, in chapter 6, the evaluation of the soot emission similarity is presented first, and the preliminary model validation is discussed. In chapter 7, a set of numerical simulation by the model developed in this study is performed under various injection strategies, and the validation is drawn against the measured data from DISI engine experiment. Finally, this work closes with a summary and conclusions in chapter 8.

Chapter 2. Turbulent Flow, Fuel Spray, and Liquid Film Modeling

2.1 Turbulent Flow Description

In this section, the fluid dynamics and turbulence theory for a chemically reacting gas are presented. The governing equation which is known as Navier-Stokes equation is introduced. Then, the Reynolds-Averaged Navier-Stokes (RANS) equations are derived, and a two-equation turbulence model for the fulfillment of modeling closure problem is introduced. The scales of turbulent flow, and the conventional and Favre averaging of fluid motion are summarized in Appendix A.

2.1.1 Conservation Equations

Fluid flows are described by a system of coupled, nonlinear, partial differential equations, which is known as Navier-Stokes equations [55]. For a non-constant density, the mass conservation equation can be written in Cartesian coordinate using tensor notation as

$$\frac{\partial \rho}{\partial t} + \frac{\partial}{\partial x_j}\left(\rho u_j\right) = \dot{S}_M \ , \tag{2.1}$$

where ρ is the density of fluid, u_j is the fluid velocity component in direction x_j, and $\dot{S}_M$ is the mass source. For an engine system consisting liquid-phase injection which interacts with the gas flow, the source term represents the change of mass due to the vaporization/condensation between two-phases. The momentum conservation equations for each direction *i* can be expressed as

$$\frac{\partial}{\partial t}(\rho u_i) + \frac{\partial}{\partial x_j}\left(\rho u_i u_j\right) = -\frac{\partial p}{\partial x_j} + \frac{\partial \tau_{ij}}{\partial x_j} + \dot{S}_F \ , \tag{2.2}$$

where p is the pressure, τ_{ij} is the stress tensor, and $\dot{S}_F$ is the momentum source. For Newtonian fluids, the stress tensor τ_{ij} accounts for the molecular rate of momentum transport, and it is written as

$$\tau_{ij} = \mu\left(\frac{\partial u_i}{\partial x_j} + \frac{\partial u_j}{\partial x_i}\right) - \frac{2}{3}\mu\frac{\partial u_k}{\partial x_k}\delta_{ij} \ , \tag{2.3}$$

where μ is the dynamic viscosity, δ_{ij} is the Kronecker delta ($\delta_{ij} = 1$ if i = j and $\delta_{ij} = 0$ otherwise). If the chemical reaction takes place in the fluid flow, additional conservation equations for species mass fraction are required. The conservation equation for the mixture enthalpy *h* is defined as

$$\frac{\partial}{\partial t}(\rho h) + \frac{\partial}{\partial x_i}(\rho h u_i) = \frac{Dp}{Dt} + \tau_{ij}\frac{\partial u_i}{\partial x_i} - \frac{\partial j_i^q}{\partial x_i} + \dot{S}_H \ , \tag{2.4}$$

where h is mixture enthalpy, j_i^q is the heat flux due to thermal diffusion and enthalpy transport by species diffusion, and $\dot{S}_H$ is the enthalpy source term. The static enthalpy includes the species heat of formation Δh_f^0 according to

$$h = \sum_{n=1}^{N} Y_n \left(\Delta h_{f,n}^0 + \int_{T_0}^{T} c_{p,n} dT\right) \ , \tag{2.5}$$

where N is the number of species involved in the reacting system, and $c_{p,n}$ is the specific heat constant of nth species. Each constituent n of a fluid mixture, whose local concentration is expressed as a mass fraction Y_n, is assumed to be governed by a species conservation equation of the form

$$\frac{\partial}{\partial t}(\rho Y_n) + \frac{\partial}{\partial x_j}(\rho Y_n u_j) = \frac{\partial}{\partial x_j}\left(\rho D_n \frac{\partial Y_n}{\partial x_j}\right) + \rho\dot{\omega} + S_i \ . \tag{2.6}$$

2.1.2 RANS and Turbulence Models

Based on the averaging schemes discussed in Appendix A, the ensemble average of Navier-Stokes equation yields the RANS equations. Note that these equations only describe the integral length and time scales, while the motion of smaller scales is modeled rather than being solved. The averaged continuity equation is derived as

$$\frac{\partial \bar{\rho}}{\partial t} + \frac{\partial}{\partial x_j}(\bar{\rho}\tilde{u}_j) = \tilde{\dot{S}}_m \ . \tag{2.7}$$

The averaged momentum equations are

$$\frac{\partial(\bar{\rho}\tilde{u}_i)}{\partial t} + \frac{\partial(\bar{\rho}\tilde{u}_i\tilde{u}_j)}{\partial x_j} = -\frac{\partial \bar{p}}{\partial x_i} + \frac{\partial \bar{\tau}_{ij}}{\partial x_j} - \frac{\partial}{\partial x_j}\left(\bar{\rho}\widetilde{u_i'' u_j''}\right) + \tilde{\dot{S}}_i \ . \tag{2.8}$$

In contrast to the continuity equation which retains the original form instead of changing the instantaneous quantities to averaged one, the third term in right-hand side is an additional term due to the average of the nonlinear convective term. This is known as Reynolds stresses, and it is determined by a turbulence model via the turbulent viscosity hypothesis which will be discussed later. The averaged enthalpy equation reads

$$\frac{\partial(\bar{\rho}\tilde{h})}{\partial t} + \frac{\partial(\bar{\rho}\tilde{h}\tilde{u}_i)}{\partial x_i} = -\frac{\overline{Dp}}{Dt} - \frac{\partial \overline{J_i^q}}{\partial x_i} - \frac{\partial}{\partial x_i}\left(\bar{\rho}\widetilde{u_i'' h''}\right) + \tilde{\dot{S}}_H \ . \tag{2.9}$$

Here, the third term similar to the momentum equation represent the nonlinear convective enthalpy transport by turbulent fluctuations, and it also needs to be modeled.

To resolve the closure problem of RANS equations, the eddy-viscosity hypothesis proposed by Boussinesq [56] was widely adopted so far. According to the hypothesis, the Reynolds stress is proportional to the mean rate of strain,

$$-\rho\langle u_j u_j\rangle + \frac{2}{3}\rho k\delta_{ij} = \rho\nu_T\left(\frac{\partial\tilde{u}_i}{\partial x_j} + \frac{\partial\tilde{u}_j}{\partial x_i}\right) = 2\rho\nu_T\tilde{S}_{ij} \tag{2.10}$$

where ν_T is the turbulent viscosity (also called eddy viscosity). It has been demonstrated that the turbulent viscosity is not a fluid intrinsic property such as molecular viscosity, but it is a flow property depends on the turbulence. Number of models were derived to model the turbulent viscosity with relevant length and velocity scales: mixing length model [57], one-equation model [58], two-equation models [59, 60] Reynolds-stress model [61]. In this study, the two-equation model based on renormalization group (RNG) analysis, *k*-*ε* RNG model [62, 63] was adopted to modeling the turbulent flow. The turbulent viscosity is modeled as $\nu_T = C_\mu {k^2}/{\varepsilon}$, and the governing equations for turbulent kinetic energy and turbulent dissipation rate is given as follow. The model coefficients are listed in Table 2.1.

Turbulent kinetic energy

$$\frac{\partial}{\partial t}(\bar{\rho}\tilde{k}) + \frac{\partial}{\partial x_j}(\bar{\rho}\tilde{k}\tilde{u}_j)$$

$$= \frac{\partial}{\partial x_j}\left(\left(\mu + \frac{\mu_t}{\sigma_k}\right)\frac{\partial \tilde{k}}{\partial x_j}\right) + \mu_t(P + P_B) - \bar{\rho}\tilde{\varepsilon}$$

$$-\frac{2}{3}\left(\mu_t \frac{\partial \tilde{u}_i}{\partial x_i} + \bar{\rho}\tilde{k}\right)\frac{\partial \tilde{u}_i}{\partial x_i} \quad .$$

(2.11)

Turbulent dissipation rate

$$\frac{\partial}{\partial t}(\bar{\rho}\tilde{\varepsilon}) + \frac{\partial}{\partial x_j}(\bar{\rho}\tilde{\varepsilon}\tilde{u}_j)$$

$$= \frac{\partial}{\partial x_j}\left(\left(\mu + \frac{\mu_t}{\sigma_k}\right)\frac{\partial \tilde{\varepsilon}}{\partial x_j}\right) + C_{\varepsilon 1}\frac{\tilde{\varepsilon}}{\tilde{k}}\left[\mu_t P - \frac{2}{3}\left(\mu_t \frac{\partial \tilde{u}_i}{\partial x_i} + \bar{\rho}\tilde{\varepsilon}\right)\frac{\partial \tilde{u}_i}{\partial x_i}\right]$$

$$- C_{\varepsilon 2}\bar{\rho}\frac{\tilde{\varepsilon}^2}{\tilde{k}} + C_{\varepsilon 3}\frac{\tilde{\varepsilon}}{\tilde{k}}\mu_t P_B + C_{\varepsilon 4}\bar{\rho}\tilde{\varepsilon}\frac{\partial \tilde{u}_i}{\partial x_i} - \frac{C_\mu \eta^3(1-\eta/\eta_0)}{1+\beta\eta^3}\frac{\rho\varepsilon^2}{k} \quad .$$

(2.12)

Table 2.1 Coefficients of the RNG k-ε turbulence model.

C_μ	σ_k	σ_ε	σ_h	σ_m
0.085	0.719	0.719	0.9	0.9
$C_{\varepsilon 1}$	$C_{\varepsilon 1}$	$C_{\varepsilon 1}$	$C_{\varepsilon 1}$	
1.42	1.68	0.0	-0.387	
		1.42 (if $P_B > 0$)		
κ	E	η_0	β	
0.4	9.0	4.38	0.012	

2.2 Modeling of Spray Injection

In DISI engine, gasoline is directly injected into the cylinder and mixed with the fresh air and residual gas during the intake and compression stroke. It occurs within a finite duration in the order of tens of milliseconds so that the air-fuel mixture is in partially-premixed state at the ignition timing. Furthermore, the deposition of fuel film induces the local fuel-rich mixture around the wall. These are known as primary sources of soot formation in DISI engines. It is worth to note that the break-up governs the air-fuel mixture distribution in the cylinder, and the spray penetration affects the location of fuel film deposition. Therefore, accurate numerical description of spray evolution is responsible to the reliable simulation results of air-fuel mixture preparation, and thereby it is of great importance to the prediction of soot emission from DISI engines.

In the field of spray research, the spray structure and quality have been extensively investigated through the measurement of spray penetration length, droplet size distribution, and velocity field between the jet and surrounding gas by high-speed imaging and phase Doppler anemometry system [64-66]. However, in the field of DISI engine simulation, the research to date has not treated the droplet size distribution as a target for spray validation in much detail. Few attempts have been made to compare the Sauter mean diameter with respect to time after injection [67], while most studies were matched the macroscopic spray morphology in a qualitative sense [68-70] or the spray penetration length [71, 72]. In this study, among the spray physics, the break-up model was calibrated against the measured droplet size distribution as well as penetration length from rig-experiment to secure the authenticity of air-fuel mixture preparation in the cylinder.

2.2.1 Sub-models of Spray Injection

Here, the sub-models for turbulent dispersion, break-up, and droplet-wall interaction are presented. Note that existing models were adopted rather than were newly developed in this study so that further information can be found in each literature.

Turbulent dispersion and inter-droplet collision

The turbulent dispersion of droplets was described by a stochastic approach [73] which assumes the droplet interacts with the isotropic turbulent flow and the velocity fluctuation by turbulence obeys a Gaussian probability density function. The injected fuel droplets interact with each other by the turbulent flows, and the inter-droplet collision would be induced to coalescence, separation, and bouncing [74]. For an injection event, the number of droplets is up to tens of thousands so that the collision process is usually modeled by cell clustering method [75] and speed-up algorithm [76]. However, for the sake of computational efficiency, the inter-droplet collision was ignored in this study.

Droplet-wall impingement

The fuel droplet impinged on the combustion chamber wall undergoes adhesion, spread, rebound, and splash depending on the incident momentum and wall temperature condition. In this study, a wall impingement model by Rosa et al. [77] was incorporated to resolve the droplet-wall interaction physics.

Droplet break-up

The Kelvin-Helmholtz (KH) and Rayleigh-Taylor (RT) model [78] was used to describe the break-up physics of multi-hole injector equipped with DISI engines. Detailed information can be found in the literature and only the break-up time and size were discussed here. The KH model describes the primary break-up of intact liquid core induced by the aerodynamic interaction between surrounding gas and liquid jet. By monitoring the Kelvin-Helmholtz wave instability at the liquid-gas interface, it is assumed that a parent parcel break-up to form the smaller droplets if the wavelength of the fastest growing wave, Λ_{KH}, is larger than the circumference of parent parcel. The radius of child droplet and the break-up time are defined as

$$r_c = B_0 \Lambda_{KH} \ , \tag{2.13}$$

$$\tau_{KH} = \frac{3.726 B_1 r}{\Lambda_{KH} \Omega_{KH}} \ , \tag{2.14}$$

where B_0 is a model constant of 0.61, B_1 is an arbitrary constant with default value of 40, r is the radius of parent parcel, and Ω_{KH} is the frequency of fastest growing wave.

The RT model depicts the secondary break-up based on the Rayleigh-Taylor instability. The air-drag decelerates the droplet momentum and leads the unstable waves on the droplet surface. If the scaled wavelength of the fastest growing wave, $C_3 \Lambda_{RT}$, is greater than the drop diameter, the model starts to track the break-up time as

$$\tau_{RT} = \frac{C_\tau}{\Omega_{RT}} \ , \tag{2.15}$$

where C_τ is a constant usually equal to unity, C_3 is adjustable constant with default value of 0.1, and Ω_{RT} is the frequency of fastest growing wave. Once the break-up time reaches the criteria, the parent droplet break-up into smaller drops whose radius is $r_c = C_3\Lambda_{RT}$. It has been noted that the C_3 as well as C_τ can be altered to regulate the rate of catastrophic break-up of dispersed droplets, whereas the B_1 can be tuned to control the initial disturbance level near the nozzle. The calibration of the model constant will be discussed in later.

2.2.2 Break-up Model Calibration: Experimental Setup

To secure the authenticity of air-fuel mixture preparation before the ignition timing, the break-up model was calibrated against the measurement data of spray penetration length and droplet size distribution obtained from a set of rig-experiments. In this study, a multi-hole DISI injector used in engine experiment, and its specification is summarized in Table 2.2. The injection foot print at the 50 mm below the nozzle tip was shown in Fig. 2.1.

The measurement of penetration length and droplet size distribution are based on the Mie-scattering theory, which postulates the Mie-scattering intensity is proportional to the square of droplet diameter if the droplet size is larger than 1 μm. For the penetration length measurement, an injector driver MOTEC UID 800 was used to control the injection event, which is connected to a pulse generator DG 535 for operating the injector needle opening/closing and defining the injection period. A high-speed ICCD camera Photron Ultima APX synchronized with the pulse generator was installed to acquire the spray images in user-defined time frame rate. A high-pressure pump was used to pressurize the fuel rail to specified injection pressure. The injection pressure was set at 100 bar, and the image of freely-evolving spray under

atmospheric pressure and ambient room temperature was obtained at the frame rate of 0.2 ms interval.

For the droplet size distribution characterization, the same injector drivers and pulse generator were used, while the high-speed ICCD camera was replaced with a Malvern Mastersizer 2000. The measurement was conducted at the location 30 and 70 mm below the injector tip. Because the data acquisition is done based on point-wise measurement while the width of the spray is much larger than the size of the laser spot, the experiment was conducted by sweeping the measurement location in horizontal directions. The injection pressure was varied from 60 to 100 bar by 20 bar step to observe the changes in the characteristics of the droplet size distribution.

In KH-RT break-up model, it has been documented that the constant C_3 can be tuned to modify the effective wavelength of RT wave, while the constant C_τ can be altered to regulate the rate of catastrophic break-up of dispersed droplets [78]. In present study, only the constant C_3 in RT break-up model was adjusted from base value 0.1 to 0.3 for matching the measured spray evolution. The set of spray sub-models were applied as same as for engine simulation to preserve the applicability of calibrated result.

2.2.3 Break-up Model Calibration: Simulation Results

Figure 2.2 to 2.4 show the measured and simulated droplet size distribution under the three injection pressures. The measurement revealed that the number of large droplets was decreased whereas that of small droplets were increased as the spray developed, and the converting amount was increased as the injection pressure elevated. It is interesting to note that the moderate break-up exists across the spray evolution.

The simulation with the base model constant showed excessive break-up rate and resulted in narrow size distribution in the range of 0 to 20 um. By contrast, the calibrated model with the constant C_3=0.3 well captures the practical physics, and the simulation results were in agreement with the measurement data.

From the Fig. 2.5, it is clear that the calibrated model is capable of reproducing the measured spray evolution and structure, while the base model shows an entirely different spray shape. It is because that the base model constant leads the shorter effective RT wavelength which promotes the break-up rate, the droplets around the periphery of spray plume break-up into much smaller droplets and thereby only the core liquid jet was left. The penetration length is directly related to the in-cylinder spray targeting as well as the spray momentum so that the under-prediction of penetration length would result in the different location of fuel film deposition and affect air-fuel mixing process, respectively.

The comparison between measured and simulated result for penetration length was depicted in Fig. 2.6. In the simulation, the penetration length is defined as the lowest location of the 95% liquid volume. The both penetration length of the base model and calibrated model coincide until 20 mm. However, they start to deviate as time proceeds where the base model under-predicts the penetration length about 10% with respect to the measurement. For a light-duty engine, the length below 60 mm is meaningful compared to the cylinder dimension so that the 10% is a quite significant discrepancy for practical usage. By contrast to the base model, the calibrated model shows good-agreement for entire penetration length up to 100 mm with less than 2% prediction error.

Table 2.2 Specification of the multi-hole DISI injector used in this study.

Parameter	Value
Injection actuation	Solenoid-type
Injector hole number	6
Injector hole diameter	220 um
Static flow rate @ 100 bar	14.7g/s

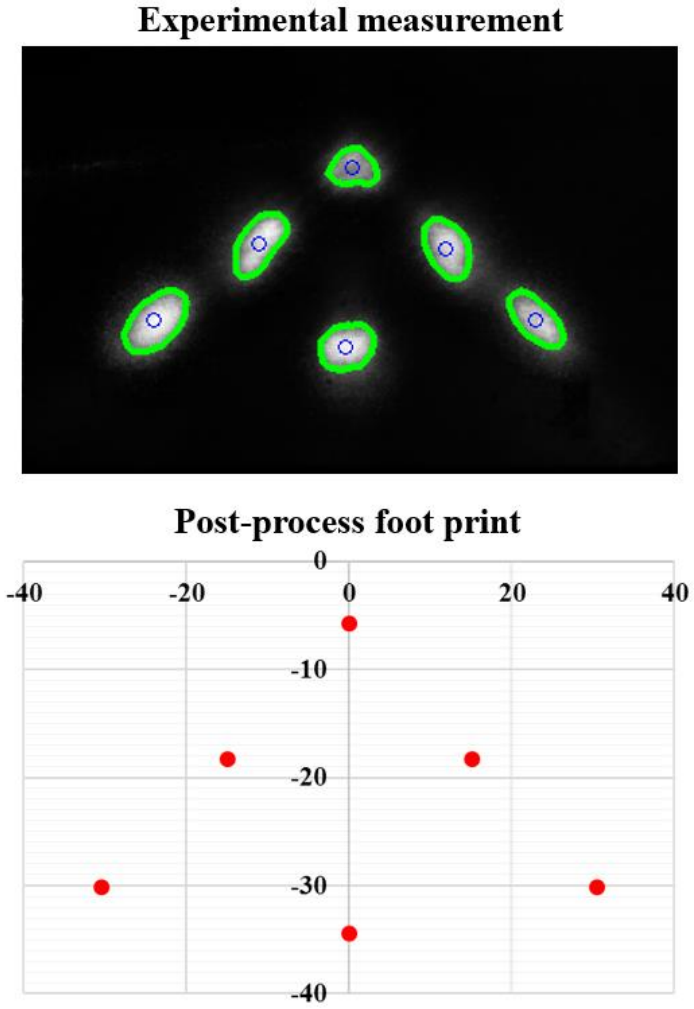

Figure 2.1 Measurement of the multi-hole injector foot print using Mie-scattering theory at 50 mm below the injector tip.

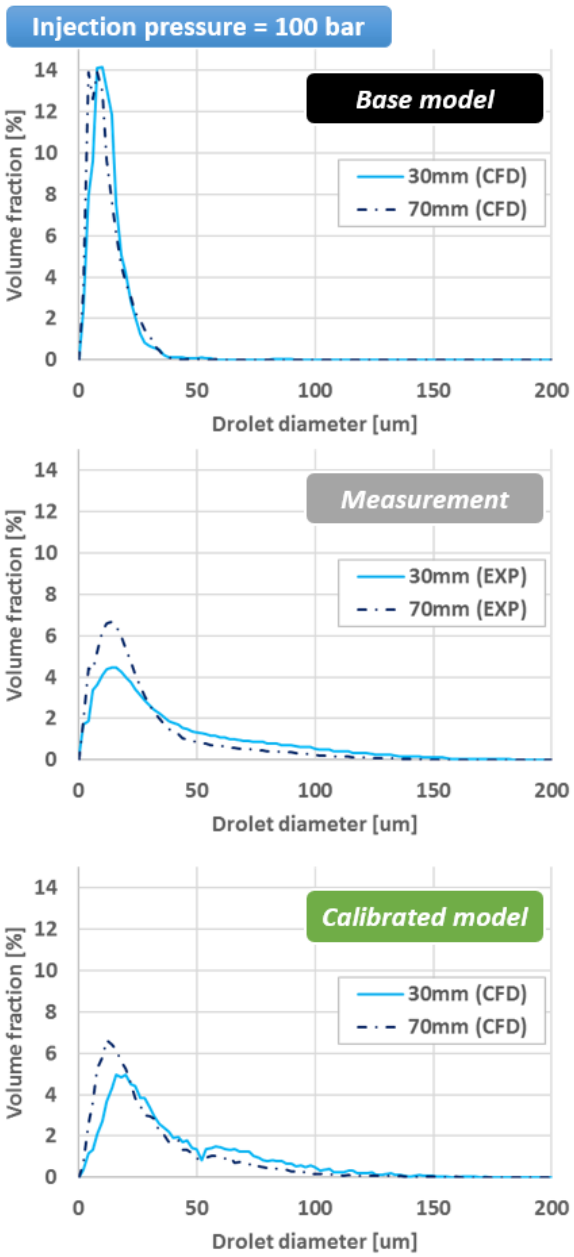

Figure 2.2 Measured droplet size distribution at 30 mm (solid line) and 70 mm (dash line) below the injector tip, and comparison of the simulation results from the base model and the calibrated model. The injection pressure was 100 bar.

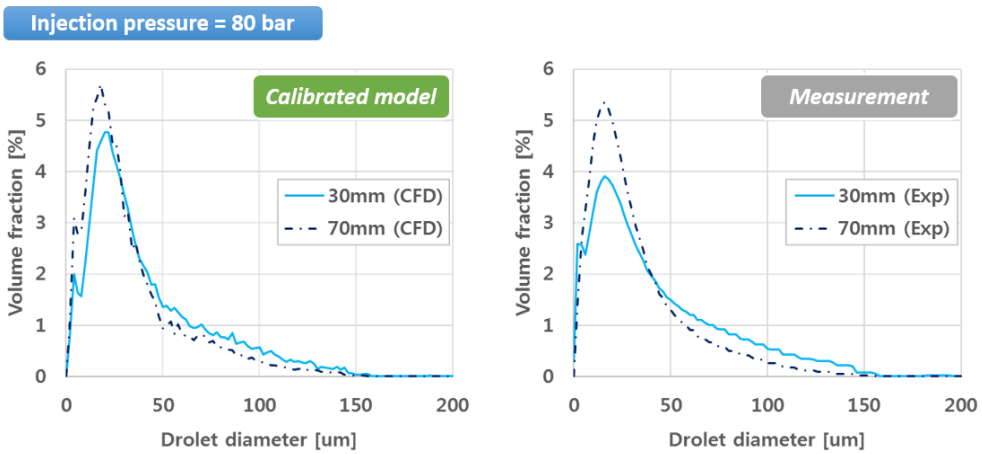

Figure 2.3 Comparison of calculated and experimental droplet size distribution at the 30 mm (solid line) and 70 mm (dash line) location under 80 bar injection pressure.

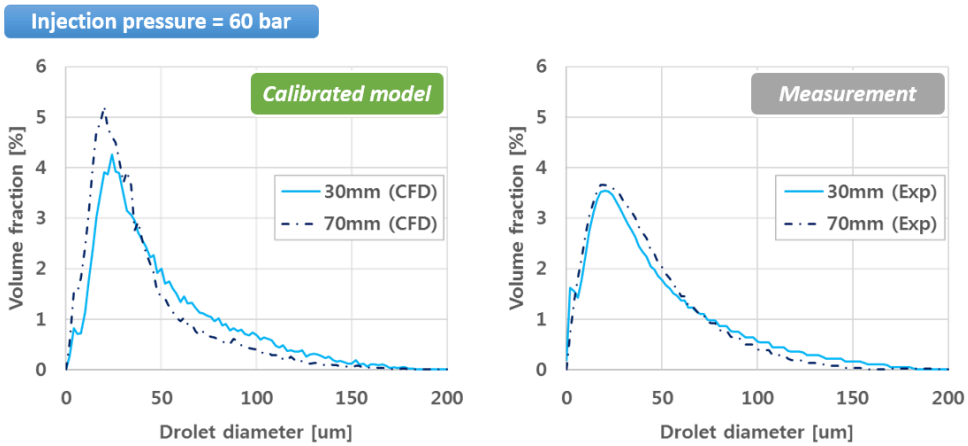

Figure 2.4 Comparison of calculated and experimental droplet size distribution at the 30 mm (solid line) and 70 mm (dash line) location under 60 bar injection pressure.

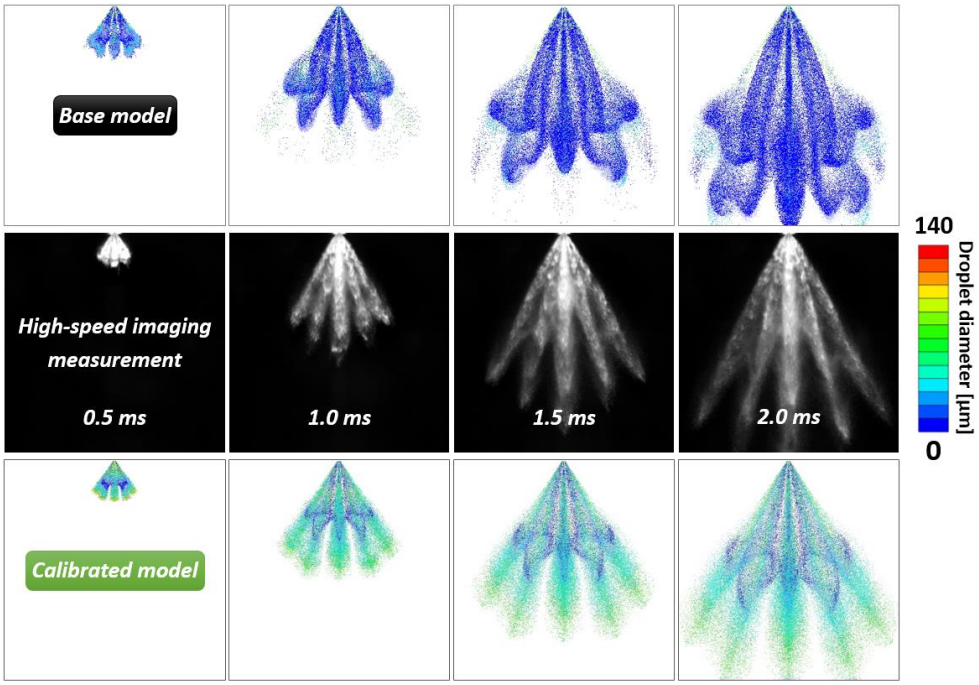

Figure 2.5 Comparison of spray morphology predicted by base (upper) and calibrated model (lower) against the measured data (center) acquired at t = 0.5, 1.0, 1.5, and 2.0 ms ASOI.

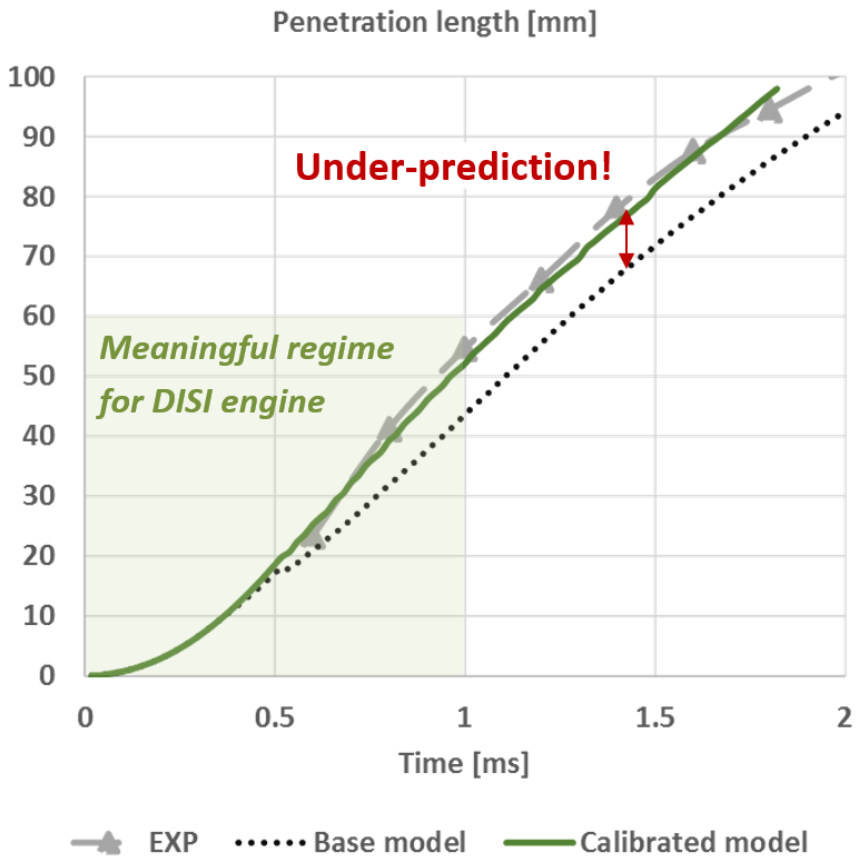

Figure 2.6 Comparison of base model (dotted line) and calibrated model's (solid line) penetration length with the measured (dash line with symbol) data at the injection pressure of 100 bar.

2.3 Modeling of Liquid Fuel Film

Based on the Eulerian approach, the fuel film dynamics were modeled according to the work of Bai and Gosman [79]. The model accounts for the multi-component evaporation and convective transport of conserved quantities within the film and from/to the gas phase. It assumes that the film is thin enough for the boundary layer approximation to apply, and the velocity profile across the film is parabolic, and the temperature and component mass fractions are piecewise linear.

The conservation equation for film mass is given by

$$\frac{\partial \rho_l}{\partial t} + \nabla \cdot (\rho_l \boldsymbol{u}_l) = \frac{\dot{m}_{inp}}{h} \tag{2.16}$$

where ρ_l is the film density, h is the film thickness, $\boldsymbol{u}_l$ is the film velocity tangential to the wall boundary surface, and $\dot{m}_{\text{inp}}$ is the mass source/sink per unit are due to droplet wall impingement or film separation. The conservation equation for film momentum is given by

$$\frac{\partial}{\partial t}(\rho_l \boldsymbol{u}_l) + \nabla \cdot (\rho_l \boldsymbol{u}_l \boldsymbol{u}_l) = -\nabla p_l + \rho_l \mathbf{g} + \nabla \cdot \tau_l + S_{imp}\delta(\xi - h) \tag{2.17}$$

where p_l is the pressure distribution within the film, τ_l is the stress tensor, S_{imp} is the momentum source corresponding to the mass source. The conservation equation for film enthalpy is given by

$$\frac{\partial}{\partial t}(\rho_l h_l) + \nabla \cdot (\rho_l \boldsymbol{u_l} h_l) = \nabla \cdot (k_l \nabla T_l) + \frac{\dot{Q}_{imp}}{h} \tag{2.18}$$

where h_l is the enthalpy, k_l is the conductivity, T_l is the film temperature, $\dot{Q}_{\text{imp}}$ is the enthalpy source corresponding to the mass source.

Film stripping

The liquid film on the piston and liner would experiences the growing instabilities on its surface due to the gravitational and axial acceleration by the piston movement, or shear force by the adjacent gas flow. Consequently, a certain portion would become detached from the wall surface and form droplets inversely. In this study, the film stripping was taken into account for by solving the dispersion equation of surface waves, in which the resonance wavelength is obtained as

$$\lambda_r = \frac{2\pi}{\rho_l g \cdot n}\left(\frac{1}{3}\rho_g \Delta U^2 - \rho_l g \cdot n\sigma_l\right) \tag{2.19}$$

When the surface wave amplitude, $h_a = \left(\frac{3}{4}\frac{1}{1.89^3}\right)^2 \pi\lambda_r$, exceeds the minimum height necessary for droplet ejection, $h_{\min} = \lambda_r/2\pi$, then a droplet with radius of $r_d = 1.89\sqrt{\lambda_r h_a/\pi}$ is detached from the liquid film.

Chapter 3. Modeling of Gasoline Surrogate Fuel

Real gasoline, as a refinery-blended hydrocarbon mixture, comprises hundreds of hydrocarbon species which vary in the number of carbon atoms between 4 and 12, and for the chemical families from paraffin to aromatics, according to the crude oil origin and refinery system. The complex product requires a simpler surrogate fuel for numerical simulation unless one would encounter an intractable computational load. The surrogate is aimed to emulate the gasoline properties within a limited number of pure hydrocarbons, and its components and compositions can be varied along the application targets, such as vaporization, auto-ignition, emission modeling. Like as the gasoline properties play the key role in the combustion and emission process, the surrogate fuel formulation takes priority over the other numerical models.

For DISI engines, the soot emission arises from the local fuel-rich mixture, so the fuel vaporization characteristics should be considered as the ultimate factor in the surrogate formulation. Furthermore, as the soot emission strongly correlates with the aromatic hydrocarbon due to its sooting-favored chemical structure, the hydrocarbon composition also should be taken into account for.

In this chapter, the gasoline surrogate formulation was conducted by following steps. Firstly, the previous work on gasoline surrogate formulation according to various application target was reviewed (Section 3.1). Secondly, the target properties with a focus on the combustion and soot emission in DISI engines were selected based on the literature review (Section 3.2). Thirdly, the chosen target properties of domestic commercial gasoline were analyzed to provide the surrogate formulation criteria (Section 3.3). Lastly, a six-component surrogate fuel was developed, and its compositions were determined, and the chemical reaction of the surrogate for combustion and emission was discussed (Section 3.4).

3.1 Literature Review

It has been asserted that a surrogate tailored for modeling of ignition process can be different from a surrogate applied for soot emission modeling [80]. Here, the literature review on the gasoline surrogate formulation for various application targets was carried out.

3.1.1 Flame propagation

In conventional SI engines, e.g. port-fuel injection engine or homogeneous DISI engine, the combustion process initiates from the electrical spark discharge then proceeds via the turbulent flame propagation. So, the laminar burning velocity and flame temperature are the key features to consider in the surrogate formulation. The former one will be discussed in Chapter 4 in detail, and the latter one is associated with the lower heating value. Iso-octane is the simplest single-component surrogate, and it has a lower heating value of 44.3 MJ/kg which is similar to that of gasoline around 44 MJ/kg. Due to its simplicity, iso-octane has been adopted for numerous simulation work [81-83]. Primary reference fuel (PRF), a binary mixture of iso-octane and n-heptane, is also a widespread surrogate for the same application target [84, 85].

3.1.2 Auto-ignition

In homogeneous-charge compression-ignition (HCCI) engines, developed for pursuing the high thermal efficiency and low harmful emissions, the spontaneous auto-ignition occurs inside the cylinder and consumes the air-fuel mixture within relatively short duration in contrast to the conventional SI engine. Thus, the auto-

ignition related characteristics are the essential ingredients to account for. Octane number is one of the representative auto-ignition property, and it is determined by the Cooperative Fuel Research (CFR) engine experiment using a primary reference fuel [86, 87], which is a paraffinic surrogate consisting iso-octane and n-heptane. Though PRF provides the representation of research octane number (RON) or motored octane number (MON) for a refinery-blended gasoline, several experimental works have shown that no single PRF composition is valid for entire operating conditions of HCCI engine [88, 89]. Because the gasoline contains not only the linear and branched paraffin but also other chemical families, e.g. olefins, naphthenes, and aromatics, and the ignition delay of latter three do not favor to possess negative temperature coefficient (NTC) region. The fuel sensitivity defines the ignition delay deviation attributed to the chemical families' NTC behaviors. To overcome the zero sensitivity of paraffinic surrogates, toluene reference fuel (TRF) as a ternary mixture of iso-octane, n-heptane, and toluene, has been proposed. Measurements in shock-tube [90], rapid compression machine [91], HCCI engine [92, 93] have been verified that the inclusion toluene is valid to mimic the auto-ignition behavior of gasoline under the broad range of investigated conditions.

3.1.3 Volatility

In DISI engines, the liquid gasoline is directly injected into the cylinder and is vaporized during the air-fuel mixing. The vaporization of liquid fuel takes finite time so that the air-fuel mixture field at the spark onset is in the partially-premixed state rather than fully homogeneous, premixed condition. Hence, the volatility plays a crucial role in the surrogate formulation for DISI engines.

It is well-known that the boiling temperature of hydrocarbon is influenced by the number of carbon atoms and the molecular structure. Unlike the definite boiling temperature for a pure hydrocarbon, gasoline fuel has a wide boiling range because it is the complex mixture of hydrocarbons as stated earlier. Two properties are used to measure the gasoline volatility: Reid vapor pressure and distillation curve. The former one is defined as the absolute vapor pressure exerted by liquid gasoline at 37.8°C (100°F), and its standard test method is established in ASTM-D323 [94]. The latter one is a set of boiling temperature against the distilled volume fraction, and its standard test method is given in ASTM-D86 [95]. The full spectrum of distillation curve for a typical gasoline ranges from 30 to 200°C.

In the volatility standpoint, the surrogates above, e.g. iso-octane, primary reference fuel, and toluene reference fuel, the boiling temperatures of each component are concentrated within 100 to 111°C so that it is far different from gasoline's volatility characteristics. Consequently, more hydrocarbon species covering from the light-end to heavy-end components were introduced as surrogate candidates in the recent fuel modeling research [96-99].

To sum up, the component and composition of gasoline surrogate vary according to intended application. Thus, the target properties should be identified first, and then the component and composition could be determined to match the real fuel properties.

3.2 Identification of Target Properties with a Focus on Soot Emission

For DISI engines, according to the above review, most important target properties for the surrogate fuel formulation are twofold. One is the volatility and density that related to the fuel vaporization and spray mixing momentum, and the other one is the burning velocity and low heating value that associated with the mass burn rate and chemical energy release. Because the aim of this study is to modeling soot formation in DISI engine, the emission characteristics also should be considered for the surrogate fuel formulation.

Efforts were made to quantify the relationship between the gasoline properties and vehicle PM emissions [100, 101]. In their work, a PM index was defined as a function of the double bond equivalent (DBE) and the vapor pressure at 443 K and evaluated the availability using 1,445 gasoline samples from various regions of the world. It implies not only volatility but also chemical structures of gasoline constituent have a significant impact on PM emission. Thus, it also should be taken into account for the target property candidate. In the following, the experimental observations for the effect of fuel quality on PM emission were briefly reviewed first, then the primary target properties were identified.

Khalek et al. [102] measured the total and solid particle mass, size and number from a DISI vehicles under FTP-75 and US06 drive cycles using three different U.S. commercial gasoline. One is similar to EPA certification gasoline for emission testing (Fuel A), and the others have the lowest (Fuel B, 151°C) and the highest final boiling point (Fuel C, 210°C), respectively. They reported that the more volatile gasoline (Fuel B) resulted in a 62% reduction of the solid particle number and an 88% reduction

in soot mass during the cold-start phase compared to Fuel C, although Fuel B has the highest aromatic content. In contrast to the Fuel B, the less volatile gasoline (Fuel C) exhibits the highest emission level, even if it has lowest aromatic content and a certain amount of oxygenates. It can be inferred that the final boiling temperature, as well as the distillation curve, predominates over the aromatic contents, and the similar results were observed from the literature [103].

The effect of aromatic content was explored in the work of Short et al. [104]. They performed a vehicle test to measure the black carbon, PM mass, and water-insoluble organic mass fractions from PFI and DISI vehicles under a unified transient testing cycle. Four different fuels were investigated: three of them have a constant octane number of 87 with various aromatic concentrations at 15%, 25%, and 35%, and fourth fuel with an octane number of 91 with 35% aromatic content. It is observed that increasing aromatic content increases BC emission facts, and one of DISI vehicles showed 356% increase in BC from 15% to 35% aromatic content.

The chemical families oxygenate, and additives also have been studied. Yinhui et al. [105] carried out an experimental study to investigate the effect of fuel properties on PM emission (PM 2.5) from modern DISI vehicles. Six test fuels with different aromatics, olefins, sulfur, methyl-cyclopentadienyl manganese tricarbonyl, and ethanol content were blended and tested to research on the PM mass, number, size distribution, and PAHs toxicity. It is reported that the fuel with 36.7% aromatic content leads the 11.5% and 47.9% increment of PM and PN emission compared to the base fuel with 28.5% aromatic content. The olefin content also affects both emissions because of its double-bond chemical structure, while the ethanol content reduces particulate emission under some certain operating conditions but the improvement was limited compared with reducing aromatics and olefins content in gasoline.

Zhu et al. [106] investigated the fuel quality on tailpipe PM emission from two DISI vehicles compliant with China 4 standard. The effects of aromatic and olefin content and distillation temperatures of 50% (T50) and 90% (T90) were examined under WLTC test mode. It is shown that the PM level was decreased by 69.7% when reducing the aromatics from 40% to 25%, while it was decreased 38.8% as T90 lowered from 185°C to 165°C, respectively. By contrast to the aromatics, reducing olefin content has a minor impact on particulate emission. As the olefin content reduced from 23% to 10% while maintaining aromatics at 40%, the PM emission factors increased by 14.1% and 21.2% during the low and medium speed phases, respectively, and decreased by 43.8% during the combined high and extra-high-speed phase. It can be deduced that the aromatic content has much more leverage than olefin for particulate emission.

In summary, it is evident that the volatility, as well as aromatic content, have a significant impact on the PM emission because of the synergetic effects by the residual-forming potential and the sooting-favored molecular structures. With these concerns in mind, the volatility, density, H/C ratio, heat of combustion, and aromatic content of gasoline were selected as target properties. The volatility can be characterized in either Reid vapor pressure (RVP) or distillation curve (DC); the latter was chosen and considered for the entire vaporization behavior. Because the knock prediction is beyond our interest, the matching of octane number was ignored in this study.

3.3 Experimental Analysis of Target Properties

In this study, a commercial summer gasoline supplied by Hyundai Oilbank was used, and its target properties were analyzed at Korea Institute of Petroleum Management. The atmospheric distillation and the quantitative determination of hydrocarbon chemical families were examined in compliance with the standard test method ASTM D86 [95] and ASTM D6839 [107]. The density measurement and the analysis of carbon and hydrogen element were performed according to Korea standard test method KS M 12185 and KS M 2963. The heat of combustion, including higher heating value and lower heating value, was measured following the ASTM D240 [108]. The analysis results are summarized in Table 3.1.

It is shown that the temperatures at distilled volume fraction of initial boiling point (IBP), 10% (T10), 50% (T50), 90% (T90), and final boiling point (FBP) were 38.0°C, 56.5°C, 86.9°C, 148.8°C, and 197.6°C, respectively, as shown in Fig. 3.1. The boiling range spanned around 160°C to obtain fully vaporized state. In addition, the liquid density at 25°C was 724.5 kg/m^3. The element analysis presented the molar ratio of hydrogen to carbon of 2.05, which is slightly higher than the other continent because of its high paraffinic hydrocarbon fraction. The H/C ratio determines not only the local equivalence ratio of the air-fuel mixture but also the heat of combustion. The lower heating value was 42.825 MJ/kg, and it laid between that of typical alkanes and aromatics.

Furthermore, the composition of gasoline was analyzed in detail. Table 3.2 shows the volume fraction with respect to the carbon atom number and hydrocarbon chemical families from the hydrocarbon composition analysis. Note that the gasoline contains oxygenates of 1.53% in a mass fraction, and the sum of total hydrocarbons does not equal to unity. In this study, the fraction of oxygenates was neglected, and

the compositions of each hydrocarbon chemical family were normalized with the measured total volume fraction of 92.23%. Also, the mono-olefins and cyclo-olefins were grouped and indicated as olefin hereafter.

From the Fig. 3.2, the paraffins took the highest fraction of 61.4%, and it was followed by the olefins and aromatics in 14.7% and 14.6%, respectively, and finally, the naphthenes held the lowest composition as 9.3%. It can be seen that the majority fraction was possessed by C_5-C_8 hydrocarbons and the rest of them was gradually decreased as the number of carbon atom became large. It is revealed that the olefins as well as naphthenes were mainly distributed under C_8, while the aromatics shared from C_7 to C_{10}.

Table 3.3 presents the volume fraction in the carbon number order from C_5 to C_{11+}, and it helps to figure out which hydrocarbon chemical families are responsible for the given carbon number. The paraffins took the majority portion until the C_8, while the olefins, naphthenes, aromatics possessed the second rank alternatively. For high carbon number as C_9 and C_{10}, the aromatic fraction was considerably increased, but it was replaced by paraffins in the C_{11+}. From the distillation curve, it can be deduced that the heaviest hydrocarbon might be the n-undecane ($C_{11}H_{24}$) which has the boiling point of 195.9°C. The aromatics hold large volume fraction in C_8 to C_{10}, and it would affect the vaporization characteristic and the sooting tendency.

Table 3.1 Analysis result of gasoline properties.

Test item		Test result	Unit	Test method
Distillation curve	Initial boiling point	38.0	°C	ASTM D86-12
	5%	51.6		
	10%	56.5		
	20%	63.0		
	30%	69.1		
	40%	77.1		
	50%	86.9		
	60%	98.3		
	70%	108.1		
	80%	123.5		
	90%	148.8		
	95%	171.6		
	Final boiling point	197.6		
Density (@ 15 °C)		724.5	kg/m^3	KS M ISO 12185:2003
Element analysis	Carbon	84.05	(m/m) %	KS M2963:2008
	Hydrogen	14.46		
Heat of combustion	HHV	45.890	MJ/kg	ASTM D240-14
	LHV	42.825		
Hydrocarbon composition analysis	Paraffins	56.64	(v/v) %	ASTM D6839-13
	Olefins	13.4		
	Naphthenes	8.55		
	Aromatics (total)	13.5		
	Aromatics (benzene)	0.64		

Table 3.2 Results of hydrocarbon composition analysis (ASTM D6839): Volume fraction with respect to the carbon atom number (C_3~C_{11+}) and hydrocarbon chemical families.

Carbon atoms	Paraffins	Mono-olefins	Cyclo-olefins	Naphthenes	Aromatics
3	0.79	0.34			
4		0.10			
5	13.05	6.24	0.63	0.67	
6	11.72	3.22	0.54	2.87	0.64
7	7.69	0.89	0.49	3.19	2.35
8	18.75	0.40	0.26	1.24	3.94
9	1.88	0.20		0.42	3.17
10	0.67	0.24		0.16	2.78
11+	2.09				0.61
Total	56.64	11.63	1.92	8.55	13.49

Table 3.3 Results of hydrocarbon composition analysis (ASTM D6839): Volume fraction with respect to carbon atom number (C_5~C_{11+}) and hydrocarbon chemical families. The shaded fraction indicates what hydrocarbon holds majority.

Carbon #	Paraffin	Olefin	Naphthene	Aromatic
5	**0.63**	**0.33**	0.03	0.00
6	**0.62**	**0.20**	**0.15**	0.03
7	**0.53**	0.09	**0.22**	0.16
8	**0.76**	0.03	0.05	0.16
9	0.33	0.04	0.07	**0.56**
10	0.17	0.06	0.04	**0.72**
11+	**0.77**	0.00	0.00	0.23

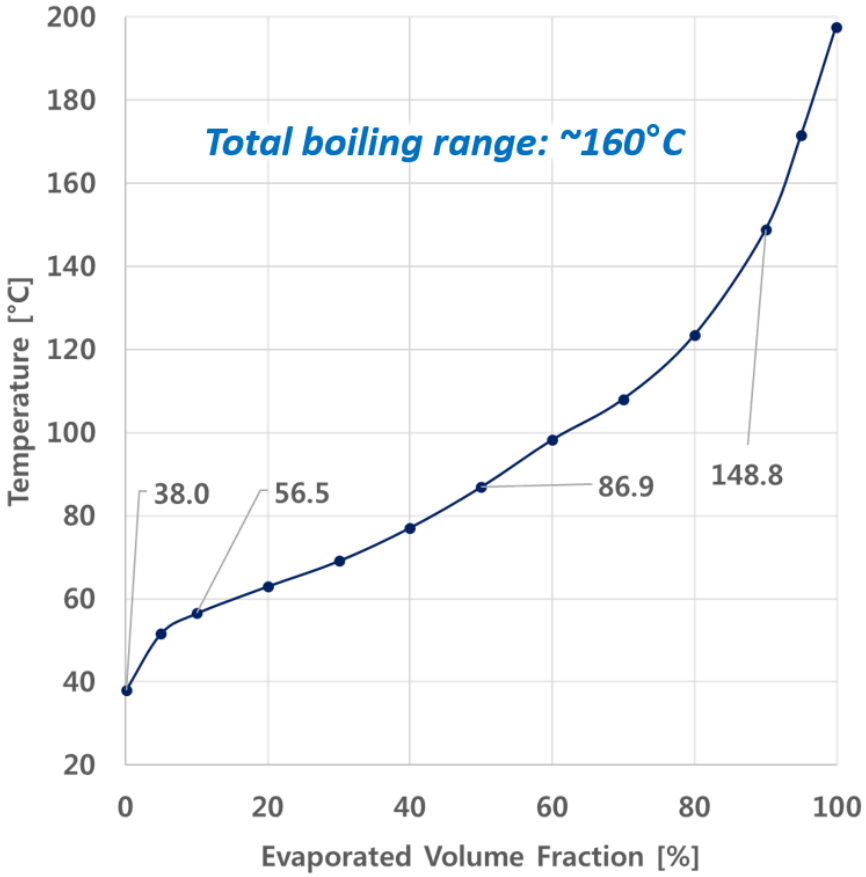

Figure 3.1 Measured distillation curve of the real gasoline.

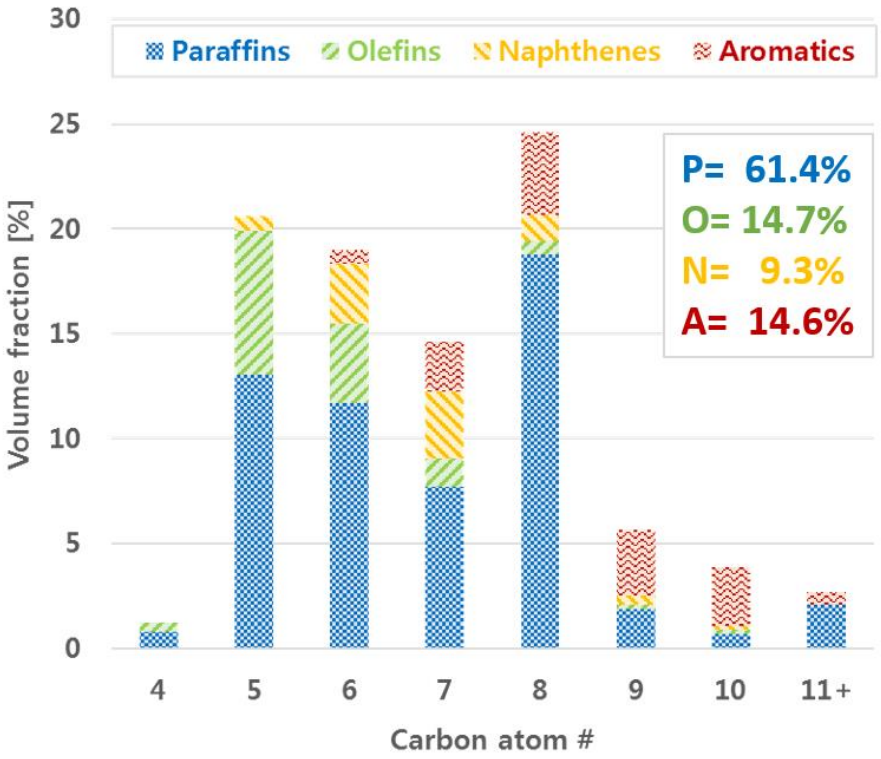

Figure 3.2 Results of hydrocarbon composition analysis: Volume fractions were arranged with respect to the carbon atom number and hydrocarbon chemical families.

3.4 Determination of Surrogate Component and Composition

In this section, the components and composition of surrogate fuel for the gasoline were determined. The distillation curve and the aromatic content took the priority during the formulation work because of their leverage on particulate emission. Hence, first the aromatic content was fixed to the measured value with normalization, 14.6%, then the components and composition were investigated to match the distillation curve as well as the other target properties. Two different approaches, one based on the chemical families and the other one based on the boiling temperature range, were used to formulate the surrogate fuel in this study. Matching the targets, the distillation curve was simulated according to the Anand et al. [109], and the density was calculated by using the linear blending of volume fraction method.

3.4.1 Basis: Chemical Families

Based on the analyzed target properties as shown in Table 3.2, the chemical families of saturated (paraffins and naphthenes), unsaturated (olefins), and aromatics were sorted in order of carbon atom, and each of them was represented by a hydrocarbon which has corresponding chemical formula. For example, hexane (C_6H_{14}) represents the saturated hydrocarbon of C_6, xylene (C_8H_{10}) serves the aromatic hydrocarbon of C_8, and so forth. The molecular structure can be varied according to their chemical bond arrangement, and hence many isomers exist as the number of carbon atoms increase. However, there are limited information for the physical and chemical properties of every isomers, so the well-known hydrocarbon was chosen as the representative.

3.4.2 Basis: Boiling Temperature

An alternative method to introduce the surrogate component is based on the boiling temperature. By dividing the boiling range from the distillation curve into several sections, a set of surrogate components that fit each temperature range can be determined. The detailed process is described as follow. First, the representative hydrocarbons of each chemical family (Table 3.2) were sorted in boiling point order. Next, they were grouped into the prescribed temperature sections, and the volume-averaged temperatures were calculated for each section by weighting the volume fraction of hydrocarbon constituents to their boiling points. Lastly, a hydrocarbon, which has boiling point close to the volume-averaged temperature of the section, was determined as the surrogate component.

3.4.3 Formulation Results and Discussion

With two proposed approach, four gasoline surrogate fuels were derived in this study. At first, Table 3.4 shows a 15-component surrogate fuel based on the chemical families of gasoline. For the sake of conciseness, the hydrocarbons which have relatively small volume fractions were lumped into one group, such as the unsaturated hydrocarbons of C_3-C_5 and C_8-C_{10}, and the saturated hydrocarbons of C_3-C_5 and C_9-C_{11}. The smallest hydrocarbon was 1-pentene (1-C_5H_{10}) to represent the unsaturated of C_3-C_5, while the largest hydrocarbon was n-pentylbenzene ($C_{11}H_{16}$) to serve the aromatic of C_{11}.

Three surrogate fuels, based on the intervals of ΔT=20, 30, 40 K, were derived and summarized in Table 3.5. It shows the surrogate constituents and compositions, and the resulted fuel properties of density and H/C ratio. Note that it was possible to

retain the aromatic fraction of real gasoline for the 10- and 7-component surrogate fuel, but it was failed in the five-component surrogate fuel. It is because that temperature section became large. In the 10-component surrogate fuel, the 1,2-dimetylbenzne (o-xylene, C_8H_{10}, 139.1°C), cumene (C_9H_{12}, 152°C), and n-pentylbenzene ($C_{11}H_{16}$, 205.6°C) represented the aromatics, while in the 7-component surrogate fuels, cumene and m-di-isopropyl benzene ($C_{12}H_{18}$, 202.8°C) served for that. The simulated distillation curve of four surrogate fuels were compared against the experimental data as shown in Fig. 3.3. All the surrogate fuels were in good agreement for describing the vaporization characteristics of real gasoline. Also, their density and H/C ratio were within 4% difference compared to the measurement.

The number of surrogate components increases the computational load for numerical simulation due to additional transport equations to be solved. Consequently, a good surrogate for CFD analysis can be considered as a surrogate satisfies the target properties with the minimum constituents. To fully emulate the wide boiling range, six hydrocarbons with different boiling points such as 2-methylbutane (iso-pentane, i-C_5H_{12}, 27.8°C), n-hexane (n-C_6H_{14}, 68.7°C), 2,2,4-trimethylpentane (iso-octane, i-C_8H_{18}, 99.2°C), o-xylene, 1,4-diethylbenzene (p-diethylbenzene, $C_{10}H_{14}$, 181.1°C), and n-undecane (n-$C_{11}H_{24}$, 195.9°C) were selected for the surrogate component. Though the gasoline comprises a certain portion of olefins and naphthenes, the representative hydrocarbons from their classes were excluded due to limited available reaction kinetics for oxidation. Finally, the composition for the six-component surrogate was determined as listed in Table 3.6. Its distillation characteristic (see Fig. 3.4), density, and H/C ratio is summarized in Table 3.7.

For an engine simulation, the surrogate fuel is directly injected and vaporized in the mixing stage, and the fuel species of gas-phase participate in the combustion process. Regarding the hydrocarbon oxidation, it is ideal to couple the reaction

kinetics to each surrogate component. However, a chemical mechanism which covers all hydrocarbon classes is not available, even if it is possible, its complexity will result in intractable computational load. Recently, Ra and Reitz [110] suggested a hybrid surrogate modeling methodology involving one surrogate to represent the fuel spray and gas-flow transport calculations and a separate surrogate for gas-phase oxidation. In their work, the group chemistry representation (GCR) was proposed to bridge the two surrogates by the hydrocarbon classes, and it has been widely adopted to various types of engine such as HCCI [111], conventional Diesel combustion and LTC [112], and DISI engine [113].

In this study, according to GCR methodology, the six-component surrogate was coupled with the chemical mechanism including PAHs reaction pathway for toluene reference fuel proposed by Raj et al. [34]. The oxidation on n-alkanes (n-heptane and n-undecane) and iso-alkanes (iso-pentane and iso-octane) were grouped and described by the chemical reactions of n-heptane and iso-octane, respectively. For the aromatics, though it has been documented that the variation in the molecular structure has much more impacts on the particulate emission than paraffin [101], the toluene was chosen as the representative component for o-xylene and p-diethyl benzene.

Table 3.4 Results of 15-component surrogate fuel, of which formulation was based on the hydrocarbon chemical families.

Carbon #	Type	Name	(v/v)%
3~5	Unsaturated	1-pentene	7.31
	Saturated	n-pentane	14.51
6	Unsaturated	1-hexene	3.76
	Saturated	n-hexane	14.59
	Aromatic	benzene	0.64
7	Unsaturated	1-heptene	1.38
	Saturated	n-heptane	10.88
	Aromatic	toluene	2.35
8	Saturated	i-octane	19.99
	Aromatic	m-xylene	3.94
8~10	Unsaturated	1-octene	1.1
9	Aromatic	cumene	3.17
9~11	Saturated	n-decane	5.22
10	Aromatic	m-cymene	2.78
11	Aromatic	n-pentylbenzene	0.61
Density @ 15°C [kg/m^3]		703.0 (-3.0%)	
H/C ratio [-]		2.063 (+0.6%)	

Table 3.5 Result of 10-, 7-, and 5-component surrogate fuel, of which formulation was based on the boiling temperature.

ΔT=20K based 10-component		ΔT=30K based 7-component		ΔT=40K based 5-component	
Name	(v/v)%	Name	(v/v)%	Name	(v/v)%
n-butane	8.10	n-butane	8.10	i-pentane	22.93
n-pentane	14.83	1-pentene	15.56	i-hexane	21.32
c-pentane	16.93	i-hexane	20.59	i-heptane	36.60
benzene	4.39	n-heptane	12.38	m-xylene	11.59
i-heptane	9.30	i-octane	28.78	m-DIPB	7.56
i-octane	27.30	cumene	11.04		
m-xylene	4.77	m-DIPB	3.56		
cumene	6.82				
n-decane	4.46	* DIPB: di-isopropyl-benzene			
n-pentylbenzene	3.10				
ρ = 722.6 kg/m^3 (-3.0%)		ρ = 695.8 kg/m^3 (-4.0%)		ρ = 700.5 kg/m^3 (-3.3%)	
H/C = 1.998 (-2.5%)		H/C = 2.082 (1.6%)		H/C = 2.082 (1.6%)	

Table 3.6 Result of the six-component gasoline surrogate fuel.

Chemical families	Component	Volume fraction [%]
iso-alkane	iso-pentane	23.0
	iso-octane	28.4
n-alkane	n-hexane	31.0
	n-undecane	3.0
aromatic	o-xylene	10.0
	p-diethylbenzene	4.6

Table 3.7 Comparison of the target properties between the gasoline and six-component surrogate fuel.

Target Property		Real fuel	Surrogate fuel	Error [%]
Distillation curve [°C]	5%	51.6	57.0	10.5
	10%	56.5	58.8	4.1
	20%	63.0	63.3	0.5
	30%	69.1	68.7	-0.6
	40%	77.1	75.6	-1.9
	50%	86.9	84.5	-2.8
	60%	98.3	95.3	-3.1
	70%	108.1	108.4	0.3
	80%	123.5	124.2	0.6
	90%	148.8	147.6	-0.8
	95%	171.6	166.8	-2.8
Density @ 15°C [kg/m^3]		724.5	702.5	-3.0
H/C ratio [-]		2.05	2.12	3.3

Table 3.8 Transition from spray surrogate to combustion surrogate by GCR.

	Spray surrogate		Combustion surrogate	
	Name	(v/v)%	Name	(v/v)%
iso-alkanes	iso-pentane	23.0	iso-octane	51.4
	iso-octane	28.4		
n-alkanes	n-hexane	31.0	n-heptane	34.0
	n-undecane	3.0		
aromatics	o-xylene	10.0	toluene	14.6
	p-diethylbenzene	4.6		

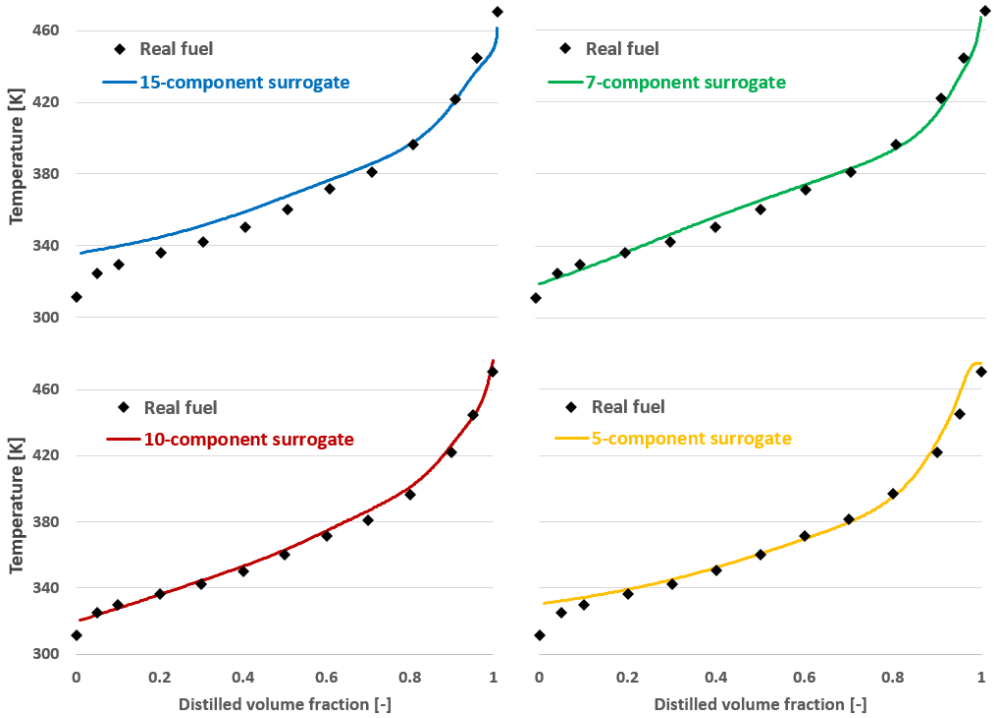

Figure 3.3 Simulated distillation curves of four different surrogate fuels were compared to the measured data: (a) 15-component; (b) 10-component; (c) 7-component; (d) 5-component surrogate fuel.

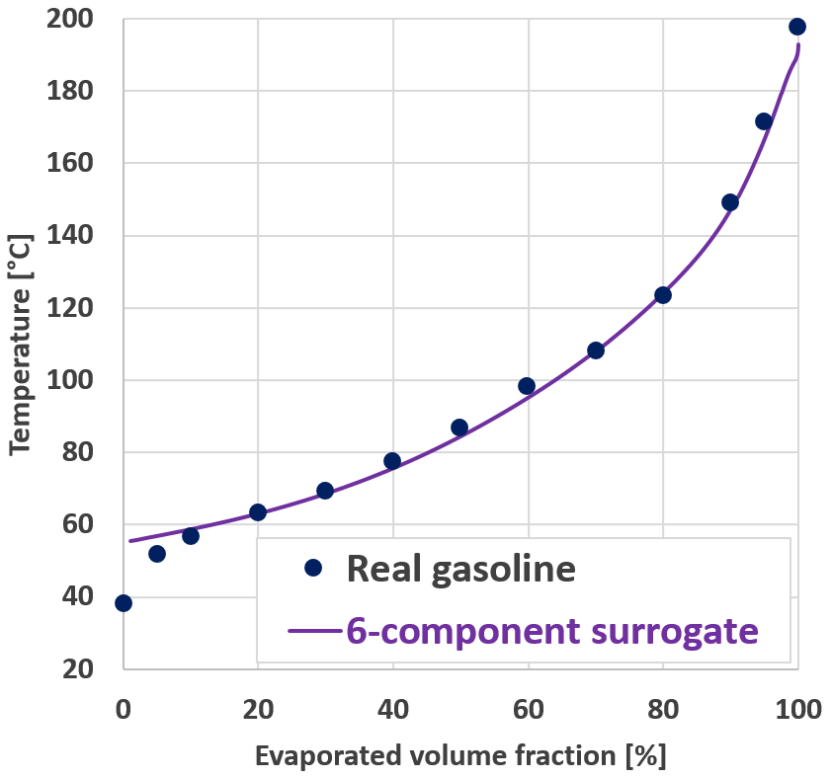

Figure 3.4 Comparison of distillation curve between the real gasoline and six-component gasoline surrogate fuel.

Chapter 4. Modeling of Partially-premixed Turbulent Combustion by *G*-Equation

For DISI engines, the soot precursors such as PAHs are formed from the local fuel-rich mixture so that the prediction of the mass burning rate in that region is of great importance. It is well known that the turbulent flame propagation is a function of the in-cylinder turbulent properties and the thermo-chemical status of the air-fuel mixture [114], so the laminar burning velocity holds the crucial role for the combustion of the fuel-rich mixture. Many efforts have been paid to measure the laminar burning velocity of pure hydrocarbons in the fundamental research field [115, 116]. However, that for the gasoline fuel has rarely conducted so far because the gasoline is a complex hydrocarbon mixture. Furthermore, there is limitations to mimic the in-cylinder condition of high temperature and combustion in the laboratory. Thus, it is required to develop an appropriate modeling methodology for the laminar burning velocity of gasoline fuel for DISI engines.

In this chapter, the ignition and combustion modeling are presented. At first, the G-equation based on level set approach was briefly summarized, which is proposed by Peters [114] and widely adopted for SI engine combustion (Section 4.1). Next, a new correlation for the laminar burning velocity of gasoline was derived (Section 4.2). Finally, a model for the spark ignition and initial flame kernel growth was discussed (Section 4.3). The regime for the turbulent premixed combustion can be referred to Appendix C.

4.1 Turbulent Premixed Combustion Modeling

Based on the flamelet concept, either progress variable *c* or non-reacting scalar *G* were widely adopted to describe the turbulent premixed combustion. The former represents the normalized temperature, $c = (T - T_u)/(T_b - T_u)$, and it assumes that the combustion system is divided into unburnt and chemical equilibrium state by an infinitely thin layer. The progress variable is bounded between zero and unity, and the transport equation for Favre-averaged progress variable can be expressed as

$$\frac{\partial}{\partial t}(\bar{\rho}\tilde{c}) + \frac{\partial}{\partial x_j}(\bar{\rho}\tilde{c}\tilde{u}_j) = \frac{\partial}{\partial x_j}\left(\bar{\rho}\widetilde{D_c}\frac{\partial \tilde{c}}{\partial x_j}\right) - \frac{\partial}{\partial x_j}\left(\bar{\rho}\widetilde{c''c''}\right) + \tilde{\omega} \quad . \tag{4.5}$$

The first term on left-hand side indicates the rate of molecular transport which is often neglected in high Reynolds number flow, and the last two terms are the rate of turbulent transport and mean reaction rate that requires modeling. Several models have been proposed for the reaction rate: Eddy Break-Up model [117], Bray-Moss-Libby model [118], Flame Surface Density model [119], Coherent Flame Model [120].

An alternative to progress variable approach, a flamelet model based on level set approach was developed by Peters [114], which is valid for both of corrugated flamelet and thin reaction zone regimes. It is assumed that the turbulent flame can be represented as ensembles of thin reactive-diffusive layers embedded in the turbulent flow field, and thereby it allows the decoupling of time scale between chemistry and turbulence. In this study, the *G*-equation model was adopted to describe the turbulent premixed combustion. Following sections briefly summarize the G-equation model and further information can be found in the literature.

4.1.1 G-Equation for Laminar Premixed Flame Propagation

The level set approach for laminar flame was introduced at first by Williams [121]. The kinematic equation of the flame including advection due to the local flow field and propagation by its laminar burning velocity is

$$\frac{d\vec{x}_f}{dt} = \vec{u} + s_L\vec{n} \quad . \tag{4.6}$$

The location of the flame front can be defined with an iso-surface of non-reacting scalar $G(\vec{x},t) = G_0$. This iso-surface separates the flow field into the unburned region with $G(\vec{x},t) < G_0$, and the burned region with $G(\vec{x},t) > G_0$. The kinematic relationship between G and $\vec{x}(t)$ reads

$$\frac{\partial G}{\partial t} + \nabla G \cdot \frac{d\vec{x}_f}{dt}\Big|_{x_0} = 0 \quad , \tag{4.7}$$

with $x = x_0$ as the reference position of the flame surface. Combining this equation with Eq. () results in the *G*-equation for laminar flames

$$\frac{\partial G}{\partial t} + \vec{u} \cdot \nabla G = s_L|\nabla G| \quad . \tag{4.8}$$

It is important to note that this equation describes the kinematic behavior of the flame and is therefore only be defined at the flame front itself. It has no meaning outside of the reference position of the flame. Then the flame front normal vector, $\vec{n} = -\nabla G/|\nabla G|$, and the curvature of the flame front, $\kappa = \nabla \cdot \vec{n}$ are defined. The *G*-equation for laminar flame requires the knowledge of the laminar burning velocity, s_L, and it is a function of unstretched laminar burning velocity and alteration of curvature and strain,

$$s_L = s_L^0 - \mathcal{D}_L \kappa - \mathcal{L}\mathcal{S} \quad , \tag{4.9}$$

with κ and $\mathcal{S}$ as the curvature and strain of the flame, respectively. These two terms represent the corrections to the planar burning velocity on turbulent flame propagation velocities in highly stratified and small scale turbulent flow field.

4.1.2 G-Equation for Turbulent Premixed Flame Propagation

Peters [114] extended the equation to cover turbulent combustion for both the corrugate flamelet and thin reaction zone regimes and derived a complete set of governing equations for the Favre-averaged value of G and G''^2, which determine the location of mean flame front and the flame brush thickness. Detailed derivation procedure is neglected and referred to the original publication, only the final outcomes are briefly introduced in this study.

For the corrugated flamelet regime, the entire reactive-diffusive layer is embedded in the turbulent flow as the Kolmogorov length scale is always larger than the flame thickness so that the same transport equation defined in laminar premixed flame can be retained here,

$$\frac{\partial G}{\partial t} + \vec{u} \cdot \nabla G = s_L^0 |\nabla G| - \mathcal{D}_L \kappa |\nabla G| - \mathcal{L}S|\nabla G| \quad . \tag{4.10}$$

For the thin reaction zone regime, as eddies at Kolmogorov scale can penetrate into the preheat zone, the inner layer replaces the thin flame $G=G_0$ defined in the corrugated flamelet regime, and the transport equation can be expressed as

$$\frac{\partial G}{\partial t} + \vec{u} \cdot \nabla G = (s_n + s_r)|\nabla G| - D_\kappa |\nabla G| \quad , \tag{4.11}$$

where s_n is the displacement speed by normal diffusion, and s_r is the displacement speed by chemical reaction at inner layer. The perturbation of preheat zone results the displacement speed not equal to the burning velocity of steady, unstretched laminar flame, however, DNS data confirmed that the order of magnitude is same as laminar burning velocity. The leading order equation valid in both regimes which is defined at the flame surface $G(\vec{x},t) = G_0$ only reads

$$\rho \frac{\partial G}{\partial t} + \rho \vec{u} \cdot \nabla G = (\rho s_L^0)|\nabla G| - (\rho D)|\nabla G| \quad . \tag{4.12}$$

Now, the transport equation for mean flame front location and its mean turbulent variation can be derived through the Favre-average and modeling closures as

$$\bar{\rho} \frac{\partial \tilde{G}}{\partial t} + \bar{\rho} \tilde{\vec{u}} \cdot \nabla \tilde{G} = (\bar{\rho} s_T)\left|\nabla \tilde{G}\right| - \bar{\rho} D_t \tilde{\kappa}\left|\nabla \tilde{G}\right| \quad , \tag{4.13}$$

$$\bar{\rho} \frac{\partial \widetilde{G''^2}}{\partial t} + \rho \frac{d\widetilde{\vec{x}_f}}{dt} \cdot \nabla \widetilde{G''^2} = \nabla_{\|} \cdot \left(\bar{\rho} D_t \nabla_{\|} \widetilde{G''^2}\right) + 2\bar{\rho} D_t \left(\nabla \tilde{G}\right)^2 - c_s \bar{\rho} \widetilde{G''^2} \frac{\tilde{\varepsilon}}{\tilde{k}} \quad . \tag{4.14}$$

The equation for mean flame front is also valid at the flame surface $\tilde{G}(\vec{x},t) = G_0$, while the outside of the surface is assumed to be a distance function and its property is kept by a re-initialization process [122]. Similar to the progress variable approach that needs the modeling of turbulent transport and reaction rate, the turbulent burning velocity should be modeled to close the *G*-equation.

4.1.3 Turbulent Burning Velocity

Turbulent burning velocity is a well-defined quantity that only depends on local mean quantities. As a pioneer work, Damköhler [123] presented theoretical

expressions for large scale turbulence and small scale turbulence based on the constant mass flux through the instantaneous turbulent flame surface area A_T and the mean turbulent flame surface area A,

$$\dot{m} = \rho_u s_L A_T = \rho_u s_T A \quad . \tag{4.15}$$

As can be seen from the equation, the ratio of turbulent burning velocity to laminar burning velocity is equal to the ratio of flame surface area. For large scale turbulence, where interaction between turbulence and flame is purely kinematic, Damköhler [123] assumed that the flame surface area ratio is proportional to the turbulent intensity over laminar burning velocity as $A_T/A \sim v'/s_L$; while for small scale turbulence, where the turbulence modifies the diffusive transport in preheat zone, it is derived by the analogy to the scaling relation for the laminar burning velocity,

$$s_L \sim \left(\frac{D}{t_c}\right)^{1/2} \quad \text{and} \quad s_T \sim \left(\frac{D_t}{t_c}\right)^{1/2} \quad , \tag{4.16}$$

which results $s_T/s_L \sim (D_t/D)^{1/2}$. Based on the Damkhöler's theoretical expression, Peters [124] derived a turbulent burning velocity correlation of premixed flame under isotropic, fully-developed turbulent flow, which valid for both of corrugate flamelet and thin reaction zone regimes as,

$$\frac{s_T - s_L^0}{s_L^0} = -\frac{a_4 b_3^2}{2b_1}\frac{l}{l_F} + \left[\left(\frac{a_4 b_3^2}{2b_1}\frac{l}{l_F}\right)^2 + a_4 b_3^2 \frac{v' l}{s_L^0 l_F}\right]^{\frac{1}{2}} \quad , \tag{4.17}$$

where the modeling constants b_1, b_3, and a_4 are defined as 2.0, 1.0, and 0.78, respectively. Because the combustion process in DISI engines is initiated by spark ignition, where the flame kernel growth from quasi-turbulent to fully-developed one,

Ewald and Peters [125] formulated the unsteady evolution effect on turbulent burning velocity as,

$$\frac{s_T - s_L^0}{s_L^0} = -\frac{a_4 b_3^2}{2b_1}\frac{l}{l_F} l^{*q+1} + \left[\left(\frac{a_4 b_3^2}{2b_1}\frac{l}{l_F} l^{*q+1}\right)^2 + a_4 b_3^2 \frac{v' l}{s_L^0 l_F} l^{*2}\right]^{\frac{1}{2}} . \quad (4.18)$$

where l^* accounts for unsteady development of turbulent flame brush by the relationship between the turbulent flame brush thickness and the turbulent length scale as $l^* = l_{f,t}/(b_2 l)$. In this study, it was adopted to compute the turbulent burning velocity with *G*-equation.

4.2 Laminar Burning Velocity of Gasoline Fuel

The burning velocity of the turbulent propagating flame can be correlated with both of the in-cylinder turbulent flow and the laminar flame properties as discussed in Section 4.1, and thereby the knowledge of the length scale, as well as the velocity of turbulent flow and laminar flame, are the essential prerequisite for combustion simulation of SI engine. In DISI engines, the direct injection of gasoline leads the inhomogeneous air-fuel mixture where locally rich or lean regions exist, and the mixture stratification strongly affects the flame propagation due to thermal and chemical effect [126]. Therefore, to reproduce the correct mass burn rate, one should be able to offer the laminar burning velocity of gasoline under wide thermochemical conditions of the partially premixed mixture.

In this study, the laminar burning velocity of gasoline was modeled as combined laminar burning velocities of iso-octane, n-heptane, and toluene based on the energy fraction mixing rule. In the following, at first, the well-known, widely adopted correlations for the laminar burning velocity of gasoline were reviewed, and their limitations were discussed. Then, its alternative modeling methodology was described. Finally, a new correlation was developed and validated against the experimental data.

4.2.1 Literature Review

Numerous form of empirical and semi-empirical correlations for the laminar burning velocity of hydrocarbons have been proposed by experimental fitting or using the thermal theory of flame propagation [127]. One of them has the simplest functional form of $s_L = s_{L,0}(T/T_0)^{\alpha}(P/P_0)^{\beta}(1-\gamma)$ for fitting the measured burning velocities, where $s_{L,0}$ represents the unstretched laminar burning velocity, α and β

indicate the temperature and pressure dependency, and γ denotes the effect of residual gas the fraction. In general, the dependency of temperature and pressure were evaluated at the room temperature of $T_0 = 298$ K and ambient pressure of $p_0 = 1$ atm, respectively. Based on the equation form several researchers were fitted the burning velocities of gasoline surrogate such as iso-octane and indolene, and it has been widely adopted for zero-dimensional or quasi-dimensional SI engine simulation (see Table 4.1).

In the field of three-dimensional analysis of DISI engines, Liang and Reitz [82] used the base form of Gülder's equation [127] and modified the burning velocity level to match the data of Metghalchi and Keck [128]. In their work, iso-octane represented the gasoline fuel. A follow-up study conducted by Yang and Reitz [129] was incorporated the PRF as gasoline surrogate and updated the correlation with an additional third-order polynomial to curve fit for different PRF numbers. Though the empirical correlations are computationally efficient to predict the laminar burning velocity, the range of equivalence ratio for measurement mainly targeted between moderate lean and rich fuel-air mixture around stoichiometric ratio. Consequently, it is appropriate for PFI engine simulation, while it has limitations for DISI engines where the air-fuel ratio varies widely due to the direct injection.

On the other hand, some studies attempted to calculate the laminar burning velocity by one-dimensional premixed flame simulation in conjunction with chemical mechanisms. The advantages of flame simulation with a valid chemical mechanism are the extension of investigating ranges over high temperature and pressure, and the exclusion of experimental uncertainties. Dahms et al. [130] employed an optimized PRF chemical mechanism for predicting flame propagation to compute the burning velocities under wide operating range. Naik et al. [42] formulated a seven-component

gasoline surrogate and derived a semi-detailed chemical mechanism from Model Fuel Library to perform the flame simulation.

Note that the alkanes, iso-octane or PRF, were usually adopted to mimic the burning velocity of gasoline. However, recent experimental work has been demonstrated that the laminar burning velocities of both PRF and gasoline start to deviate for stoichiometric and rich mixtures, whereas that of TRF retains the satisfactory agreement over the entire range of investigated equivalence ratios [131-133]. The different response between PRF and TRF can be attributed to the effect of aromatic chemistry because it has a different laminar burning velocity compared to alkanes. Accordingly, it has been pointed out that the inclusion of toluene for accurately emulating the burning velocity of gasoline is as important as its role in allowing better predictions of auto-ignition delay.

In summary, the existing empirical correlations are inappropriate for DISI engines so that it is needed to develop a predictive model for the burning velocity of gasoline. Regarding the derivation of correlations, the numerical flame simulation can be an alternative to provide the theoretically correct solutions compared to the experimental approach.

4.2.2 Modeling Methodology

Based upon above concerns, the gasoline was represented as TRF surrogate, and its laminar burning velocity was obtained by flame simulation in this study. The mass fractions of TRF component were determined according to the GCR methodology as discussed in Section 3.4. It is worth mentioning that the mass fraction ratio would be varied by the locations in the cylinder because of the direct injection of liquid fuel as

well as the different volatility of each fuel component. For instance, the aromatics in surrogate fuel have high boiling temperatures and thereby vaporize slower than the light-end elements. As a result, the ratio of aromatics in near wall region is greater than in-cylinder core region due to the presence of wall impingement of fuel droplet and the lower vaporization rate of liquid film.

The compositional variation of TRF leads a difficult issue for the flame simulation because it introduces the fuel dimension in addition to the change of temperature, pressure, and equivalence ratio. To lighten the computational load, a mixing rule based on energy fraction was adopted in this study. Sileghem et al. [131] have shown that the combined burning velocities of iso-octane, n-heptane, and toluene by the mixing rule are capable of reproducing the burning velocity of TRF. Similar results have been documented in the experimental research of [132], so the mixing rule approach can be regarded as an accurate and efficient way to calculate the laminar burning velocity of the fuel blend.

Therefore, in this study, the laminar burning velocity of gasoline was modeled as combined laminar burning velocities of iso-octane, n-heptane, and toluene based on the energy fraction mixing rule. To provide the high-quality flame data, the flame simulations of each fuel were performed by PREMIX module of CHEMKIN-PRO in conjunction with detailed chemical mechanisms of iso-octane [134], n-heptane [135], and toluene [136]. To cover the wide range of in-cylinder thermochemical condition of DISI engines, the temperature range of 400 to 900 K, pressure of 5 to 25 bar, and equivalence ratio of 0.5 to 2.0 were investigated, respectively. Table 4.2 summarizes the input and conditions of flame simulation.

Laminar burning velocities were obtained from the steady, freely propagating, adiabatic flames without radiative heat transfer. The governing equations for

continuity, energy, species, and equation of state were solved by the damped modified Newton algorithm, where the diffusive and convective terms use central and upwind differencing respectively. The diffusion transport of chemical species was calculated using a mixture-averaged formula, and the computational domain was discretized using conventional finite differencing techniques with adaptive grid control based on solution curvature and gradient, which results in a non-uniform grid spacing. The both criteria of gradient and curvature were set as 0.1 in this study. It has been discussed that the grid size dependency between the criteria of 0.05 and 0.1 shows less than 1% difference in laminar burning velocity [137].

4.2.3 New Correlation for Laminar Burning Velocity of Gasoline

For the sake of computational efficiency during CFD simulation, the database for laminar burning velocities of each fuel component was curve-fitted to an algebraic equation. The functional form of the equation is same as the simplest form as stated in Section 4.1.1, and the full equation is written as

$$s_{L,i} = a_i \exp[1 - \exp\{b_i(\phi - \phi_m)\} - \exp\{-\zeta(\phi - \phi_m)\} + \xi(\phi - \phi_t)^2] \left(\frac{T}{T_0}\right)^{\alpha(\phi)} \left(\frac{P}{P_0}\right)^{\beta(\phi)} (1 - 2.1Y_{\text{dil}}), \tag{4.19}$$

$$\alpha(\phi) = \sum_{i=0}^{5} \alpha_i \phi^i \quad \text{and} \quad \beta(\phi) = \sum_{i=0}^{5} \beta_i \phi^i \quad . \tag{4.20}$$

Because the burning velocities of alkanes and that of aromatics are different, the fuel dependent constants a_i and b_i were introduced to account for the different shapes where subscript i denotes ith fuel component. The temperature and pressure dependency were evaluated at the reference value of $T_0 = 600$ K and $P_0 = 5$ bar,

respectively, and they were defined as fifth-order polynomial form as a function of equivalence ratio. The constants in fitting equation are summarized in Table 4.3, and the polynomial coefficient will be discussed in later.

For the diluent effect, Metghalchi and Keck [128] was experimentally derived a correlation, $1 - 2.1Y_{\mathrm{dil}}$, for a stoichiometric iso-octane/air flame. In their work, a mixture of 15% carbon dioxide and 85% nitrogen by volume was used to simulate combustion products. Similar correlations has been reported in previous work, e.g. $1 - 2.5Y_{\mathrm{dil}}$ by Ryan and Lestz [138], and $1 - 2.06{V_{\mathrm{dil}}}^{0.73}$ by Rhodes and Keck [139]. Recent numerical simulation work of Bhattacharya et al. [140] revealed that the simulated mixture can well-resolve both the physical effect of heat capacity and the chemical effect of dissociation on burning velocity. Thus the correlation by Metghalchi and Keck [128] was adopted instead of adding diluent dimension for flame simulation.

Figure 4.1 presents the calculated and fitted laminar burning velocity of iso-octane, n-heptane, and toluene at 600 K and 5 bar. Note that the newly derived correlation showed a good agreement with the database, thus validating the algebraic model and confirming the correctness of the fitting results. The values of s_L for n-heptane flame yielded the fastest burning velocity for investigated equivalence ratio, whereas iso-octane flame exhibited the slowest burning velocity except the extremely rich mixtures of $\phi > 1.7$, from where toluene flame took the minimum value. The laminar burning velocity of toluene laid between the iso-octane and n-heptane in lean branch, while it tended to lean towards that of iso-octane in rich branch where $\phi > 1.2$. The investigated thermochemical condition is nearly impossible for experimental measurement due to safety issue, so there is no comparable result to validate the calculation results. Instead, the similar behavior has been observed in the work of Dirrenberger et al. [132] under 358, 398 K and 1 atm as plotted in Fig. 4.2.

The simulated laminar burning velocities of three hydrocarbon flames at the reference pressure ($P_0 = 5$ bar) are shown in Fig. 4.3, as a function of unburned temperature for equivalence ratios ϕ=0.8, 1.0, 1.4, and 2.0. The slopes of temperature dependences were different for a given equivalence ratio, so that the constant value for the exponent α is not proper to use. Furthermore, regardless of fuel component or equivalence ratio, they were changed from lower value to higher one with respect to the reference temperature ($T_0 = 600$ K). It implies that the range selection would influences the fitting result as well as the final outcome of laminar burning velocity. In order to secure the valid polynomial-fitting, the range was divided into low temperature regime from 400 to 600 K and high temperature regime from 600 to 900 K, respectively.

For both regimes, the average slopes of temperature dependence as a function of equivalence ratio for three hydrocarbon flames are depicted in Fig. 4.4. The dash line indicates the curve-fitting result by a fifth-order polynomial, and the coefficients are summarized in Table 4.4. The R-squared values of each fuel component for low-temperature regime are 0.957, 0.978, and 0.980, while that for high-temperature regime is 0.936, 0.968, and 0.953, respectively.

The simulated laminar burning velocities of three hydrocarbon flames at the reference temperature ($T_0 = 600$ K) are plotted in Fig. 4.5, as a function of pressure for equivalence ratios ϕ=0.8, 1.0, 1.4, and 2.0. Similarly, the pressure dependence was also varied according to the equivalence ratio, and it requires higher-order fitting rather than previous work [128]. However, in contrast to the temperature dependence, the slopes were almost constant for investigated pressure range. The average pressure dependence as a function of equivalence ratio for three hydrocarbons are shown in Fig. 4.6. The coefficients of fifth-order polynomial are listed in Table 4.5, and the R-squared values of three hydrocarbon flames are 0.972, 0.992, and 0.977, respectively.

Based on the above temperature and pressure dependence, the laminar burning velocity from the flame simulation and the predicted one by the correlation for iso-octane/air flame were compared as shown in Fig. 4.7. An excellent agreement was found in all cases, thus verifying the correctness of correlation. Similar results were obtained for n-heptane/air flame and toluene/air flame, and they were not shown here. It is noteworthy that using the correlation can efficiently calculate the laminar burning velocity in a flame-containing cell at a given condition. Thus, it is expected that not only the accuracy but also the efficiency can be secured by the developed correlation.

Table 4.1 Empirical correlations for laminar burning velocity of gasoline and gasoline surrogate found in the literature.

	Metghalchi and Keck [128]	Gülder [127]	Rhodes and Keck [139]
		Investigated Condition	
Fuel	Indolene	Iso-octane	Indolene
T	298-700 K	300-500 K	350-550 K
P	0.4-50 atm	1-8 bar	0.4-12 atm
ϕ	0.8-1.5	0.7-1.4	0.7-1.6
Y_{dil}	0-0.2	-	0-0.3
		Derived Correlation	
$s_{L,0}$	$27.58 - 78.34(\phi - 1.13)^2$	$\mathrm{W}\phi^{\eta}\exp[-\xi(\phi - 1.075)^2]$	$30.5 - 54.9(\phi - 1.21)^2$
α	$2.18 - 0.8(\phi - 1)$	1.56	$2.4 - 0.271\phi^{3.51}$
β	$-0.16 + 0.22(\phi - 1)$	-0.22	$-0.357 + 0.14\phi^{2.77}$
γ	$2.1Y_{\mathrm{dil}}$	-	$2.06{Y_{\mathrm{dil}}}^{0.773}$

Table 4.2 Simulation conditions for the 1-D premixed flame.

	iso-octane	*n*-heptane	Toluene
Chemical Mechanism	Mehl et al. [134]	Mehl et al. [135]	Nakamura et al. [136]
Computation code	PREMIX in CHEMKIN-PRO		
Temperature [K]	400, 500, 600, 700, 800, 900		
Pressure [bar]	5, 10, 15, 20, 25		
Equivalence ratio [-]	0.5 to 2.0 by 0.1 step		

Table 4.3 Model constants in the newly derived fitting equations.

	iso-octane	*n*-heptane	Toluene
a_i	2.25	2.5	2.35
b_i	1.95	1.9	2
ζ	1.85		
ξ	9		
ϕ_m	1.1		
ϕ_t	1.5 (if $\phi > 1.5$, otherwise 0)		

Table 4.4 Coefficients for fitting temperature dependency.

$\alpha(\phi)$	α_0	α_1	α_2	α_3	α_4	α_5
High temperature regime (600-900 K)						
iso-octane	-2.564	40.879	-94.888	92.663	-40.318	6.488
n-heptane	6.253	-3.876	-8.627	13.795	-6.094	0.818
Toluene	1.450	16.212	-40.638	37.634	-14.362	1.892
Low temperature regime (400-600 K)						
iso-octane	-0.610	29.461	-75.525	78.128	-35.367	5.856
n-heptane	2.368	14.331	-45.612	50.307	-23.321	3.901
Toluene	0.105	24.815	-63.708	64.374	-28.146	4.469

Table 4.5 Coefficients for fitting pressure dependency.

$\beta(\phi)$	β_0	β_1	β_2	β_3	β_4	β_5
iso-octane	-1.299	0.601	5.019	-8.817	5.203	-1.024
n-heptane	-0.954	-1.319	8.365	-11.400	6.147	-1.161
Toluene	0.135	-6.040	16.668	-18.303	8.776	-1.527

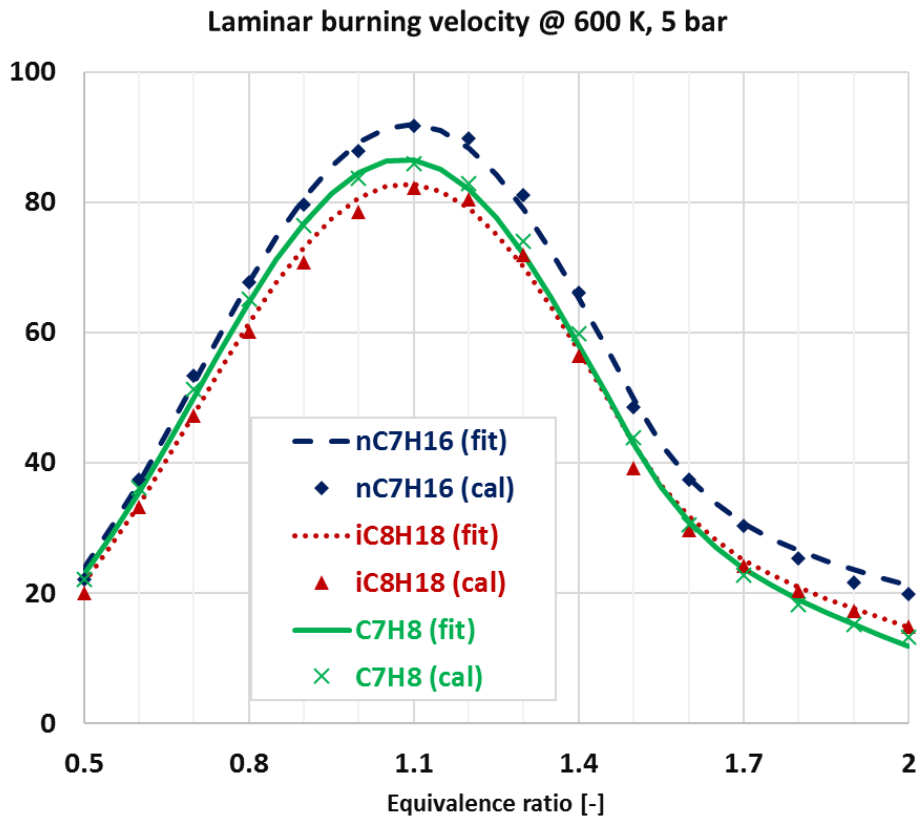

Figure 4.1 Calculated and fitted laminar burning velocity of iso-octane (red, dotted line), n-heptane (blue, dash line), and toluene (green, solid line) at 600 K and 5 bar condition.

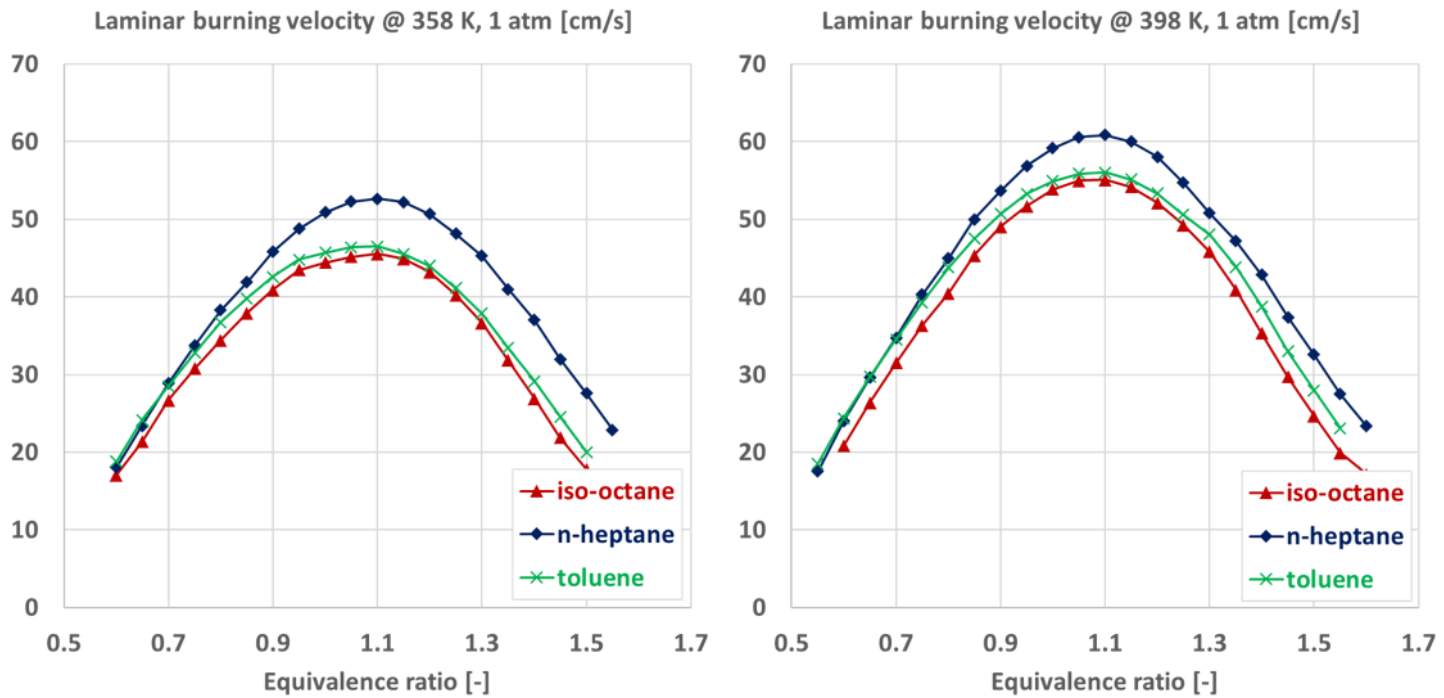

Figure 4.2 Measured laminar burning velocity of iso-octane (triangle), n-heptane (diamond), and toluene (cross) at (a) 358 and (b) 398 K and 1 atm condition [132].

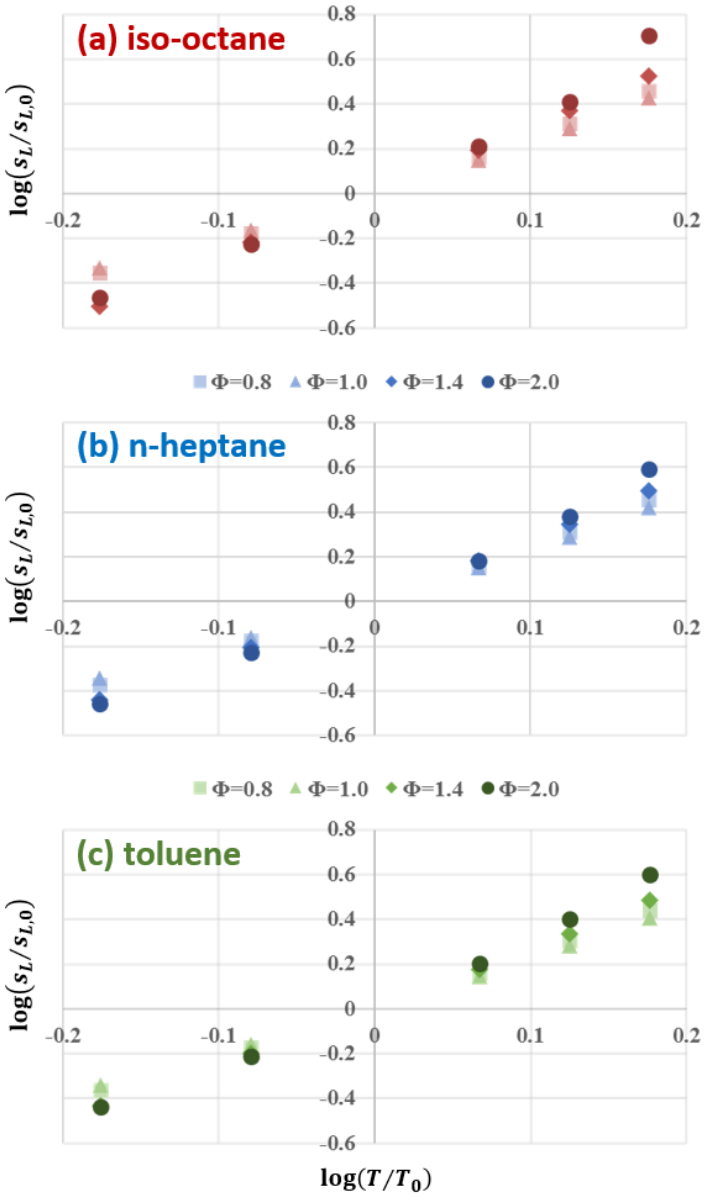

Figure 4.3 Log-log plots for the temperature dependency of laminar burning velocities of (a) iso-octane/air, (b) n-heptane/air flame, and (c) toluene/air from 400 K to 900 K with respect to reference condition of 600 K and 5 bar.

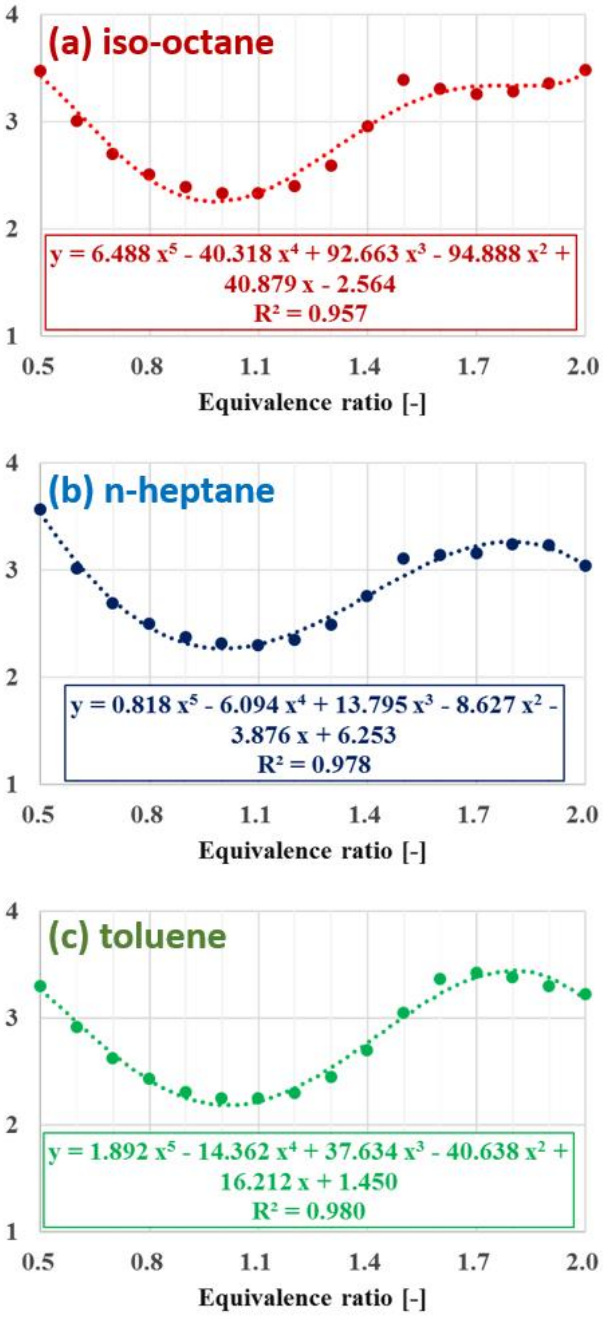

Figure 4.4 Fitting equations for average slope of temperature dependency of (a) iso-octane/air flame, (b) n-heptane/air, and (c) toluene/air flame.

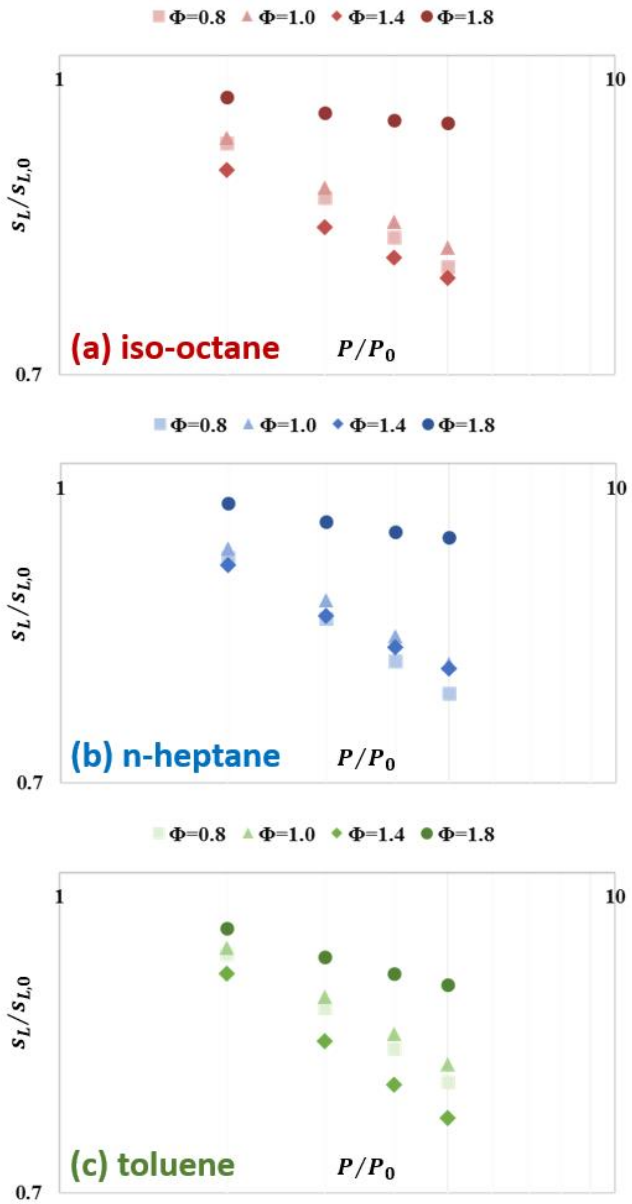

Figure 4.5 Log-log plots for pressure dependency of laminar burning velocities of (a) iso-octane/air, (b) n-heptane/air, and (c) toluene/air flame from 5 to 25 bar with respect to reference condition of 600 K and 5 bar.

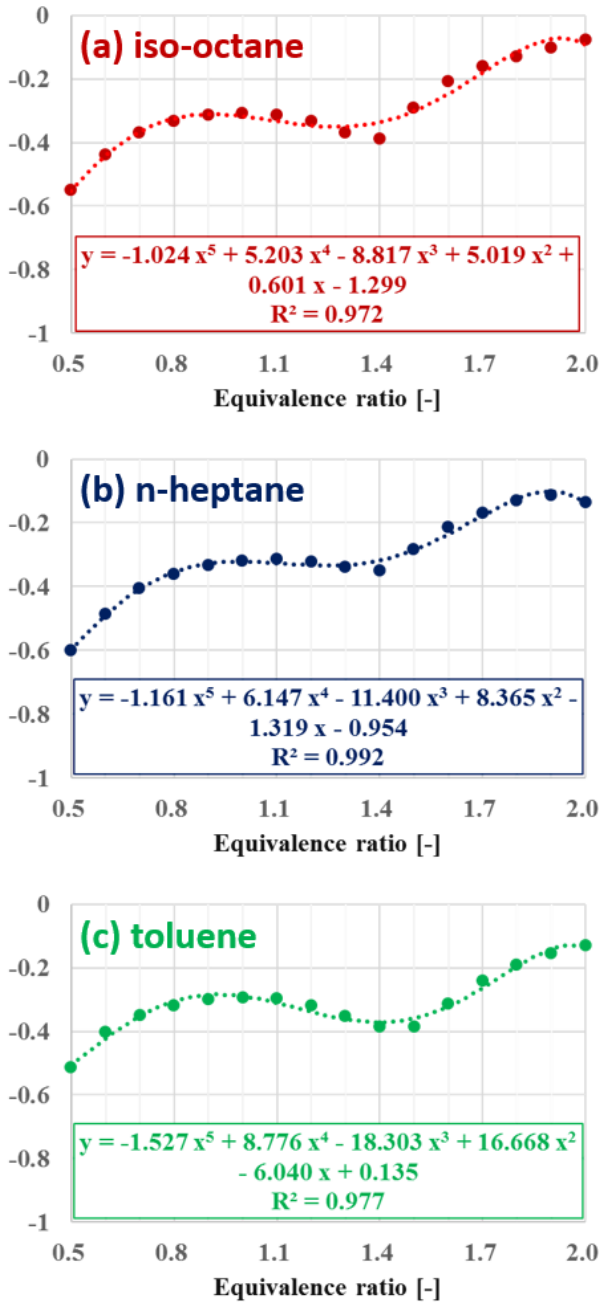

Figure 4.6 Fitting equations for average slope of pressure dependency of (a) iso-octane/air, (b) n-heptane/air, and (c) toluene/air flame.

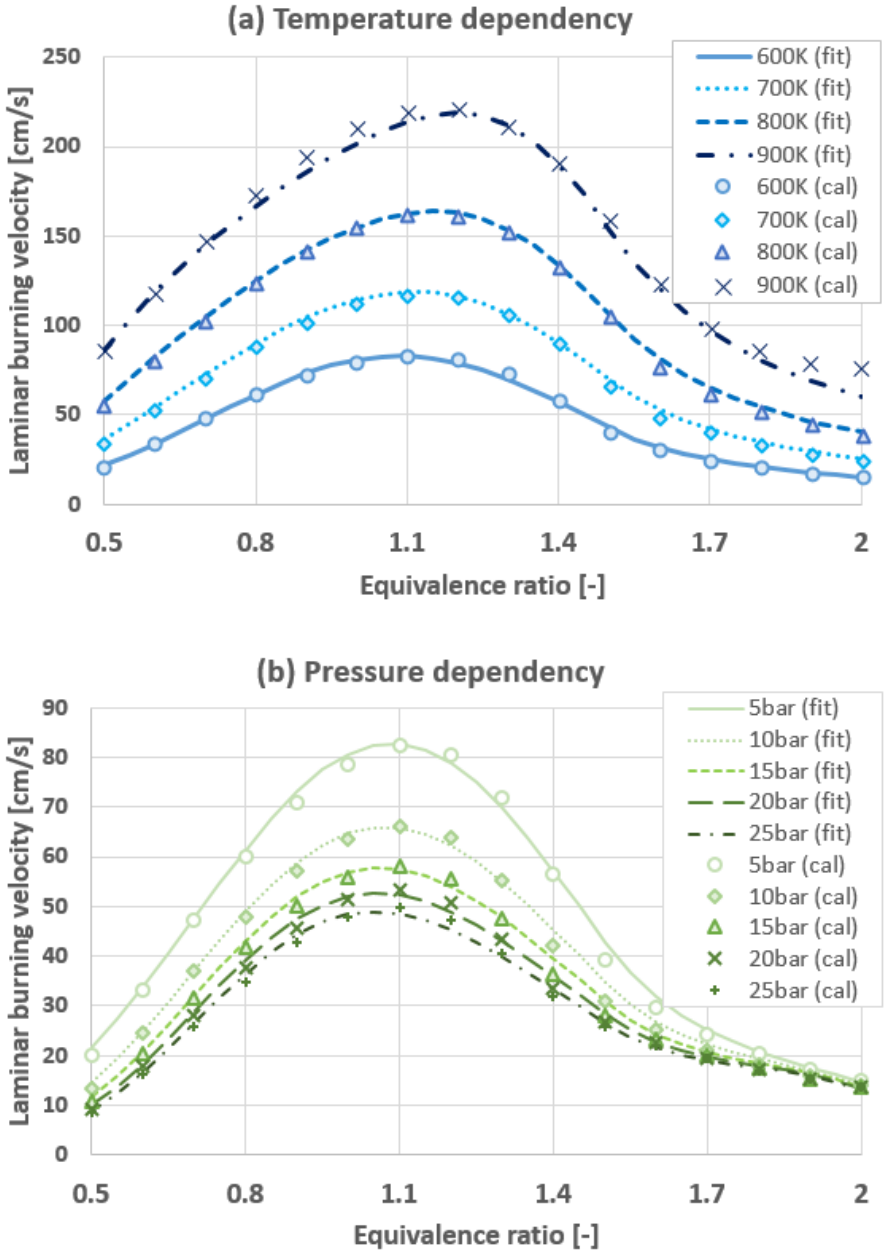

Figure 4.7 Laminar burning velocities of iso-octane/air premixed flame under wide thermodynamic conditions: (a) temperature dependency; (b) pressure dependency

4.3 Spark Ignition Modeling

At the ignition timing, the electrical breakdown between the electrodes forms the cylindrical plasma channel, and the propagating ionized streamers start to transfer the coil ignition energy into the air-fuel mixture around the spark plug. Then a small flame kernel is initialized, and its growth is assisted by the heat conduction and mass diffusion of the plasma energy during the arc and glow discharge phases.

In this study, only the flame kernel evolution during the arc and glow discharges was modeled because the breakdown phase lasts for the extremely short period. It is assumed that the adiabatic flame temperature, as well as normal combustion products of chemical equilibrium, were inside the flame kernel. Also, the rise of in-cylinder pressure due to the kernel growth was neglected. For a single spherical flame kernel with radius of ~1 mm at the spark onset, the rate of volume change can be derived by combining the mass burning rate $\dot{m}_k = \rho_u A_k s_{\text{eff}}$ with the ideal gas law as

$$\frac{dV_k}{dt} = \frac{\rho_u}{\rho_b} A_k \left[s_{T,\kappa} + s_{plasma} \right] \tag{4.21}$$

where V_k is the kernel volume, A_k is the kernel surface area, ρ_u and ρ_b are the unburned and burned gas densities, respectively. The effective burning velocity, s_{eff}, is comprised of the burning velocity which consider the turbulent burning velocity and the effect of laminar and turbulent curvature [125], and the plasma velocity [141], and the detailed derivation can be found in the literature. Note that the plasma velocity accounts for the effect of spark energy deposition on the volume expansion instead of the kernel temperature increase. The transition from ignition to turbulent combustion model was determined when the kernel size is comparable to the integral length scale, according to the work of Tan and Reitz [141].

Chapter 5. Detailed Soot Model Framework with Flamelet Library Approach

The soot formation consists of the gas-phase chemical reaction and the solid-phase soot aerosol dynamics [19, 142], and the overall process is depicted in Fig. 5.1. Behind of the flame front, the fuel and oxidizer undergo the oxidation and pyrolysis depending on the thermos-chemical condition, and the reaction of small hydrocarbon radicals tend to form the first aromatic ring in the fuel-rich mixture. Further chemical reactions grow the product to PAHs, and the reactions occur in the order of molecular size and are in the gas-phase.

With the initiation of soot nucleation by the dimerization of PAHs, a soot nucleus is formed which is in order of 1 nm and consisting 60-100 carbon atoms. The produced soot particles are subjected to chemical growth by the HACA mechanism on radical sites and physical growth by PAH condensation. A collision between the particles, known as coagulation, leads the larger particles formation. The particle agglomeration takes place at a later stage, and it produces soot aggregates in a fractal shape. The particulate oxidation occurs throughout in the whole process, and it is mainly driven by the reaction with oxygen molecules and hydroxyl radicals.

In the previous research on engine soot modeling, the pyrene ($C_{16}H_{10}$) was most widely used for the soot precursor [29, 40, 42] otherwise the non-PAH such as parent fuel or acetylene were adopted [30, 31], and their concentrations were calculated by the well-stirred reactor (WSR) approach during the CFD run. Due to the computational load, several numerical works implemented the reduced chemical mechanism consisting less than 100 species and resulting in the pyrene as the final PAH. Regarding the soot modeling, various models from the semi-empirical to the

detailed one have been proposed for Diesel engine application. However, only the semi-empirical models have been adopted for DISI engines so far.

Frenklach [19] demonstrated that the formation and growth of aromatic species bridge the main combustion zone chemistry and soot formation. Moreover, the experimental findings assert the considerable contribution of larger PAHs to the soot nucleation [34]. Thus, it is important to predict the PAH concentration behind of the flame front accurately. Also, it is worth exploring the state-of-the-art model of the soot aerosol dynamics for the DISI engine application. Therefore, in this study, the flamelet library approach and two soot models, a semi-empirical model and a detailed model, were combined to describe the in-cylinder soot formation.

This chapter is divided into two part: one for modeling of burned composition including PAH concentration by the flamelet library approach, and the other one for modeling of soot aerosol dynamics by four-step semi-empirical model and MOMIC. Firstly, the flamelet equations for laminar premixed flame and turbulent premixed flame are discussed (Section 5.1). Next, the result of generated flamelet library under wide thermos-chemical conditions is presented (Section 5.2), and the issues of flamelet library approach is discussed (Section 5.3). For the soot modeling, first, the soot modeling approach to date in the literature is reviewed to clarify the hierarchy of soot model (Section 5.4). Then, the soot modeling works based on the semi-empirical approach and MOMIC are presented (Sections 5.5 and 5.6).

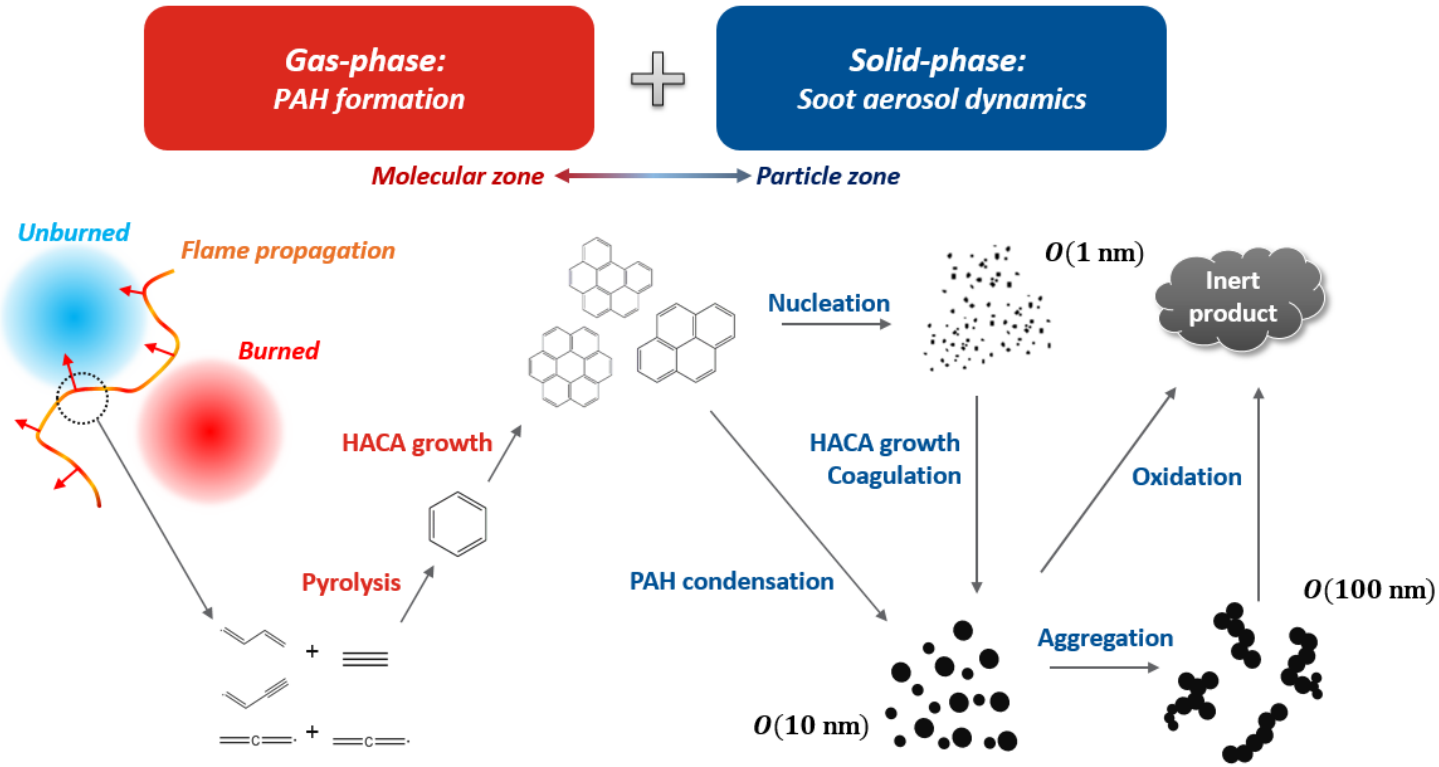

Figure 5.1 Fundamentals of soot processes including PAHs formation and soot aerosol dynamics.

5.1 Flamelet Equations for Premixed Combustion

The geometrical location and shape of turbulent premixed flame are offered by the G-equation model, while the chemical structure across the pre- and the post-flame region is yet to be determined. Several methodologies were suggested for engine CFD simulation. One is to assume chemical equilibrium for burned region. It is effective for the heat release prediction, but it has limitations to simulate the pollutant formation which undergoes slow chemistry. The other one is to assume the cell behind of flame front as a perfectly-stirred reactor (i.e. WSR) and to incorporate the chemical reaction directly during the simulation. It has been widely adopted for engine application. However, the chemical mechanism size should be small as the computational load is proportional to the number of species involved.

The flamelet library approach is an alternative method, which is capable of offering detailed chemical species profile along with either flamelet coordinate G or mixture fraction Z. It has the advantage to reduce the computational load because the library is generated before the simulation and is called with respect to the thermo-chemical condition of a computational cell. Consequently, a detailed chemical mechanism can be employed without load increment. In the following, the flamelet equation for the premixed combustion is presented first.

5.1.1 Laminar Premixed Flame

The laminar, steady, unstretched flame propagation satisfies the continuity normal to the flame front as $\rho u = \rho_u s_L^0 = \text{const}$, where ρ_u is the unburned gas density, and s_L^0 is unstretched laminar burning velocity related to the state of the

unburned. Then the laminar flamelet equation can be derived with the assumption of isobaric and negligible thermal diffusion as

$$(\rho_u s_L^0)\frac{\partial Y_i}{\partial x_n} = \frac{\partial}{\partial x_n}\left(\rho D_i \frac{\partial Y_i}{\partial x_n}\right) + \dot{\omega}_i \quad . \tag{5.1}$$

5.1.2 Turbulent Premixed Flame

With the flamelet assumption, the turbulent premixed flame can be seen as an ensemble of thin reactive-diffusive layers embedded within an otherwise non-reacting turbulent flow. In the corrugated flamelet regime, the turbulence and flame interaction is purely kinematic so that the entire laminar flame structure is conserved. According to Peters [114], the laminar flamelet equation for the corrugated flamelet regime can be expressed as

$$\rho s_L \sigma \frac{\partial Y_i}{\partial G} = \frac{\partial}{\partial G}\left(\rho D_i \sigma^2 \frac{\partial Y_i}{\partial G}\right) + \dot{\omega}_i \quad , \tag{5.2}$$

where the flame coordinate x_n in equation above is transformed with $x_n = (G - G_0)/\sigma$, and σ represent the gradient of flame surface defined as $G(\vec{x}, t) = G_0$. Its form is same as the equation for laminar premixed flame. For the thin reaction zone regime, the flamelet equation that only valid in the inner layer can be written as

$$\rho \frac{\partial Y_i}{\partial t} = \frac{\partial}{\partial G}\left(\rho D_i \sigma^2 \frac{\partial Y_i}{\partial G}\right) + \dot{\omega}_i \quad , \tag{5.3}$$

where the unsteady effect by turbulence interaction was considered. By combining equations above, a flamelet equation that valid in both corrugated flamelet regime and thin reaction zone regime is derived as

$$\rho \frac{\partial Y_i}{\partial t} + \rho s_L \sigma \frac{\partial Y_i}{\partial G} = \frac{\partial}{\partial G}\left(\frac{\rho \chi}{\widehat{Le_i}} \frac{\partial Y_i}{\partial G}\right) + \dot{\omega}_i \quad , \tag{5.4}$$

where χ is scalar dissipation rate of scalar G with $\chi = 2D\sigma^2$, and $\widehat{Le_i}$ is D/D_i for inner reaction zone and $\widehat{D}/\left(\widehat{D} + D_i\right)$ for outside the inner reaction zone. Ewald [143] has pointed out that the flamelet equations of corrugated flamelet regime and thin reaction zone regime only differ in the assumption of Lewis number outside the inner layer. With the unity laminar Lewis number assumption, the species profile would be similar to each other so that the flamelet equation for corrugated flamelet regime is enough to obtain the species profile. Accordingly, several research has adopted equation instead of equation due to complexity [144, 145]. Therefore, in this study, the equation (5.1) was used for flamelet library generation.

5.2 Generation of Flamelet Library

5.2.1 Chemical Mechanism and Numerical Setup

To calculate the flamelet equation, a chemical mechanism is required to provide the reaction rate. Regarding the simulation of soot emission, the PAHs are the key precursors to soot formation so that the prediction of PAHs concentration has significant importance. Appel et al. [146] asserted that correctness of the particle dynamics relies on the accuracy of the species profiles supplied by the gas phase sub-model, those that defined the soot particle nucleation and surface growth rates. Hence, PAH reaction kinetics were considered for mechanism selection in this study.

Numerous chemical mechanisms including PAH reaction have been proposed in the literature. Wang and Frenklach [147] developed a detailed kinetic model of PAH formation, growth, and oxidation in laminar premixed acetylene and ethylene flames. It can predict the PAH growth up to four aromatic rings, pyrene ($C_{16}H_{10}$). Slavinskaya and Frank [47] formulated a semi-detailed chemical kinetics to predict the PAHs up to five aromatic rings in methane and ethane flames. Recently, Raj et al. [34] developed a reaction mechanism for TRF with an emphasis on the formation of large PAHs up to coronene ($C_{24}H_{12}$). There is a coherent argument that, without an accurate estimate of the concentration of PAHs formed in a flame zone, a reliable prediction of soot observables such as soot volume fraction, number density and particle size distribution from soot models cannot be obtained.

In this study, the mechanism developed by Raj et al. [34] was adopted to calculate the flamelet equation. The mechanism consisting 226 chemical species and 2121 reactions describes the high-temperature oxidation of TRF, which is consistent to the surrogate fuel developed in Chapter 3 by coupling the GCR methodology.

To generate the flamelet library, the PREMIX module in CHEMKIN [148] was used with variations in unburned gas temperature of 600 to 800 K by 100 K step, the pressure of 5 to 30 bar by 5 bar step, and the equivalence ratio of 0.5 to 3.5 by 0.1 step, respectively. The governing equations for continuity, energy, species, and equation of state were solved by the damped modified Newton algorithm, where the diffusive and convective terms use central and upwind differencing respectively. The diffusion transport of chemical species was calculated using a mixture-averaged formula, and the computational domain was discretized using conventional finite differencing techniques with adaptive grid control based on solution curvature and gradient, which results in a non-uniform grid spacing. The both criteria of gradient and curvature were set as 0.1 in this study.

5.2.2 Results of Flamelet Library

Figure 5.2 presents the temperature and species mass fraction of i-C_8H_{18}, O_2, CO_2, CO, OH, C_2H_2, and coronene at an engine-relevant condition, T=700 K and p=20 bar, for equivalence ratios of 0.8, 1.0, 1.6, and 2.4 respectively. It is shown that the fuel and oxygen were consumed while the CO_2 and CO were produced across the flame front. With respect to the stoichiometric equivalence ratio, the CO formation level was inversely proportional to that of CO_2 because there was abundant/depleted oxygen to oxidize the fuel; accordingly, the flame temperature in burned region peaked at slightly fuel-rich mixture (not shown here) and decreased for both lean and rich equivalence ratio. The acetylene shows similar profile against the OH radical. However, its production level increased as the mixture fraction became strengthened. Unlike species above, coronene production lasts for a distance behind of the flame front; it is evident that the PAH growth proceeded in slow chemistry.

Figure 5.3 illustrates the mass fraction of acetylene and PAHs with respect to the equivalence ratio at the two different location under T=700 K and p=20 bar. One is the 1 mm behind of OH maximum position and the other one is 20 mm behind of that. The former one is almost right behind of the flame front so that most of parent fuel were oxidized into the small hydrocarbons such as acetylene, and the large molecules like PAHs showed lower concentration. However, as the chemical reaction continues in the post-flame region, the PAHs concentration were increased while that of acetylene diminished because of the HACA growth.

Figure 5.4 more clearly depicts the post-flame reaction behind of the premixed flame at T=600 K and p=5 bar. For the major combustion product, e.g. carbon dioxide, it reached the chemical equilibrium right after the reaction layer and retained the constant concentration. However, the PAHs and their related chemical species continued the chemical reaction under the slow chemistry. The acetylene was mainly produced in the fuel-rich condition due to the thermal cracking of parent hydrocarbon fuels, and it was subjected to the HACA growth for assisting the PAH formation and growth. The pyrene, four-membered aromatic ring, was also formed in the fuel-rich regime but slower than the acetylene production. Then, it was also converted to larger PAHs and hence its concentration was reduced. The chemical mechanism used in this study [34] predicts the coronene as the final product of PAH species, so there is no consumption of coronene for the further growth.

The effect of temperature and pressure on the concentration of chemical species, which are related to the soot nucleation and surface growth, was investigated. Figure 5.5 present the mass fraction of acetylene, pyrene, and coronene along the temperature and pressure variation under φ=3 condition. It is shown that the acetylene mass fraction was increased as the temperature elevation, while it decreased as the pressure reduction. For a given temperature, a high pressure environment induces thin laminar

flame thickness. So, the consumption of acetylene and thereby the production of PAHs brought forward as the flame thickness became thinner. Other chemical species, such as carbon dioxide and carbon monoxide, were followed the basic principle of the combustion physics; the carbon dioxide was decreased while the carbon monoxide was increased as the temperature elevation due to the water-gas shift reaction.

Recalling the concentration of PAHs behind of flame front as shown in Fig. 5.3, not only the coronene but also the other PAHs contribute the total PAH concentration as well. Thus, it is relevant to consider the PAHs which have perceptible mass fraction for the soot precursors, and it will be discussed in the following section.

To sum up, the flamelet equation provides a detailed chemical structure of every species in the C-H-O system. The PAHs and soot related species were produced by following slow chemistry behind of flame front, and it was drastically increased around the equivalence ratio of 1.5. In addition to the mixture strength, the pressure is highly influential to PAH formation.

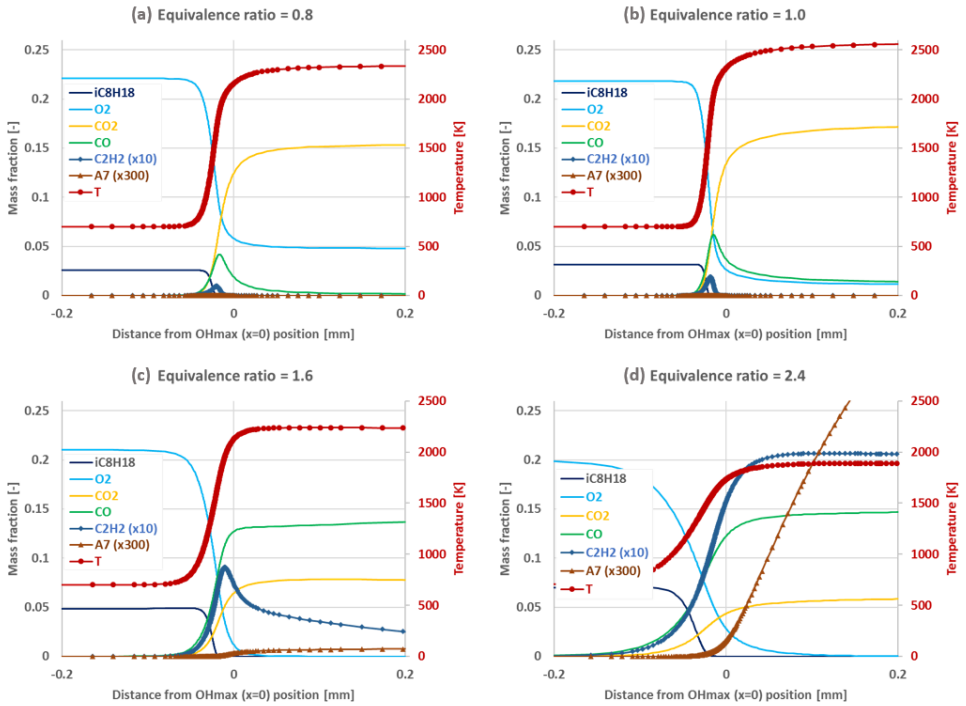

Figure 5.2 Solution of laminar flamelet equation at (a) Φ=0.8, (b) Φ=1.0, (c) Φ=1.6, and (d) Φ=2.4 under T=700 K, p=20 bar condition.

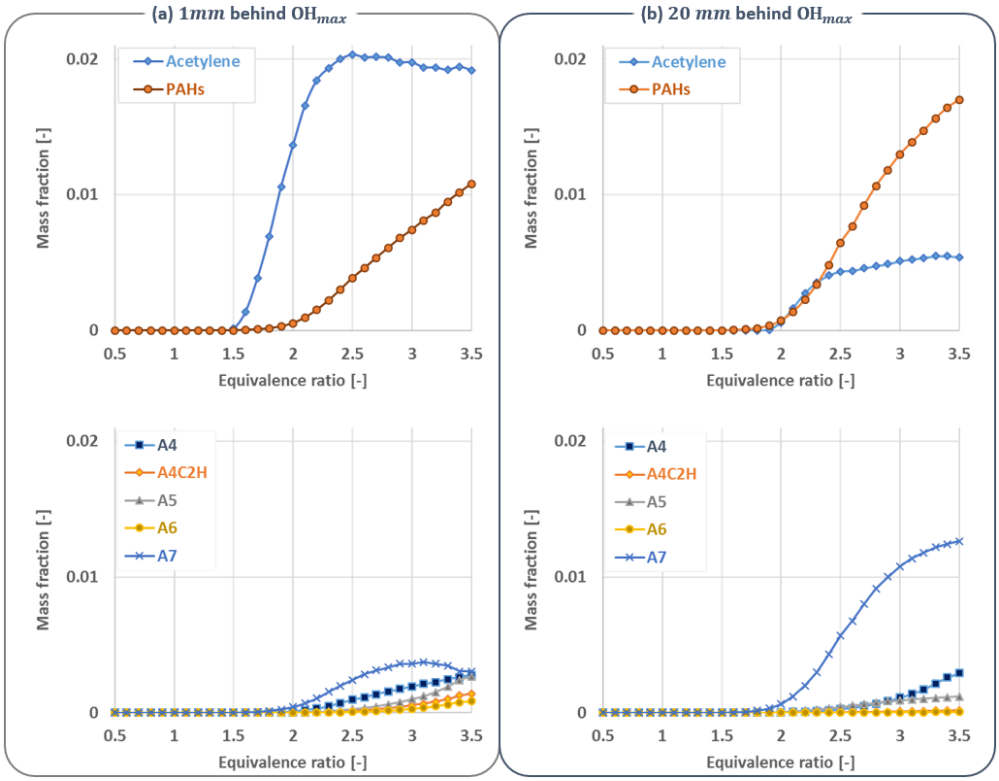

Figure 5.3 Flamelet solution of T=700 K and p=20 bar condition: mass fraction of acetylene and five representatives PAHs (a) at the 1 mm behind (b) at the 20 mm behind of the flame front, which is defined as the location of maximum OH radicals.

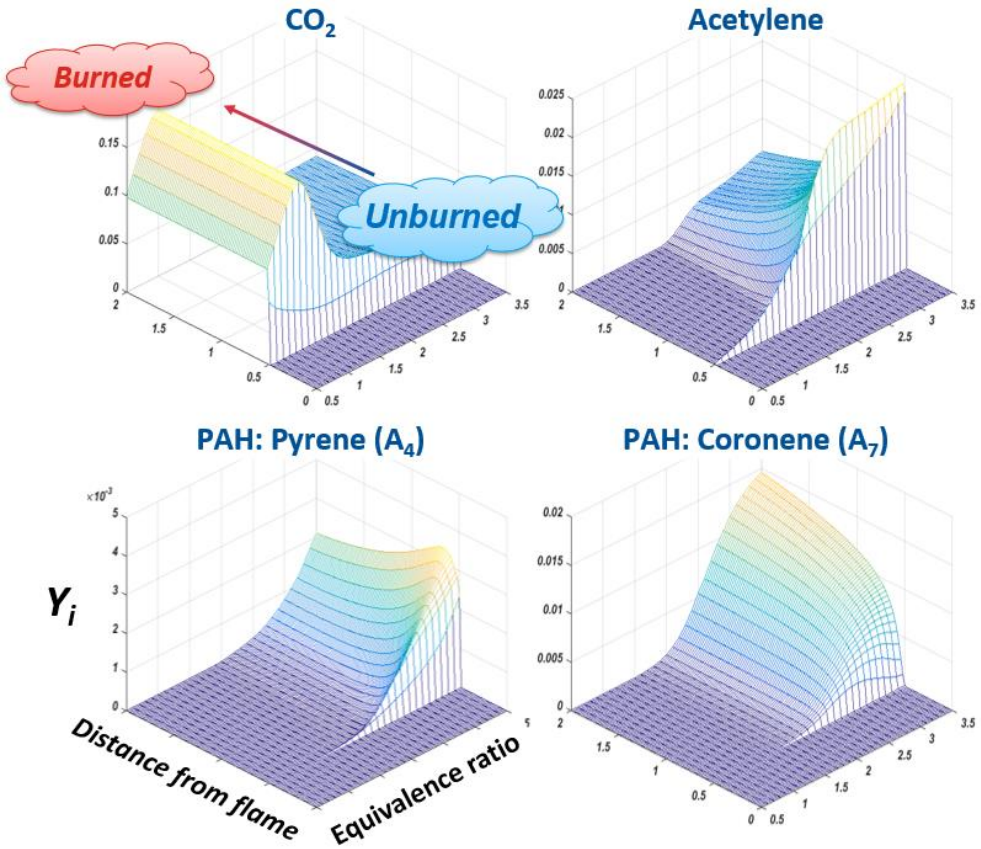

Figure 5.4 Flamelet solutions as a function of flame distance and equivalence ratio for the mass fraction of carbon dioxide, acetylene, pyrene, and coronene at T=600K and p=5bar condition.

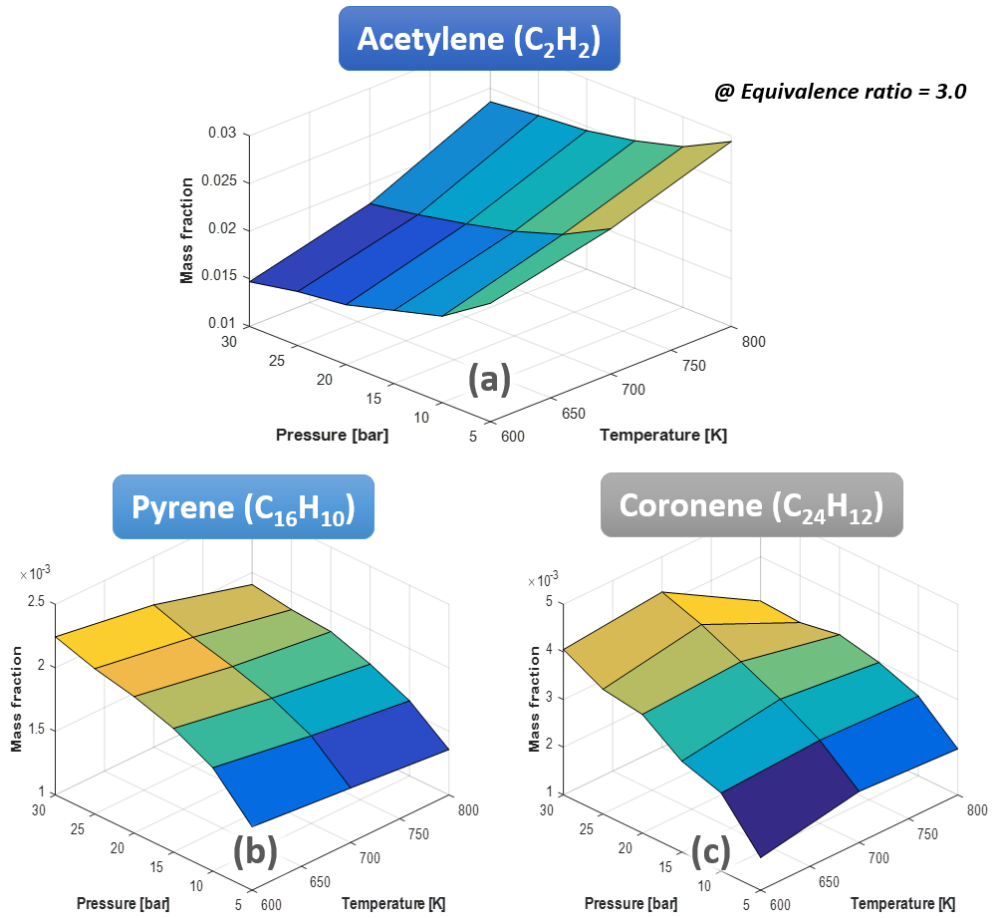

Figure 5.5 The effect of pressure (left axis) and temperature (right axis) on the chemical species that is related to soot nucleation and surface growth: (a) acetylene; (b) pyrene; (c) coronene.

5.3 Modeling Issues on Flamelet Library Approach

In this section, the modeling issue on the flamelet library approach is discussed. Despite the exclusion of online calculation for chemical kinetics, the mapping of all the species into the CFD domain would deteriorate the computational efficiency achieved by the flamelet library approach. In addition, the flamelet solution describes the detailed flame structure including the reaction layer, in which the resolution is finer than the CFD grid spacing. Since most of the chemical species are produced and consumed in the inner layer, the major combustion products including the PAHs are enough if one focus on the fully-burned region.

Meanwhile, the flamelet solution is given in one-dimensional form as a function of flame distance coordinate, while the mapping domain is in three-dimension so that it was difficult to apply one-to-one correspondence. In another word, a computational cell behind of flame front has multiple values of flame distance in three-dimensional CFD domain and thereby its flamelet solution would not be unique. Moreover, there are CO/H2 oxidation as well as PAH formation in burned region according to the slow chemistry and the changes of in-cylinder thermodynamic condition. Hence, the flamelet solution can be regarded as the initial condition for the post-flame reaction rather than the final chemical state that remains unchanged.

To summarize, it is needed to select the species and to determine the referencing point from the flamelet solution. In this study, among the full chemical species of the reaction mechanism, only the generic combustion products, as well as the intermediates related to the post-flame reaction, were considered for the library tabulation as listed in Table 5.1. For the selected species, their burned concentrations were extracted at the distance of four times flame thickness from the inner layer defined as the location of the maximum concentration of OH radical. Most of the

combustion products almost reach their chemical equilibrium at the distant, while the PAHs continue to react due to its slow chemistry. In practice, the turbulent mixing and chemical reaction including the formation of PAHs as well as pollutants co-exist behind of the flame front. One should incorporate another chemical reaction kinetics to account for the PAHs formation, but it weakens the advantage of library approach. Therefore, for the sake of computational efficiency, it is assumed that the further reactions of PAHs were neglected in CFD domain and the referenced composition from flamelet library was assigned to be the initial value for the pollutant models calculation.

Finally, the species concentration in the CFD simulation can be determined with the consideration of the turbulent fluctuation on the air-fuel mixture. It is based on the presumed β-PDF [149] as same as the treatment on turbulent burning velocity. The resultant mass fraction of a chemical species was calculated as

$$\widetilde{Y_i} = \tilde{Y}_{i,u}\left(1-\tilde{P}_f\right) + \tilde{P}_f \int_0^1 \tilde{Y}_{i,b}\left(\tilde{T}_u, p, Z\right) P\left(Z; \tilde{Z}, \widetilde{Z''^2}\right) dZ \quad , \tag{5.5}$$

where Y_i is the species mass fraction, $\tilde{T}_u$ is the mean unburned gas temperature, p is the pressure, $\tilde{Z}$ and $\widetilde{Z''^2}$ are the mean mixture fraction and its variance, respectively. The probability of finding a flame front, $\tilde{P}_f$, is defined by

$$\tilde{P}_f\left(\tilde{G}; \tilde{G}_0, \widetilde{G''^2}\right) = \frac{1}{2} + \frac{1}{2} erf\left(\frac{\tilde{G}-\tilde{G}_0}{\sqrt{2\widetilde{G''^2}}}\right) \quad . \tag{5.6}$$

Table 5.1 Species lumping for flamelet library tabulation.

Representative PAH	Original PAHs to be lumped
A_4 ($C_{16}H_{10}$)	Pyrene
	2-ethynylphenanthrene
	acephenanthrylene
	Fluoranthene
A_4C_2H ($C_{18}H_{10}$)	1-ethynylpyrene
	2-ethynylpyrene
	4-ethynylpyrene
A_5 ($C_{20}H_{12}$)	benzo[a]pyrene
	benzo[e]pyrene
A_6 ($C_{22}H_{12}$)	benzo[ghi]perylene
A_7 ($C_{24}H_{12}$)	coronene

5.4 Literature Review: Soot Modeling Approach

The soot evolution consists of the soot nucleation from the gas-phase PAHs molecules' dimerization, and the surface growth/oxidation as well as the coagulation/aggregation. Numerous models have been developed for describing the soot processes, and they can be divided into three categories: empirical model, semi-empirical model, and detailed model.

The empirical model is based on the simplest concept of soot formation and soot oxidation. Most famous one is the Hiroyasu's two equation model [35], in which the soot formation is directly linked to the fuel concentration whereas the soot oxidation is governed by the oxygen attack. Despite its simplicity, the rate of formation and oxidation are expressed in Arrhenius equation that requires calibration for each test case, and hence it is not predictive to use in the simulation for wide operating conditions.

Multi-step phenomenological model, as an extended version of the two-equation model, incorporates the global rate expressions of the physical processes of soot evolution. As a pioneering work, Fusco et al. [36] proposed an eight-step phenomenological model. The fuel pyrolysis results in the formation of acetylene and soot radical precursor. Consequently, the soot is formed by the precursor radical inception and is grown by the acetylene absorption. The number of soot particles is decreased by the coagulation, while the mass of soot particle is reduced by the oxygen attack. All the physical processes are expressed with global reaction step in Arrhenius form, and the calibration is required. Several models have been proposed with the slight modification of physical processes, and it was popular to modeling the soot emission in Diesel engines [37, 38, 150].

Semi-empirical model partially captures some aspects of physical and chemical dynamics of soot formation and evolution. It is usually coupled with a chemical reaction mechanism for the soot precursor prediction, and the soot processes are calculated with a phenomenological approach. Leung et al. [151] developed a soot model in which the chemical reaction mechanism predicts the acetylene concentration for soot inception. The other soot processes, such as surface growth by acetylene absorption, oxidation by O_2 molecule, and the particle coagulation were described by a set of Arrhenius equations. Similar to their work, Tao et al. [150] proposed a soot model for diesel spray combustion where the surface reaction of HACA mechanism was replaced the acetylene absorption for soot mass growth. Recently, Vishwanathan and Reitz [29] also suggested a semi-detailed model for diesel and low-temperature combustion engine based on the approach of Leung et al. [151].

A detailed model aims to describe each of the key underlying physio-chemical processes, to the extent that those are known. Three model frameworks have been proposed: MOMIC [54], sectional method [152], and Monte-Carlo simulation [153]. Since the soot particles intrinsically have developed a size distribution by their aerosol dynamic interaction, the detailed model captures the particle size distribution either indirectly or directly, along with the total number density and volume fraction prediction. In addition, the Monte-Carlo simulation can provide the chemical structure of soot by tracking the soot surface area, a number of primary particles, and each PAH shape including a number of an armchair, zigzag, free edge, bay sites. Though the utmost detailed prediction can be obtained by this approach, it is computationally expensive to apply in three-dimensional CFD domain.

5.5 Soot Modeling by Semi-Empirical Approach

5.5.1 Soot Nucleation

Nucleation is the formation of the first soot particle from the collision and condensation of PAH molecules. In the conventional semi-empirical model proposed earlier, one PAH was considered for the nucleation step, and the number of carbon atoms in the PAH was converted to the soot nucleus with same carbon number [150, 151]. In this study, the five PAHs range from pyrene ($C_{16}H_{10}$) to coronene ($C_{24}H_{12}$) were considered as the soot precursor, and their initial concentration was provided from the flamelet library.

The soot nuclei were formed by the dimerization of two PAHs through either homogeneous nucleation or heterogeneous nucleation, so the entire reaction pathways for soot nuclei production were 15 routes. In addition, the nucleation rate was referred to work of Wang et al. [154] in that the process was irreversible with zero activation energy and the collision efficiencies of each PAH were considered.

5.5.2 Coagulation

Coagulation occurs when two soot particles collide and coalesce to form a single spherically shaped particle, thereby decreasing the number density and holding the combined mass of particles constant. This physics is usually described by the Smoluchowski's equation [155] as

$$nC(S) \xrightarrow{\omega_{\mathrm{cg}}} C(S) \qquad \omega_{\mathrm{cg}} = \frac{1}{2} k_{\mathrm{cg}} N^2 \quad [/\mathrm{cm}^3 \cdot \mathrm{s}] \tag{5.7}$$

where subscript cg denotes the coagulation process, k_{cg} is the collision frequency, and N is the soot number density. Several works on semi-empirical soot modeling were considered the coagulation in the free-molecular regime only, however, it is needed to take the continuum regime into account due to the high combustion pressure in the cylinder. Thus, the collision frequencies according to the coagulation regime by Frenklach [54] were adopted in this study, where the Knudsen number was used for the regime determination.

Free-molecular regime (Kn > 10): $k_{\mathrm{fm}} = 4\varepsilon\sqrt{\frac{6k_B T d_{\mathrm{soot}}}{\rho_{\mathrm{soot}}}}$ (5.8a)

Near-continuum regime (Kn < 0.1): $k_{\mathrm{nc}} = \frac{8k_B T}{\mu}(1 + 1.257\mathrm{Kn})$ (5.8b)

Transition regime: $k_{\mathrm{cg}} = \frac{k_{\mathrm{fm}} k_{\mathrm{nc}}}{k_{\mathrm{fm}} + k_{\mathrm{nc}}}$ (5.8c)

where ε is the van der Waals enhancement factor of 2.2, k_B is the Boltzmann constant, d_{soot} and ρ_{soot} are the soot diameter and density, and Kn is the Knudsen number defined as $\mathrm{Kn} = 2\lambda/d_{soot}$.

5.5.3 Surface Growth

The soot nuclei undergo the mass growth via the chemical reaction or the physical condensation of PAHs on its surface. In this study, only the surface growth by the chemical reaction was considered. It is demonstrated that the acetylene is the principal species that reacts on the surface of soot nuclei, and this carbon addition process follows the first-order kinetics in the laminar premixed flame [156, 157]. Accordingly, most studies were adopted the acetylene absorption concept [38, 151,

158]. In this study, the reaction rate by Leung et al. [151] was implemented, in which the soot mass growth is proportional to the square root of soot surface area.

$$nC(S) + \mathrm{C_2H_2} \xrightarrow{\omega_{\mathrm{sg}}} (n+2)C(S) + \mathrm{H_2},$$

$$\omega_{\mathrm{sg}} = 6 \times 10^3 \exp\left(\frac{-12100}{T}\right)[C_2H_2]\sqrt{A_{\mathrm{soot}}} \qquad [\mathrm{mol/cm^3 \cdot s}] \qquad (5.9)$$

where subscript sg indicates the surface growth process, and A_{soot} is the surface area of soot particle.

5.5.4 Surface Oxidation

In contrast to the surface growth, the surface oxidations via oxygen molecules and OH radicals reduce the soot mass while kept the soot number density to be unmodified. For the oxidation through oxygen molecules, a semi-empirical correlation was derived from the extensive measurement [159] and it is widely used in phenomenological and numerical models of the combustion system. Recently, Ladommatos et al. [160] carried out an experimental investigation on the oxidation rate of Diesel soot particle under atmospheric pressure by varying the temperature and oxygen partial pressure and modified the NSC model coefficients. In this study, the correlation was incorporated for the soot oxidation via oxygen molecules, and its reaction step and rate constant can be written as follow.

$$C(S) + \frac{1}{2}\mathrm{O_2} \xrightarrow{\omega_{\mathrm{ox},O_2}} CO,$$

$$\omega_{\mathrm{ox},O_2} = \frac{12}{M_{C(S)}}\left[\left(\frac{k_A p_{O_2}}{1+k_Z p_{O_2}}\right)x + k_B p_{O_2}(1-x)\right]A_{\mathrm{soot}} \quad [\mathrm{mol/cm^3 \cdot s}] \tag{5.10a}$$

$$x = 1/\{1 + k_T/(k_B p_{O_2})\} \tag{5.10b}$$

$$k_A = 30\exp\left(-\frac{15800}{T}\right) \quad [\mathrm{g/cm^2 \cdot s \cdot atm}] \tag{5.11a}$$

$$k_B = 8\times10^{-3}\exp\left(-\frac{7640}{T}\right) \quad [\mathrm{g/cm^2 \cdot s \cdot atm}] \tag{5.11b}$$

$$k_Z = 1.51\times10^{5}\exp\left(-\frac{49800}{T}\right) \quad [\mathrm{g/cm^2 \cdot s}] \tag{5.11c}$$

$$k_T = 27\exp\left(\frac{3000}{T}\right) \quad [\mathrm{/atm}] \tag{5.11d}$$

where subscript ox indicates the oxidation process, p_{O_2} is the oxygen partial pressure, and $M_{C(S)}$ is the molecular weight of carbon as 12 g/mol, respectively.

For the soot oxidation via OH radicals, the empirical correlation proposed by Fenimore and Jones [161] was adopted in this study. The rate step can be schematically written as

$$C(S) + OH \xrightarrow{\omega_{\mathrm{ox,OH}}} CO + H$$

$$\omega_{\mathrm{ox,OH}} = 10.5833\gamma_{\mathrm{OH}}\frac{[\mathrm{OH}]}{[X]}\sqrt{T}A_{\mathrm{soot}} \quad [\mathrm{mol/cm^3 \cdot s}] \tag{5.12}$$

where γ_{OH} is the collision efficiency as 0.13, $[\mathrm{OH}]$ is the molar concentration of OH radicals, and $[X]$ is the total molar concentration, respectively.

5.6 Soot Modeling by MOMIC

To explore the predictability of state-of-the-art model for the DISI engine application, the MOMIC was incorporated for the soot aerosol dynamics, and more detailed documentation can be found in [54, 162]. The following sections describe a set of modified moment equations for each process. It is worth noting that the modification was performed to introduce additional PAHs as well as the reaction steps, and neither the supplemental new model constant nor the change of parameter value was considered in this study. Thus, for the sake of brevity, the list of parameter values was omitted and left to refer to the literature.

5.6.1 General description

The rth moments of the particle size density function (PSDF) is defined as $M_r = \sum_{i=1}^{\infty} i^r N_i$ where *i* is the discrete size of the particle, and N_i is the number density of the ith particle class. The smallest particles have a mass of carbon $m_1 (= m_C)$, and the particles of class *i* have a mass $m_i = i m_1$. The first four moments were used to yield statistical information of the system, and the particle mean diameter, total particle volume fraction, and number density can be obtained as below, respectively.

$$\bar{d}_p = d_1 \mu_{1/3}, \quad V_p = \frac{m_1}{\rho} \mu_1 M_0, \quad N = M_0 \tag{5.13}$$

In the above equations, $\rho = 1.86$ g/cm^3 is the soot nuclei density, and $\mu_r (= M_r / M_0)$ is the reduced moment. The population dynamics of a particle ensemble undergoing simultaneous nucleation (R), coagulation (G), and surface reaction (W) is obtained as

$$\dot{M}_0 = R_0 - G_0,$$

$$\dot{M}_1 = R_1 + W_1,$$

$$\dot{M}_r = R_r + G_r + W_r, \text{ for r} \geq 2.$$

(5.14)

The calculation starts with the nucleation where the PAH concentration exists. Unlike the generic soot modeling approach that directly relates the fuel to the soot precursor, this model relies on a sound physical basis. The transport of the produced soot particle was considered as

$$\bar{\rho}\frac{\partial \widetilde{M}_r}{\partial t} + \bar{\rho}\tilde{\vec{u}} \cdot \nabla \widetilde{M_r} = \bar{\rho}\nabla\left(D_p \nabla \widetilde{M_r}\right) + \widetilde{\dot{M}_r} \quad (5.15)$$

where D_p is the turbulent soot diffusivity and $\dot{M}_r$ is the rate of rth moment.

5.6.2 Nucleation

Recently, Wang et al. [154] proposed a soot model for the counterflow diffusion flame of ethylene and adopted eight PAHs for the soot nucleation. To improve the computational efficiency, only five PAHs were selected: Pyrene (A_4), ethynyl-pyrene (A_4C_2H), benzo[e]pyrene (A_5), benzo[ghi]perylene (A_6), and coronene (A_7). Then, the nucleation pathway has a total of 15 routes, comprising five homogeneous and ten heterogeneous nucleations. The source term by particle nucleation is

$$R_r = \sum_{k=1}^{15} j_{nuc,k}^{r} \times r_{C,k} \quad (5.16)$$

where j_{nuc} is the j[th] class of new particle created by nucleation, r as a superscript denotes the r[th] moments, and k as a subscript denotes the k[th] nucleation reaction. The PAHs collision rate in the k[th] nucleation, $r_{c,k}$, can be expressed as

$$r_C = \frac{1}{2}\sum_{i=1}^{n}\sum_{j=1}^{n}\beta\sqrt{\frac{8\pi k_B T}{\mu_{i,j}}}\left(\frac{d_i}{2}+\frac{d_j}{2}\right)^2 N_i N_j \tag{5.17}$$

where subscript i,j represent the PAH species, β is the collision efficiency, k_B is the Boltzmann constant, T is the gas temperature, $\mu_{i,j}$ is the reduced mass, d_i is the collision diameter of the PAH molecule, and N_i is the number density of PAH molecules.

5.6.3 Coagulation

The coagulation regime can be divided into two parts by the criterion of the Knudsen number, the free molecular regime for large Kn and the continuum regime for small Kn. The source term for coagulation in the free-molecular regime reads

$$G_0 = \frac{1}{2}K_f M_0^2\langle\varphi_{0,0}\rangle \tag{5.18a}$$

$$G_r = \frac{1}{2}K_f M_0^2\sum_{k=1}^{r-1}\binom{r}{k}\langle\varphi_{k,r-k}\rangle \tag{5.18b}$$

where $\langle\varphi_{x,y}\rangle$ is the grid function. K_f is the collision frequency in the free-molecular regime and is defined as

$$K_f = \varepsilon\sqrt{\frac{6k_B T}{\rho}}\left(\frac{3m_1}{4\pi\rho}\right)^{1/6} \tag{5.19}$$

where ε is the van der Waals enhancement factor of 2.2. The source term for coagulation in the continuum regime reads

$$G_0 = K_c M_0^2 \left[1 + \mu_{-1/3}\mu_{1/3} + K_c'\left(\mu_{-1/3} + \mu_{1/3}\mu_{-2/3}\right)\right]$$

$$G_r = \frac{1}{2}K_c \sum_{k=1}^{r-1} \binom{r}{k} \left[2\mu_k\mu_{r-k} + \mu_{k+\frac{1}{3}}\mu_{r-k-\frac{1}{3}} + \mu_{k-\frac{1}{3}}\mu_{r-k+\frac{1}{3}} + \right.$$

$$\left. + K_c'\left(\mu_{k-\frac{1}{3}}\mu_{r-k} + \mu_k\mu_{r-k-\frac{1}{3}} + \mu_{k-\frac{2}{3}}\mu_{r-k+\frac{1}{3}} + \mu_{k+\frac{1}{3}}\mu_{r-k-\frac{2}{3}}\right)\right] M_0^2 \tag{5.20}$$

where K_c is the collision frequency in the continuum regime and is defined as

$$K_c = \frac{2k_B T}{\eta}, \quad K_c' = 1.257\text{Kn} \tag{5.21}$$

where η is the molecular viscosity. Between the two regimes, the harmonic means of the source term were used as a transition regime.

5.6.4 Surface Growth/Oxidation

The surface growth of the particles occurs via physical and chemical reactions. The one describes the condensation of PAH molecules on the particle surface, while the other represents the HACA growth of the particles. The PAH condensation occurs via the five selected PAHs and its source term reads

$$W_{r,cond} = \sum_{is=1}^{5} r_{is} N_a \pi M_0 \times \left[\sum_{l=0}^{r-1} \binom{r}{l} (\Delta j)^{r-l} \left(d_{is}^2\mu_1 + 2d_{is}d_1\mu_{l+\frac{1}{3}} + d_1^2\mu_{l+\frac{2}{3}}\right)\right]$$

(5.22)

where the subscript denotes the corresponding PAH species, Δj is the mass added by the given reaction, and d_{is} is the collision diameter of the PAH species. The collision rate, r_{is}, is calculated by multiplying the PAH-soot free-molecular collision rate by the collision efficiency and the van der Waals enhancement factor.

The HACA growth of a particle is mainly driven by a chemical process on the active site. In the current study, the mechanism proposed by Wang et al. [154], which is based on the combined work of Appel et al. [146] and Hwang and Chung [163] considering the odd-carbon species of CH_3 and C_3H_3 and the even-carbon species of C_2H, are responsible for the H-abstraction reactions. The source term for HACA growth reads

$$W_{r,HACA} = r_{is} N_a \pi d_1^2 M_0 \left[\sum_{l=0}^{r-1} \mu_{l+2/3}\right] \tag{5.23}$$

The reaction rate between the PAH species and surface sites on the particle can be written as

$$r_{is} = A_{is} T^{B_{is}} exp(-E_a/RT)[PAH]\alpha\Gamma_{Csoot*} \tag{5.24}$$

where A_{is}, B_{is}, E_{is} are the rate constants, α is the available site fraction, and Γ_{Csoot*} is the surface site density.

5.6.5 Post-Flame Reaction Modeling

The soot models were combined with the G-equation and flamelet library, and each model solves the transport equation for the soot volume fraction and soot number density, or the moments. Meanwhile, the pollutant formation such as NO and CO production were also simulated in this study.

In DISI engine, the CO concentration in post-flame varies due to the dissociation and oxidation between CO and CO2, and it is kinetically controlled depending on the in-cylinder temperature during the combustion and expansion stroke. Hence, an H2/CO combustion kinetics [164] was incorporated to resolve the post-flame reaction. In addition, as the NO formation undergoes slow chemistry in burned region, and the fraction of thermal-NO predominates among the engine-out nitrogen oxides due to high in-cylinder temperature, therefore the extended Zeldovich mechanism with the value of rate constant in Heywood [3] was adopted. For solving these reactions, the concentration of intermediate species of H, O, and OH were referred to the flamelet library.

Chapter 6. Experimental and Numerical Setup and Preliminary Model Evaluation

6.1 Experimental and Numerical Setup

In this section, at first, the experimental setup of a single cylinder DISI engine and a set of measurement systems on the test bench are described, and the pressure data acquisition and post-processing methodologies are discussed. Then, the numerical setup for DISI engine simulation including the computational mesh, initial/boundary conditions is delineated. The setup for all the engine experiment and simulation conducted in this study will be referred to this section, and only the operating conditions will be introduced hereafter.

6.1.1 Engine specifications

In this study, a naturally aspirated single cylinder DISI engine was used to acquire experimental validation data, in which a side mounted fuel injector was installed. The detailed engine specifications are given in Table 6.1. The engine also can be operated in PFI mode with its injector installable intake manifold.

The test engine was connected to a 190 kW AC dynamometer (AVL Eblin). The temperature and flow rate of coolant and engine lubricant oil were controlled via dynamometer system. A Compact-RIO platform that allowed for handling the real-time data communication and signal processing was implemented to control and monitor the engine parameters. The injection signal and ignition trigger were also controlled by this system during the engine operation. A broadband lambda sensor

(Horiba, MEXA-110λ) was implemented to measure the air-fuel ratio at the exhaust pipe. Based on the measured lambda, the fuel mass was tuned to a target air-fuel ratio.

6.1.2 Pressure Data Acquisition and Post-Processing

Two pressure transducers, an absolute pressure sensor (Kistler 4043A2, 0-2 bar) and a relative pressure sensor (Kistler 6052A, up to 250 bar) were installed in the intake manifold and at the engine head, respectively. Signals from each pressure sensor were amplified by a charge amplifier (Kistler 5019A) and piezo-resistive amplifier (Kistler 4603), respectively, and were recorded by using a combustion analyzer (AVL IndiModule). Before the data logging, the top dead center (TDC) calibration is conducted by finding the maximum pressure with the compensation of thermal loss angle. During the pressure signal acquisition, the signal passes a hardware low-pass filter in the charge amplifier with 50 kHz cutoff frequency, and it is post-processed via the combustion analyzer where 40 kHz cutoff frequency is applied in a software program. In addition, the pressure data was pegged with respect to the absolute pressure of intake manifold at bottom dead center (BDC).

To obtain the reliable experimental data, total 300 cycles of in-cylinder pressure acquired in 0.1 CA sampling rate were averaged for combustion analysis. All the experiments were conducted at the steady-state condition and satisfied the cycle of variation (COV) under 2%. The measured in-cylinder data was post-processed *via* in-house Matlab code to derive the net indicated effective pressure (nIMEP), gross indicated effective pressure (gIMEP), 5, 10, 50, and 90% of mass fraction burned (MFB5, 10, 50, 90) timing, heat release rate (HRR), and cumulative heat release rate (cHRR). The following equations referred from Heywood [3] were used in this study.

$$\text{nIMEP} = \frac{W_{c,in}}{V_d} = \frac{\int_{\text{intake}}^{\text{exhaust}} PdV}{V_d} \tag{6.1}$$

$$\text{gIMEP} = \frac{W_{c,ig}}{V_d} = \frac{\int_{\text{compression}}^{\text{expansion}} PdV}{V_d} \tag{6.2}$$

$$\text{HRR:} \quad \frac{dQ}{d\theta} = \frac{\gamma}{\gamma-1} P \frac{dV}{d\theta} + \frac{1}{\gamma-1} V \frac{dP}{d\theta} \tag{6.3}$$

$$\text{cHRR: } Q(\theta) = \frac{\int_{\text{-30° CA bTDC}}^{\theta} \dot{Q}(\theta\prime) d\theta\prime}{\int_{\text{-30° CA bTDC}}^{\text{90° CA aTDC}} \dot{Q}(\theta\prime) d\theta\prime} \tag{6.4}$$

6.1.3 Exhaust Emission Measurement

The gaseous exhaust emission, CO_2, CO, NO_x, THC as well as a residual O_2 fraction, were measured by an exhaust gas analyzer HORIBA MEXA-7100 DEGR. All the gas compositions are indicated in volume fraction; for NO_x and THC under wet condition, while the CO_2, CO, O_2 are under dry condition. The measuring probe was located at the 300 mm downstream of the exhaust pipe, and the probe gas enters into preheater to prevent the water condensation in sampling line.

For the particulate emission, a Cambustion DMS500 instrument was installed at 400 mm downstream of the exhaust, to measures the particle size/number spectrum from 5 nm to 2.5 μm with 10Hz sampling rate. AVL SmokeMeter 415S was also incorporated to determine the soot concentration, which using the filter paper to collect the soot particles and measuring the soot content via the photoelectric method.

6.1.4 Computational Mesh

The commercial CFD code STAR-CD v4.24 [165] was used, and the ES-ICE toolkit was incorporated to generate an engine mesh as shown in Fig. 6.1. The mesh contained approximately 160,000 – 881,000 grid points depending on the piston position from TDC to BDC. The average cell size was approximately 1 mm through the whole cylinder domain of which has its maximum volume at BDC, while the cell spacing is further reduced around 0.3 mm at TDC to capture the large gradient species and temperature due to combustion. Also, a cell layer was wrapped entire computational domain to ensure the normal flow and thermal physics behavior adjacent to the wall.

Additional cells have been attached to the intake and exhaust port section to allow the fully-developed flow profile at the head-port entrance. To reduce the computational cost, the intake port and exhaust port were excluded after the intake valve close (IVC) and exhaust valve close (EVC) timings, respectively. The computational grid corresponds to the valve opening/closing, and the piston reciprocating event is handled by the moving mesh algorithm provided by ES-ICE during simulation.

6.1.5 Initial and Boundary Conditions

A well-calibrated GT-Power model, which describes the aforementioned experimental system, was used to provide the pressure and temperature boundary conditions of the intake and exhaust ports, respectively. It has advantages to provide boundary conditions of intake and exhaust temperature, which cannot be measured in the experiment due to slow response time of thermocouple. Note that the not only the

pressure but also the temperature is of great importance to accurately predict the residual gas fraction as well as the air-fuel mass trapped in the cylinder.

For cold operating conditions, a set of constant wall temperatures of 348 K, 353 K, and 438 K corresponding to the cylinder liner, combustion dome, and piston face, respectively, were imposed, and a wall function model proposed by [166] was used. The intake port wall temperature is relatively lower than in-cylinder condition because there is no direct exposure to the combustion heat and continuous cooling by fresh air, as a consequence, the temperature of 323 K was set at the intake port and valve stem region. In contrast to the intake port, the exhaust port is hotter, and thereby 533 K was imposed. For hot operating condition, the temperatures were adjusted as 413 K, 423 K, 463K, 358 K, and 533 K, respectively.

Table 6.1 Specifications of single-cylinder research DISI engine

Parameter	Specifications
Engine type	Spark ignition
Fuel injection system	Wall-guided direct injection
Displacement volume	499 cc
Bore × Stroke	86 mm × 86 mm
Connecting rod	146.25 mm
Compression Ratio	9.5
Exhaust Valve Open (EVO) / Close (EVC)	54º CA bBDC / 10º CA bTDC
Intake Valve Open (IVO) / Close (IVC)	10º CA bTDC / 50º CA aBDC

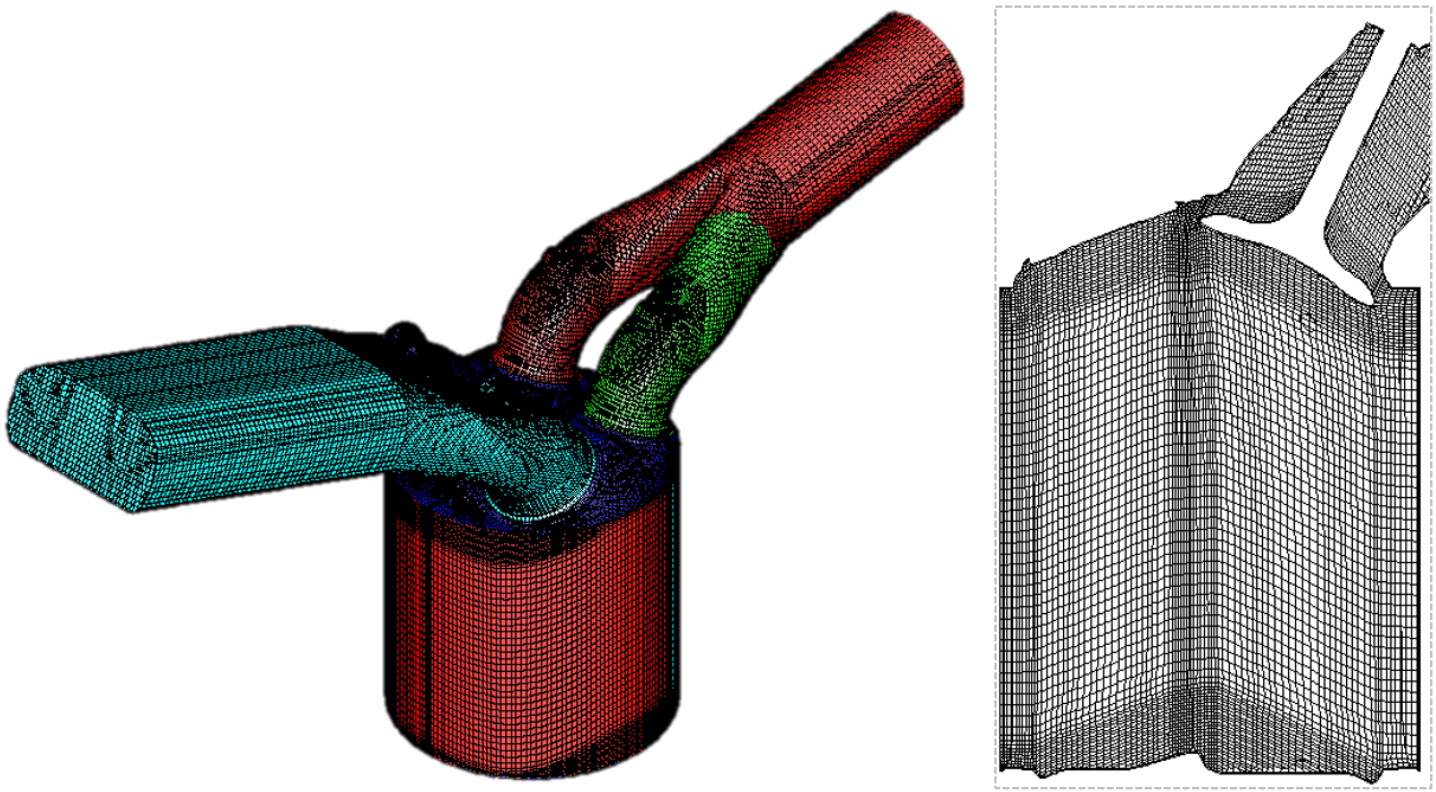

Figure 6.1 Computational mesh of the DISI engine.

6.2 Experimental Investigation of Soot Emission Similarity between TRF and Gasoline

In this section, the modeling assumption of combustion surrogate and kinetics were verified through the engine experiment. The PAH is closely correlated with the hydrocarbon chemical families because of its distinct molecular structure, and it affects the soot nucleation and growth as well. Several experimental research have been documented that an aromatic hydrocarbon with a high boiling point tend to produce more soot emission [100, 101]. Thus, not only the mixture distribution but also the fuel constituent is responsible for the soot emission in DISI engines.

In the CFD simulation, the six-component surrogate eventually participates the combustion process through iso-octane, n-heptane, and toluene chemistry based on the GCR methodology as discussed in Chapter 3. Meanwhile, in the practical engine experiment, the real gasoline contains various aromatics and allows diverse PAHs reaction pathway. Indeed, the composition analysis result reported that the gasoline used in this study consists the aromatics in the range of C_6 to C_{11}, so that there may exist a certain difference in soot emission level between simulation and experiment due to the modeling assumption. Therefore, it is worth to conduct a preliminary investigation on soot emission similarity between TRF and gasoline in the engine experiment. In the following, the experimental setup and operating condition are presented first, and then the investigation results are discussed in detail.

6.2.1 Engine Operating Condition

TRF as the combustion surrogate according to GCR methodology, its composition of iso-octane, n-heptane, and toluene were correlated to that of spray surrogate by hydrocarbon chemical families: iso-pentane and iso-octane (51.4%), n-hexane and n-undecane (34%), o-xylene and p-diethylbenzene (14.6%) in volume fraction, respectively. The low heating value of TRF is 43.73 MJ/kg by the linear blending of volume fraction, which is 2.1% higher than that of gasoline.

For the experimental investigation of engine, the key is to set identical operating environment for different condition. The direct injection may lead inhomogeneous mixture distribution due to different volatilities of TRF and gasoline so that the port-fuel injection was adopted to secure the premixed status. Two port fuel injectors, which were installed in the intake port runners, inject the fuel toward the backside of intake valves under the rail pressure of 6 bar. The fuel injection was done at 710º CA bTDC which allows nearly one cycle term between the injection and ignition events.

To promote the fuel vaporization, the coolant and lubricant oil temperatures were set at 85ºC for warm-up the chamber wall. Aided by combustion heat, the temperature was sufficient to fully vaporize the TRF in which the highest boiling point is 111ºC for toluene. However, it was still low to cover the entire boiling range of gasoline. The gasoline residue was expected to be vaporized during the mixing process.

In addition, the combustion phase was retained as same as possible by fixing the engine load at nIMEP 6 bar and the MFB50 at 15º CA aTDC. It is an attempt to derive the same thermodynamic condition between two fuels along the combustion process which would affect the soot process. The soot emission level was measured by varying the equivalence ratio of air-fuel mixture from 0.9 to 1.6, of which the engine was in

stable operation with COV under 2%. As the mixture goes richer, the burning velocity is lowered due to the intrinsic laminar flame characteristics, so that the ignition timing was advanced to compensate the delayed mass burn rate. Table 6.2 summarizes the operating condition in detail.

6.2.2 Experimental Results

Figure 6.2 and 6.3 show the in-cylinder pressure as well as the heat release rate for both fuels under the variation of equivalence ratio from 0.9 to 1.6. It can be seen that the peak pressures were located around 20° CA aTDC and the trailing pressure traces of all conditions are almost same. The spark timing was advanced to compensate the lower laminar burning velocity for fuel-rich or fuel-lean conditions, so the initial pressure rise of those cases became faster than others. The in-cylinder pressures of TRF and gasoline for each equivalence ratio condition were compared in Fig. 6.4, and it is clear that the not only the combustion phase but also the pressure trace was almost identical. Therefore, it can be concluded that the TRF was capable of emulating the combustion proceeded by turbulent flame propagation, and the in-cylinder thermodynamic conditions for a given equivalence ratio between TRF and gasoline were in good agreement.

Regarding the soot emission, Figure 6.5 shows the soot concentration as well as the soot number density of both fuels measured by DMS500. It is revealed that the soot mass and number were drastically increased around equivalence ratio between 1.3 and 1.4, which is in agreement with the previous research [24, 44, 46]. For the soot concentration, the emission levels under equivalence ratio of 1.3 were almost negligible because they were around the measurable limit. Likewise, the number

density level is around in the order of 10^7 for the equivalence ratio less than 1.3, and it can be treated as a base level from a near stoichiometric flame front.

The soot concentration exhibited a substantial increment starting from φ=1.3 to φ=1.6; increasing factor of 31.4, 19.6, and 11.3 for TRF, and that of 33.6, 10.0, and 11.2 for gasoline, were resulted with the equivalence ratio elevation by 0.1 step, respectively. Accordingly, the soot number density also showed significant increment; 6.5, 3.9, and 2.8 for TRF, and 5.5, 2.6, 2.9 for gasoline, were resulted in the same variation. Recalling the solutions of flamelet equation, a considerable production of acetylene, as well as PAHs around equivalence ratio of 1.5, were shown in the previous chapter.

It is interesting to see that the trend of soot emission between TRF and gasoline were the same. However, the absolute level of gasoline was always higher than that of TRF as shown in Fig 6.5. Despite the same volume fraction of the aromatic content of gasoline was set as toluene composition in the TRF, the gasoline contains the aromatics from C_6 to C_{11+} and hence it tended to produce more soot precursors than TRF. Thus, it can be concluded that the difference of emission level originated from the hydrocarbon constituents in the fuel. By comparing the emission difference in quantitatively, the soot concentration and number density of gasoline did not exceed in the factor of two from that of TRF for the equivalence ratio larger than 1.3, and it became smaller as the air-fuel ratio being rich.

From the boiling temperature standpoint, the TRF always has a chance to fully vaporize before the ignition since the engine run at the warm-up condition and with closed valve injection. If one assumes that the gasoline does not vaporize entirely so there might be liquid residue at the ignition timing, then the residue fraction will be increased as the strengthening of the mixture. It could deteriorate the soot emission

level further, and widen the gap of soot emission level between TRF and gasoline. However, it can be seen that the discrepancy was slightly reduced from φ=1.3 to 1.6, rather than being increased as above assumption. Thus, it can be considered that little liquid gasoline left during the combustion and its effect on soot emission was so small as to be almost insignificant.

In summary, the TRF and gasoline had the similarity in terms of soot emission level, including soot concentration as well as soot number density, when the soot formation was only affected by the chemical reaction under premixed state. Therefore, with the correct prediction of air-fuel mixture field, the surrogate transition from spray surrogate to combustion surrogate by GCR is valid for soot emission modeling.

Table 6.2 Experimental condition for PFI engine fueled with TRF and gasoline

Parameter	Specification
Engine speed	2000 rpm
Engine load	IMEP 6 bar
Ignition timing	MFB50 @ 15º CA aTDC
Injection timing	710º CA bTDC
Injection pressure	6 bar
Fuel	TRF, gasoline
Equivalence ratio	0.9 to 1.6 by 0.1 step

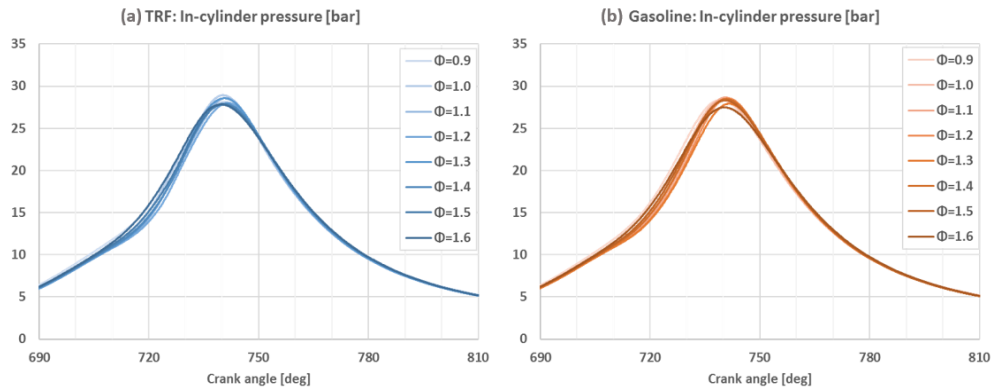

Figure 6.2 Measured in-cylinder pressure from the PFI engine experiment with the variation of global equivalence ratio from 0.9 to 1.6: (a) TRF and (b) Gasoline.

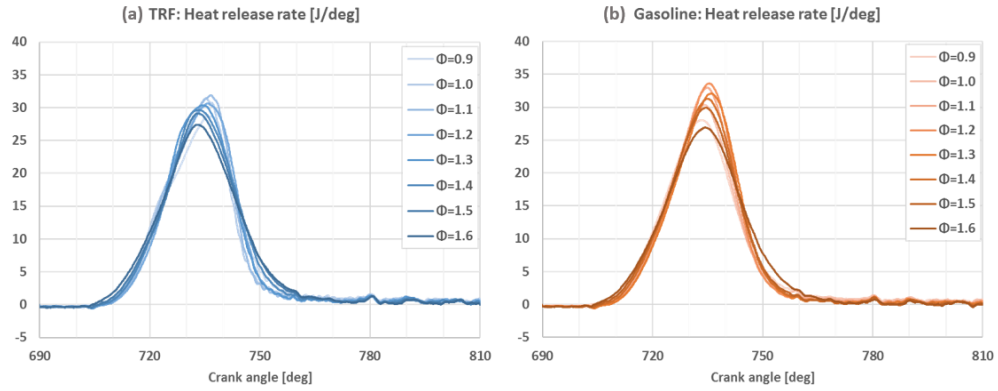

Figure 6.3 Measured heat-release rate from the PFI engine experiment with the variation of global equivalence ratio from 0.9 to 1.6: (a) TRF and (b) Gasoline.

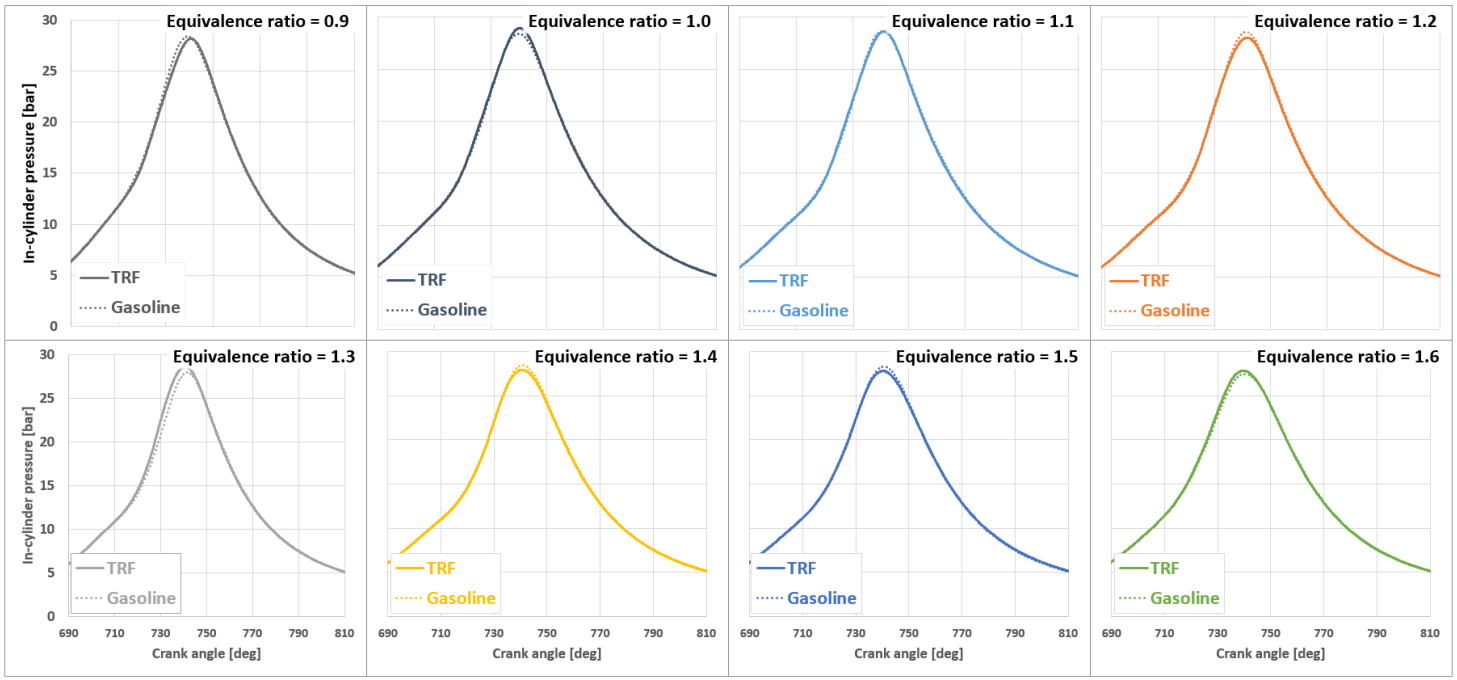

Figure 6.4 Comparison of in-cylinder pressure between TRF and Gasoline in the PFI engine experiment according to the variation of global equivalence ratio.

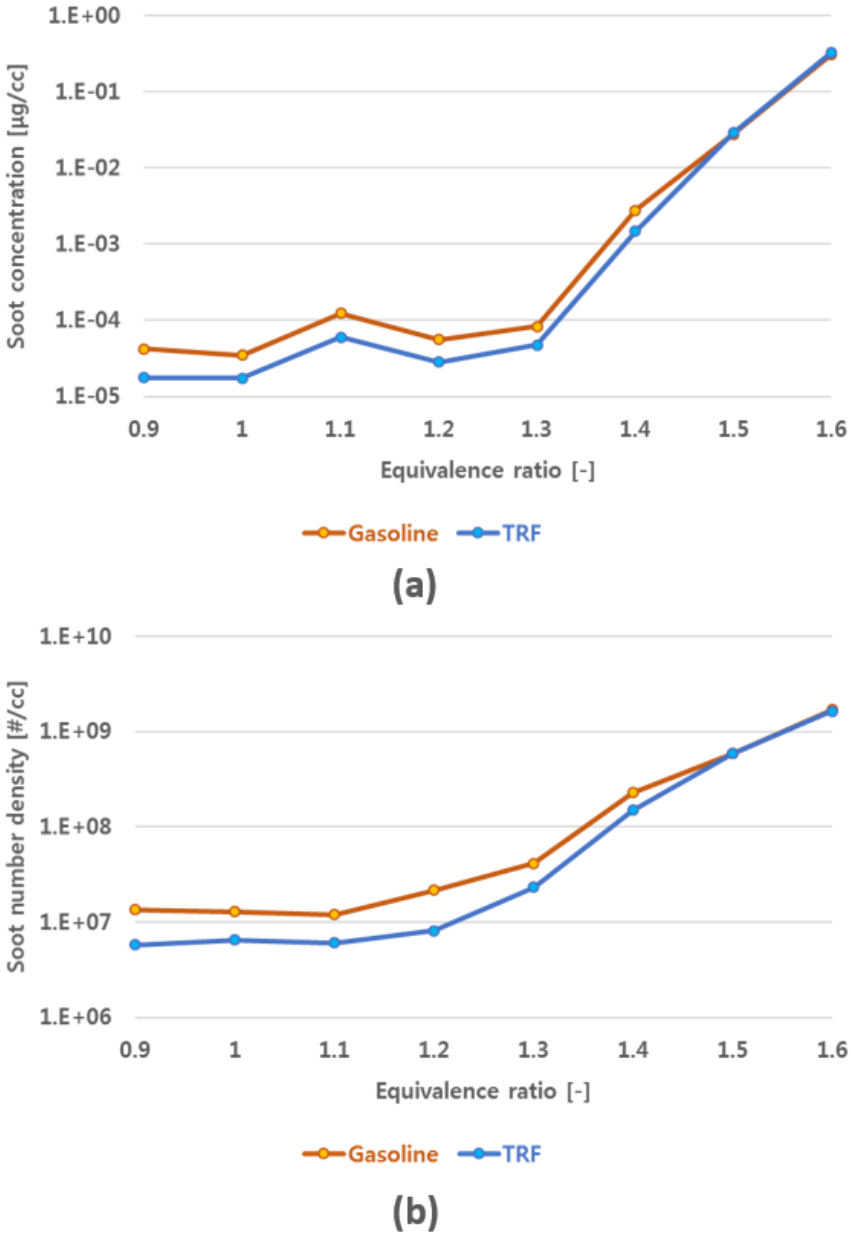

Figure 6.5 Measured (a) soot concentration and (b) soot number density from the PFI engine experiments.

6.3 Model Evaluation under Catalyst Heating Condition

Before starting the engine simulation for soot emission, it is worth to conduct a preliminary evaluation for the developed and calibrated models in this study. So far, each model was validated against the experimental data from the fundamental experiment, but the integrated models have not yet applied and verified in the engine condition.

Ideally, the in-cylinder optical measurement for the air-fuel mixture distribution and combustion process would be effective for the model validation. Despite the fact that the laser induced fluorescence (LIF) can obtain the two-dimensional fuel vapor distribution where the laser sheet beam passes, it is difficult to re-construct the three-dimensional distribution by a single measurement. In addition, the high-speed imaging is feasible to access the flame propagation in the free combustion chamber volume optically, but it is hard to capture the flame behavior near the wall surface. Furthermore, the optical measurement in the engine has limitations to imitate the practical operating condition due to the durability of the optical window under normal combustion run.

Therefore, the model evaluation was done against the data from a metal engine experiment, where the in-cylinder combustion pressure and soot emission were measured. To explore the wide model applicability, the engine was operated with two injection strategies under a catalyst heating condition. The effects of incorporating the surrogate fuel, calibrated break-up, and laminar burning velocity (LBV) of gasoline on the combustion and soot emission, were examined by comparing them with the existing models from the literature.

6.3.1 Engine Operating Condition

The single-cylinder DISI engine was run at 1500 rpm with the intake manifold pressure of 0.91 bar. The spark-ignition was done at 10° CA aTDC which is to increase the exhaust heat flux by late-combustion for catalyst heating. The temperatures of coolant and lubricant oil were kept in 40°C. Two different dual-injection strategies were adopted while targeting the stoichiometric air-fuel ratio; one has a successive dual-injections during the intake stroke (Early Dual-Injection), and the other split the injections into intake and compression stroke (Early/Late Injection), respectively. These are the typical operating strategies for catalyst heating phase and the detailed conditions were listed in Table 6.3.

6.3.2 Case Setup for CFD Simulation

Under the catalyst heating condition, the six-component surrogate fuel, calibrated break-up, and LBV of gasoline were evaluated against the existing models found in the literature. To clarify the effect of model introduction on the combustion and soot emission results, a base set consisting iso-octane, KH-RT model with base constant, and the LBV correlation suggested by Metghalchi and Keck [128] were established, and each model was replaced with the model developed in this study as shown in Table 6.4.

6.3.3 Model Evaluation Results

In this section, the simulation results in Early Dual-Injection and Early/Late Injection are presented. For the model evaluation criteria, the MFB05/10/50/90 were

used for the combustion process to see whether the prediction is within the standard deviation of 100 cycles data. Regarding the soot emission, the soot concentration should be predicted within 50% difference compared to experimental data, while for the soot number density only the qualitative trend was examined.

Early Dual-Injection

Figure 6.6 presents the air-fuel mixture distribution and the fuel film deposition of three cases at the ignition timing. For the early-dual injection strategy, there was more time available for mixing so that the air-fuel ratio tended towards the stoichiometric. It is revealed that most of the mixture was within the equivalence ratio range from 0.8 to 1.2, and there was the only slight difference between the model's effect. However, by magnifying the y-axis scale to focus on the air-fuel mixture that has $\varphi > 1.5$, a remarkable difference was observed. For the Case A and Case B where the break-up calibration was omitted, there were a little fuel-rich mixture in the cylinder; while for the Case C, the order of magnitude differed from the previous two cases. The figure also indicates the qualitative comparison of fuel film deposition on the chamber wall between three cases. For the Case C, the film deposition on the liner was significant, and the thickness was much higher than Case B.

Though the surrogate fuel describes the wide boiling range of real gasoline so that it has a much higher boiling point compared to the iso-octane, the droplet size reduction by fast break-up predominates the vaporization results. It can be concluded that not only the volatility as intrinsic fuel property but also the break-up as extrinsic spray physics are of great importance for mixture formation process in DISI engines. As indicated in Section 2.2, most studies focused on matching the penetration length as a quantitative comparison or the spray morphology as a qualitative comparison, but

the droplet size distribution was neglected from the simulation target. In this study, both characteristics were quantitatively resolved, and thereby the authenticity of prediction can be ensured.

Figure 6.7 shows the temporal evolution of fuel film mass for three cases in the Early Dual-Injection strategy. The overall trend between Case B and Case C were similar except the initial deposition amount, while the film behavior of Case A was totally different from the others. The film mass is related to the spray momentum and droplet properties such as viscosity and surface tension, and the film evaporation is governed by the liquid fuel volatility. Consequently, the Case B and Case C only differed at the spray momentum so that the film mass showed the discrepancy, and the film vaporization proceeded at the same rate. However, the iso-octane (Case A) behaved faster vaporization rate due to the low boiling point.

The simulation results of in-cylinder pressure are depicted in Fig. 6.8 (a). Regardless of fuel and spray model variations, the combustion pressure was almost identical under the same LBV model, and their traces were shown faster burning rate compared to the Case D. It is because that the overall air-fuel mixture distribution were similar to each other except the local fuel-rich region around the fuel film. Figure 6.8 (b) shows the combustion phase in terms of MFB quantitatively, and it is clear that the models developed in this study (Case D) was able to reproduce well-matched results.

It is interesting to focus on the mass burning rate after MFB90 for Case C and D as shown in Fig. 6.9. In the Case C, the LBV was drastically decreased as the MFB reaches 90% and it had almost near-zero value afterward. However, under the same air-fuel mixture distribution, a significant level of LBV was retained for case D. Aided with the section contour for the in-cylinder mixture distribution as displayed in Fig

6.10, it is shown that the fuel-lean mixture took place in front of propagating flame. The LBV proposed by Metghalchi and Keck [128] intrinsically returns near-zero value due to its parabolic type fitting curve. By magnifying the center of piston bowl, it led an incomplete combustion for fuel-rich mixture in Case C even though its combustion rate was faster than that of Case D.

Finally, the soot concentration results comparison between experimental data and four simulation cases are plotted in Fig. 6.11. The iso-octane fuel and non-calibrated break-up model (Case A and B) resulted in negligible soot emission, whereas the developed models (Case D) agreed within the evaluation criteria. As discussed in above, the Case C resulted in lower soot than Case D due to unrealistic LBV at the fuel-rich mixture. It was confirmed with the temporal evolution of soot concentration, the initiation of soot formation in the Case C was slower than that in the Case D despite its faster combustion rate.

Early/Late Injection

The injection strategy is usually adopted to improve the cold start-ability by delivering the ignitable mixture to the spark plug. Figure 6.12 shows the in-cylinder air-fuel mixture formation of case D from 100° CA bTDC to ignition timing with 10° CA interval. As it can be seen from the figure, the first injection took place at the mid of intake stroke to form a lean-homogeneous mixture, and the second injection was done at the late of the compression stroke, where the spray targeted to the piston bowl and reflected toward the spark plug. According to the mixture distribution at the ignition timing depicted in Fig. 6.13, it is revealed that the Case A and B were failed to deliver ignitable air-fuel mixture to the spark plug. It is because that the fast break-up rate (Case A and B) and low boiling point (Case A) resulted in the relatively

enhanced vaporization, and diminished the spray momentum for traveling toward the spark plug. By contrast, the six-component fuel along with calibrated break-up model brought the air-fuel mixture around the spark plug at the ignition event. Subsequently, the mixture covered the spark plug as time proceeds.

The simulation of combustion process confirms the above observation. Figure 6.14 presents the in-cylinder pressure trace and the combustion phase of four simulation cases. It can be seen that the Case A and B resulted in misfire and no pressure rise, but both of the Case C and D have succeeded in the normal combustion and their combustion phases were almost within the evaluation criteria. To investigate the ignition phase in detail, the local equivalence ratio of air-fuel mixture around the spark plug was monitored and plotted in Fig. 6.15. For the Case A and B, the equivalence ratio was 0.4 to 0.6, and it is too lean to ignite successfully. Here, it is worth to note that the experimental data of in-cylinder pressure for 100 cycles did not show a misfire cycle. Furthermore, the pollutants measured by HORIBA emission analyzer indicated that the O_2 and THC fraction were in the normal level proving complete combustion (see Table 6.5).

Finally, the model developed in this study (Case D), the simulation result of soot concentration as well as the number density for early dual injection and early/late injection were compared against the measured data as shown in Fig. 6.16. The results were in good agreement and satisfied the evaluation criteria well. To sum up, the validity of the six-component surrogate fuel, break-up model calibration, and the laminar burning velocity of gasoline model have been proved by either fundamental measurements, such as distillation curve, penetration length, and droplet size distribution, and the literature data, or the practical engine simulation as discussed above. It is expected that the developed models can be applied to further engine simulation with proven authenticity.

Table 6.3 Investigated condition for fuel and spray model evaluation.

Parameter	Specification	
Engine speed	1500 rpm	
Intake manifold pressure	0.91 bar	
Injection strategies	Early Dual-Injection	Early/Late Injection
Injection timing	1st: 285° CA bTDC 2nd: 275° CA bTDC	1st: 220° CA bTDC 2nd: 48° CA bTDC
Injection split ratio	1st: 50%, 2nd: 50%	1st: 60%, 2nd: 40%
Injection pressure	100 bar	
Ignition timing	10° CA aTDC	
Target excess air (λ) ratio	1.0	

Table 6.4 Case setup for model evaluation.

	Fuel Model	Break-up Model	LBV Model
Case A (Base)	iso-octane	Base	Metghalchi & Keck
Case B	6-comp. surrogate	↑	↑
Case C	↑	Calibrated	↑
Case D (This work)	↑	↑	TRF w/ mixing rule

Table 6.5 Measured emission by HORIBA analyzer in the Early/Late Injection case.

Emission	Unit	Value
O2	[%]	0.82
CO	[ppm]	6350
THC		686

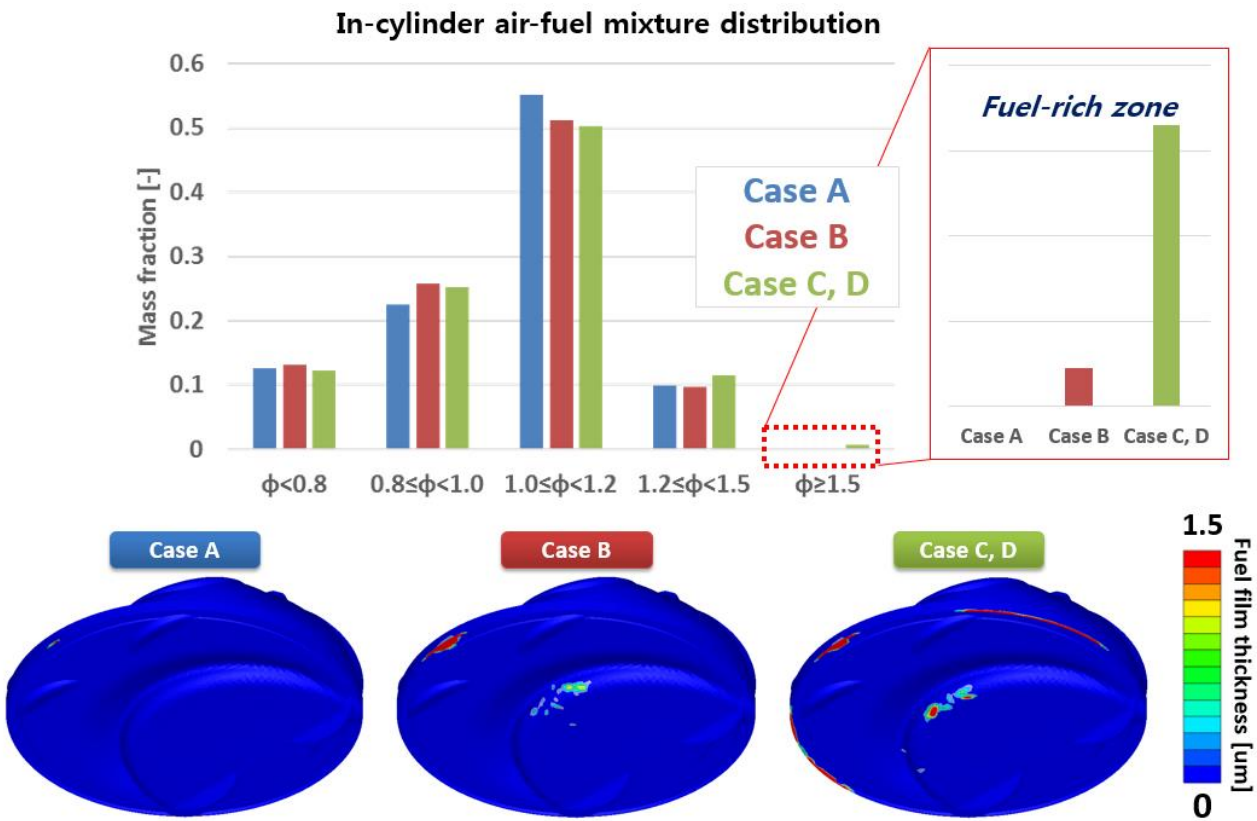

Figure 6.6 Early Dual-Injection: In-cylinder air-fuel mixture distribution and the fuel film deposition at the ignition timing for Case A to Case D.

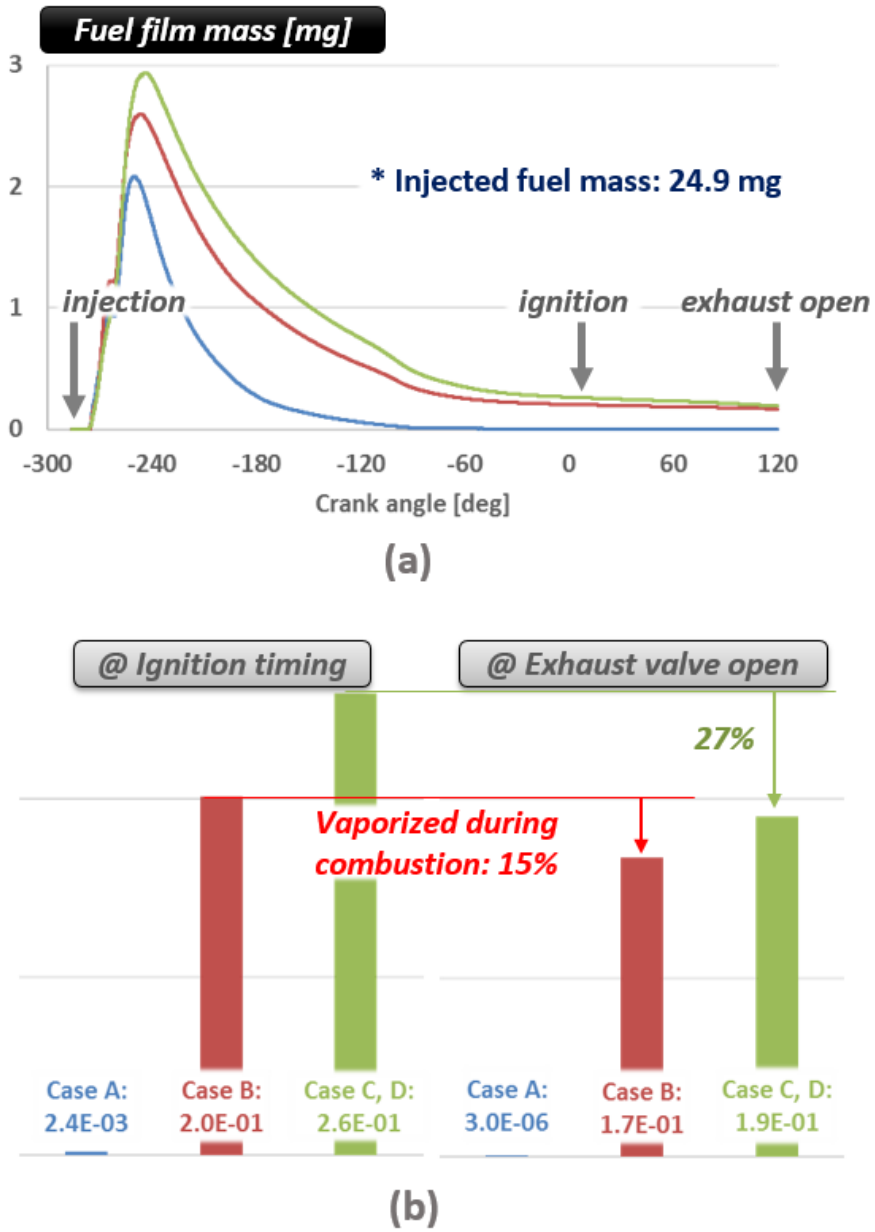

Figure 6.7 Early Dual-Injection: (a) Time history of fuel film mass and (b) vaporized film mass during the combustion.

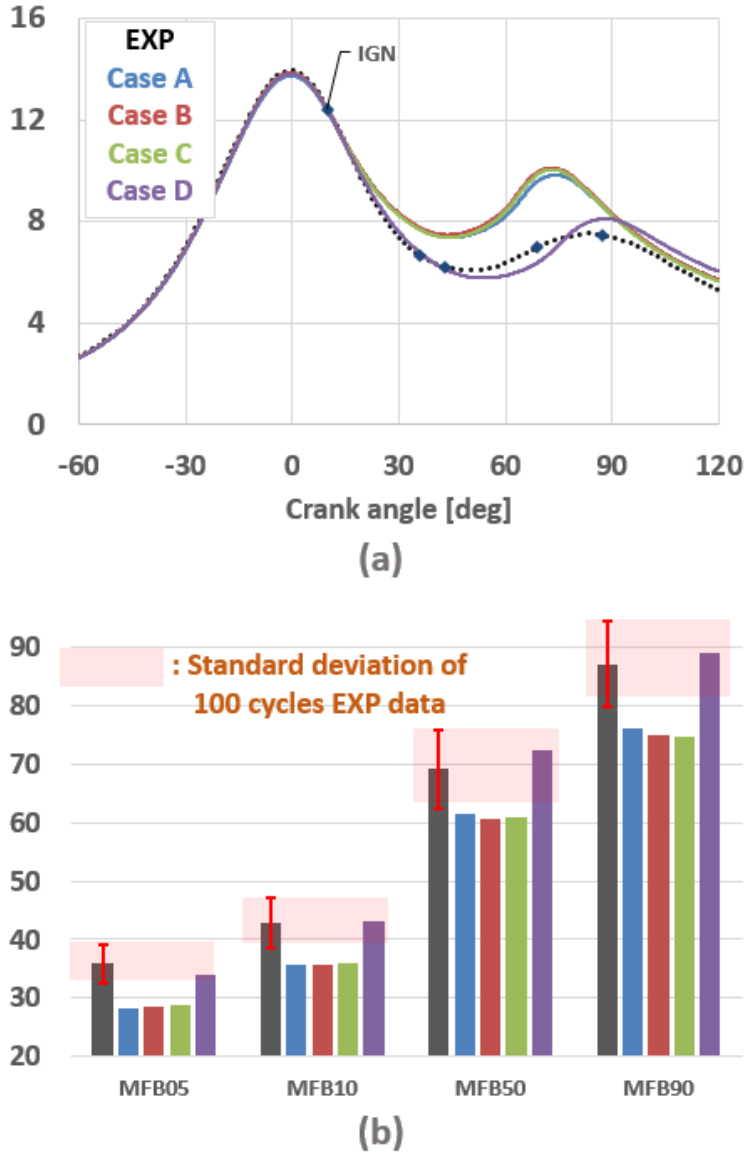

Figure 6.8 Early Dual-Injection: (a) In-cylinder pressure and (b) combustion phase of MFB05, MFB10, MFB50, and MFB90, where the standard deviations of 100 cycle data were indicated by shaded box.

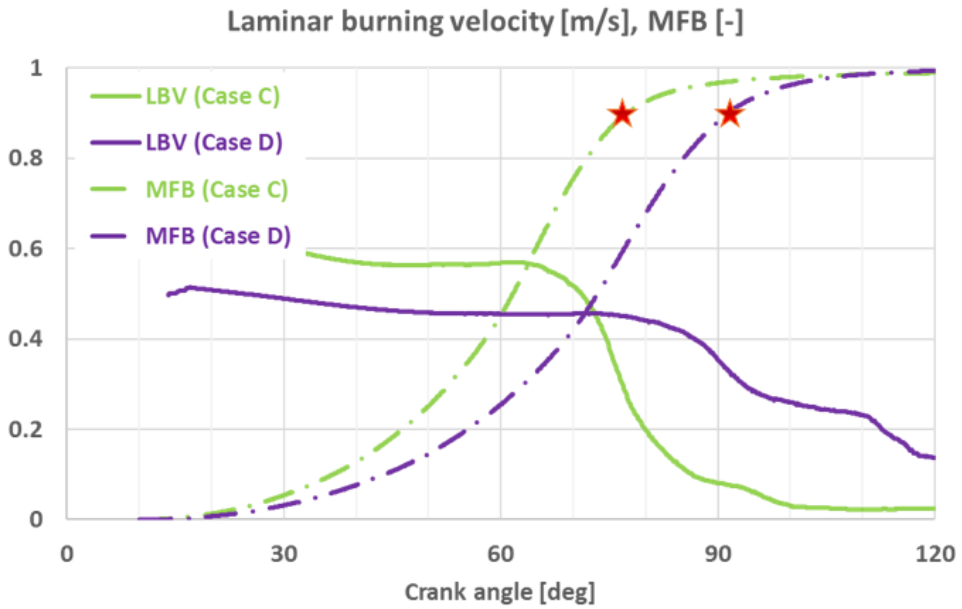

Figure 6.9 Early Dual-Injection: Time history of laminar burning velocity (solid line) and MFB (chain line) of case C and D during combustion process. The MFB90 timing was denoted by red-star symbol.

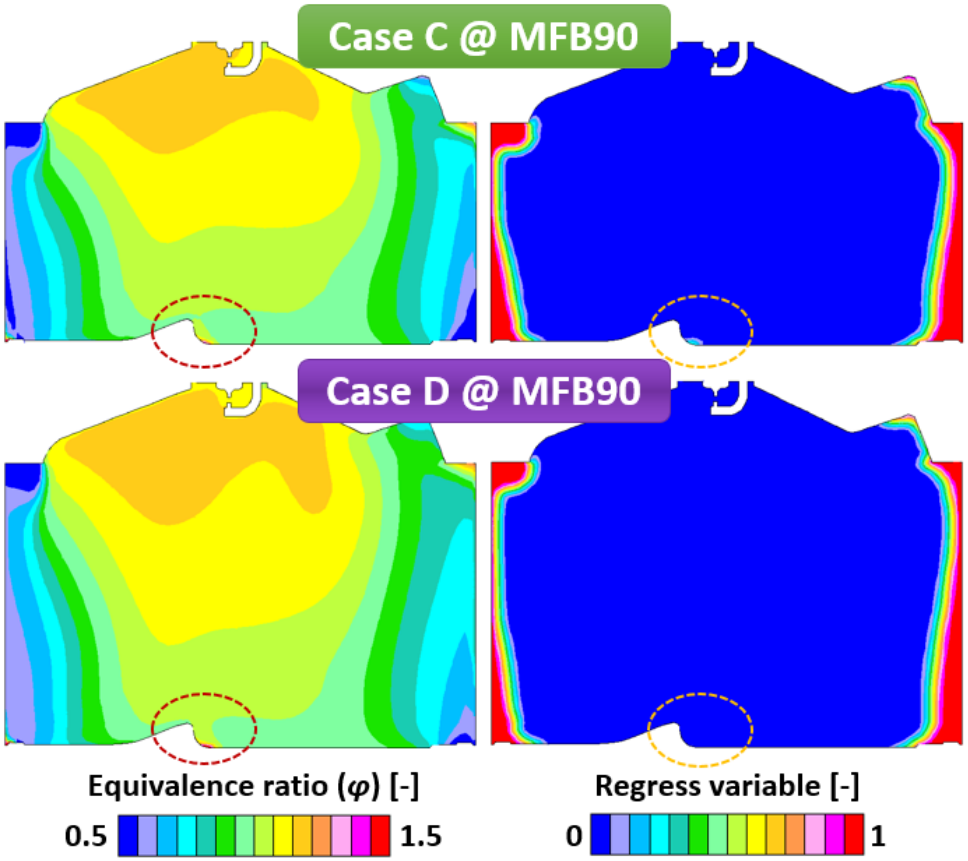

Figure 6.10 Early Dual-Injection: In-cylinder section contour of equivalence ratio and mass burning status by regress variable at the MFB90 timing.

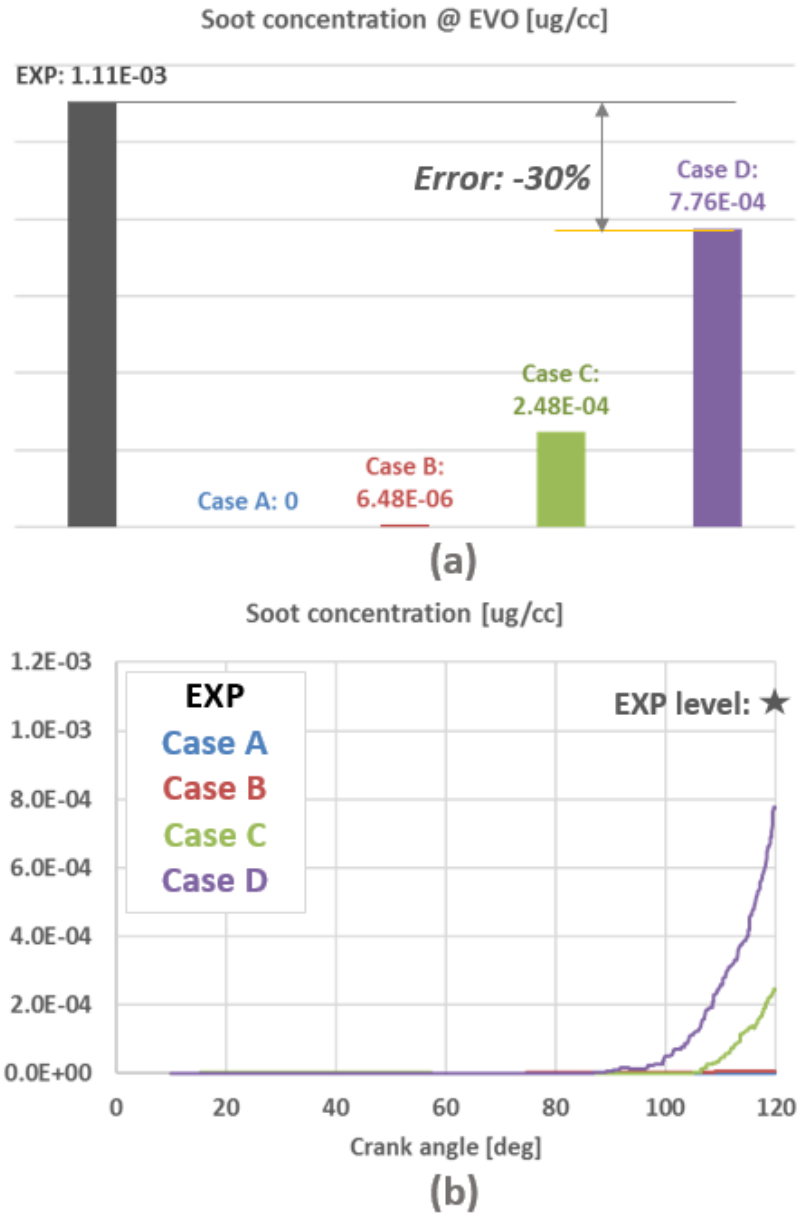

Figure 6.11 Early Dual-Injection: (a) Measured and simulated soot concentration and (b) its time history during the combustion process.

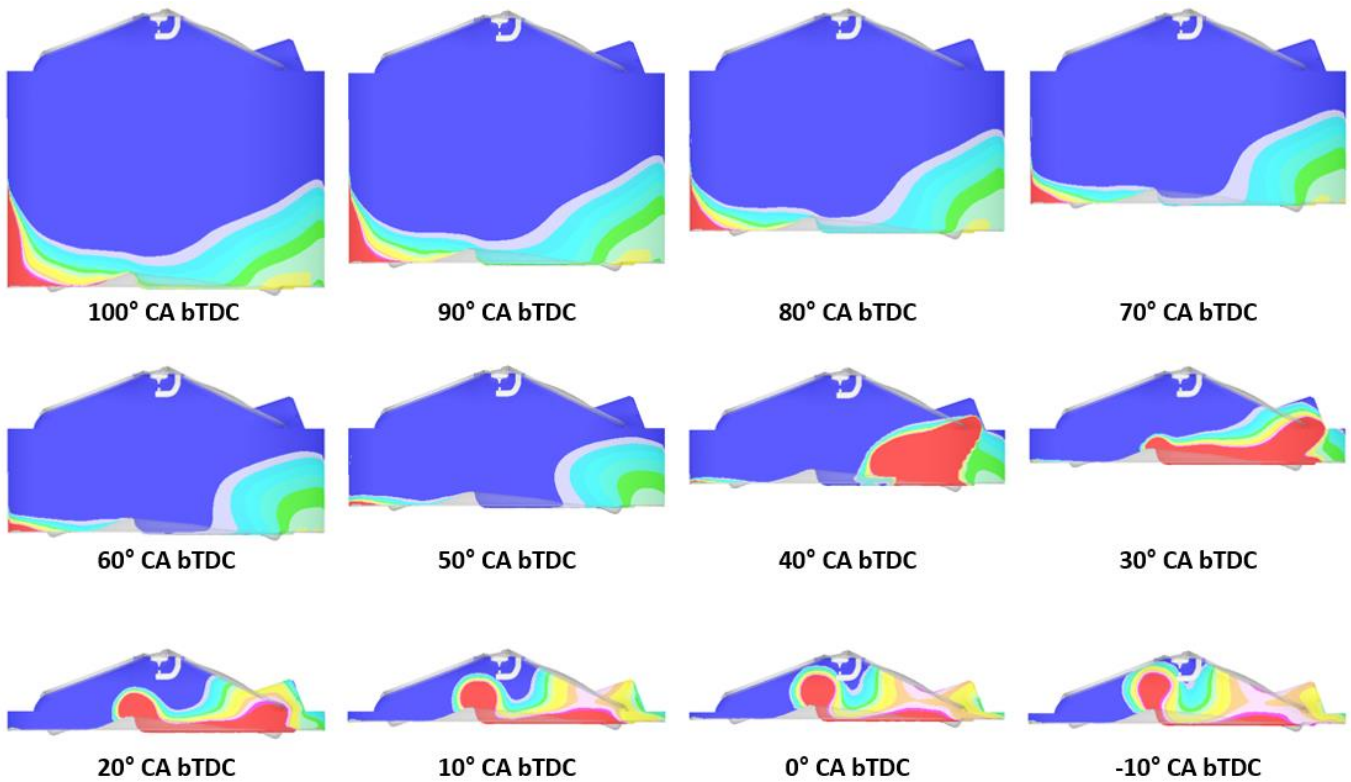

Figure 6.12 Early/Late Injection: Air-fuel mixture formation from 100° CA bTDC to ignition timing with 10° CA interval.

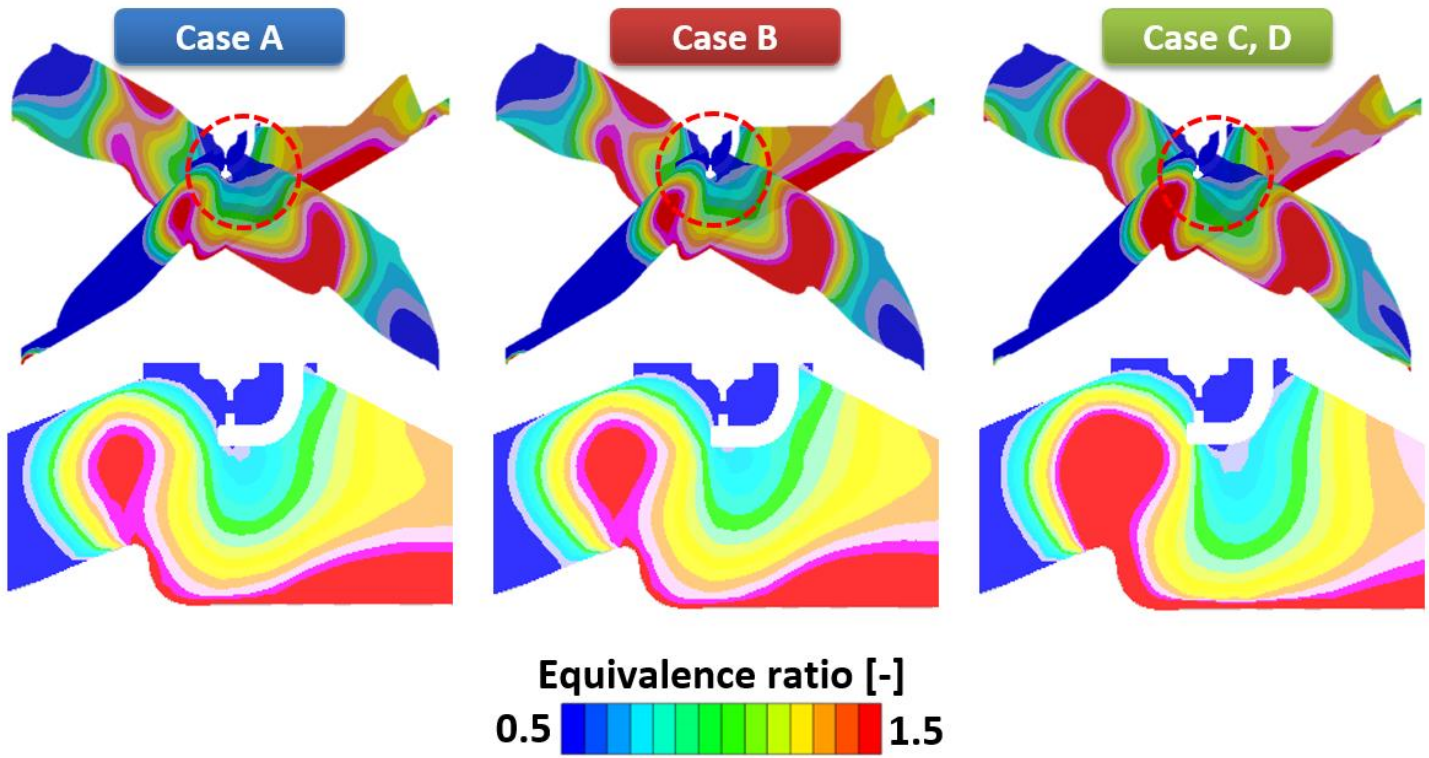

Figure 6.13 Early/Late Injection: Air-fuel mixture distribution at the ignition timing.

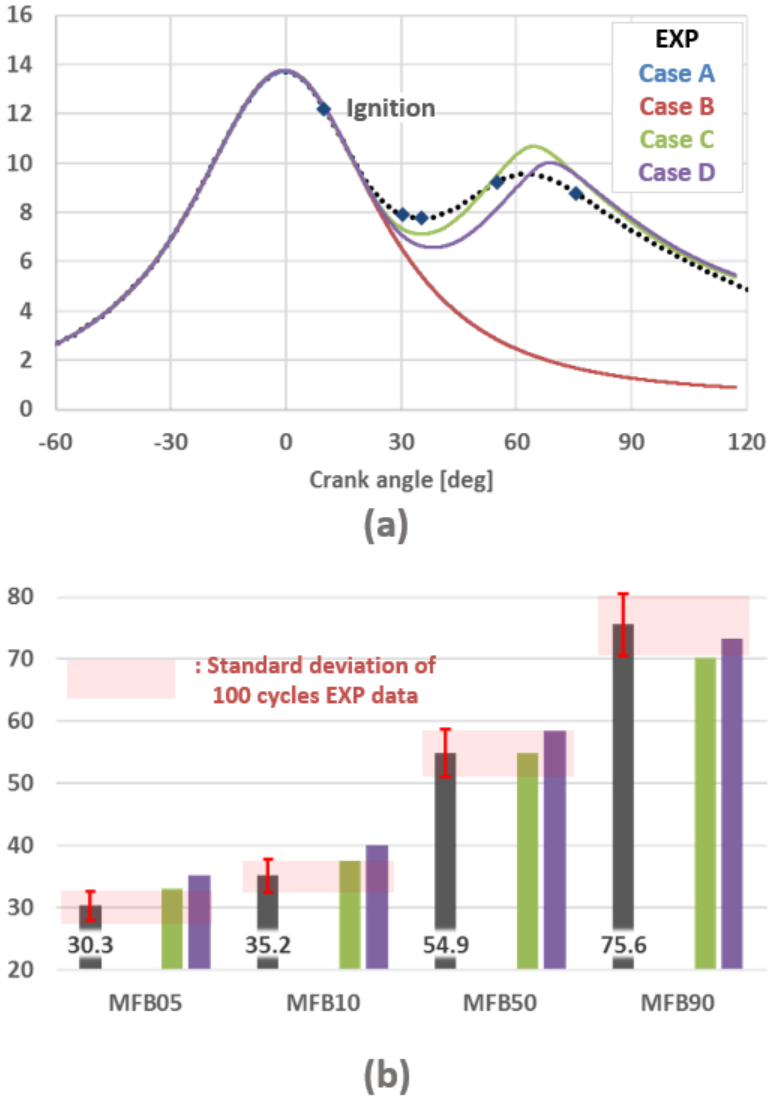

Figure 6.14 Early/Late Injection: (a) In-cylinder pressure and (b) combustion phase of MFB05, MFB10, MFB50, and MFB90, where the standard deviation of 100 cycle data were indicated by shaded box.

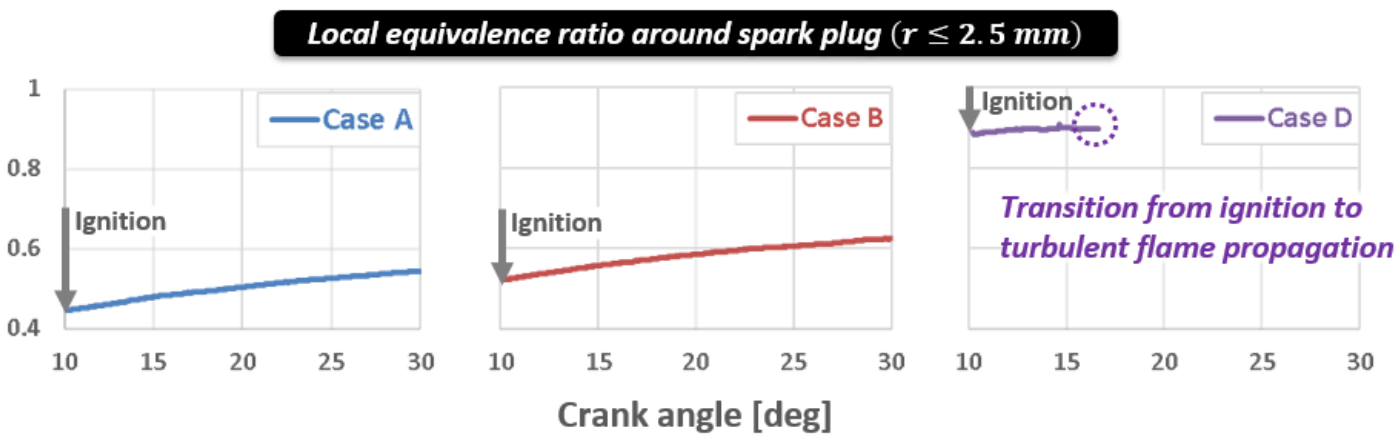

Figure 6.15 Early/Late Injection: Monitoring of local equivalence ratio around spark plug.

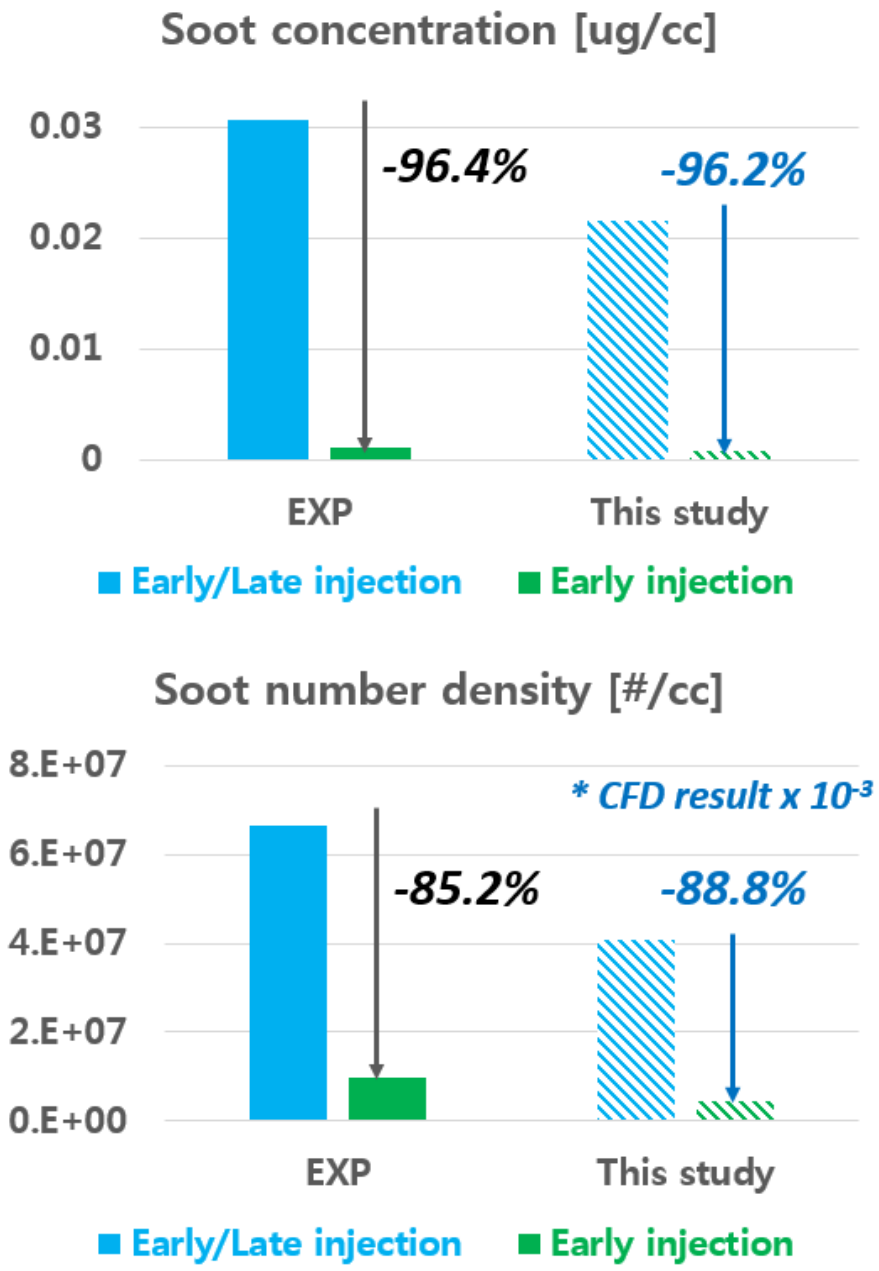

Figure 6.16 Comparison of relative soot reduction according to injection strategy.

Chapter 7. Model Application to DISI Engine

In this study, the combustion and soot emission models were validated against the experimental data from the DISI engine. It has been demonstrated that injection strategy and coolant temperature have a significant responsibility to the soot emission [7, 11, 167-170]. Thus, the number of injections and the coolant temperature were varied in the engine experiment, and the measured data were used for the model validation.

Ideally, the soot model validation should check whether the model can predict the correct concentration of PAHs' behind of the flame front [146]. However, the engine experiment is almost intractable to quantify the produced amount from the combustion and consumed by the soot nucleation, hence, the verification of the key soot process was unavoidably neglected. Instead, the simulation results were compared to the engine-out soot emissions measured by the Cambustion DMS 500 and AVL Smoke Meter in terms of the soot number density, soot concentration, and soot size distribution.

First of all, the semi-empirical model proposed in this study was adopted to simulate the in-cylinder soot formation under the cold-operation with multiple injection strategies (section 7.1). Then, the effect of wall temperature on soot emission was investigated and the model sensitivity to the flamelet library was discussed (section 7.2). Furthermore, MOMIC for soot aerosol dynamics was implemented to explore the predictability of the state-of-the-art approach for DISI engine application (section 7.3). Finally, the discussion on the modeling and simulation of soot emission in DISI engines were drawn (section 7.4).

7.1 Effect of Multiple Injection on Soot Emission

7.1.1 Engine Operating Condition and Experimental Observation

For the validation of semi-empirical soot model, the engine experiment was performed under a steady-state, cold-operating condition where multiple injections were adopted. The engine was run at 1,600 rpm, and the coolant temperature was set as 30°C. The fuel was injected at 305° CA bTDC with 100 bar injection pressure, and its delivery was controlled to match the stoichiometric air-fuel ratio. For the multiple injections, the number of injections was varied from single shot to triple shots with the equal split ratio, and the dwell time between the injection events was set as 0.5 ms interval. It is ideal to secure the equivalent thermodynamic conditions in the cylinder for all injection cases, so the IMEP and MFB50 were kept in the same level, 8.3 bar and 20° CA aTDC, respectively. Table 7.1 summarizes the operating conditions.

Before discussing the numerical simulation results, the measured soot emission levels according to the multiple injections are presented first. Figure 7.1 shows the soot number density measured by DMS500, and the soot concentration by both emission analyzers. It can be seen that the number density was reduced by 35.3% as the number of injections increased from single to dual, and 37.3% as that varied from dual to triple, respectively. A similar trend was observed for the soot concentration; the soot emission reduced by 50.4% and 67.8%, respectively. The measurement by Smoke Meter indicates the soot emission level by the index of filter smoke number (FSN), and it results in 1.77, 1.14, 0.40 FSN corresponding to the single, dual, triple injection, respectively.

7.1.2 Numerical Analysis: Air-Fuel Mixing Process

As the soot emission in DISI engines is strongly correlated with the air-fuel mixture field and the fuel film region, it is pertinent to analyze them before the investigation of combustion and soot emission process. Figure 7.2 depicts the prepared air-fuel mixture at the ignition timing through a set of in-cylinder section views. Here, the equivalence ratio (φ) denotes the cell-wise calculated value rather than the global one. Overall distribution was similar to each injection case: the air-fuel mixture in the center of cylinder exhibited around stoichiometric, while that near the spark plug was slightly rich. The volume of fuel-rich mixture was increased as the multiple injection applied as shown in the top view contour. However, from these qualitative observation, it is hard to find the air-fuel mixture of which equivalence ratio is larger than 1.5. Note that the φ=1.5 is based on the discussion in Chapter 5, where it was shown that the PAHs production was prominent around that value.

The quantitative air-fuel mixture distribution at the ignition timing indicated that most of the mixture were in the range of $0.8 \leq \varphi < 1.2$, and no extremely fuel-rich mixture ($\varphi \geq 1.5$) were found at the spark timing (see Fig. 7.3). Meanwhile, the multiple injection strategy helps the mixture to be evenly distributed around stoichiometric air-fuel ratio. From the temporal evolution of air-fuel mixture distribution as plotted in Fig. 7.3 (b), it is shown that the two branches for $0.8 \leq \varphi < 1.0$ and $1.0 \leq \varphi < 1.2$ were being merged as the number of injection increase. To sum up, regardless of the multiple injections, overall air-fuel mixture was well-mixed in the moderate equivalence ratio throughout the cylinder volume.

The fuel film deposition on the combustion chamber, as well as the gaseous mixture on the wall adjacent cell-layer, are shown in Fig. 7.4. It turns out that the fuel film was mainly deposited inside the piston bowl and on the bowl lip periphery, where

the spray impingement took place at the injection event. The vaporized air-fuel mixture location was coincidence to the film area. Thus, the primary soot sources in DISI engines can be regarded as the liquid fuel film and its corresponding local fuel-rich mixture near the wall. By quantifying the fuel film, the single injection resulted the film area of 1.29×10^{-3} m^2, mean film thickness of 1.62 μm, and film mass of 1.13 mg, and it is followed by the dual injection in 1.15×10^{-3} m^2, 1.49 μm, and 0.93 mg; by the triple injection in 9.98×10^{-4} m^2, 1.11 μm, and 0.53 mg, respectively.

Finally, the time history of fuel film mass in the single injection is depicted in Fig. 7.5. The total film mass of the single injection was the highest, while that of the triple injection holds the lowest amount. The dual and triple injections are effective to split the fuel mass by half or one-third per injection event, and thereby the spray penetration length can be shortened compared to that in the single injection case. Accordingly, it prevent the liquid film deposition on the piston surface. It is confirmed by the multi-stage film deposition observed in the initial trace as shown in the graph.

In this study, the gasoline was modeled by the six-component surrogate so that the liquid film was also made up of the hydrocarbon constituents. The individual component in fuel film exhibited own vaporization characteristics as illustrated in Fig. 7.5 (b). The iso-pentane possess the third volume fraction, 23%, in the surrogate fuel. However, it has the lowest boiling point (27.8°C) so that most of the liquid iso-pentane was vaporized during the spray traveling in the free space, and thereby the smallest film mass was left. For the heavy and high boiling point components, such as p-diethylbenzene and n-undecane, the last mass fraction in fuel film was comparable to any other element. In the fuel film, the aromatic hydrocarbon and heavy-end component remaining longer than others due to their high boiling points. Thus, the film deposition causes not only the locally fuel-rich mixture but also the sooting-favored hydrocarbon.

In summary, the effect of multiple injection on the soot emission can be regarded as the reduction of fuel film by virtue of decreased spray penetration. Though the mixture homogeneity was improved, the noticeable changes was found in the liquid fuel film rather than the partial-mixing. Thus, for the multiple injection strategy, it is expected that the suppression of fuel film leads the low soot emission level.

7.1.3 Numerical Analysis: Combustion Process

Here, the combustion process is investigated before analyzing the soot emission. Figure 7.6 compares the in-cylinder pressure between the experimental data and the simulation results, and displays the prediction error with respect to each MFB timings. From the pressure curve, it can be seen that the in-cylinder mass was well-predicted and its differences were around 2% error at the ignition timing. For all cases, the simulation under-predicts the mass burning rate before the MFB50, while it predicts the slightly faster combustion for the later stage. The maximum pressure differences were mainly occurred in MFB05 and MFB10 timing, but overall prediction was acceptable as the differences did not exceed 5% error bound.

The in-cylinder temperatures of single injection case including mass-averaged of unburned, burned, and total mixture are presented in Fig. 7.7. The behavior of other two injection cases were similar, so they are not displayed here. It is shown that the unburned temperature ranged from 550 K to 750 K during the combustion. Hence, it is confirmed that the boundary conditions of laminar burning velocity (400-900 K) as well as flamelet library model (600-800 K) are sufficient to covere the encounterable thermodynamic conditions in DISI engines. The combustion of the fresh air-fuel mixture was terminated around 40° CA aTDC, while the post-flame reaction was

continued until the exhaust valve opening event under the thermodynamic conditions of the burned gas temperature and the expansion pressure trace.

The mass-averaged turbulent burning velocity and the laminar burning velocity ahead of the flame front are presented in Fig. 7.8. During the early stage of combustion, the flame propagation speed was assisted by the enhanced turbulent intensity ahead of flame as well as the elevated cylinder temperature. Meanwhile, the turbulent properties started to decrease after the TDC with the cylinder expansion, whereas the cylinder temperature continued to increase until the peak pressure. Correspondingly, the integral length scale and the turbulent intensity were diminished, while the laminar burning velocity was raised higher as shown in the figure. Since the turbulent burning velocity is a function of turbulent flows and laminar flame's properties, so it is affected by both factors. As a result, the turbulent burning velocity exhibited a plateau period until MFB50 and then diminished.

Figure 7.9 depicts the in-cylinder combustion process *via* propagating flame front, cylinder temperature, and the concentration of carbon monoxide (CO) as well as nitric oxide (NO). Note that the carbon monoxide and nitric oxide are inversely correlated because the former is evolved from fuel-rich mixture whereas the latter is produced with its maximum at the slight fuel-lean mixture. As discussed in the previous section, the fuel-rich mixture was concentrated inside the piston bowl so that the CO production was in agreement to the mixture field. In addition, the dissociation of CO_2 in the high cylinder temperature, as well as the oxidation of CO along the cylinder expansion, were exist during the combustion process so that CO fraction is closely related to the in-cylinder temperature condition. It is shown that there is a concurrence of maximum CO concentration with the burned gas temperature as plotted in Fig. 7.10 and Fig. 7.7. On the contrary, the NO production undergoes the slow chemistry behind of flame front; majority of NO concentration located in the

center of cylinder, and its trace was almost monotonically increased toward the maximum value.

7.1.4 Numerical Analysis: Soot Formation

Based upon the above detailed investigation on the mixing and combustion process, the soot emission was analyzed in both qualitative and quantitative ways. Figure 7.11 shows the time history of mean soot number density and mean soot volume fraction for three different injection strategies. The soot number density as well as the soot volume fraction started to increase from 15° CA aTDC, and the number density reached their peak value around 28° CA aTDC then it is subjected to decrease for last expansion stroke. The sharp increment and reduction were the common behavior for all cases. For the soot volume fraction, their maximum location were retarded than that of soot number density, which was shown around 40° CA aTDC. Similarly, the volume fraction of soot particles was also reduced but its reduction rate was moderate compared to the soot number density. As the multiple injection applied, it is shown that the soot emission levels were decreased.

The simulation results of soot number density, as well as soot concentration, were compared to the experimental data as shown in Fig. 7.12. The overall trend of soot reduction was captured, and the soot concentration was predicted within the same order of magnitude. However, the predicted reduction rate of soot concentration according to the multiple injections was lower than measured one; the experimental results showed the 50.6% and 67.7% reduction by the transition from single to dual, dual to triple injection, while the simulation results indicated 7.6% and 56.3%, respectively. In addition, the soot number density was far beyond the measured value; the prediction almost 160-220 times larger than the experimental data.

For the over-prediction of soot number density, it is proper to examine the soot size distribution because the practical soot particles system is poly-dispersed and varies the particle size and mass. Figure 7.13 shows the experimental and simulation results of soot size distribution for three cases. Though the semi-empirical model assumes a spherical particle for a computational cell, i.e. mono-dispersed system, the size distribution can be obtained by arranging the soot number density of a cell along its soot mean diameter for whole cylinder domain. The model predicts the reduction of number density according to the multiple injection, but the overall size was distributed in smaller diameter than the experimental data. There were large soot particles in the engine-out emission regardless of the multiple injection, of which ranges in 50-200 nm. The injection strategy affects the absolute level of the soot emission but retains the distribution shape, which behaved as bi-modal function. In the simulation, the biggest soot particles resulted from the single injection case, which has the diameters of 10-30 nm. As the particle size distribution was off-predicted, the soot number density was also over-predicted as well.

From now on, the detailed analysis for the soot formation in DISI engines, as well as the investigation for the reduction mechanism of soot emission level according to the multiple injection, were drawn and discussed. Recalling the in-cylinder mixture distribution at the ignition timing, there were a certain amount of fuel film remaining on the piston face, but no extremely fuel-rich mixture were found for all cases. Figure 7.14 displays the time history of in-cylinder air-fuel mixture distribution in terms of the local equivalence ratio. It is revealed that the considerable film vaporization existed as the flame reaching the near-wall region due to excessive heat transfer to the wall, and thereby the concentration of fuel-rich mixture were increased. These primary soot sources were formed during the combustion, even though no fuel-rich mixture had been found before the spark onset.

The time history of film mass also confirms the physics as shown in Fig. 7.15. The MFB was about 3% at the TDC position but the burned volume was quite large due to the low density of burned gas, and the heat of combustion started to accelerate the film vaporization. Consequently, a substantial film mass were being vaporized within short duration around 30° CA, and it contributed to increase the fuel-rich mixture near the wall which presented in Fig 7.14.

Figure 7.16 clearly summarizes the vaporized film mass from ignition event to MFB90 timing for three cases. It is shown that the remaining film mass at the ignition were 4.0%, 3.3%, and 1.9% of the injected mass of single injection, dual injection, and triple injection case, respectively. During the combustion process, the fuel film were decreased in 67.1%, 69.6%, and 73.7% for each multiple injections strategy, respectively. Thus, almost 1.4~2.7% of injected mass were being vaporized and subjected to participate in the combustion where oxidizer far less than the required amount. It is confirmed that the primary soot source in DISI engines is the wall wetting rather than the inhomogeneous mixture due to partial-mixing.

Figure 7.17 shows the temporal evolution of mass fraction of coronene (A_7), soot number density, and the mean soot diameter during the combustion process. The soot nucleation initiated from the piston bowl and the soot particles produced *via* PAH dimerization, and they were advected away from the wall into the free space. During the soot particle travels inside the cylinder, the oxidation predominated in the fuel-lean region and thereby the soot mass was diminished, while the coagulation occurred in the whole domain where particle exists.

The time history of PAHs formation and destruction in conjunction with the soot number density trace are plotted in Fig. 7.18. It can be seen that the soot particle production was in accordance with the PAH formation, where the significant PAH

reaction took place from firing TDC to 40° CA aTDC. For the initial stage of soot emission in the cylinder, the considerable PAH formation from the fuel-rich mixture near the wall supplied the abundant soot precursors for the nucleation process, and thereby both PAHs and soot particles were grown rapidly. Then, the PAH formation were mitigated due to the depletion of fuel-rich sources as well as the liquid film mass, and the nucleation of the soot particles was also slow-down. The maximum of two traces were almost coincided and being sharply reduced. Note that the graph for the soot number density in Fig. 7.18 uses log-scale. For the PAH consumption, it was governed by the soot nucleation, while the soot number density reduction was affected by the coagulation physics.

As the primary source of soot emission was a localized quantity near the wall, so the gradient analysis can properly measure the local intensity of fuel and PAHs' concentration. The equation for calculating the gradient of each cell reads

$$|\nabla Y_{PAH}|(\vec{x},t) = \sqrt{\left(\frac{\partial Y_{PAH}}{\partial x}\right)^2 + \left(\frac{\partial Y_{PAH}}{\partial y}\right)^2 + \left(\frac{\partial Y_{PAH}}{\partial z}\right)^2} \tag{7.1}$$

$$|\nabla Z|(\vec{x},t) = \sqrt{\left(\frac{\partial Z}{\partial x}\right)^2 + \left(\frac{\partial Z}{\partial y}\right)^2 + \left(\frac{\partial Z}{\partial z}\right)^2} \tag{7.2}$$

where Y_{PAH} is the summation of five PAHs' mass fraction, $(\vec{x},t)$ denotes the cell location and the time step in the CFD simulation. If one assume that a uniform gradient in grid size of 1 mm^3 and the gradient magnitude is larger than 5,

$$|\nabla Z| = \sqrt{3\left(\frac{\partial Z}{\partial x}\right)^2} > 5 \quad \rightarrow \quad \frac{\partial Z}{\partial x} \sim 2.9 \quad \rightarrow \quad \Delta\varphi \sim 0.05 \tag{7.3}$$

the local equivalence ratio is varied about 0.05 across the computational cell.

The gradient of mixture fraction and PAHs' concentration of the single injection case are displayed in Fig. 7.19. The large gradient of mixture fraction located around the combustion chamber wall. For the gradient of PAHs' concentration, the noticeable magnitude located on the piston surface where the fuel film exists, and its strength was diminished after 60° CA aTDC. It was in agreement with the PAH behavior as indicated in Fig. 7.18. In addition, the mass-averaged gradient of mixture fraction and that of PAH concentration were calculated for the soot nucleation ongoing cells only. The results for three injection cases are shown in Fig. 7.20. It is interesting to see that there was no large difference between the multiple injections strategy. It means that inside the nucleation cell the strength of mixture fraction or PAH concentration not significantly differed according to the multiple injections. However, the soot emission results shown in Fig. 7.12 still indicates the soot reduction as the number of injection increased.

The in-cylinder mass fraction of soot nucleation ongoing cell of three injection cases are plotted in Fig. 7.21. It is revealed that the mass fraction of the mixture under soot nucleation was the highest in the single injection case, and it was followed by the dual and triple injection, respectively. Figure 7.22 support the physics by showing the film deposition area with respect to the injection cases. The in-cylinder section cut for the soot formation at the 80° CA aTDC are shown in Fig. 7.23. It can be seen that not only inside the piston bowl but also the liner opposite to the injector mounting were the primary soot sources in the single injection case. By contrast, the triple injection inherently resulted low fuel film wetting on the wall, so the soot formation occurred only inside the piston bowl.

Therefore, it can be concluded that the multiple injection effectively suppress the fuel film deposition on the combustion chamber wall, and reduces the soot emission level by increasing the number of injection for a cycle.

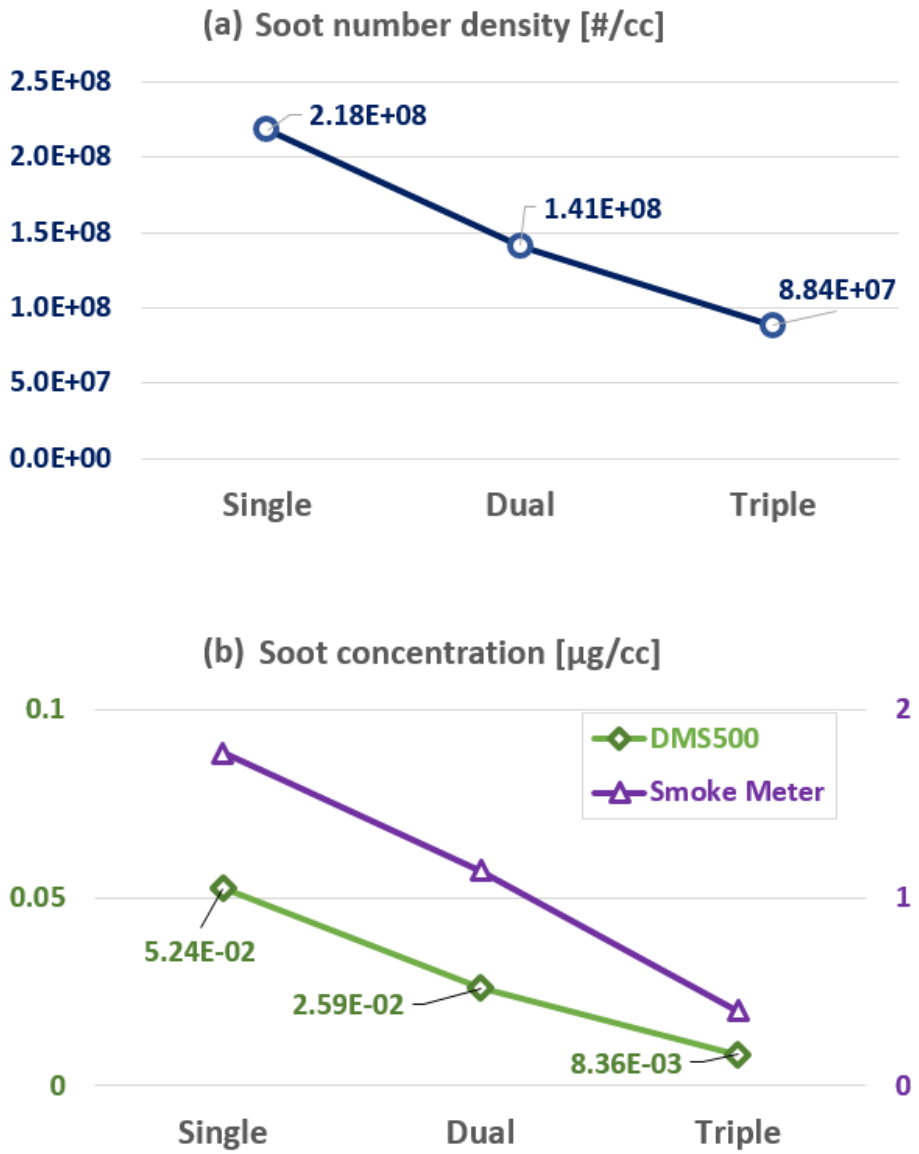

Figure 7.1 Measured soot emission from the DISI engine experiment with the multiple injections: (a) soot number density [#/cc] by DMS500; (b) soot concentration [µg/cc] by DMS500 and Smoke Meter.

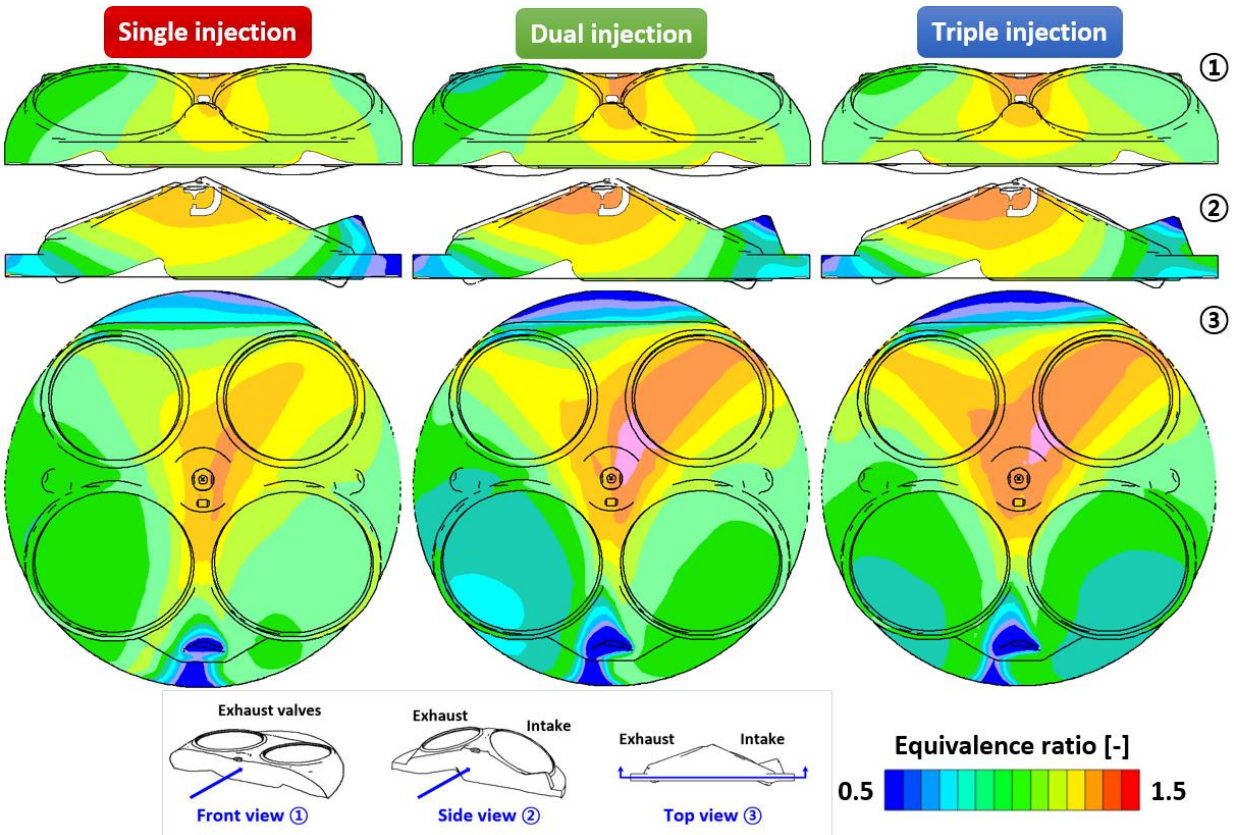

Figure 7.2 In-cylinder section cut for air-fuel mixture distribution at the ignition timing.

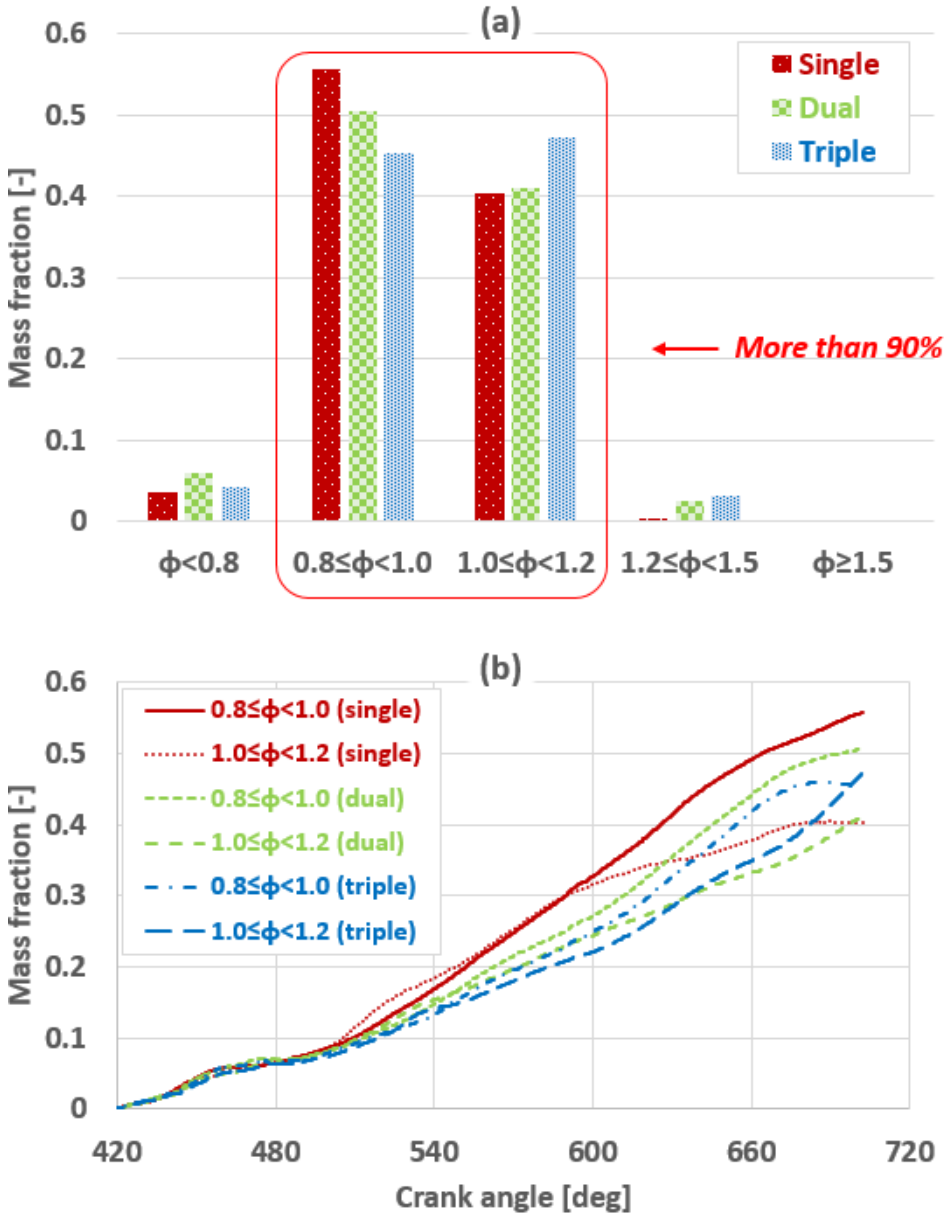

Figure 7.3 (a) Air-fuel mixture distributed within five equivalence ratio sections at the ignition timing; (b) temporal evolution of air-fuel mixture in the range of $0.8 \leq \varphi < 1.2$.

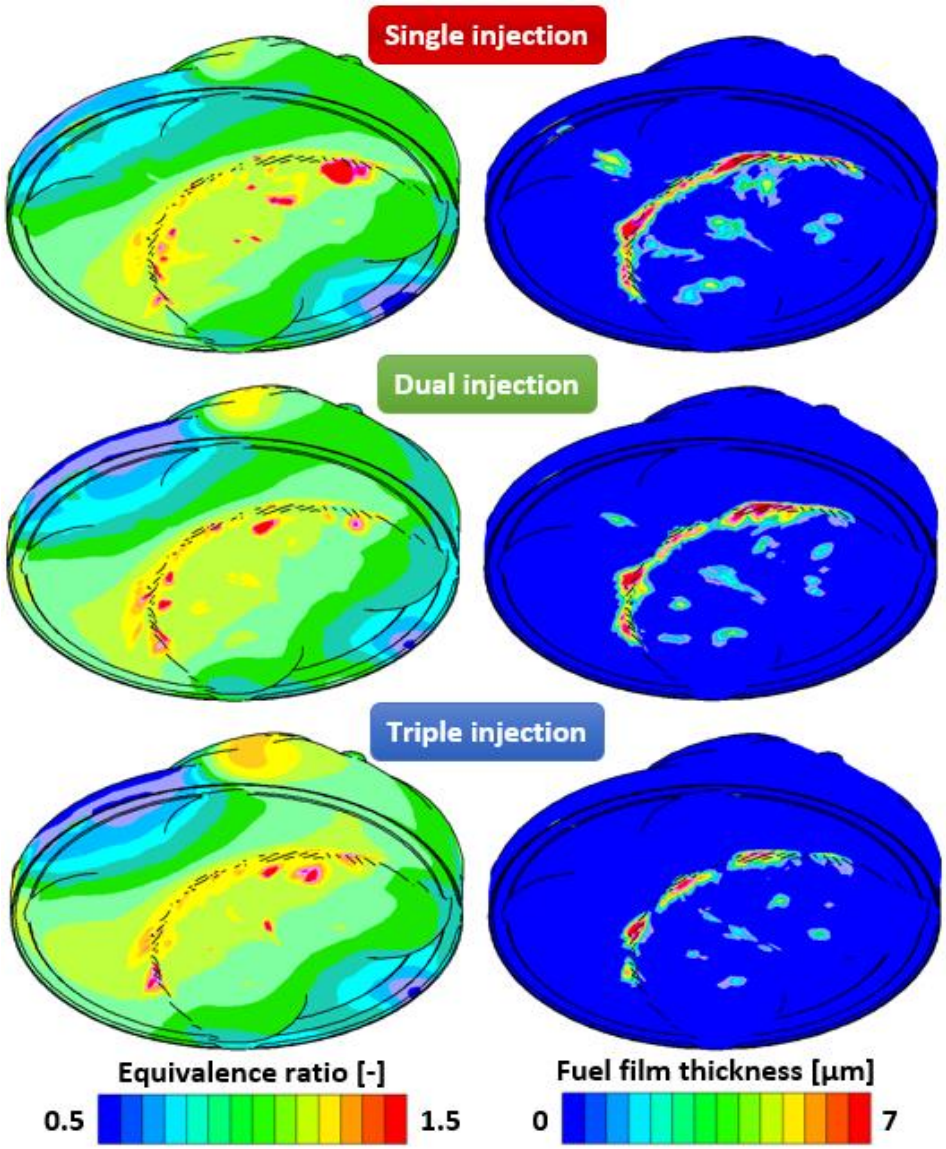

Figure 7.4 Air-fuel mixture distribution on the wall surface and thickness of liquid fuel film on the piston surface at the ignition timing.

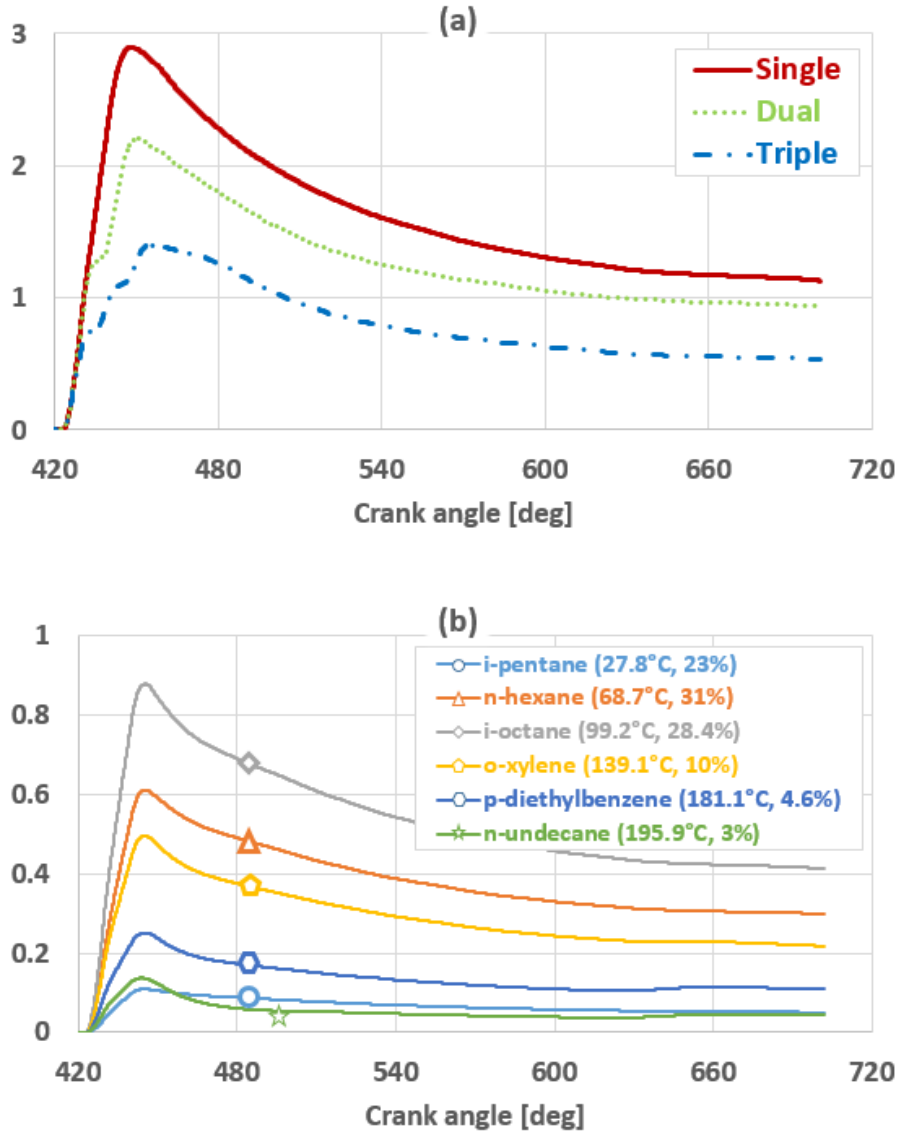

Figure 7.5 Results of fuel film mass [mg]: (a) time history during the intake and compression stroke for three multiple injection cases; (b) fuel component mass in the film deposited on the piston surface of the single injection case.

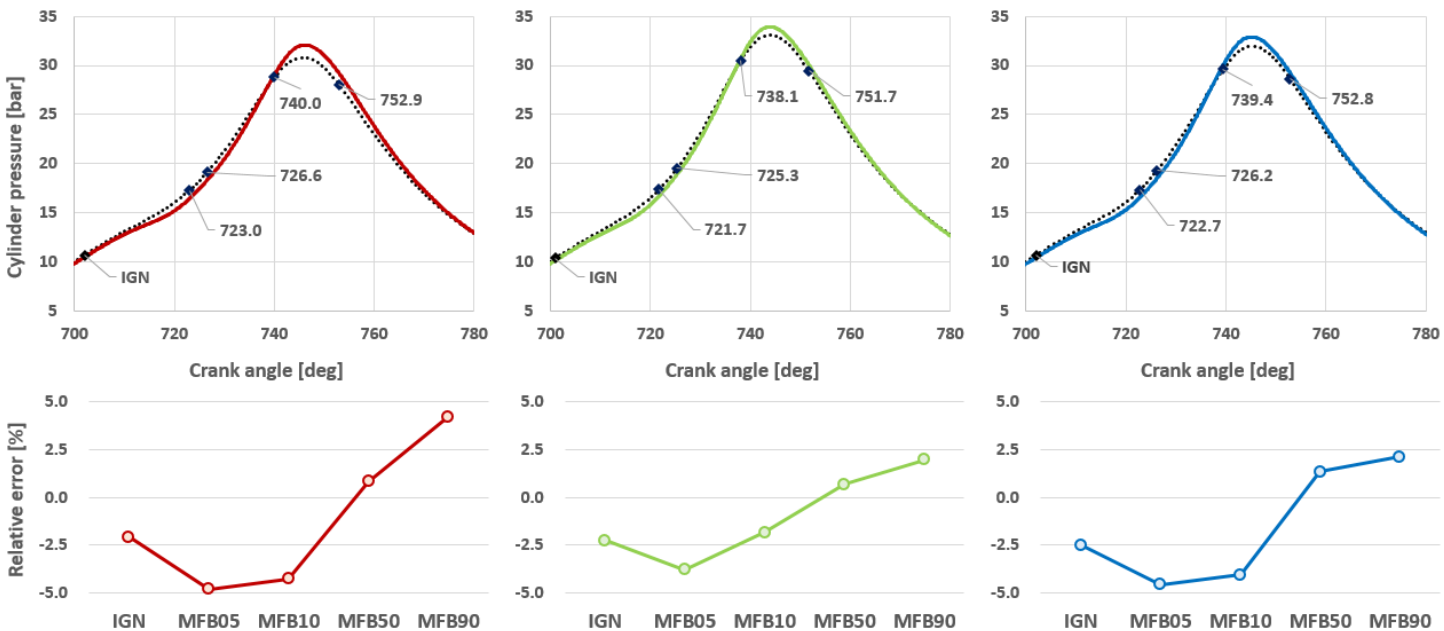

Figure 7.6 Comparison of in-cylinder pressure between experimental data and simulation results and its relative error at the MFB timing.

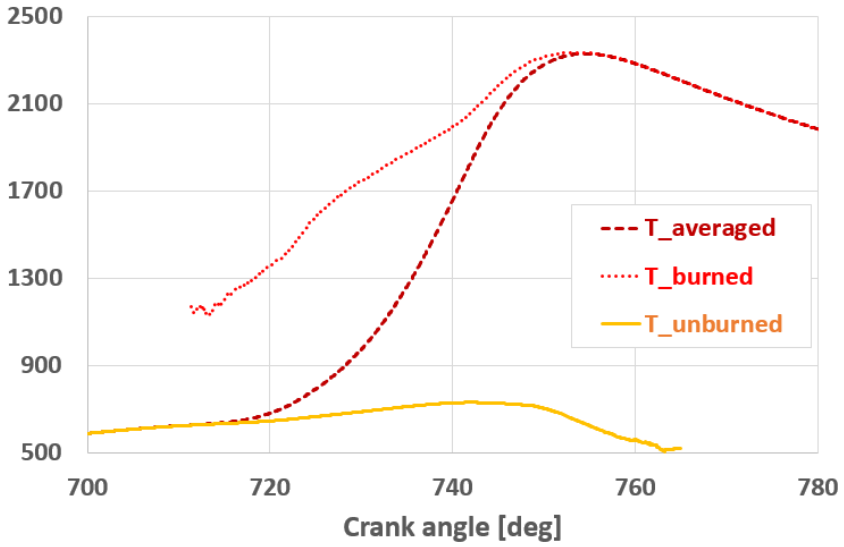

Figure 7.7 Mass-averaged cylinder temperature of the single injection case: unburned mixture (solid line), burned mixture (dotted line), and total mixture (dash line).

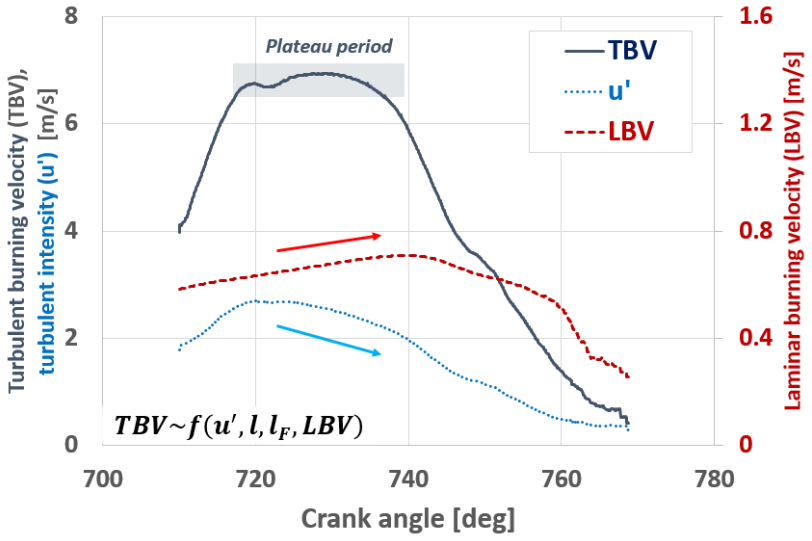

Figure 7.8 Time history of turbulent burning velocity (solid line), turbulent intensity (dotted line), and laminar burning velocity (dash line) of the single injection case.

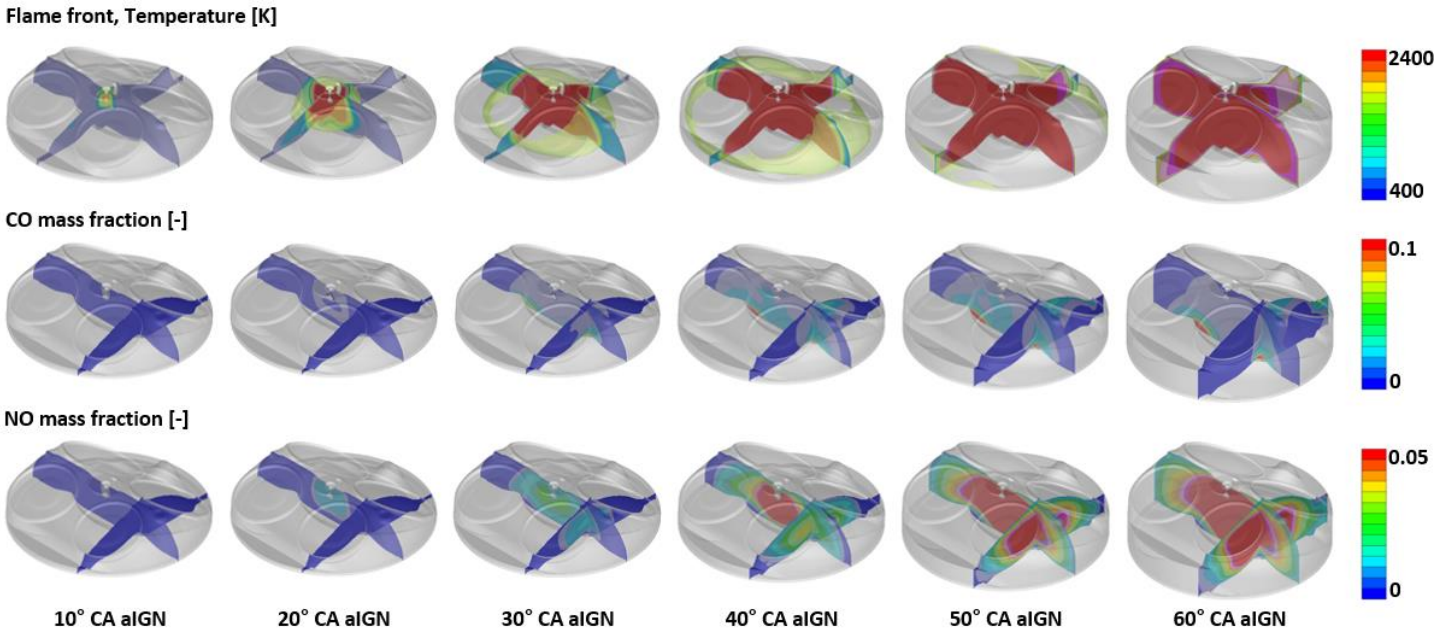

Figure 7.9 In-cylinder combustion process of the single injection case: propagating turbulent flame, cylinder temperature, CO and NO mass fraction.

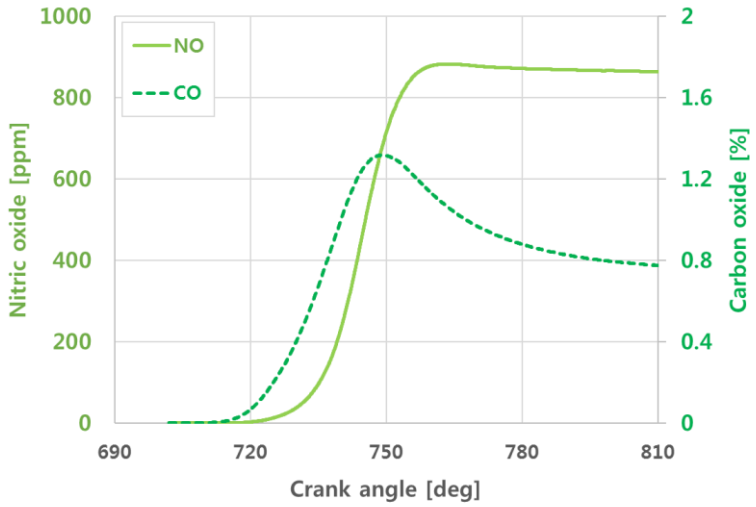

Figure 7.10 Time history of CO and NO production of the single injection case during the combustion process.

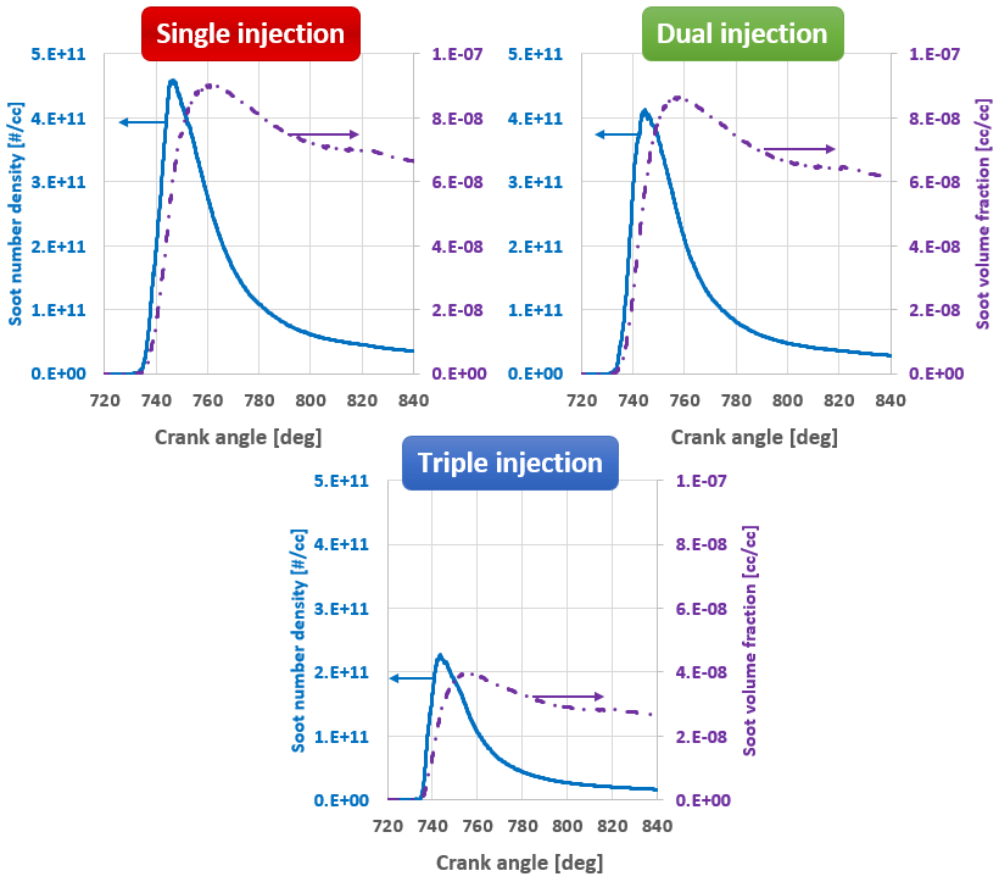

Figure 7.11 Time history of soot number density (solid line) and soot volume fraction (chain line) for three multiple injection cases.

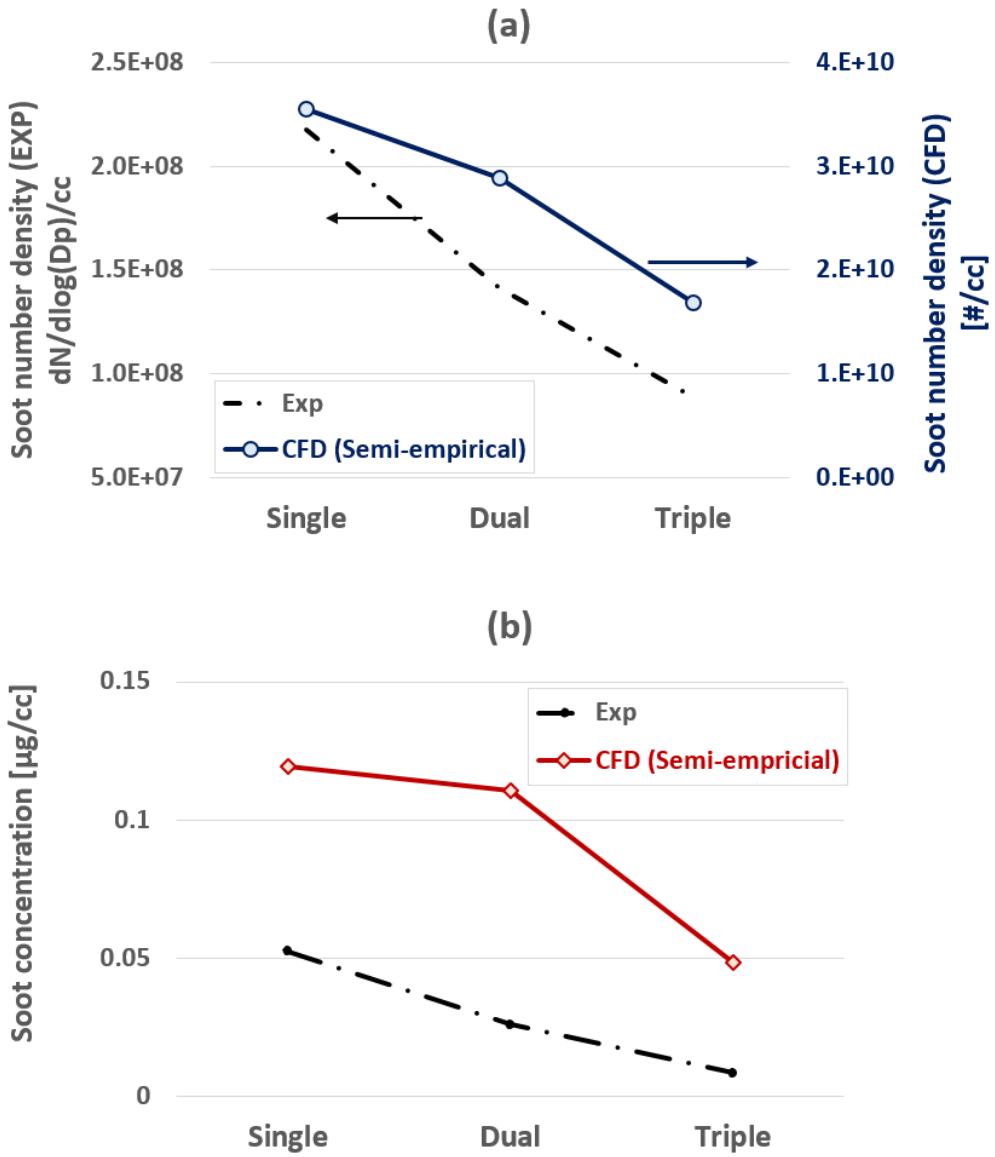

Figure 7.12 Comparison of experimental data (chain line) and simulation results (solid line) for soot emission: (a) soot number density; (b) soot concentration

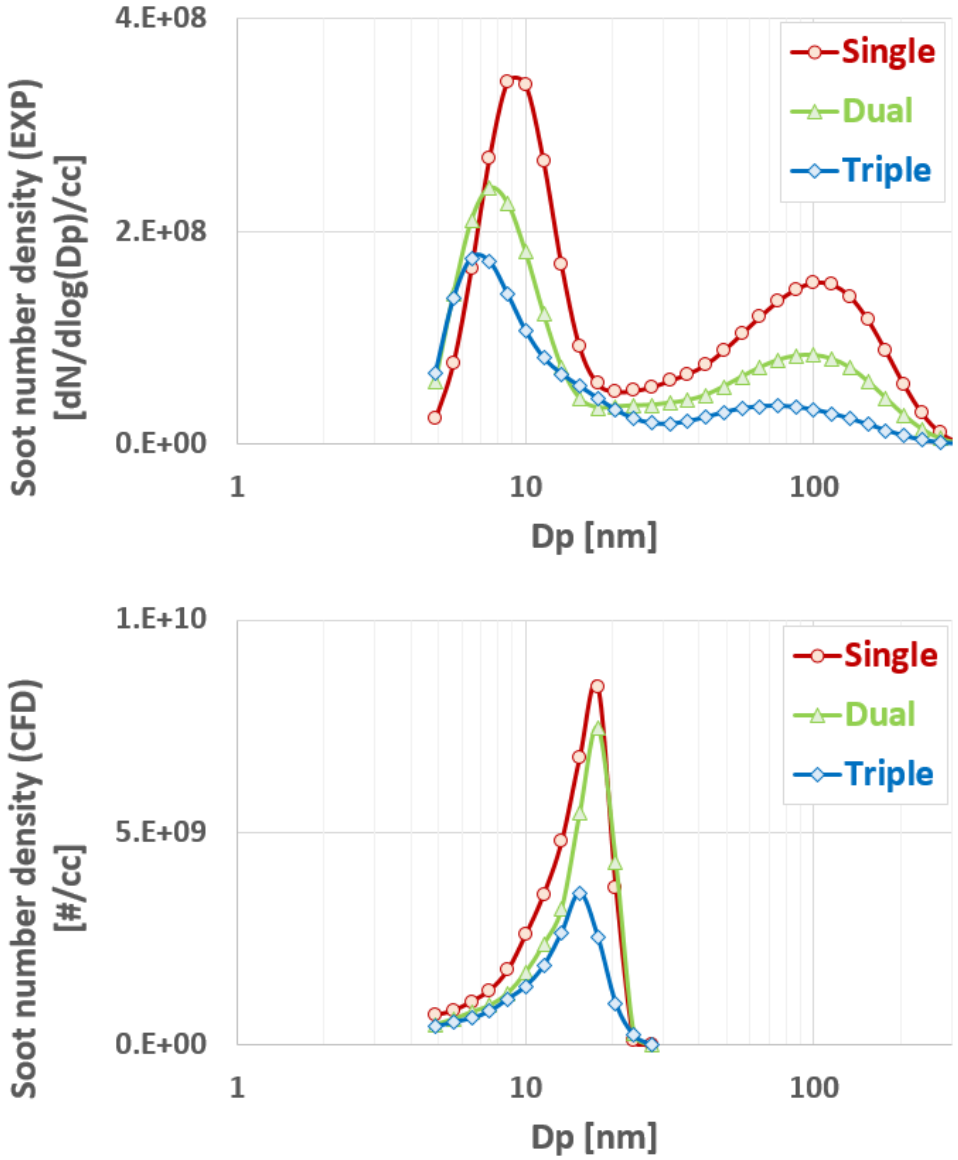

Figure 7.13 Comparison of experimental data (upper) and simulation results (lower) for soot size distribution according to multiple injection strategy.

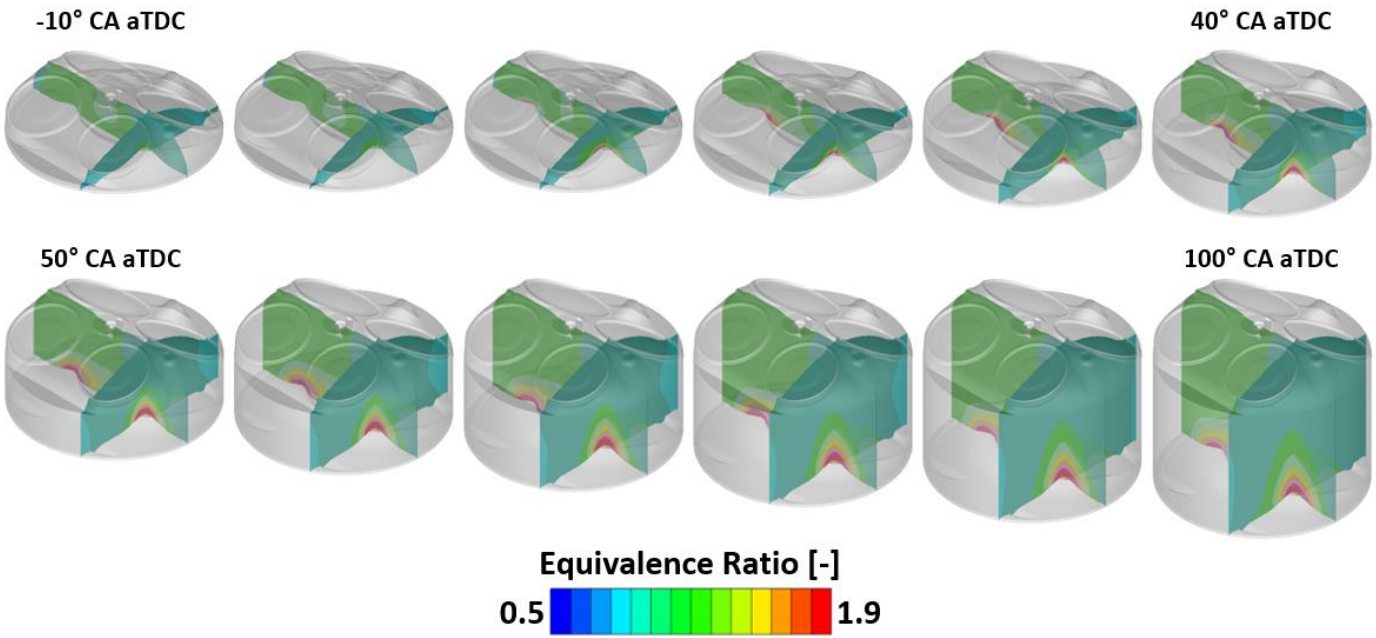

Figure 7.14 In-cylinder section view of air-fuel mixture of the single injection case from the ignition to the exhaust valve opening by 10° CA interval.

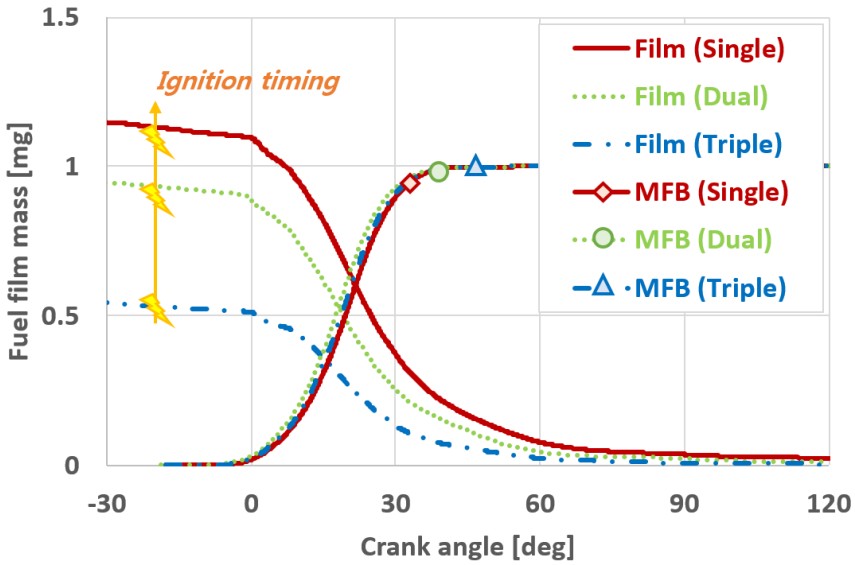

Figure 7.15 Time history of fuel film mass and MFB for three injection cases.

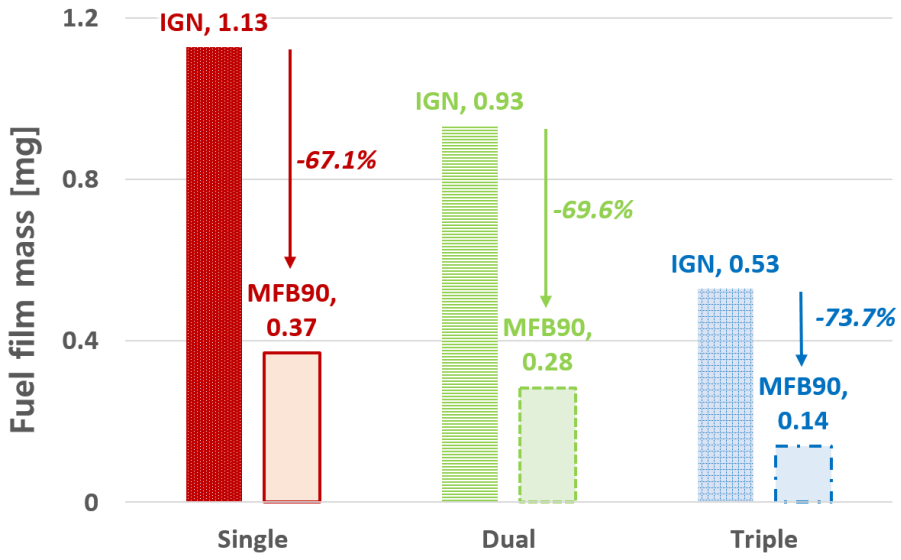

Figure 7.16 Vaporized fuel film mass during the combustion process for three injection cases.

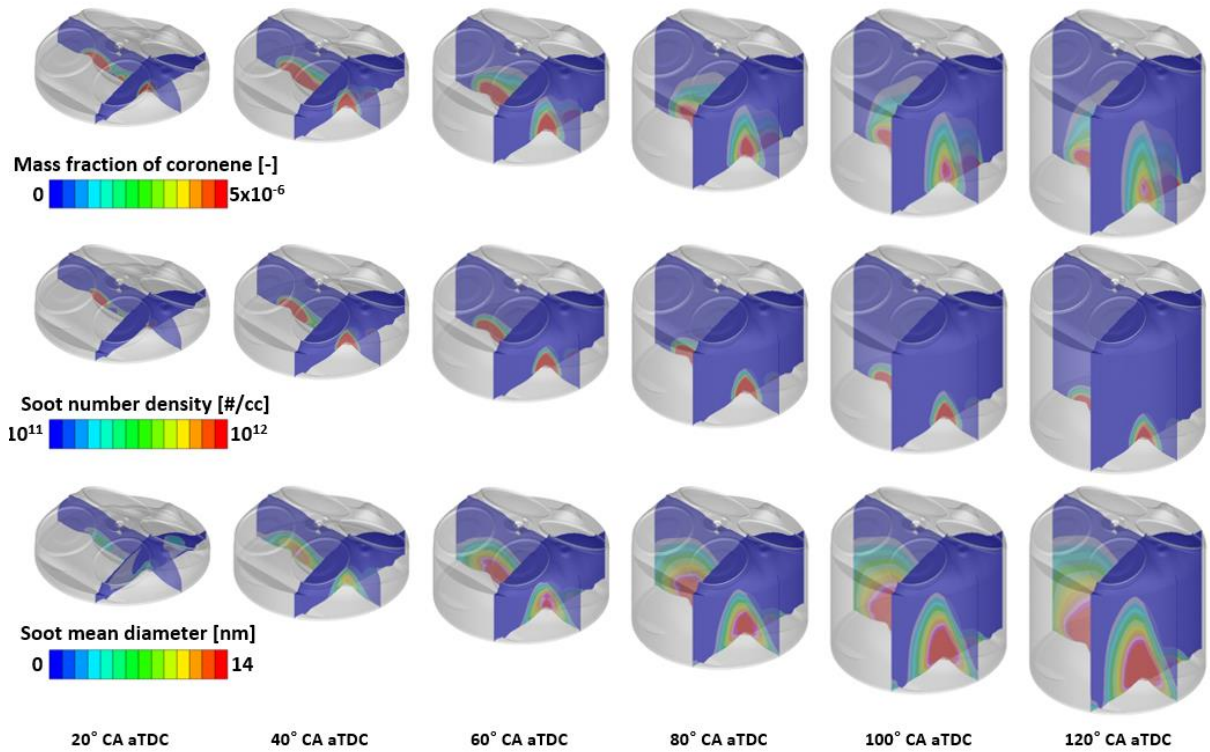

Figure 7.17 In-cylinder section view for mass fraction of coronene, soot number density, and soot mean diameter in the single injection case.

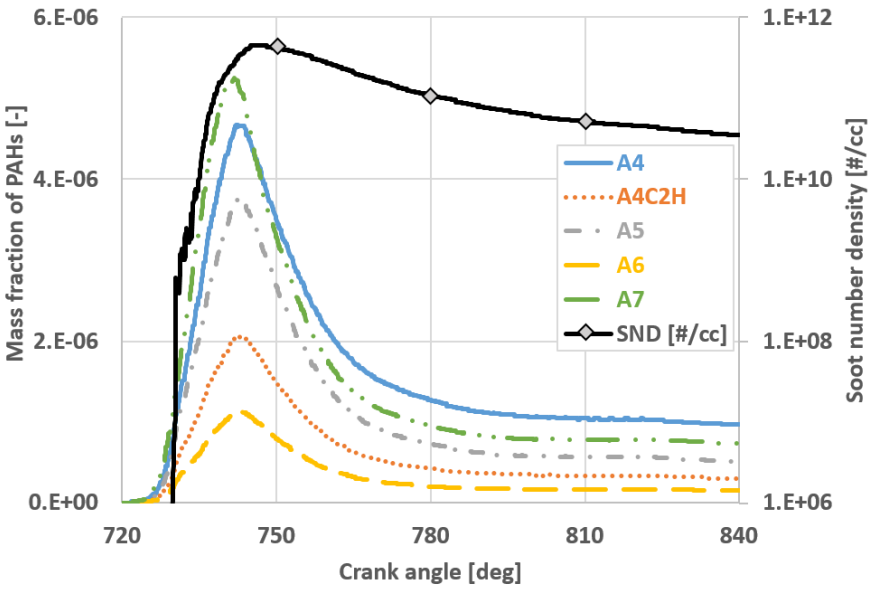

Figure 7.18 Time history of five representative PAH species during the combustion in the single injection case.

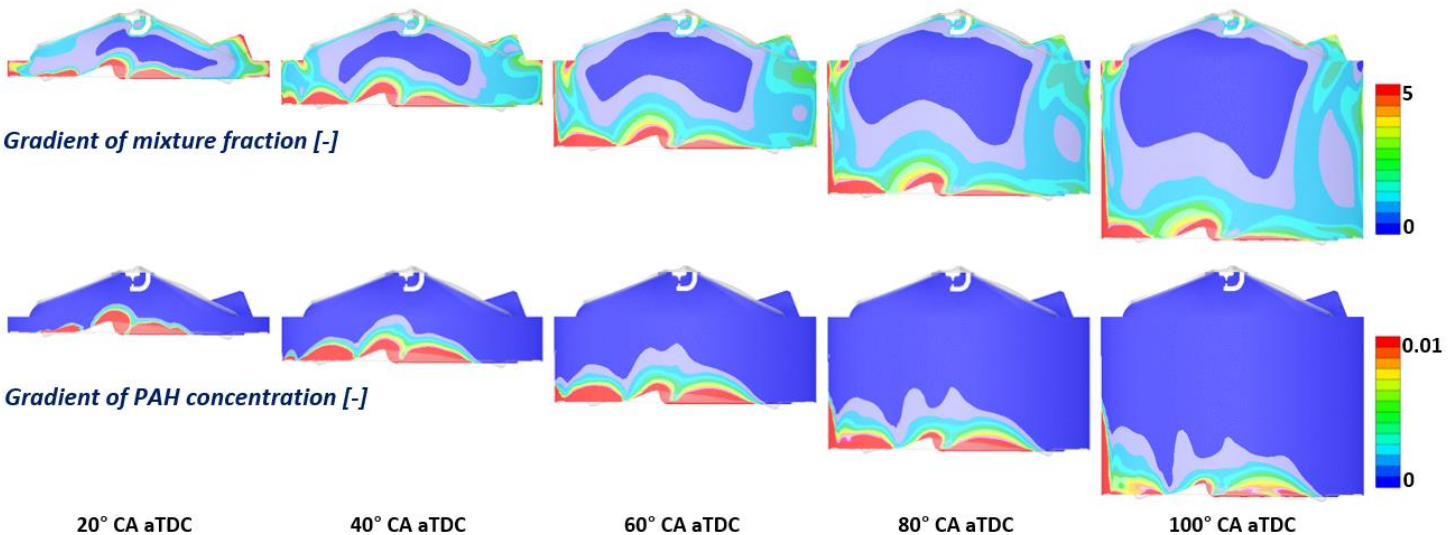

Figure 7.19 Results of gradient analysis for the mixture fraction (upper) and PAH concentration (lower) from 40° CA to 100° CA after ignition with 20° CA interval for the single injection case.

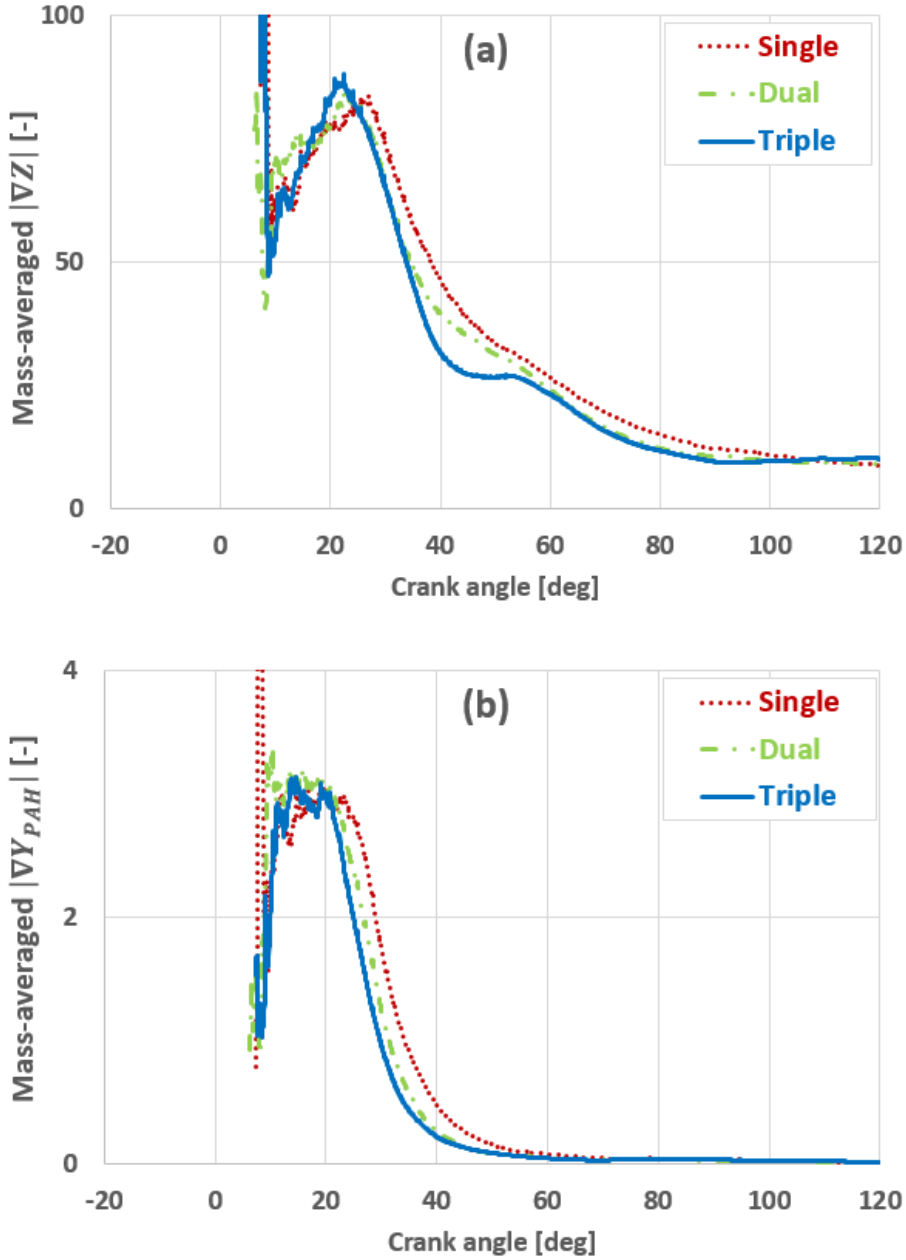

Figure 7.20 Properties of soot nucleation ongoing cells: (a) mass-averaged $|\nabla Z|$ and (b) mass-averaged $|\nabla Y_{PAH}|$

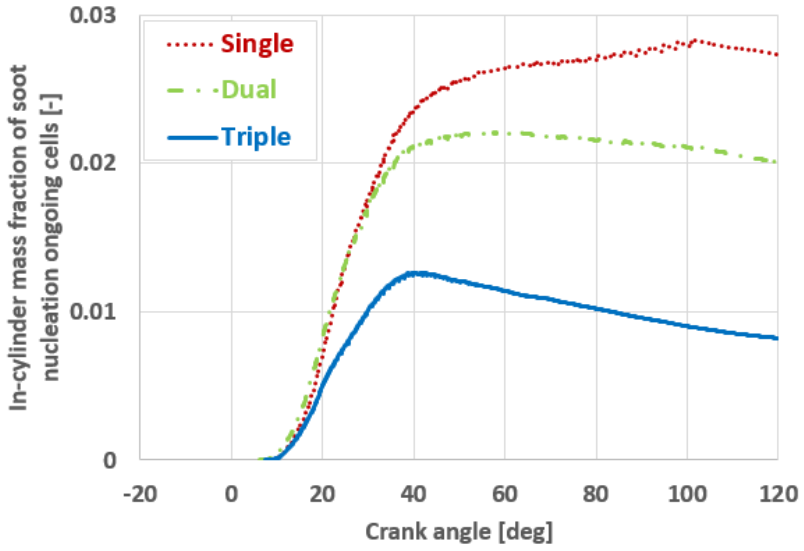

Figure 7.21 In-cylinder mass fraction of soot nucleation ongoing cells for three cases of multiple injection

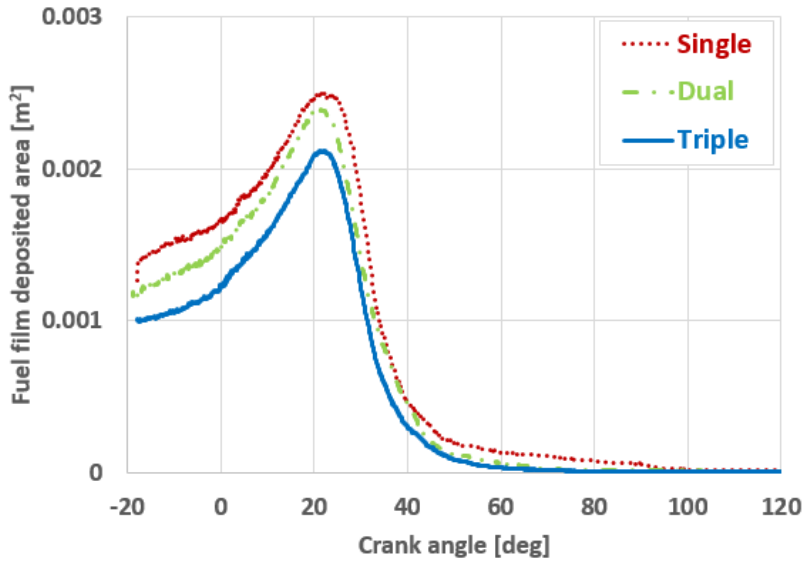

Figure 7.22 Time history of fuel film deposited area during the combustion for three cases of multiple injection

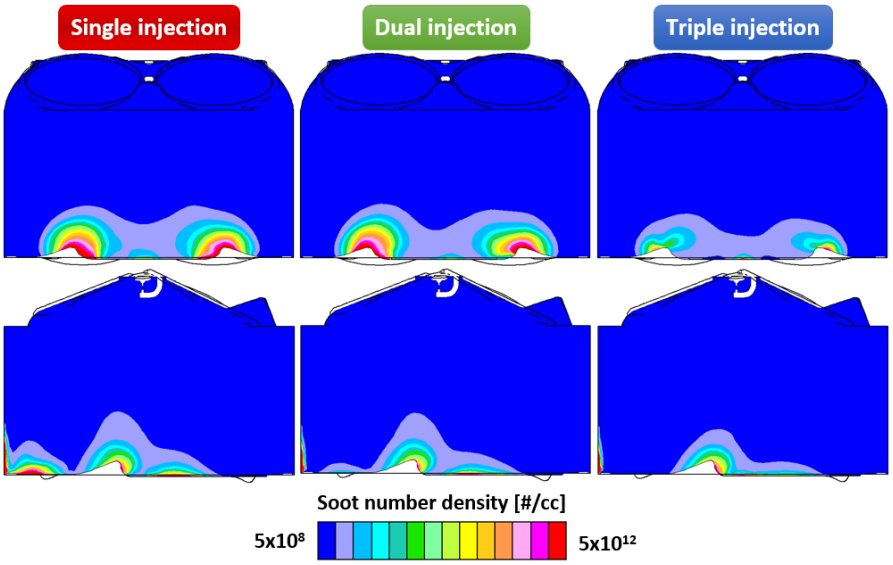

Figure 7.23 In-cylinder section cut of front view (upper) and side view (lower) for the soot number density at the 100° CA after ignition.

7.2 Effect of Wall Temperature on Soot Emission

7.2.1 Numerical Analysis: Effect of Wall Temperature

It has been reported that the wall temperature, i.e. the cold start or fully warmed-up state, has great impact on the soot emission in DISI engines [7, 11]. Thus, the effect of wall temperature on soot emission should be appropriately resolved by the CFD simulation. Note that the fuel film was mainly deposited on the piston surface, so it is pertinent to vary the piston temperature and to investigate its effect on soot emission level. The experimental research found that the piston temperature was linearly proportional to the coolant temperature, and its correlation slope was around 0.4. So, if the coolant temperature was heated up from 30°C to 80°C, the piston temperature would be elevated in 20°C.

In this study, the piston temperature of 438 K was chosen as base point which was adopted for the cold-operating simulation, and it was increased as for 453 K (ΔT=15 K), 463 K (ΔT=25 K), and 473 K (ΔT=35K), respectively. The numerical setting was same as the single injection case investigated in the previous section, and the semi-empirical soot model was incorporated to simulate the soot formation in the DISI engine.

The fuel film deposition has considerable responsibility to soot emission by forming the localized fuel-rich mixture near the wall. Figure 7.24 illustrates the time history of the fuel film during the mixing process for three different piston temperature. It is shown that the fuel film formation was greatly suppressed in the high temperature condition, and thereby there was almost negligible film left at the ignition timing.

Figure 7.25 presents the soot emission level according to the variation of piston surface temperature. Overall trend was in agreement to the literature findings, where the increment of wall temperature reduced the soot emission. It is worth to note for the reduction rate with respect to the temperature variation. As the piston surface temperature increased in 15 K from 438 K to 453 K, the soot concentration as well as soot number density were decreased in 63%. A substantial reduction was found between the 453 K and 463 K, in which the soot number density was diminished in 97%, while the soot concentration recorded 99% abatement, respectively. Furthermore, there was no soot formation in the 473 K condition. It is confirmed that the lowered film formation according to the elevated piston surface temperature, and it directly influenced on the primary soot sources in the cylinder.

To sum up, the simulation was capable of resolving the effect of wall temperature on the soot emission. Note that it is hard to measure the exact temperature distribution of the entire wall boundary of the combustion chamber, so there is a certain limitation to match the absolute soot emission level.

7.2.2 Model Sensitivity to PAH Concentrations

In this study, the chemical compositions including PAHs' concentration were provided from the flamelet library. As discussed in Chapter 5, the one-dimensional solution resulted from the laminar premixed flamelet equation, and a point corresponding to the four times of laminar flame thickness was chosen to be tabulated in the flamelet library. Since the PAHs' concentrations are closely related to the soot formation, so it is needed to investigate the sensitivity of soot model against the library input.

Three referencing points from the 1-D flamelet solution were compared. One is the base configuration as four times of laminar flame thickness and the others are 5 mm and 20 mm behind of the OH maximum location. In addition, the soot precursor was also altered by replacing the five representatives PAHs with the one PAH, pyrene. The numerical simulation was performed under the single injection case, and its soot concentration was compared to the base configuration.

Figure 7.26 shows the model sensitivity of concentration and component of PAHs on the soot emission. It is indicated that the soot concentration was increased by the factor of 1.8 as the referencing point was changed. The variation was almost proportional to the raw data in the library, where the averaged-increment was 2.1 for all pressure and temperature conditions. For the component change, a substantial reduction in the soot concentration was observed; the resultant from the pyrene as the soot precursor was about the 15% of the base configuration. These results imply two important things. First, the growth of PAHs indeed undergoes the slow chemistry behind of the flame front. However, the concentration level is not changed dramatically. If one selects the farther point, the variation will increase further, but the location is not relevant for the turbulent combustion mapping. Second, the larger PAHs have a considerable impact on soot emission, which is consistently asserted in the literature. Thus, it is more appropriate to adopt PAH bigger than pyrene, even though the pyrene has been used for the most common soot precursor in the engine modeling field.

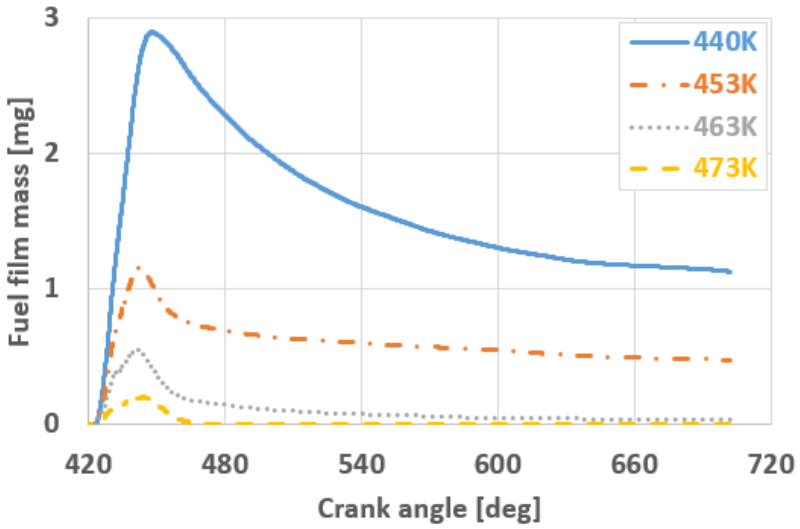

Figure 7.24 Time history of fuel film mass deposited on the combustion chamber wall according to the variation of piston temperature: 440 K (base, solid line), 453 K (chain line), 463 K (dotted line), and 473 K (dash line).

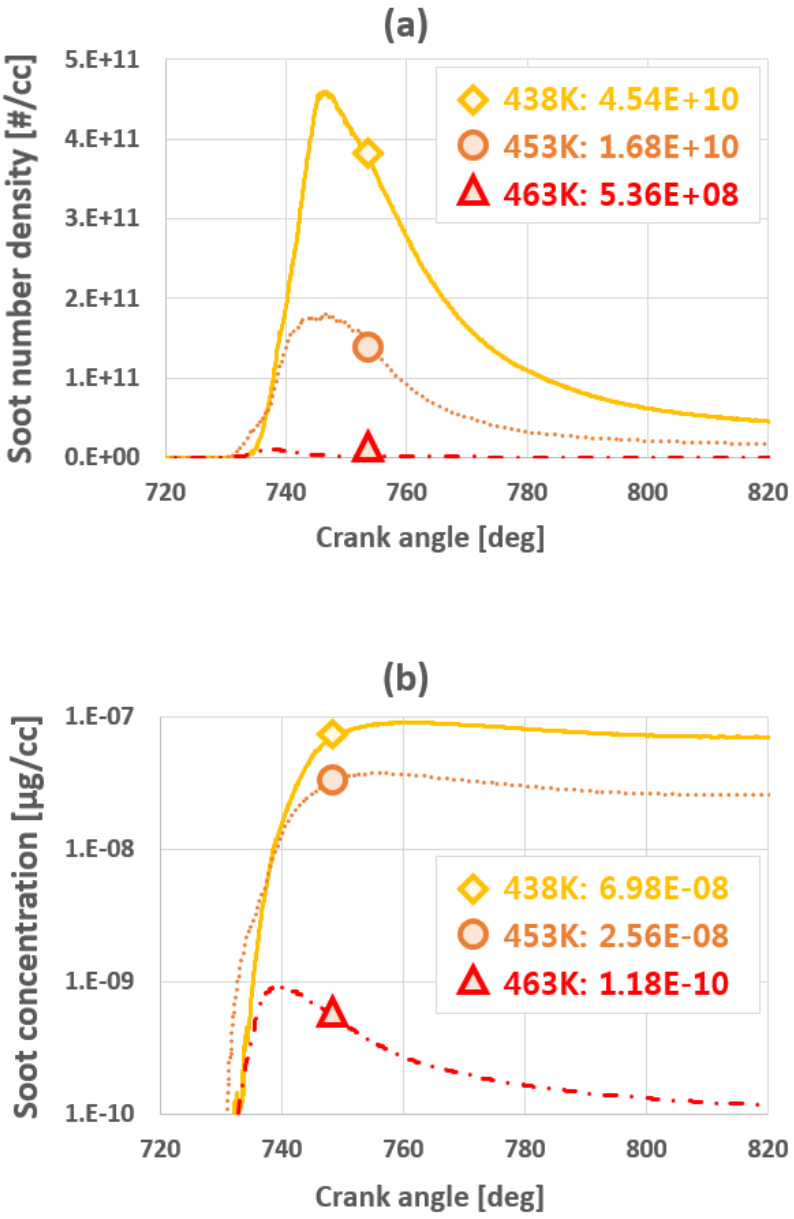

Figure 7.25 Simulation results of soot emission level according to the piston temperature variation from 438 K to 463 K with single injection strategy: (a) soot number density; (b) soot concentration.

	Base	Case A	Case B	Case C
Flamelet Library Referencing Location	$4 \times l_f$	$5\ mm$	$20\ mm$	$4 \times l_f$
PAH species	5 species (A_4 ~ A_7)			A_4 only

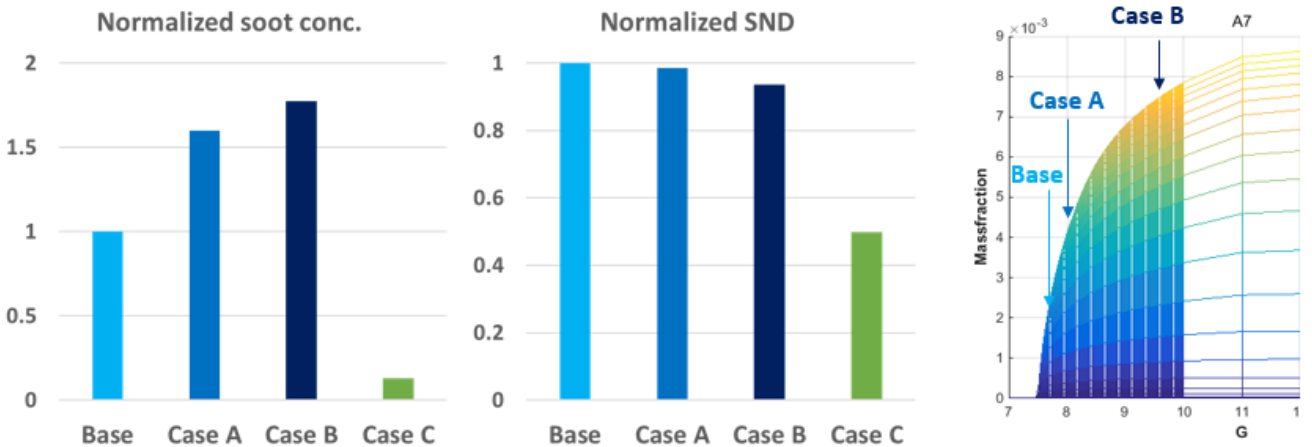

Figure 7.26 Results of model sensitivity to the PAH concentrations by varying the referencing location for the flamelet library and the soot precursors.

7.3 Engine Simulation with MOMIC

To explore the predictability of the state-of-the-art soot model for DISI engines, MOMIC was incorporated for simulating the multiple injection cases. The mixing and combustion processes are the same as described in the previous section, so only the soot emission was analyzed here.

Figure 7.27 illustrates the in-cylinder soot formation in terms of soot number density and soot mean diameter in the single injection case. Similar results from the semi-empirical model were found; the soot particles produced in the fuel-rich mixture where the perceptible PAHs' concentration exists, and the soot was advected away by the mean flow and diffusion transport. The soot mean diameter became smaller as it diffused into the free space due to the oxidation.

The soot number density and the soot concentration according to the multiple injection strategies are compared with that of the semi-empirical model and plotted in Fig. 7.28. It is revealed that the soot concentration of MOMIC was slightly higher than that of the semi-empirical model, 25.7%, 14.0%, and 15.9% in the single, dual, and triple injection, respectively. However, for the soot number density, the results by the MOMIC were significantly larger than semi-empirical predictions; 50.5%, 98.9%, 99.3% for each injection strategy, respectively.

The MOMIC incorporated the additional reaction pathway for the HACA growth; The H-abstraction from the soot particles' surface not only governed by the H radicals but also proceeded by the methyl (CH_3), ethynyl (C_2H), and propargyl (C_3H_3) radicals [163]. These reactions were considered by the active site reaction model, while the semi-empirical soot model adopted the acetylene absorption as the simplified approach. In addition, MOMIC considered the PAH condensation for the physical

growth, which is omitted in the semi-empirical model. Taken together, two distinct modeling method might result in the differences in the soot emission level.

For the large discrepancies in the soot number density, recall the definition of number density in MOMIC here,

$$M_0 = \sum_{i=1}^{\infty} N_i \ . \tag{7.4}$$

It is defined as the total sum of number density of each particle class which is discretized as $m_i = im_C$. Therefore, the zeroth moment of particle size distribution inherently contains the number density of low carbon atom class which has substantial number density compared to others. By contrast, the smallest particle predicted from the semi-empirical model comprises 100 carbon atoms, which is equivalent to d=1.28 nm sphere. So, the difference in the soot number density was raised from the two distinct descriptions for the particle system.

Unlike the assumption made in the semi-empirical model, mono-dispersed spherical soot particle, MOMIC calculates the moments of the particle system and obtains the statistical properties such as mean, variance, skewness, and kurtosis. Thus, the mean diameter is a number-average diameter of a particle system, and it is hard to apply the same analysis for the evolution of soot size distribution as done in the previous section. In summary, MOMIC predicts the soot emission trend similar to the semi-empirical model, while the absolute levels are different due to the modeling approach. However, there is no appreciable improvement to compensate the reduction slope discrepancy.

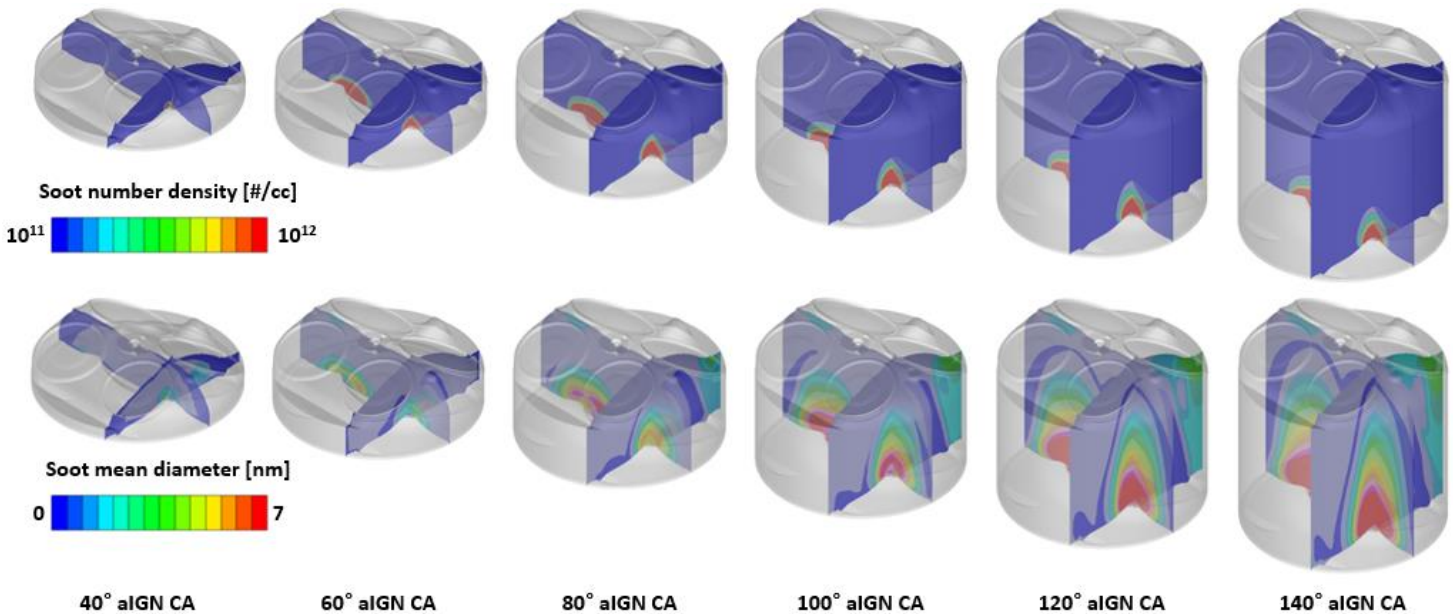

Figure 7.27 In-cylinder soot formation results of the single injection case: soot number density (upper), soot mean diameter (lower).

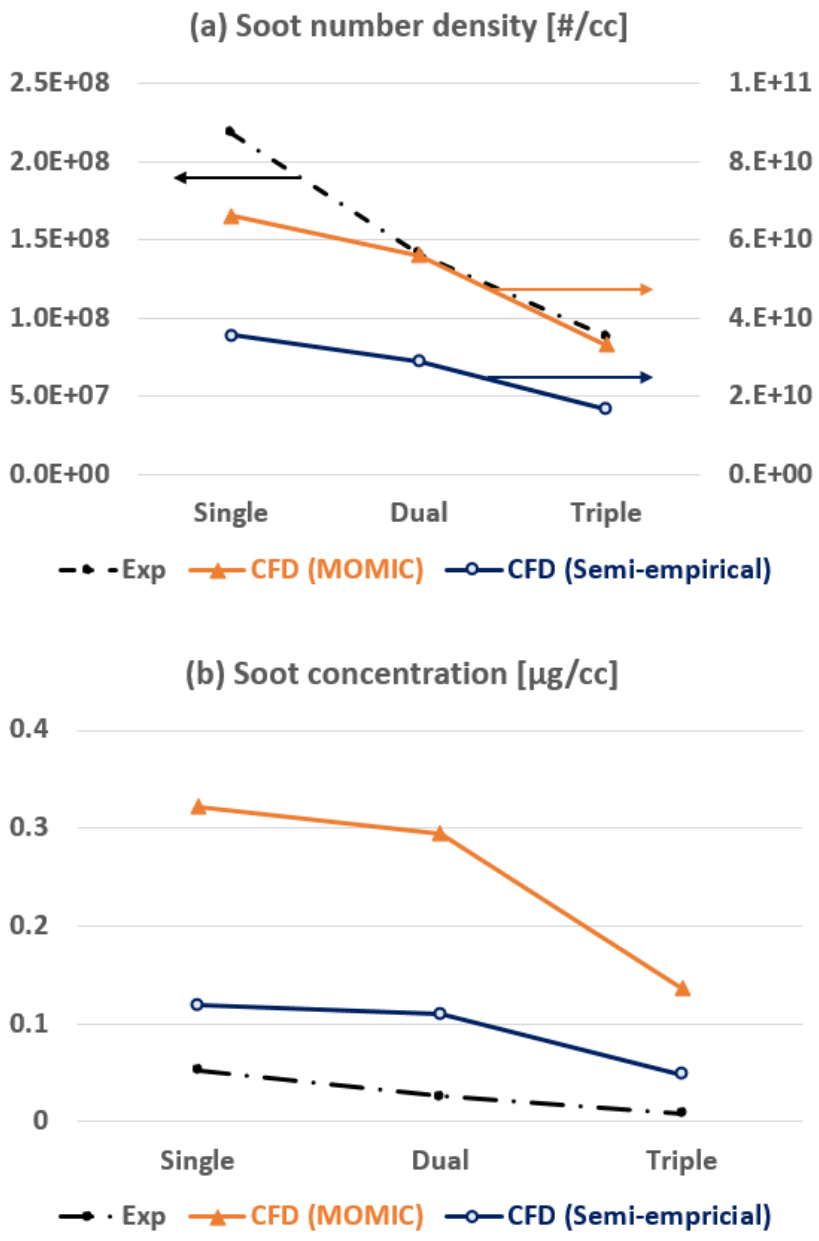

Figure 7.28 Comparison of semi-empirical model and MOMIC for soot emission results: (a) soot number density, (b) soot concentration.

7.4 Further Discussion on Soot Emission Prediction

Based on the models developed in this study, the soot emissions from DISI engines were able to be predicted physically. However, the current model still faces major challenges arising from its limitations. It is valuable to note the limitations and shortcomings for further improvements. Four major estimated limitations of the current model framework are discussed: mixture distribution, fuel film sources, particle growth in engine environments, and turbulent transport. Note that the modeling of soot emissions in engines by the RANS scheme involves more limiting issues than those listed below. However, it is beyond the scope of the present study.

Mixture Distribution

The mixture distribution should be accurately predicted because it has predominant effects on PAH formation. The air-fuel mixing, fuel physical properties, and liquid film behavior are responsible for the final state of the mixture. The influence of the surface temperature of the liquid film has been investigated, and a modeling of spray-wall interaction was suggested to resolve the spray cooling effect when film deposition exists [50, 51]. The consideration of these issues in the simulation is expected to lead to further improvement in the prediction accuracy.

Fuel Film Sources

It is known that the pool fire from the film deposited area and the droplets burning around the coked injector are the major contributors to the soot emissions. The measured emissions indeed have particulate portions that arise from those sources

because the engine was operated under the cold wall condition, which induces significant film deposition. With regard to modeling, however, it is challenging to resolve the flame-wall interaction because of the numerical issue in the near-wall treatment. In addition, the pool fire is a multi-phase combustion phenomenon, so it requires additional modeling work. Therefore, the current model only takes account for the reaction of the air-fuel mixture in the gaseous phase and omits the soot formation from the burning of the liquid droplet as well as fuel film.

Particle Growth in Engine Environments

The simulation results showed that the soot concentration was in agreement with the experimental data by differing its level in factor of magnitude, however, the soot number density was far beyond the measured data. Furthermore, the size distribution was smaller than the experimental result. It implies that there are under-estimation of particle growth by the coagulation and aggregation physics. The combustion process of DISI engines undergoes in the condition of high pressure and temperature, so that there might be some unresolved physics in the simulation. In addition to the possibility of liquid droplet/film burning as discussed above, the particulate growth is still cannot be predicted well. Further studies are needed to be focused on the aerosol dynamics in the engine application, and it left for the future work.

Turbulent Transport

Though the engine combustion occurs under turbulent flows, the laminar flamelet approach enables the decoupling of the turbulence and chemical reaction of the flame front. The major combustion products almost follow the fast chemistry in

the burned region, but the pollutants such as nitric oxide and particulates have longer reaction time scales, so the turbulence effect on their chemistry should be considered. It is reported that the turbulence can increase the particle collision frequency while suppressing the surface growth rate [171]. In this respect, the turbulent effect cannot be ignored in soot emission modeling. However, it is impossible to implement the chemical reaction mechanism for engine CFD simulation, so the detailed soot model was only based on the flamelet assumption and exclude the turbulent effects on PAH and soot formation.

Chapter 8. Conclusions

In this study, the combustion and soot emission models for DISI engines were developed, and the results of CFD simulation for the various engine operation conditions were validated against the experimental data.

First of all, the six-component surrogate fuel was derived with the focus on the soot emission from DISI engines, where the boiling range and the aromatic content hold great responsibilities. To obtain the practical basis of surrogate fuel, the gasoline properties including the distillation curve, hydrocarbon composition, heating value, and density were analyzed through a set of standard test method. Then, the component and composition of surrogate fuel were determined by matching the distillation curve with the highest priority and keeping the same aromatic content of gasoline. Finally, the six-component surrogate fuel that consists of iso-pentane (23.0%), n-hexane (31.0%), iso-octane (28.4%), o-xylene (10%), p-diethylbenzene (4.6%), and n-undecane (3%) were derived in this study. It is revealed that the surrogate fuel was able to reproduce the distillation curve within the 3% error except the first distilled volume fraction of 5%, and the density as well as the H/C ratio within 3.3% difference, respectively. Regarding to the chemical reaction kinetics of the surrogate fuel during the combustion process, the surrogate fuel was linked with the TRF surrogate by GCR approach.

The KH-RT break-up model was calibrated against to the droplet size distribution and penetration length data obtained from a set of rig-experiment. The model constant of RT break-up model that governs the break-up time constant was altered for the calibration. It is indicated that the base model constant over-predicts the break-up rate and results narrow size distribution which concentrated near 10 um. Consequently, the spray morphology as well as the penetration length showed unrealistic behavior

compared to the measurement data. However, the calibrated model was capable of matching the moderate break-up throughout the entire size distribution range, and thereby reproducing the practical spray morphology. Finally, the penetration length was in agreement within 2% error.

The laminar burning velocity of gasoline fuel was newly derived in this study with the consideration on the mass burning rate in the fuel-rich mixture. Recent experimental findings asserted that the laminar burning velocities of aromatic hydrocarbon has different behavior compared to that of the paraffinic hydrocarbon. So, in this study, the laminar burning velocities of iso-octane, n-heptane, and toluene were employed and blended by the energy fraction based mixing rule. To obtain the high fidelity results on engine-relevant condition, the detailed chemical mechanisms developed in LLNL were adopted in conjunction with the PREMIX module, and the laminar burning velocities of three hydrocarbon were calculated under the wide range of pressure (5-25 bar), temperature (400-900K), and equivalence ratio (0.5-2.0) to cover the in-cylinder condition of DISI engines. The fitting equations for the calculated laminar burning velocity of each hydrocarbon were derived as a function of equivalence ratio, pressure and temperature dependence terms. Finally, the energy fraction based mixing rule was adopted to calculate the burning velocity of gasoline. As a result, the developed laminar burning velocity model is capable of providing the realistic behavior in either fuel-rich or fuel-lean branch, in contrast to the widespread models used in SI engine simulation that showed negative or near-zero values.

In this study, the detailed soot model framework was suggested that comprised of the flamelet library for predicting the PAH concentration, and two soot models of semi-empirical-approach and MOMIC. To achieve high-quality supplication of flame data, the detailed chemical kinetics for TRF oxidation including the PAH reaction pathway up to coronene was adopted. The premixed laminar flamelet equation was

solved under the temperature of 600-800 K, pressure of 5-30 bar, equivalence ratio of 0.5-3.5 conditions. From the flamelet result, it is shown that the PAH concentration has significant growth around the equivalence ratio of 1.5. Finally, the major combustion product as well as five representative PAHs were selected for the library generation. Finally, the semi-empirical soot model was developed in this study in which the soot nucleation has 15 reaction pathways by five representative PAHs from the flamelet library. Furthermore, MOMIC was adopted to explore the state-of-the-art soot model in DISI engine application.

To validate the models developed in this study, the preliminary model evaluation was carried out. First, the soot emission similarity between TRF and gasoline was verified in PFI engine experiment by varying the equivalence ratio from 0.9 to 1.6 while maintaining the combustion phase in terms of fixed MFB50 and nIMEP. It is shown that the soot number density as well as soot concentration increase drastically around equivalence ratio between 1.3 and 1.4 for both fuel. The emission level of TRF was always slightly lower than gasoline at $\varphi<1.3$, and the gap slightly reduced in fuel-rich condition.

Next, the surrogate fuel, calibrated break-up model, and the correlation of the laminar burning velocity of gasoline were evaluated and compared against the existing base model under catalyst heating condition. The validity of each model have been proved by either fundamental measurements, such as distillation curve, penetration length, and droplet size distribution, and the literature data, or the practical engine simulation as discussed above. It is expected that the developed models can be applied to further engine simulation with proven authenticity.

Finally, the effect of split injection and injection timing on soot emission were investigated in this study. It turns out that the spray penetration length is reduced as

the number of split injection increase for a fixed fuel mass, so that the triple injection allows the minimum fuel film deposition as well as fuel-rich mixture in gas-phase. The deposited film area of single and dual injection were similar, however, the second injection contributed to the film deposition in dual injection case were diminished and thereby the fuel film mass differs in factor of 1.5 from the single injection case. The soot emission level follows the ratio of fuel-rich fraction and the film mass, and it was well captured by the numerical models developed in this study.

The soot formation arises from the PAH concentration which were mainly takes place in the piston bowl, and the soot particles were advected into the free-volume space inside the cylinder. It is shown that the soot number density as well as soot concentration undergo significant growth under the continuous supplication of PAH precursors; however, with the exhaustion of them due to the PAH dimerization for soot nucleation, the soot number density starts to decrease due to the coagulation physics prevail over entire cylinder space. The soot concentration also decrease due to the surface oxidation by the particle advection into lean region. The model is capable to predict the soot concentration within the factor of error, while captures the soot number density in qualitative trend only.

The effect of wall temperature on soot emission were investigated by varying the piston surface temperature from 440 K to 473 K. It was indicated that the film mass was affected by the temperature elevation, where 3.5% of injected fuel mass was deposited on the wall in T=440 K while no fuel film was found in T=473K. The predicted soot emission also followed the film reduction trend as well. Thus, the precise knowledge of wall temperature is required prior to match the soot emission against the experimental data unless the qualitative trend should be focused. In addition, the model sensitivity to the PAH concentrations were examined by adjusting the referencing location of the flamelet solution and by replacing the five PAHs with

pyrene. It was shown that the soot emission results were sensitive to the soot precursor selection, and it proved the validity of the five PAHs used in this study.

Finally, MOMIC was implemented to explore the predictability of the state-of-the-art model for DISI engine application. The soot number density by MOMIC was larger than that by semi-empirical model in factor of 1.9, while the soot concentration was higher in factor of 2.7. Though the MOMIC predicts the soot emission trend similar to the semi-empirical model, the absolute levels are different due to the modeling approach. In addition, there is no appreciable improvement to compensate the reduction slope discrepancy.

The combustion and soot emission models, in conjunction with six-component surrogate fuel and calibrated break-up model, showed the capability to predict the entire in-cylinder physics from the air-fuel mixing, combustion, and soot formation in physical manner. But at the same time, it still leaves some room for the further model improvement, such as spray-wall interaction and turbulence interaction. However, the model was able to predict the soot emission trend according to the engine operating strategy variation. Thus, it is expected that the model developed in this study could be adopted for the optimization of combustion chamber design and operating strategies in the engine development process.

Bibliography

1. Díaz, S., U. Tietge, and P. Mock, *CO2 emissions from new passenger cars in the EU: Car manufacturers' performance in 2015.* ICCT Briefing, 2016.
2. *On the Road toward 2050: Potential for Substantial Reduction in Light-Duty Vehicle Energy Use and Greenhouse Gas Emissions*, J. Heywood and D. Mackenzie, Editors. 2015, Massachusetts Institute of Technology.
3. Heywood, J., *Internal combustion engine fundamentals*. 1988: McGraw-Hill Education.
4. Schumann, F., et al., *Potential of spray-guided gasoline direct injection for reduction of fuel consumption and simultaneous compliance with stricter emissions regulations.* International Journal of Engine Research, 2013. **14**(1): p. 80-91.
5. Steimle, F., et al., *Systematic Analysis and Particle Emission Reduction of Homogeneous Direct Injection SI Engines*. 2013, SAE International.
6. Price, P., et al., *Cold Start Particulate Emissions from a Second Generation DI Gasoline Engine*. 2007, SAE International.
7. Farron, C., et al., *Particulate Characteristics for Varying Engine Operation in a Gasoline Spark Ignited, Direct Injection Engine*. 2011, SAE International.
8. Piock, W., et al., *Strategies Towards Meeting Future Particulate Matter Emission Requirements in Homogeneous Gasoline Direct Injection Engines.* SAE Int. J. Engines, 2011. **4**(1): p. 1455-1468.
9. Whitaker, P., et al., *Measures to Reduce Particulate Emissions from Gasoline DI engines.* SAE Int. J. Engines, 2011. **4**(1): p. 1498-1512.
10. Choi, K., et al., *Size-resolved engine exhaust aerosol characteristics in a metal foam particulate filter for GDI light-duty vehicle.* Journal of Aerosol science, 2013. **57**: p. 1-13.

11. Sabathil, D., et al., *The Influence of DISI Engine Operating Parameters on Particle Number Emissions*. 2011, SAE International.
12. Ketterer, J.E. and W.K. Cheng, *On the Nature of Particulate Emissions from DISI Engines at Cold-Fast-Idle.* SAE Int. J. Engines, 2014. **7**(2): p. 986-994.
13. Rossbach, M., et al. *Investigations of the formation and oxidation of soot inside a direct injection spark ignition engine*. in *Proceedings of the International Conference and Exhibition: The Spark Ignition Engine of the future*. 2009.
14. Berndorfer, A., et al., *Diffusion Combustion Phenomena in GDi Engines caused by Injection Process*. 2013, SAE International.
15. Dahlander, P. and S. Hemdal, *High-Speed Photography of Stratified Combustion in an Optical GDI Engine for Different Triple Injection Strategies*. 2015, SAE International.
16. *Euro 5/6 standards (2009/2014): Regulation 715/2007 and several comitology regulations*. Available from: http://www.dieselnet.com/standards/eu/ld.ph#stds.
17. Palmer, H.B. and C.F. Cullis, *The formation of carbon from gases.* Chemistry and physics of carbon, 1965. **1**: p. 265-325.
18. Whitby, K. and B. Cantrell. *Atmospheric aerosols- Characteristics and measurement*. in *International Conference on Environmental Sensing and Assessment, Las Vegas, Nev*. 1976.
19. Frenklach, M., *Reaction mechanism of soot formation in flames.* Physical Chemistry Chemical Physics, 2002. **4**(11): p. 2028-2037.
20. Frenklach, M. and H. Wang, *Detailed mechanism and modeling of soot particle formation*, in *Soot formation in combustion*. 1994, Springer. p. 165-192.
21. Calcote, H.F., *Mechanisms of soot nucleation in flames—a critical review.* Combustion and Flame, 1981. **42**: p. 215-242.
22. Frenklach, M., et al. *Detailed kinetic modeling of soot formation in shock-tube pyrolysis of acetylene*. in *Symposium (International) on Combustion*. 1985. Elsevier.

23. Bartok, W. and A.F. Sarofim, *Fossil fuel combustion: a source book.* 1991.

24. Kayes, D. and S. Hochgreb, *Mechanisms of particulate matter formation in spark-ignition engines. 1. Effect of engine operating conditions.* Environmental Science & Technology, 1999. **33**(22): p. 3957-3967.

25. Kayes, D. and S. Hochgreb, *Mechanisms of particulate matter formation in spark-ignition engines. 2. Effect of fuel, oil, and catalyst parameters.* Environmental science & technology, 1999. **33**(22): p. 3968-3977.

26. Kayes, D. and S. Hochgreb, *Mechanisms of particulate matter formation in spark-ignition engines. 3. Model of PM formation.* Environmental science & technology, 1999. **33**(22): p. 3978-3992.

27. Velji, A., et al., *Investigations of the Formation and Oxidation of Soot Inside a Direct Injection Spark Ignition Engine Using Advanced Laser-Techniques*. 2010, SAE International.

28. Kaminaga, T., J. Kusaka, and Y. Ishii, *A three-dimensional numerical study on exhaust gas emissions from a medium-duty diesel engine using a phenomenological soot particle formation model combined with detailed chemistry.* International Journal of Engine Research, 2008. **9**(4): p. 283-296.

29. Vishwanathan, G. and R.D. Reitz, *Development of a practical soot modeling approach and its application to low-temperature Diesel combustion.* Combustion Science and Technology, 2010. **182**(8): p. 1050-1082.

30. Kwon, H., et al., *Combustion and emission modelling of a direct-injection spark-ignition engine by combining flamelet models for premixed and diffusion flames.* Combustion Theory and Modelling, 2012. **16**(6): p. 1089-1108.

31. Kim, J., et al., *Numerical Analysis of Pollutant Formation in Direct-Injection Spark-Ignition Engines by Incorporating the G-Equation with a Flamelet Library*. 2014, SAE International.

32. Dong, Z., et al., *CFD Modeling of Mixture Preparation and Soot Formation in a Downsized Gasoline Direct Injection Engine*. 2016, SAE International.

33. Blanquart, G., P. Pepiot-Desjardins, and H. Pitsch, *Chemical mechanism for high temperature combustion of engine relevant fuels with emphasis on soot precursors.* Combustion and Flame, 2009. **156**(3): p. 588-607.

34. Raj, A., et al., *A reaction mechanism for gasoline surrogate fuels for large polycyclic aromatic hydrocarbons.* Combustion and Flame, 2012. **159**(2): p. 500-515.

35. Hiroyasu, H. and T. Kadota, *Models for Combustion and Formation of Nitric Oxide and Soot in Direct Injection Diesel Engines*. 1976, SAE International.

36. Fusco, A., A. Knox-Kelecy, and D. Foster. *Application of a phenomenological soot model to diesel engine combustion*. in *Proceedings of the International Symposium COMODIA*. 1994.

37. Kazakov, A. and D.E. Foster, *Modeling of Soot Formation During DI Diesel Combustion Using a Multi-Step Phenomenological Model*. 1998, SAE International.

38. Liu, Y., et al., *Application of A Multiple-Step Phenomenological Soot Model to HSDI Diesel Multiple Injection Modeling*. 2005, SAE International.

39. Hong, S., et al., *Development and application of a comprehensive soot model for 3D CFD reacting flow studies in a diesel engine.* Combustion and Flame, 2005. **143**(1): p. 11-26.

40. Zhong, B.-J., et al., *3-D simulation of soot formation in a direct-injection diesel engine based on a comprehensive chemical mechanism and method of moments.* Combustion Theory and Modelling, 2012. **16**(1): p. 143-171.

41. Aubagnac-Karkar, D., et al., *Sectional soot model coupled to tabulated chemistry for Diesel RANS simulations.* Combustion and Flame, 2015. **162**(8): p. 3081-3099.

42. Naik, C.V., et al., *Simulation and Analysis of In-Cylinder Soot Formation in a Gasoline Direct-Injection Engine Using a Detailed Reaction Mechanism*. 2014, SAE International.

43. Jiao, Q. and R.D. Reitz, *Modeling soot emissions from wall films in a direct-injection spark-ignition engine.* International Journal of Engine Research, 2015. **16**(8): p. 994-1013.

44. Jiao, Q. and R.D. Reitz, *Modeling of Equivalence Ratio Effects on Particulate Formation in a Spark-Ignition Engine under Premixed Conditions*. 2014, SAE International.

45. Wang, H., et al., *Development of an n-heptane/toluene/polyaromatic hydrocarbon mechanism and its application for combustion and soot prediction.* International Journal of Engine Research, 2013. **14**(5): p. 434-451.

46. Sukegawa, Y. and K. Oryoji, *3D Modeling of Particulate Matter from Spark Ignition Engines.* SAE Int. J. Engines, 2015. **8**(2): p. 419-425.

47. Slavinskaya, N.A. and P. Frank, *A modelling study of aromatic soot precursors formation in laminar methane and ethene flames.* Combustion and Flame, 2009. **156**(9): p. 1705-1722.

48. Marinov, N.M., et al., *Aromatic and polycyclic aromatic hydrocarbon formation in a laminar premixed n-butane flame.* Combustion and flame, 1998. **114**(1): p. 192-213.

49. Jiao, Q. and R.D. Reitz, *The Effect of Operating Parameters on Soot Emissions in GDI Engines.* SAE Int. J. Engines, 2015. **8**(3): p. 1322-1333.

50. Köpple, F., et al., *Investigation of the Parameters Influencing the Spray-Wall Interaction in a GDI Engine - Prerequisite for the Prediction of Particulate Emissions by Numerical Simulation.* SAE Int. J. Engines, 2013. **6**(2): p. 911-925.

51. Köpple, F., et al., *A Novel CFD Approach for an Improved Prediction of Particulate Emissions in GDI Engines by Considering the Spray-Cooling on the Piston*. 2015, SAE International.

52. Vogt, R., V. Scheer, and U. Kirchner. *Eigenschaften von Partikeln im Abgas moderner Motorkonzepte*. in *Internationalen Wiener Motorensymposium*. 2007. Wiener.

53. Glassman, I., *Combustion. 3rd*. 1996, Academic Press, San Diego, California.

54. Frenklach, M., *Method of moments with interpolative closure.* Chemical Engineering Science, 2002. **57**(12): p. 2229-2239.

55. Pope, S.B., *Turbulent flows*. 2001, IOP Publishing.

56. Boussinesq, J., *Essai sur la théorie des eaux courantes*. 1877: Imprimerie nationale.

57. Prandtl, L., *Bericht über Untersuchungen zur ausgebildeten Turbulenz.* Z. Angew. Math. Mech, 1925. **5**(2): p. 136-139.

58. Prandtl, L., *Über ein neues formelsystem für die ausgebildete turbulenz, nachr. d. akad. d. wiss.* Göttingen, Math.-nat. Klasse, 1945: p. 6-20.

59. Jones, W. and B. Launder, *The prediction of laminarization with a two-equation model of turbulence.* International journal of heat and mass transfer, 1972. **15**(2): p. 301-314.

60. Launder, B. and B. Sharma, *Application of the energy-dissipation model of turbulence to the calculation of flow near a spinning disc.* Letters in heat and mass transfer, 1974. **1**(2): p. 131-137.

61. Launder, B., G.J. Reece, and W. Rodi, *Progress in the development of a Reynolds-stress turbulence closure.* Journal of fluid mechanics, 1975. **68**(03): p. 537-566.

62. Yakhot, V. and S.A. Orszag, *Renormalization group analysis of turbulence. I. Basic theory.* Journal of scientific computing, 1986. **1**(1): p. 3-51.

63. Yakhot, V. and L.M. Smith, *The renormalization group, the ε-expansion and derivation of turbulence models.* Journal of Scientific Computing, 1992. **7**(1): p. 35-61.

64. Mitroglou, N., J. Nouri, and C. Arcoumanis, *Spray structure from double fuel injection in multihole injectors for gasoline direct-injection engines.* Atomization and Sprays, 2009. **19**(6).

65. Kay, P.J., et al., *Studies of gasoline direct-injection sprays at elevated ambient gas temperatures and pressures*. Atomization and Sprays, 2012. **22**(4).

66. Oh, Y., S. Lee, and S. Park, *Modeling of n-heptane sprays injected through multi-hole type GDI injector.* Atomization and Sprays, 2012. **22**(3).

67. Lucchini, T., et al., *Development and application of a computational fluid dynamics methodology to predict fuel–air mixing and sources of soot formation in gasoline direct injection engines.* International Journal of Engine Research, 2014. **15**(5): p. 581-596.

68. Costa, M., et al., *Study of mixture formation and early flame development in a research GDI (gasoline direct injection) engine through numerical simulation and UV-digital imaging.* Energy, 2014. **77**: p. 88-96.

69. Zheng, Z., X. Tian, and X. Zhang, *Effects of split injection proportion and the second injection time on the mixture formation in a GDI engine under catalyst heating mode using stratified charge strategy.* Applied Thermal Engineering, 2015. **84**: p. 237-245.

70. An, Y.-z., et al., *Development of a soot particle model with PAHs as precursors through simulations and experiments.* Fuel, 2016. **179**: p. 246-257.

71. Costa, M., U. Sorge, and L. Allocca, *CFD optimization for GDI spray model tuning and enhancement of engine performance.* Advances in Engineering Software, 2012. **49**: p. 43-53.

72. Kim, T., J. Song, and S. Park, *Effects of turbulence enhancement on combustion process using a double injection strategy in direct-injection spark-ignition (DISI) gasoline engines.* International Journal of Heat and Fluid Flow, 2015. **56**: p. 124-136.

73. Gosman, A. and E. Loannides, *Aspects of computer simulation of liquid-fueled combustors.* Journal of Energy, 1983. **7**(6): p. 482-490.

74. O'Rourke, P.J., *Collective drop effects on vaporising liquid sprays*, in *Department of Mechanical and Aerospace Engineering*. 1981, Princeton University.

75. Nordin, N., *Complex Chemistry Modelling of Diesel Spray Combustion*, in *Department of Thermo and Fluid Dynamics*. 2001, Charlmers University of Technology.

76. Schmidt, D.P. and C. Rutland, *A new droplet collision algorithm.* Journal of Computational Physics, 2000. **164**(1): p. 62-80.

77. Rosa, N., et al., *A new droplet-wall interaction model*, in *ICLASS-2006*. 2006: Kyoto, Japan.

78. Patterson, M.A. and R.D. Reitz, *Modeling the Effects of Fuel Spray Characteristics on Diesel Engine Combustion and Emission*. 1998, SAE International.

79. Bai, C. and A.D. Gosman, *Mathematical Modelling of Wall Films Formed by Impinging Sprays*. 1996, SAE International.

80. Pitz, W.J., et al., *Development of an Experimental Database and Chemical Kinetic Models for Surrogate Gasoline Fuels*. 2007, SAE International.

81. Kwon, H., et al., *Premixed Combustion Modeling in an SI Engine Considering the Burned Gas Composition*. 2005, SAE International.

82. Liang, L. and R.D. Reitz, *Spark Ignition Engine Combustion Modeling Using a Level Set Method with Detailed Chemistry*. 2006, SAE International.

83. Knop, V. and E. Essayem, *Comparison of PFI and DI Operation in a Downsized Gasoline Engine.* SAE Int. J. Engines, 2013. **6**(2): p. 941-952.

84. Yang, S., et al., *Improvements to Combustion Models for Modeling Spark-Ignition Engines Using the G-equation and Detailed Chemical Kinetics.* SAE Int. J. Fuels Lubr., 2008. **1**(1): p. 1009-1025.

85. Yang, S., E. Pomraning, and M. Jia, *Simulations of gasoline engine combustion and emissions using a chemical-kinetics-based turbulent premixed combustion modeling approach.* Proceedings of the Institution of Mechanical Engineers, Part D: Journal of Automobile Engineering, 2016: p. 0954407016661448.

86. *Standard Test Method for Research Octane Number of Spark-Ignition Engine Fuel*. 2016, ASTM International.

87. *Standard Test Method for Motor Octane Number of Spark-Ignition Engine Fuel*. 2016, ASTM International.

88. Kalghatgi, G.T., *Auto-Ignition Quality of Practical Fuels and Implications for Fuel Requirements of Future SI and HCCI Engines*. 2005, SAE International.

89. Thirouard, B., J. Cherel, and V. Knop, *Investigation of Mixture Quality Effect on CAI Combustion*. 2005, SAE International.

90. Gauthier, B., D.F. Davidson, and R.K. Hanson, *Shock tube determination of ignition delay times in full-blend and surrogate fuel mixtures.* Combustion and Flame, 2004. **139**(4): p. 300-311.

91. Lee, K., Y. Kim, and K. Min, *Development of a reduced chemical kinetic mechanism for a gasoline surrogate for gasoline HCCI combustion.* Combustion Theory and Modelling, 2010. **15**(1): p. 107-124.

92. Pera, C. and V. Knop, *Methodology to define gasoline surrogates dedicated to auto-ignition in engines.* Fuel, 2012. **96**: p. 59-69.

93. Knop, V., C. Pera, and F. Duffour, *Validation of a ternary gasoline surrogate in a CAI engine.* Combustion and Flame, 2013. **160**(10): p. 2067-2082.

94. *Standard Test Method for Vapor Pressure of Petroleum Products (Reid Method)*. 2015, ASTM International.

95. *Standard Test Method for Distillation of Petroleum Products and Liquid Fuels at Atmospheric Pressure*. 2016, ASTM International.

96. Naik, C.V., et al., *Applying Detailed Kinetics to Realistic Engine Simulation: the Surrogate Blend Optimizer and Mechanism Reduction Strategies.* SAE Int. J. Engines, 2010. **3**(1): p. 241-259.

97. Ahmed, A., et al., *A computational methodology for formulating gasoline surrogate fuels with accurate physical and chemical kinetic properties.* Fuel, 2015. **143**: p. 290-300.

98. Su, M. and C. Chen, *Heating and evaporation of a new gasoline surrogate fuel: A discrete multicomponent modeling study.* Fuel, 2015. **161**: p. 215-221.

99. Elwardany, A., S. Sazhin, and H.G. Im, *A new formulation of physical surrogates of FACE A gasoline fuel based on heating and evaporation characteristics.* Fuel, 2016. **176**: p. 56-62.

100. Aikawa, K., T. Sakurai, and J.J. Jetter, *Development of a Predictive Model for Gasoline Vehicle Particulate Matter Emissions.* SAE Int. J. Fuels Lubr., 2010. **3**(2): p. 610-622.

101. Aikawa, K. and J.J. Jetter, *Impact of gasoline composition on particulate matter emissions from a direct-injection gasoline engine: Applicability of the particulate matter index.* International Journal of Engine Research, 2014. **15**(3): p. 298-306.

102. Khalek, I.A., T. Bougher, and J.J. Jetter, *Particle Emissions from a 2009 Gasoline Direct Injection Engine Using Different Commercially Available Fuels.* SAE Int. J. Fuels Lubr., 2010. **3**(2): p. 623-637.

103. Kim, Y., et al., *Fuel Effect on Particle Emissions of a Direct Injection Engine*. 2013, SAE International.

104. Short, D.Z., et al., *Components of particle emissions from light-duty spark-ignition vehicles with varying aromatic content and octane rating in gasoline.* Environmental science & technology, 2015. **49**(17): p. 10682-10691.

105. Yinhui, W., et al., *The impact of fuel compositions on the particulate emissions of direct injection gasoline engine.* Fuel, 2016. **166**: p. 543-552.

106. Zhu, R., et al., *Effects of aromatics, olefins and distillation temperatures (T50 & T90) on particle mass and number emissions from gasoline direct injection (GDI) vehicles.* Energy Policy, 2017. **101**: p. 185-193.

107. *Standard Test Method for Hydrocarbon Types, Oxygenated Compounds, and Benzene in Spark Ignition Engine Fuels by Gas Chromatography*. 2016, ASTM International.

108. *Standard Test Method for Heat of Combustion of Liquid Hydrocarbon Fuels by Bomb Calorimeter*. 2017, ASTM International.

109. Anand, K., et al., *Surrogate model development for fuels for advanced combustion engines.* Energy & Fuels, 2011. **25**(4): p. 1474-1484.

110. Ra, Y. and R.D. Reitz, *A combustion model for IC engine combustion simulations with multi-component fuels.* Combustion and flame, 2011. **158**(1): p. 69-90.

111. Anand, K., et al., *Combustion simulations of the fuels for advanced combustion engines in a homogeneous charge compression ignition engine.* International Journal of Engine Research, 2013. **14**(2): p. 191-208.

112. Anand, K., et al., *Modeling Fuel and EGR Effects under Conventional and Low Temperature Combustion Conditions.* Energy & Fuels, 2013. **27**(12): p. 7827-7842.

113. Yang, S., et al., *Integration of a discrete multi-component fuel evaporation model with a G-equation flame propagation combustion model and its validation.* International Journal of Engine Research, 2012. **13**(4): p. 370-384.

114. Peters, N., *Turbulent combustion*. 2000: Cambridge university press.

115. Ranzi, E., et al., *Hierarchical and comparative kinetic modeling of laminar flame speeds of hydrocarbon and oxygenated fuels.* Progress in Energy and Combustion Science, 2012. **38**(4): p. 468-501.

116. Egolfopoulos, F.N., et al., *Advances and challenges in laminar flame experiments and implications for combustion chemistry.* Progress in Energy and Combustion Science, 2014. **43**: p. 36-67.

117. Spalding, D. *Mixing and chemical reaction in steady confined turbulent flames*. in *Symposium (International) on Combustion*. 1971. Elsevier.

118. Bray, K., P.A. Libby, and J. Moss, *Flamelet crossing frequencies and mean reaction rates in premixed turbulent combustion.* Combustion Science and Technology, 1984. **41**(3-4): p. 143-172.

119. Bray, K. and P.A. Libby, *Recent developments in the BML model of premixed turbulent combustion*. 1994, Academic Press New York. p. 115-151.

120. Candel, S., et al., *Coherent flamelet model: applications and recent extensions.* Recent advances in combustion modelling, 1990. **6**: p. 19-64.

121. Williams, F., *Turbulent combustion.* The mathematics of combustion, 1985. **2**: p. 267-294.

122. Sussman, M., P. Smereka, and S. Osher, *A level set approach for computing solutions to incompressible two-phase flow.* Journal of Computational physics, 1994. **114**(1): p. 146-159.

123. Damköhler, G., *Der einfluss der turbulenz auf die flammengeschwindigkeit in gasgemischen.* Berichte der Bunsengesellschaft für physikalische Chemie, 1940. **46**(11): p. 601-626.

124. Peters, N., *The turbulent burning velocity for large-scale and small-scale turbulence.* Journal of Fluid mechanics, 1999. **384**: p. 107-132.

125. Ewald, J. and N. Peters, *On unsteady premixed turbulent burning velocity prediction in internal combustion engines.* Proceedings of the combustion institute, 2007. **31**(2): p. 3051-3058.

126. Ra, Y., *Laminar flame propagation in a stratified charge*. 1999, Massachusetts Institute of Technology.

127. Gülder, Ö.L., *Correlations of Laminar Combustion Data for Alternative S.I. Engine Fuels*. 1984, SAE International.

128. Metghalchi, M. and J.C. Keck, *Burning velocities of mixtures of air with methanol, isooctane, and indolene at high pressure and temperature.* Combustion and flame, 1982. **48**: p. 191-210.

129. Yang, S. and R.D. Reitz, *Integration of a continuous multi-component fuel evaporation model with an improved G-equation combustion and detailed chemical kinetics model with application to GDI engines*. 2009, SAE Technical Paper.

130. Dahms, R.N., et al., *Understanding ignition processes in spray-guided gasoline engines using high-speed imaging and the extended spark-ignition model*

SparkCIMM. Part A: Spark channel processes and the turbulent flame front propagation. Combustion and flame, 2011. **158**(11): p. 2229-2244.

131. Sileghem, L., et al., *Laminar burning velocity of gasoline and the gasoline surrogate components iso-octane, n-heptane and toluene.* Fuel, 2013. **112**: p. 355-365.

132. Dirrenberger, P., et al., *Laminar burning velocity of gasolines with addition of ethanol.* Fuel, 2014. **115**: p. 162-169.

133. Mannaa, O., et al., *Laminar burning velocities at elevated pressures for gasoline and gasoline surrogates associated with RON.* Combustion and Flame, 2015. **162**(6): p. 2311-2321.

134. Mehl, M., et al. *Chemical kinetic modeling of component mixtures relevant to gasoline*. in *European Combustion Meeting*. 2009.

135. Mehl, M., et al., *Kinetic modeling of gasoline surrogate components and mixtures under engine conditions.* Proceedings of the Combustion Institute, 2011. **33**(1): p. 193-200.

136. Nakamura, H., et al., *An experimental and modeling study of shock tube and rapid compression machine ignition of n-butylbenzene/air mixtures.* Combustion and Flame, 2014. **161**(1): p. 49-64.

137. Sarathy, S.M., et al., *A comprehensive chemical kinetic combustion model for the four butanol isomers.* combustion and flame, 2012. **159**(6): p. 2028-2055.

138. Ryan, T.W. and S.S. Lestz, *The Laminar Burning Velocity of Isooctane, N-Heptane, Methanol, Methane, and Propane at Elevated Temperature and Pressures in the Presence of a Diluent*. 1980, SAE International.

139. Rhodes, D.B. and J.C. Keck, *Laminar Burning Speed Measurements of Indolene-Air-Diluent Mixtures at High Pressures and Temperatures*. 1985, SAE International.

140. Bhattacharya, A., et al., *Effects of exhaust gas dilution on the laminar burning velocity of real-world gasoline fuel flame in air.* Energy & Fuels, 2015. **29**(10): p. 6768-6779.

141. Tan, Z. and R.D. Reitz, *An ignition and combustion model based on the level-set method for spark ignition engine multidimensional modeling.* Combustion and flame, 2006. **145**(1): p. 1-15.

142. Tree, D.R. and K.I. Svensson, *Soot processes in compression ignition engines.* Progress in Energy and Combustion Science, 2007. **33**(3): p. 272-309.

143. Ewald, J., *A level set based flamelet model for the prediction of combustion in homogeneous charge and direct injection spark ignition engines*. 2006: Cuvillier.

144. Nilsson, P. and X.-S. Bai, *Level-set flamelet library approach for premixed turbulent combustion.* Experimental Thermal and Fluid Science, 2000. **21**(1): p. 87-98.

145. Huang, Y., *Modeling and simulation of combustion dynamics in lean-premixed swirl-stabilized gas-turbine engines*, in *Mechanical Engineering*. 2003, The Pennsylvania State University.

146. Appel, J., H. Bockhorn, and M. Frenklach, *Kinetic modeling of soot formation with detailed chemistry and physics: laminar premixed flames of C 2 hydrocarbons.* Combustion and Flame, 2000. **121**(1): p. 122-136.

147. Wang, H. and M. Frenklach, *A detailed kinetic modeling study of aromatics formation in laminar premixed acetylene and ethylene flames.* Combustion and flame, 1997. **110**(1): p. 173-221.

148. *CHEMKIN-PRO 15101*. 2010, Reaction Design: San Diego, CA.

149. Girimaji, S., *Assumed β-pdf model for turbulent mixing: Validation and extension to multiple scalar mixing.* Combustion Science and Technology, 1991. **78**(4-6): p. 177-196.

150. Tao, F., V.I. Golovitchev, and J. Chomiak, *A phenomenological model for the prediction of soot formation in diesel spray combustion.* Combustion and Flame, 2004. **136**(3): p. 270-282.

151. Leung, K.M., R.P. Lindstedt, and W. Jones, *A simplified reaction mechanism for soot formation in nonpremixed flames.* Combustion and flame, 1991. **87**(3-4): p. 289-305.

152. Colket, M. and R. Hall, *Description and discussion of a detailed model for soot formation in laminar premixed flames*. United Technologies Report No. UTRC91-20, August, 1991. **9**: p. 91-21.

153. Balthasar, M. and M. Kraft, *A stochastic approach to calculate the particle size distribution function of soot particles in laminar premixed flames.* Combustion and Flame, 2003. **133**(3): p. 289-298.

154. Wang, Y., A. Raj, and S.H. Chung, *Soot modeling of counterflow diffusion flames of ethylene-based binary mixture fuels.* Combustion and Flame, 2015. **162**(3): p. 586-596.

155. Von Smoluchowski, M., *Drei vortrage uber diffusion. Brownsche bewegung und koagulation von kolloidteilchen.* Z. Phys., 1916. **17**: p. 557-585.

156. Harris, S.J. and A.M. Weiner, *Surface growth of soot particles in premixed ethylene/air flames.* Combustion Science and Technology, 1983. **31**(3-4): p. 155-167.

157. Harris, S.J. and A.M. Weiner, *Chemical kinetics of soot particle growth.* Annual Review of Physical Chemistry, 1985. **36**(1): p. 31-52.

158. Liu, F., et al., *Numerical modelling of soot formation and oxidation in laminar coflow non-smoking and smoking ethylene diffusion flames.* Combustion Theory and Modelling, 2003. **7**(2): p. 301-315.

159. Nagle, J. and R. Strickland-Constable. *Oxidation of Carbon between 1000-2000 C*. in *Proceedings of the fifth carbon conference*. 1962. Pergamon Press London.

160. Ladommatos, N., H. Song, and H. Zhao, *Measurements and predictions of diesel soot oxidation rates.* Proceedings of the Institution of Mechanical Engineers, Part D: Journal of Automobile Engineering, 2002. **216**(8): p. 677-689.

161. Fenimore, C.P. and G.W. Jones, *Oxidation of soot by hydroxyl radicals.* The Journal of physical chemistry, 1967. **71**(3): p. 593-597.

162. Frenklach, M. and S.J. Harris, *Aerosol dynamics modeling using the method of moments.* Journal of colloid and interface science, 1987. **118**(1): p. 252-261.

163. Hwang, J. and S. Chung, *Growth of soot particles in counterflow diffusion flames of ethylene.* Combustion and flame, 2001. **125**(1): p. 752-762.

164. Li, X., et al., *Uncertainty analysis of the kinetic model prediction for high-pressure H 2/CO combustion.* Proceedings of the Combustion Institute, 2015. **35**(1): p. 617-624.

165. *STAR-CD v4.24*. 2015, CD-adapco.

166. Angelberger, C., T. Poinsot, and B. Delhay, *Improving Near-Wall Combustion and Wall Heat Transfer Modeling in SI Engine Computations*. 1997, SAE International.

167. Noyori, T., *Experimental Study of Smoke Emission on Small-Displacement Spark-Ignition Direct-Injection Engine*. 2006, SAE International.

168. Dimou, I., K. Kar, and W. Cheng, *Particulate Matter Emissions from a Direct Injection Spark Ignition Engine under Cold Fast Idle Conditions for Ethanol-Gasoline Blends.* SAE Int. J. Engines, 2011. **4**(1): p. 1738-1746.

169. Su, J., et al., *Particle Number Emissions Reduction Using Multiple Injection Strategies in a Boosted Spark-Ignition Direct-Injection (SIDI) Gasoline Engine.* SAE Int. J. Engines, 2014. **8**(1): p. 20-29.

170. Chung, J., et al., *Study on the Effect of Injection Strategies on Particulate Emission Characteristics under Cold Start Using In-cylinder Visualization*. 2016, SAE International.

171. El-Asrag, H., et al., *Simulation of soot formation in turbulent premixed flames.* Combustion and Flame, 2007. **150**(1): p. 108-126.

172. Kolmogorov, A.N. *The local structure of turbulence in incompressible viscous fluid for very large Reynolds numbers*. in *Dokl. Akad. Nauk SSSR*. 1941. JSTOR.

173. Bray, K.N.C. *Studies of the turbulent burning velocity*. in *Proceedings of the Royal Society of London A: Mathematical, Physical and Engineering Sciences*. 1990. The Royal Society.

174. Borghi, R., *On the structure and morphology of turbulent premixed flames*, in *Recent advances in the Aerospace Sciences*. 1985, Springer. p. 117-138.

175. Peters, N. *Laminar flamelet concepts in turbulent combustion*. in *Symposium (International) on Combustion*. 1988. Elsevier.

176. Poinsot, T., D. Veynante, and S. Candel. *Diagrams of premixed turbulent combustion based on direct simulation*. in *Symposium (international) on combustion*. 1991. Elsevier.

177. Echekki, T. and E. Mastorakos, *Turbulent combustion modeling: Advances, new trends and perspectives*. Vol. 95. 2010: Springer Science & Business Media.

178. Abraham, J., F.A. Williams, and F.V. Bracco, *A Discussion of Turbulent Flame Structure in Premixed Charges*. 1985, SAE International.

179. Ewald, J. and N. Peters. *A level set based flamelet model for the prediction of combustion in spark ignition engines*. in *15th International Multidimensional Engine Modeling User's Group Meeting, Detroit, MI*. 2005.

180. Dahms, R., et al., *Pollutant formation modelling in natural gas SI engines using a level set based flamelet model.* International Journal of Engine Research, 2008. **9**(1): p. 1-14.

Appendix A. Scales of Turbulent Flow and Averaging

The distinct feature of turbulent flows is the occurrence of eddies of different length scales [55]. The largest eddies, which are created by instabilities in the mean flow, are themselves subject to inertial instabilities and rapidly break-up or evolve into yet smaller vortices. The smaller eddies are unstable, and they pass their energy onto even smaller structures and so on. It is well-known as energy cascade hypothesis. According to the theory suggested by Kolmogorov [172] for homogeneous isotropic turbulence, it assumes that there is a constant transfer of kinetic energy from the large scales to the small scales and that this energy is being consumed at the small scales by viscous dissipation.

The turbulent kinetic energy of an isotropic turbulent flow can be analyzed through the Fourier transform of the velocity fluctuation from two-point correlation measurement. The turbulent kinetic energy, k, is obtained either from the energy spectrum regarding wavenumber (κ) or by the Reynolds stress tensor as follow,

$$k = \int_0^\infty E(\kappa)d\kappa \quad \text{and} \quad k = \frac{1}{2}\langle u_j' u_j' \rangle \ . \tag{A.1}$$

The turbulent dissipation, ε, represent the energy transfer rate of turbulent kinetic energy in the inertia subrange, and it is given as

$$\varepsilon = 2\frac{\mu}{\rho}\langle S_{ij} S_{ij} \rangle \quad \text{and} \quad \varepsilon \sim \frac{v'^3}{l} \tag{A.2}$$

where S_{ij} is rate of strain tensor, v' is the eddy turnover velocity, and l is a length scale of turbulent flow.

From the turbulent kinetic energy spectrum point of view, the length scale of most energy-containing turbulent eddies is called the integral length scale (l_t). These eddies gain the kinetic energy from the mean flow field by turbulent production due to mean velocity gradient. According to the definition of Bray [173], the integral length scale is defined as

$$l_t = a_1 \frac{v'^3}{\varepsilon}, \qquad a_1 = 0.37 \tag{A.3}$$

The eddy turnover velocity can be obtained from the isotropic turbulent assumption, $v' = \sqrt{2k/3}$. The turbulent energy of integral length scale is transferred to smaller scales, and it is assumed that the turbulent production from integral length scale is balanced with the turbulent dissipation in the small scales. This range is called inertia subrange, and it is followed by the dissipative scale, also known as Kolmogorov length scale. The transferred turbulent kinetic energy is converted into the thermal energy by the viscous forces at molecular level. Dimensional analysis defines the Kolmogorov length scale as

$$\eta = \left(\frac{\nu^3}{\varepsilon}\right)^{1/4} . \tag{A.4}$$

The time and velocity scales of Kolmogorov eddies are given as

$$v_\eta = (\nu\varepsilon)^{\frac{1}{4}} \text{ and } t_\eta = \left(\frac{\nu}{\varepsilon}\right)^{\frac{1}{2}} . \tag{A.5}$$

Here two averaging schemes for modeling the reacting fluid flow, ensemble-averaging, and Favre-averaging, are introduced. According to Reynolds

decomposition, each variable f is split into a mean component $\bar{f}$ and a fluctuating component f', leading to

$$f = \bar{f} + f'. \tag{A.6}$$

For the mean component $\bar{f}$, either ensemble averaging or time-averaging is available. The ensemble averaging is based on the statistical approach,

$$\bar{f}_N = \frac{1}{N}\sum_{i=1}^{N} f_i \tag{A.7}$$

where N is the number of realizations, over which the instantaneous values f_i are averaged.

For flows with large density changes as occur in combustion, it is convenient to introduce a density-weighted average $\tilde{f}$, called Favre-average, by splitting f into $\tilde{f}$ and f'' as

$$f = \tilde{f} + f'' \ . \tag{A.8}$$

This averaging procedure is defined by requiring that the average of the product of f'' with the density ρ (rather than f'' itself) vanishes,

$$\overline{\rho f''} = 0 \ . \tag{A.9}$$

Then the definition for $\tilde{f}$ can be derived as follow,

$$\overline{\rho f} = \overline{\rho}\tilde{f} + \overline{\rho f''} = \bar{\rho}\tilde{f} \quad \text{and} \quad \tilde{f} = \frac{\overline{\rho f}}{\bar{\rho}} \ . \tag{A.10}$$

Appendix B. Conservation Equations for Liquid Spray

The liquid spray injected against the in-cylinder gas can be treated as dispersed phase interacts with the continuous phase, and the modeling framework for the multiphase flow is based on the Eulerian-Lagrangian method. The Eulerian approach is adopted to describe the continuum phase of ambient gas as well as the liquid film, while the Lagrangian approach is used to resolve the dispersed phase of liquid fuel. The conservation equations for droplets in the Lagrangian framework are summarized as follow [165], where the subscript d denotes the droplet and non-subscript quantities are taken to refer to the fluid.

Momentum

The momentum equation for a droplet of mass m_d is

$$m_d \frac{d\boldsymbol{u}_d}{dt} = \boldsymbol{F}_{dr} + \boldsymbol{F}_p + \boldsymbol{F}_b + \boldsymbol{F}_{am} \tag{B.1}$$

where $\boldsymbol{u}_d$ is the instantaneous velocity of droplet. The drag force, F_{dr}, is defined as $\frac{1}{2} C_d \rho A_d |\boldsymbol{u} - \boldsymbol{u}_d| (\boldsymbol{u} - \boldsymbol{u}_d)$ where C_d is drag coefficient, A_d is droplet surface area, ρ and u are the density and instantaneous velocity of gas; the pressure force, F_p, is given by $-V_d \nabla p$, where V_d is the droplet volume; the body force originated from the gravity and acceleration present in a non-inertial coordinate frame, F_b, is expressed as $m_d[\mathbf{g} - \boldsymbol{\omega} \times (\boldsymbol{\omega} \times \boldsymbol{r}) - 2(\boldsymbol{\omega} \times \boldsymbol{u}_d)]$, where $\mathbf{g}$ is the gravitational acceleration, $\boldsymbol{\omega}$ is the angular velocity, and $\mathbf{r}$ is the distance vector. The last term represents the 'virtual mass' force, i.e. that required to accelerate the carrier fluid 'entrained' by the droplet, and the equation read $-C_{\text{am}} \rho V_d \frac{d(\boldsymbol{u}_d - \boldsymbol{u})}{dt}$, where C_{am} is the virtual mass coefficient.

Mass

For a miscible liquid multi-component droplets, the mass rate of change reads

$$\frac{dm_d}{dt} = -\varepsilon_i \frac{W_i}{\sum_{j=1}^{N} \varepsilon_j W_j} A_d K_g p_t \, ln \frac{(\varepsilon_i p_t - p_{vi,\infty})}{(\varepsilon_i p_t - X_{i,l} p_{vi,s}^0)} \tag{B.2}$$

where W_i is the molecular weight of component i, K_g is the mass transfer coefficient, and p_t, $p_{\mathrm{vi},\infty}$, and $p_{\mathrm{vs},\infty}$ are the gas pressure, and partial pressure of component i in the droplet surrounding and at the liquid-vapor interface.

Energy

The droplet energy equation is expressed as

$$m_d c_{p,d} \frac{dT_d}{dt} = -A_d q_d'' + h_{\mathrm{fg}} \frac{dm_d}{dt} \tag{B.3}$$

where $c_{p,d}$ is the specific heat constant of droplet, T_d is the droplet temperature, q_d'' is the surface heat flux in $q_d'' = h(T_d - T)$, and h_{fg} is latent heat vaporization.

Appendix C. Turbulent Premixed Combustion Regime

Turbulent premixed combustion means that the fuel and oxidizer are fully premixed at the molecular state and chemically react with each other in turbulent flow condition. Its structure and reaction status can be affected by the surrounding flow, and it has been characterized with a few non-dimensional number related to the length and velocity scales of turbulence and chemical reaction [174-176]. Figure C.1 shows the regime diagram of turbulent premixed combustion as proposed by [175], in terms of the normalized turnover velocity of integral length scale by laminar burning velocity, v'/s_L, and the normalized integral length scale by laminar flame thickness, l/l_F, respectively. Based on the normalized length and velocity scales, four additional non-dimensional parameters were incorporated to classify the combustion regime as follow.

Firstly, turbulent Reynolds number defines the ratio of inertia force to viscous force,

$$\mathrm{Re} \equiv \frac{v'l}{\upsilon} = \frac{v'}{s_L}\frac{l}{l_F} = 1 \ , \tag{C.1}$$

where the unity of Schmidt number ($\mathrm{Sc} = \upsilon/D$) is assumed. Secondly, turbulent Damköhler number characterizes the ratio of flow time at integral length scale (t_f) to the chemical reaction time (t_c),

$$\mathrm{Da} = \frac{t_f}{t_c} = \frac{l}{v'}\frac{s_L}{l_F}. \tag{C.2}$$

Thirdly, the second turbulent Karlovitz number defines the ratio of chemical reaction time scale to flow time scale at Kolmogorov length scale (t_η),

$$\mathrm{Ka} = \frac{t_c}{t_\eta} = \frac{l_F^2}{\eta^2} = \frac{v_\eta^2}{s_L^2} \ , \tag{C.3}$$

where the η denotes the Kolmogorov length scale as discussed in Appendix A. Lastly, the second turbulent Karlovitz number is defined as

$$\mathrm{Ka}_\delta = \frac{l_\delta^2}{\eta^2} = \delta^2 \mathrm{Ka} \tag{C.4}$$

where l_δ denotes the inner layer thickness of a laminar premixed flame. The turbulent Reynolds number divide the laminar and turbulent regime and we will focus on the latter one. When the turbulent intensity is smaller than the laminar burning velocity, $v'/s_L < 1$, the laminar flame propagation always compensates the flame wrinkling due to the turbulent perturbation. It is so called the wrinkled flamelet regime, and it is not of practical interest.

The corrugated flamelet regime is defined as when the turnover velocity of integral length scale is larger than the laminar burning velocity, $v'/s_L > 1$, and the laminar flame thickness is smaller than Kolmogorov length scale, $\mathrm{Ka} < 1$. The former indicates the eddy turnover motion corrugates the flame front, and the corrugated flame cannot be compensated by the kinematic advance of flame front. Despite the corrugation by turbulence, the entire reactive-diffusive flame thickness is still smaller than the Kolmogorov length scale so that the chemical and diffusive transport are preserved. In other word, the flame-turbulent interaction is purely kinematic.

Then the thin reaction zone regime is confined as the entire flame thickness is larger than Kolmogorov length scale, $\mathrm{Ka} > 1$, while the inner layer thickness is smaller than that one $\mathrm{Ka}_\delta < 1$. It implies the smallest eddies can penetrate into the reactive-diffusive flame without perturbing the inner layer, so that the diffusive

transports of chemical species are affected while the reaction layer remains to be unmodified.

The last one is the broken reaction zone, in which the Kolmogorov length scale becomes smaller than the inner layer thickness, $\mathrm{Ka}_\delta \geq 1$. As eddies penetration into the reaction layer, the chemical reaction became extinguished due to excessive heat loss towards the preheat zone. Similar to the wrinkled flamelet regime, it is not of practical interest.

Experimental observations on premixed flame under a wide range of flow, thermo-chemical conditions declared that its structure is remarkably robust [177]. Also, it has been demonstrated that the combustion process for a typical spark-ignition engine lies predominantly in the corrugated flamelet and thin reaction zone regimes [178-180]. Hence the flamelet concept, thin reactive-diffusive layers embedded within an otherwise non-reacting turbulent flow field, can be introduced for the turbulent premixed combustion modeling [114].

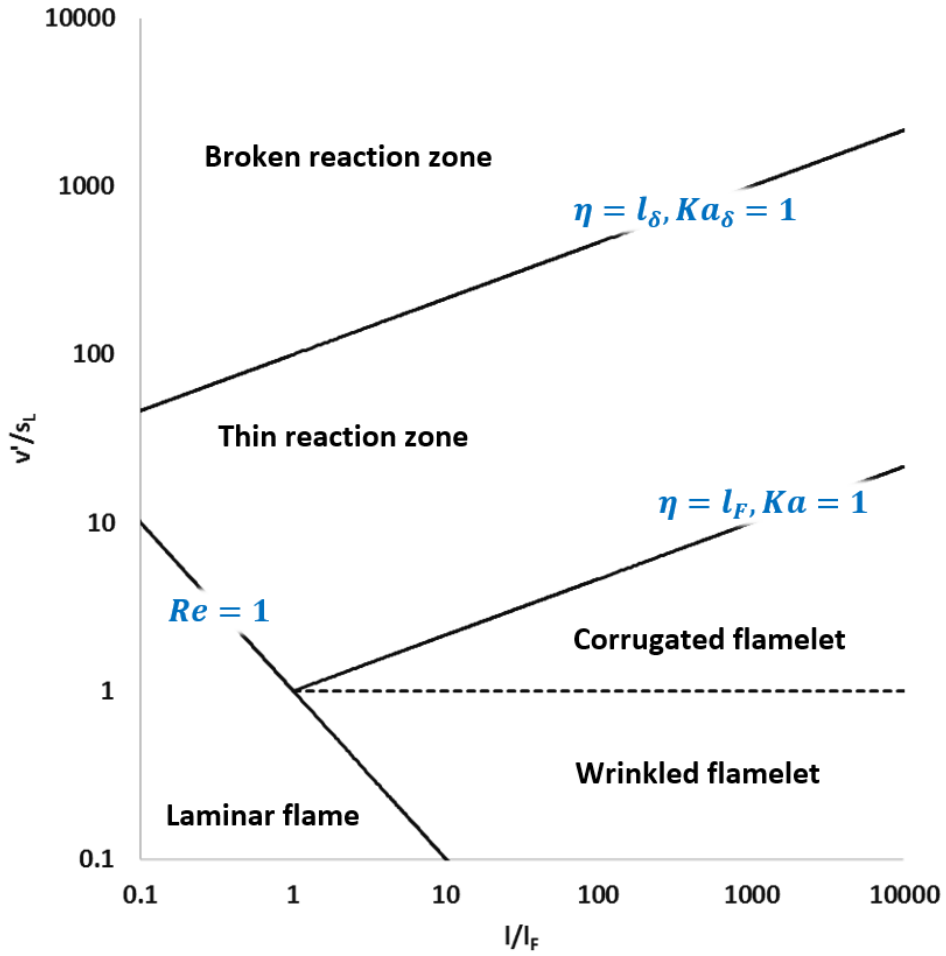

Figure C.0.1 Diagram of turbulent premixed combustion regime [114].

국 문 초 록

전 세계적으로 지구 온난화와 환경문제가 대두됨에 따라 운송수단에서 배출되는 이산화탄소에 대한 규제가 날이 갈수록 강화되고 있다. 직접분사식 가솔린 엔진은 과급 시스템과 결합하여 기존 포트분사식 엔진 대비 출력과 열효율을 향상시킬 수 있는 장점을 지니며 차세대 엔진 기술로 주목 받고 있다. 그러나 연료를 실린더 내 직접 분사함에 따라 입자상물질 배출이 증가하고, 개수농도 수준이 입자상물질 여과 장치를 탑재한 디젤 엔진보다 높은 것으로 보고되어 중대한 환경 이슈로 부각되었다. 2017 년부터 시행되는 배기규제는 직접분사식 가솔린 엔진의 입자상물질 개수를 $6x10^{11}$/km 로 규제하고 있으며, 후처리 장치 없이 이를 만족하기 위해서는 엔진 연소실 형상 및 운전 전략의 최적화가 필수 불가결하다.

직접분사식 가솔린 엔진에서는 부분 예혼합된 연료-공기가 형성되고, 전기 점화에 따른 연소 과정 중에 국부적으로 농후한 지역과 연료 액막이 점착된 벽면 근처에서 입자상물질이 생성되는 것으로 알려져 있다. 이는 디젤 엔진이 확산 연소 중에 연료분무 중심에서 입자상물질이 배출되는 구조와 다르며, 또한 엔진의 입자상물질 배출 모델링에 관한 기존 연구가 대부분 확산 화염을 기반으로 이루어졌기 때문에 직접분사식 가솔린 엔진에 적합한 모델 개발이 필요하다.

본 연구에서는 연료-공기 혼합기장의 거동, 연료가 농후한 영역의 연소에 착안하여 직접분사식 가솔린 엔진의 연소 및 입자상물질 배출 모델을 개발하였다. 우선 모사 연료와 분무 분열 모델링을 수행하였다. 각 모델은 휘발유의 본질적인 증발 특성과 연료 인젝터의 고유한 무화 특성을 고려한 것으로, 전기 점화 이후 연소 과정의 초석이 되는 연료-공기 혼합기장을 보다 정확히 예측하는데 주안점이 있다. 연료 모델은 실제 휘발유의 증류성상 및 방향족 함량을 측정한 성분분석 결과를 기반으로 이를 모사할 수 있는 6 성분

가솔린 모사 연료로 구성되었다. 분무 분열은 Kelvin-Helmholtz/Rayleigh-Taylor 모델을 이용하였고 리그 시험에서 계측된 액적크기분포 및 분무관통길이 결과를 기반으로 개정되었다.

연소 과정은 G-Equation 모델을 기반으로 부분예혼합 난류화염전파를 모사하였다. 연료가 농후한 영역에서의 연소율을 정확히 예측하기 위해 가솔린 연료의 층류화염속도를 모델링 하였다. 파라핀 계열 탄화수소의 층류화염속도를 가솔린 연료에 적용한 기존 연구와는 달리, 방향족 탄화수소가 연료가 농후한 당량비 영역에 미치는 영향을 고려하였다. 따라서 이소옥탄, 노멀헵탄, 톨루엔의 층류화염속도를 다양한 온도, 압력, 당량비 조건에 대하여 1 차원 화염 시뮬레이션을 통해 계산하였고, 이를 각 연료에 대한 대수방정식으로 곡선 근사를 수행한 후 에너지 분율 기반으로 혼합하였다.

입자상물질 배출은 다환형 방향족 탄화수소의 형성으로부터 개시되어 입자상물질의 핵화, 엉김, 표면성장 및 산화로 이어지는 물리 현상임에 착안하여 화염소 라이브러리를 도입한 상세 입자상물질 모델 구조를 제안하였다. 화염면 후단의 기연 조성은 층류 화염소 방정식을 통해 라이브러리로 구축되었고, 주요 연소 생성물을 비롯하여 입자상물질의 전구체가 되는 다환형 방향족 탄화수소 화학종들도 포함하였다. 이는 시뮬레이션 중에 화학반응을 직접 계산하여 Pyrene($C_{16}H_{10}$)을 얻는 기존 연구와 달리, 시뮬레이션 수행 전 라이브러리를 구축하는 방식으로 시뮬레이션의 추가 비용 없이 상세화학반응 메커니즘을 도입하고, Coronene($C_{24}H_{12}$)까지의 농도를 계산하였다. 상기 연소 모델은 4 단계 준-실험 입자상물질 모델과 연소 모델을 결합하였고, 더 나아가 모멘트법 기반 에어로졸 모델과 결합하여 입자상물질의 배출 수준을 예측하였다.

본 연구에서 개발된 연소 및 입자상물질 배출 모델은 우선 촉매가열 조건에서 다양한 분사시기를 갖는 단기통 엔진 실험 데이터와 비교하여 예측도를 평가하였다. 해석 결과 연료 및 분무 분열 모델은 기존 연구들의 모델 대비 농후한 연료-공기 혼합기장과 연료 액막량을 적합하게 모사하고 있음을 확인하였고, 층류화염속도 모델의 확장된 당량비 예측 범위를 통해 실험

질량연소율을 정확하게 계산할 수 있음을 검증하였다. 또한 냉간 조건에서 다단 분사 전략으로 운전되는 단기통 엔진 실험을 수행하였고, 연소 및 입자상물질의 개수와 농도 수준을 계측하였다. 본 연구에서 개발된 연소 모델이 실험의 실린더 압력을 질량연소율 기준 5% 이내로 잘 추종할 수 있음을 확인하였고, 연료 분사 다단화에 따른 입자상물질 배출 저감의 경향을 적합하게 예측할 수 있음을 검증하였다.

따라서 본 연구는 직접분사식 가솔린 엔진의 혼합기 형성 및 농후한 영역의 연소를 주안점으로 연소 및 입자상물질 배출을 모델링하였고, 엔진 실험 결과와 비교하여 모델의 예측 가능도를 평가하고 검증하였다. 본 연구의 결과는 향후 엔진 개발 단계에서 연소실 형상 및 운전 전략 최적화에 활용될 수 있을 것으로 기대된다.

주요어 : 직접분사식 가솔린 엔진, 연소, 입자상물질, 가솔린 모사 연료, 화염소 라이브러리, 상세 입자상물질 모델 구조

학 번 : 2010-20663